# INVESTIGATION OF THE RESIN FILM INFUSION PROCESS FOR MULTI-SCALE COMPOSITES BASED ON THE STUDY OF RESIN FLOW, VOID FORMATION AND CARBON NANOTUBE DISTRIBUTION

By

Simon Baril-Gosselin

Thesis submitted
in partial fulfilment of the requirements
for the Doctorate in Philosophy degree in
Mechanical Engineering

Ottawa-Carleton Institute for Mechanical and Aerospace Engineering
Faculty of Engineering
University of Ottawa

# Acknowledgements

I would like to express my deepest gratitude to my supervisor Professor François Robitaille without whom this work would not have been possible. I am grateful for his support, encouragement and great patience throughout this work. His inspiring advices and criticism guided this thesis towards completion.

The Natural Sciences and Engineering Research Council of Canada (NSERC) and Consortium for Research and Innovation in Aerospace in Quebec (CRIAQ) are also gratefully acknowledged for their support of the collaborative project COMP-510 between Bombardier Aéronautique, Nanoledge (Axson), McGill University and the University of Ottawa on the fabrication of multi-scale composites through resin film infusion (RFI).

I would like to thank all my colleagues of the COMP-510 project, namely Professor Pascal Hubert, Mostafa Yourdkhani and Wenjiao Liu from McGill University, Antoine De Brux from Bombardier Aéronautique and Patrice Lucas from Nanoledge for their support on RFI and nano-materials. I am especially grateful to my colleague Yue El-Hage from the University of Ottawa with whom I shared the joys and difficulties of fabricating multi-scale composites.

I would like to thank all the people at the University of Ottawa that supported me during this work. Many thanks to undergraduate students Cedric Eveleigh and Jaime Ocanã who participated in the experimental manipulations for the in-situ characterisation of the RFI process, and to Dr Mohammed Yandouzi for his advices on optical microscopy and SEM.

I would like to thank the people at the Aerospace Research Centre of National Research Council Canada, particularly Dr Chun Li and Hugo Laurin, that provided equipment and support for the characterisation of the physico-chemical properties of the materials used in this work. Their contribution enabled the development of a more complete description of the RFI process.

Finally, I would like to thank my friends and family for their support and encouragement. Most particularly to Marina Pushkareva for her understanding and love during these last years, and to my mother Johanne Baril and father Alain Gosselin for giving me the motivation to pursue my goals.

## Abstract

The aerospace industry is steadily increasing its use of polymer-matrix composites (PMCs) in airframe structures as it seeks to benefit from the high specific in-plane strength of laminated structural PMCs. However, PMC laminates suffer from low interlaminar shear strength due to their weaker polymer-matrix. Minimising risks of delamination is of paramount importance towards improving the safety of PMC structures. Multi-scale composites that are reinforced by both continuous fibres and nano-particles were identified as a potential solution for improving toughness and reducing risks of delamination in PMCs.

An important challenge in the fabrication of multi-scale PMCs is to ensure that nano-particles are dispersed uniformly within the matrix. This is only achieved through minimal filtration of nano-particles during processing. The short resin flow lengths enabled by the resin film infusion (RFI) process make this process a prime candidate for the fabrication of multi-scale PMCs.

The main objective of this thesis is to validate the possibility of using out-of-autoclave RFI for fabricating multi-scale carbon fibre composites featuring epoxy resins modified with carbon nanotubes (CNTs). The work is accomplished in 5 phases.

In phase 1, preliminary work investigates the fabrication of PMCs with and without CNTs, using out-of-autoclave RFI. Results show that the types of reinforcement and matrix have strong effects on the porosity and interlaminar strength of PMCs. These results ushered the need for more thorough investigation and understanding of the RFI process, beyond what is available in the literature.

Phases 2 to 4 focus on understanding how the choices of materials and types of stacking configuration can affect parts made using RFI. Phase 2, the in-situ characterisation of resin saturation during RFI is performed. Results enable a detailed analysis of the way in which resin flows around and inside yarns. Phase 3 consists in the characterisation of void formation during RFI. Two types of voids are observed: flow-induced voids resulting from either the merging of resin flow fronts; and gas-induced voids resulting from resin volatiles going out of solution and remaining in the resin matrix. In this work, the greatest source of

porosity was caused by volatiles. In phase 4, the distribution and filtration of CNTs during RFI processing is characterised. Results show that processing choices can limit filtration and that clustering of CNTs prevents a uniform dispersion of CNTs in PMCs.

Finally, the possibility of using RFI for making a multi-scale PMC demonstrator part is investigated. The work culminated with the successful fabrication of a delta-stringer panel.

This thesis makes several important contributions to the knowledge pertaining to multi-scale PMC processing and performance, and to RFI. Firstly, it provides a robust description of RFI processing beyond was it available in literature, through in-situ observations of resin flow and void formation. Secondly, it assesses the viability of RFI for producing multi-scale PMCs featuring CNTs. In-situ observations of RFI processing enabled the identification of mechanisms leading to a loss of CNT dispersion during processing, partly explaining the minimal improvements in the interlaminar properties of composites observed when adding CNTs to the matrix. Thirdly, the fabrication of a delta-stringer panel made of a multi-scale PMC was successful, making it the first validation of the scalability of out-of-autoclave RFI processing for manufacturing multi-scale PMCs. The work presented herein contributed to the dissemination of knowledge; one conference paper was presented at ICCM20 (20$^{th}$ International Conference on Composite Materials), and another was presented at CANCOM2017 (10$^{th}$ Canadian-International Conference on Composites), and one journal article written in collaboration with project partners was submitted to Composites Science and Technology.

# Table of contents

# List of figures

# List of tables

# Nomenclature

## Latin Symbols

| | |
|---|---|
| $A$ | Area [$m^2$] |
| $CF$ | Fabric cover factor |
| $CF_x$ | Linear fabric cover factor |
| $d_f$ | Fibre diameter [m] |
| $d_s$ | Spacing [m] |
| $F_S$ | Flow shape factor for the capillary pressure |
| $N_{plies}$ | Number of plies |
| $P_C$ | Capillary pressure [Pa] |
| $P_M$ | Mechanical pressure [Pa] |
| $t$ | Thickness [m] |
| $t_y$ | Yarn thickness [m] |
| $V$ | Volume [$m^3$] |
| $V_f$ | Global fibre volume fraction |
| $V_{fy}$ | Fibre volume fraction inside yarns |
| $V_v$ | Void volume fraction |
| $V_y$ | Yarn volume fraction |
| $w_y$ | Yarn width [m] |

## Greek Symbols

| | |
|---|---|
| $\gamma$ | Surface tension [$mJ/m^2$] |
| $\theta_C$ | Contact angle [°] |
| $\rho$ | Density [$kg/m^3$] |
| $\rho_s$ | Surface density [$g/m^2$] |

# Acronyms

| | |
|---|---|
| CNT | Carbon nanotube |
| CRIAQ | Consortium for Research and Innovation in Aerospace in Quebec |
| CVFEM | Control volume finite element method |
| FEM | Finite element method |
| ILSS | Interlaminar shear strength |
| MWCNT | Multi-walled carbon nanotube |
| PMC | Polymer matrix composite |
| RFI | Resin film infusion |

# Chapter 1

# Introduction

## 1.1 Background

The aerospace industry is steadily increasing its use of polymer-matrix composites (PMCs) in airframe structures as it seeks to benefit from the high specific in-plane strength of laminated structural PMCs. However, PMC laminates suffer from low interlaminar shear strength due to their weaker polymer-matrix. In the case of brittle thermosetting polymer matrices e.g. epoxy, cracks can propagate rapidly between reinforcement layers resulting in catastrophic failure. Hence, minimising the risk of delamination is of paramount importance for improving the safety of PMC structures.

Several solutions exist for toughening PMCs and lowering the crack propagation rate, including 1) use of 3D reinforcements [1, 2], and 2) modification of polymer matrices through new formulations and/or toughening agents [3–6]. Promising toughening agents were identified in the form of nano-reinforcements having a high aspect ratio such as carbon nanotubes (CNTs). However, even for a constant loading of the same CNTs, improvements in mechanical properties resulting from their addition differ widely based on processing conditions and CNT distribution within the matrix [7, 8]. Nonetheless, in an encouraging scenario Geng et al. [9] observed a 60% improvement in impact fracture toughness achieved by adding only 0.25 wt% of multi-walled carbon nanotubes (MWCNTs) to a neat epoxy. Another advantage of CNTs is that unlike polymer-based toughening agents [10–12] they do not affect adversely the glass transition temperature of

polymer matrices, and they can even lead to increases the glass transition temperature [5, 7, 9].

Unfortunately, the use of polymer resins loaded with nano-reinforcements, hereafter termed nano-modified resins, in the fabrication of PMCs remains limited due to difficulties in processing. Firstly, the increase in resin viscosity caused by the addition of nano-reinforcements leads to poorer processability compared with neat resins [5, 13]. Secondly, it is challenging to obtain PMCs featuring nano-modified resins, hereafter termed multi-scale PMCs, with a uniform distribution of nano-reinforcement, resulting in potentially weaker regions of neat resin. This can be attributed to a marked tendency of nano-reinforcements towards agglomeration when they are given sufficient mobility [14, 15], but also to filtering caused by the dense fibre network of fabric reinforcements [13, 16, 17].

Currently, a robust solution for manufacturing multi-scale PMCs effectively at an industrial scale is still lacking. The solution for mitigating both the effect of viscosity increase from nano-modification, as well as the effect of nano-reinforcement filtration, lies in minimising the resin flow distance. Since PMCs are often made by laminating thin reinforcements, the processing technique should favour through-thickness resin flow as opposed to in-plane flow. Moreover, it has been shown that nano-reinforcements such as CNTs tend to align in the resin flow direction when subjected to sufficient levels of shear stress [18]. Such alignment would be particularly useful in improving the weak interlaminar properties of PMCs as nano-modified polymers are stronger when their nano-reinforcements (e.g. CNTs) are aligned in the loading direction [19, 20]. Thus, in the ideal case, the selected processing technique should lead to a multi-scale PMC that is reinforced by continuous in-plane fibre reinforcements and through-thickness nano-reinforcements (Figure 1.1).

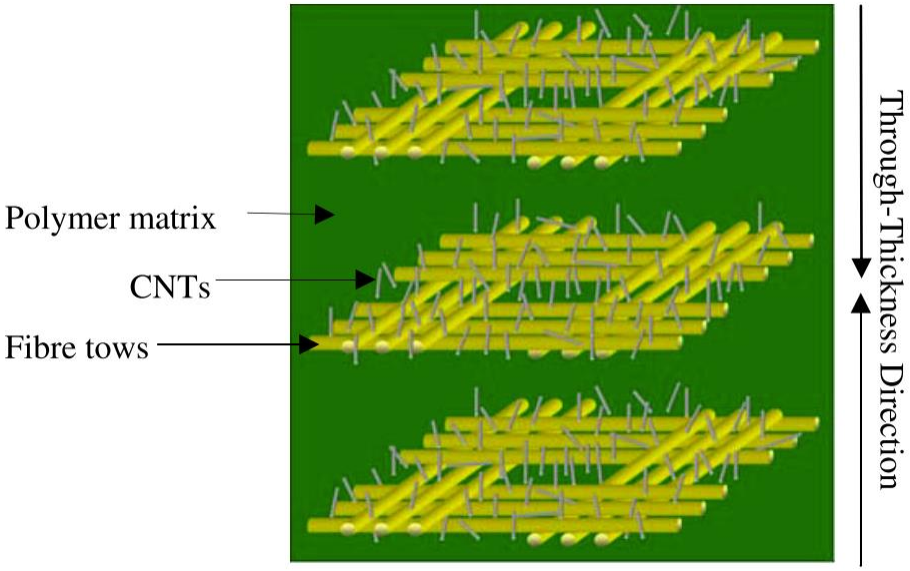


Figure 1.1: Lay-up of fabric impregnated with MWCNT/epoxy [21]

Resin film infusion (RFI) was identified [5, 6] as a potential process for manufacturing multiscale PMCs with nano-modified resins. In this process, resin films and fabric layers are stacked with various possible levels of interleaving. The stacks are then processed through vacuum bagging in- or out-of-autoclave in a way that is generally similar to manufacturing based on pre-preg materials (Figure 1.2). The advantages of RFI for multi-scale PMCs are that the initial nano-reinforcement distribution within the resin film can be controlled and made consistent, and that short resin flow lengths in the through-thickness direction can limit filtering and possibly orient the nano-reinforcements. However, no exhaustive analysis of RFI for manufacturing multi-scale PMCs was reported, aside from limited data collected from tensile, compressive and interlaminar fracture toughness testing [5, 6].

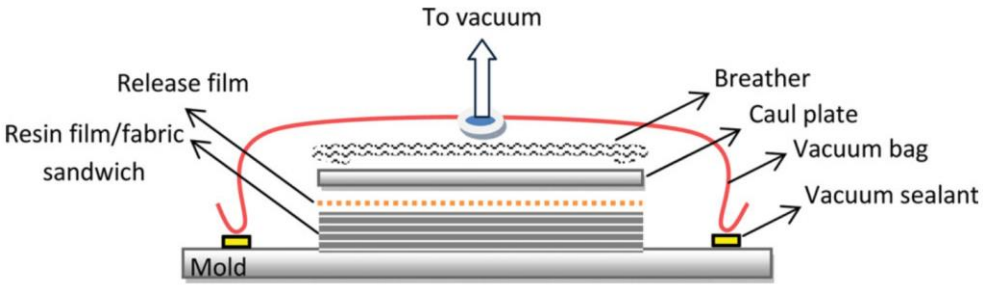


Figure 1.2: Schematic of the RFI process [5]

The lack of information regarding PMCs manufactured using RFI spurred collaborative project CRIAQ (Consortium for Research and Innovation in Aerospace in Quebec) COMP-510, aiming at developing and characterising multi-scale PMCs featuring CNT nano-modified epoxies. The project involved two academic institutions, University of Ottawa and McGill University, and two industrial partners, Bombardier Aerospace and Axson, formerly Nanoledge. Project partners investigated the physico-chemical, mechanical, thermal and electrical properties of nano-modified epoxies and multi-scale PMCs, as well as their processability.

## 1.2 Objectives

The CRIAQ COMP-510 project led to this thesis. The main objective of the work presented herein is to validate the viability of out-of-autoclave RFI processing for fabricating multi-scale carbon fibre PMCs featuring epoxy modified with CNTs, following a methodology that can be used at industrial scale. Ultimately, the project sought to develop technical knowledge on how a manufacturer such as Bombardier may identify and control processing parameters that enable the reliable production of high quality multi-scale PMC structures, defined in this work as PMCs featuring high interlaminar strength. This can be achieved by minimising the void content an ensuring a uniform distribution of the CNTs.

The viability of the process is investigated through the characterisation of many physical and technical aspects of RFI including material properties, stack compaction behaviour, impregnation kinematics, void content, fibre volume fraction, homogeneity of the nano-reinforcement distribution and interlaminar strength.

A thorough quantitative description of the RFI process is developed through experiments conducted using a wide array of materials and processing parameters. The materials tested include fabric reinforcements featuring different architectures such as weaves and non-crimp fabrics, and resin films with various properties including different viscosities and CNT loadings. The processing parameters tested include the level of interleaving of stacks of fabric reinforcement plies and resin films, the bagging

arrangement and the geometry of parts. Based on these parameters, the core of the work focused on three aspects of manufacturing that have a direct control on the quality of PMCs: 1) *resin flow kinematics* to understand how to maximise resin saturation in PMCs, 2) *void formation* to understand how to minimise defects and strengthen PMCs, and 3) *distribution and filtration of CNTs* to maximise the uniformity of the matrix properties and thus improve the interlaminar shear strength of PMCs. Finally, a delta-stringer demonstrator panel is fabricated to assess the scalability of the process towards industrial usage.

High-level milestones achieved through this thesis work are as follows:

1. Identification of processing parameters affecting quantifiably the quality of PMCs processed through RFI, in terms of void content, fibre volume fraction and interlaminar strength.
2. Quantitative description of the kinematics of saturation through in-situ experiments and simulations of resin flow performed at various scales.
3. Characterisation of the mechanisms leading to void formation based on in-situ observations.
4. Characterisation of CNT filtration and evolution of CNT dispersion during processing.
5. Fabrication of a demonstrator part for assessing the industrial scalability of RFI for manufacturing multi-scale PMCs.

The author analysed all results and performed most technical tasks involved. However, the milestones above would not have been reached without the contribution of several great people. RFI panels were made in collaboration with Yue El-Hage and were used for her M.A.Sc. degree on heat transfer in PMCs as well as for this thesis on RFI processing. Two undergraduate students from the University of Ottawa, Cedric Eveleigh and Jaime Ocanã, helped with collecting data from in-situ resin flow experiments and mechanical testing, and contributed to the fabrication of demonstrator parts. Mostafa Yourdkhani and Wenjiao Liu from McGill University helped with the fabrication of the multi-scale PMC demonstrator. Hugo Laurin and Dr Chun Li from National Research

Council of Canada Aerospace provided rheology data for the resins. Patrice Lucas from Axson and Prof. Pascal Hubert from McGill University supplied nano-modified epoxy resins for making multi-scale composites. Finally, Prof. François Robitaille, supervisor of the author, provided much needed guidance and support.

## 1.3 Contributions

The work performed towards the completion of the thesis led to four original contributions in the field of engineering.

1. The work is the first to characterise quantitatively and in full the mechanisms driving resin impregnation into fabric reinforcements in the RFI process at the scales of fibres, yarns and parts, taking spatial variation of parameters into consideration. This is achieved by testing various types of fabrics and resin films, providing a large database for assessment. The information provides a better understanding of resin flow and how to control it when using RFI. This led to the proposal of guidelines for minimising flow-induced voids for the production of safer PMC parts.

2. The work is the first to characterise quantitatively and in full the mechanisms driving the formation of voids resulting from out-of-solution volatile gases during RFI processing. This is achieved through direct monitoring of the kinematics of out-of-solution volatile gases during processing and through testing various types of fabrics and resin films, providing a large database for assessment. The knowledge developed led to the proposal of guidelines for controlling the amount of out-of-solution volatile gases during processing, resulting in safer PMC parts.

3. The work is the first to characterise in full the evolution of CNT distribution during RFI processing. The two major causes affecting CNT distribution are the filtration from the fabric reinforcement during resin flow and the clustering of CNTs that occurs due to low resin viscosities reached during RFI processing. The wide diversity of materials tested enabled the formulation of guidelines for the selection of fabrics and levels of resin film interleaving for manufacturing multi-scale PMCs.

4. The work results in the fabrication of demonstrator parts, leading to the first assessment of the scalability of RFI for manufacturing multi-scale PMCs.

In addition, the work contributed to the dissemination of knowledge; one conference paper was presented at ICCM20 ($20^{th}$ International Conference on Composite Materials), and another was presented at CANCOM2017 ($10^{th}$ Canadian-International Conference on Composites), and one journal article written in collaboration with project partners was submitted to Composites Science and Technology.

## 1.4 Thesis outline

This thesis is divided into 11 chapters. Core chapters 4 to 10 discuss all experiments and results that were required for fulfilment of the thesis objectives.

Chapter 1 describes the rationale of the thesis, its objectives and contributions.

Chapter 2 presents a literature review of the current state-of-the-art on RFI processing. It defines the RFI process and its various forms, and discusses the experimental and modelling work that was done previously towards investigating the process parameters that affect resin infusion and PMC quality. In addition, it investigates previous work that was made for the fabrication of multi-scale PMCs.

Chapter 3 presents the research plan. It discusses the approach selected towards achieving a detailed and complete description of the RFI process. The chapter also details the equipment and characterisation methods used in achieving the research goals.

Chapter 4 presents the characterisation of resins selected for the work. It describes the resin viscosity, surface tension, contact angle and CNT distribution of resin films.

Chapter 5 presents the characterisation of fabrics selected for the work. It focuses on the geometrical description, permeability and compaction behaviour of dry fabrics.

Chapter 6 discusses the effect of processing parameters on the quality of PMCs in terms of void content, fibre volume fraction and interlaminar strength. Parameters tested

include fabric architecture, resin formulation, CNT loading, bagging method and level of interleaving. Processing issues observed in PMCs are then studied in greater details in chapters 7 to 9.

Chapter 7 studies the kinematics of resin flow in RFI through in-situ observations of the process, and numerical simulations. The work investigates the effects that the level of stack interleaving, fabric architecture, resin formulation and CNT loading have on flow separation and saturation time.

Chapter 8 studies the formation of voids during RFI processing through in-situ characterisation of resin saturation. Three types of void formation mechanisms are investigated, namely flow-induced voids from resin flow separation, flow-induced voids from excessive wicking, and gas-induced voids due to out-of-solution volatiles. In this work, the latter was found to be the most important contributor to void formation and is studied more exhaustively.

Chapter 9 studies the evolution of CNT distribution during RFI processing through the characterisation of CNT filtering and CNT clustering. The work investigates the effects that the direction of resin flow, level of stack interleaving and fabric architecture have on CNT filtration. The work also investigates the effect of the resin viscosity on the formation of CNT clusters.

Chapter 10 describes the design process for the fabrication of delta-stringer panels through RFI. Different fabrication methods are evaluated, leading to the selection of a method for making a full-scale technological demonstrator. The work culminates with the fabrication and comparison of neat PMC and multi-scale PMC demonstrators.

Chapter 11 discusses and summarises the contributions of the thesis. It also provides an outlook for the use of RFI as a method for producing multi-scale PMCs.

# Chapter 2

## Literature review

This chapter presents an assessment of the current state of RFI practice, and state of the art for multi-scale composites. It is divided in five sections. Firstly, the RFI process is described and its main benefits are discussed. Then, resin flow and void formation, the two main aspects of RFI relevant to manufacturing of PMCs, are presented in their respective sections. Then, a section is dedicated to the use of CNTs in PMCs. It describes CNTs and the way in which they can be integrated into polymers and PMCs. The review ends with a conclusion.

### 2.1 Resin film infusion

RFI is a liquid composite moulding (LCM) process for manufacturing PMC parts. The process relies on through-thickness resin infusion for impregnating dry fabric reinforcements prior to part consolidation. RFI uses a hot-melt resin generally supplied in film form, although strip [22] and powder [23, 24] forms can also be used. RFI part manufacturing consists in stacking resin films with dry fabric reinforcements, vacuum bagging the stack and curing in an oven or in an autoclave in a procedure similar to PMC manufacturing using fabrics pre-impregnated with resin (pre-pregs). During processing, resin films melt and liquid resin infuses into the reinforcements. Infusion is driven by the external pressure applied through the autoclave, vacuum and/or press, and also by capillary forces.

Two main variations of the RFI process exist, differentiated by the stacking configuration of the resin films and dry fabric reinforcements. The first variation consists in

separating the resin and reinforcement into distinct stacks that are superimposed for manufacturing. This method, referred hereafter as the bulk RFI method, has all the resin placed on one side of the reinforcement, either above or below (Figure 2.1.a). The second method, referred hereafter as the interleaved RFI method, uses resin films interleaved between plies of dry fabric reinforcement (Figure 2.1.b). Interleaving can be achieved during lay-up; alternatively, commercial materials already interleaved are available in the form of partially impregnated fabric reinforcements (semi-pregs). SP Systems were the first to offer such commercial product (SPRINT™) [25] but other companies also offer similar products, including Hexcel (HexFIT®) [26] and Umeco/Cytec (ZPREG) [27].

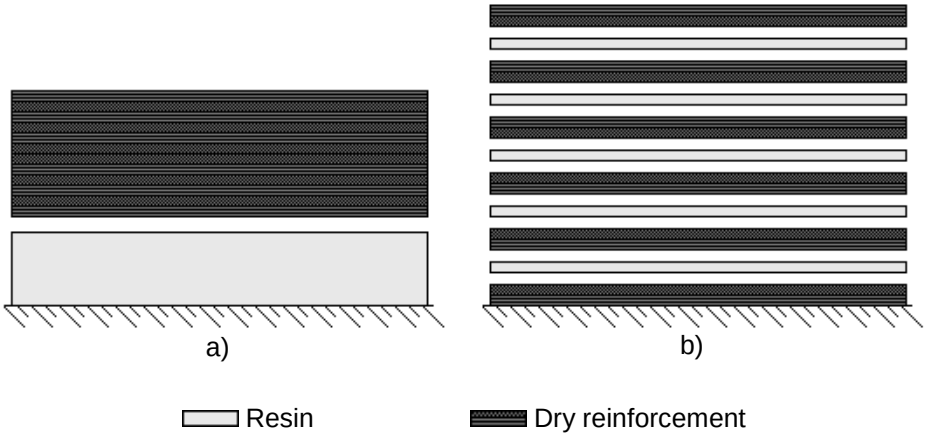


Figure 2.1: RFI variations based on the stacking sequence: a) bulk method and b) interleaved method

Resin film infusion was originally patented (US 4,622,091) in 1986 by Letterman on behalf of the Boeing Company [28]. It was developed for addressing concerns with pre-preg PMC manufacturing.

Firstly, separating the fabric reinforcement from the resin in the bulk RFI method enabled the use of stitched preforms that can improve interlaminar properties by reducing crack propagation in PMCs, and improve residual strength after impact due to the presence of through-thickness reinforcement fibres [29–32].

Secondly, the dry fabric reinforcement in RFI provides channels for evacuating gas, effectively acting as a breather [4, 22]. This lowers greatly the risk of air and volatile entrapment compared to pre-preg, eliminating the need for an autoclave for collapsing any entrapped air or volatiles. Frost et al. [22] manufactured automotive body panels with three different out-of-autoclave semi-preg materials and noticed that the greater breathability of the dry fabric reinforcement lowered the surface roughness of PMC parts by 10% to 50% compared with pre-preg parts.

Thirdly, B-stage resin in the pre-preg requires storage in a freezer for slowing the cure reaction, but even at low temperatures pre-preg remains perishable. When expired, both the resin and the fabric are discarded. In RFI, only B-stage resin films require storage in a freezer for extending their shelf life. Absence of the fabric in the freezer increases resin storage capacity and most importantly, when the resin expires the fabric is not discarded, enabling great savings [24]. However, this advantage does not apply to semi-preg products that are discarded like pre-pregs.

Fourthly, RFI manufacturing can enable lower labour costs than pre-preg PMC manufacturing. Benefits are greater with the bulk RFI method due to the possibility of using near net-shape preforms that reduce lay-up time substantially compared to the ply collation of pre-pregs [23, 29]. Working on the Air Force SBIR program, Stenard et al. [33] showed that the use of RFI with braided performs enabled labour time of 4 hours for RFI lay-up, down from 8 hours for pre-preg lay-up. Commercially available semi-preg products applicable towards the interleaved RFI method can also reduce labour costs due to the possibility of using thicker plies compared with pre-preg, reducing handling steps for ply stacking [22].

The RFI process also distinguishes itself from common LCM processes such as resin transfer moulding (RTM) and vacuum-assisted resin transfer moulding (VARTM). As opposed to most LCM processes, RFI relies on short distance through-thickness infusion for impregnating fabric reinforcements instead of long distance in-plane infusion. Shorter infusion distances in RFI enable the use of higher viscosity resins that feature toughening agents, reducing the risks of catastrophic failure in PMC parts [3, 34, 35]. For very short

infusion distances, as seen with the interleaving RFI method, high viscosity pre-preg resins are suitable for RFI processing. Greater infusion distances in the bulk method require resins of slightly lower viscosity for completing the impregnation. Nevertheless, resins of much higher viscosity can be used, compared with in-plane infusion [28]. Shorter infusion distances also reduce particle filtering from the fabric reinforcement; this enabled Anand et al. [5] to use RFI for manufacturing PMCs with epoxy reinforced with CNTs. Shorter infusion distances also make RFI more suitable for manufacturing larger PMC parts [34, 35]. RFI involves less equipment and less disposables as no infusion system, resin pump and tubing are required. Furthermore, shorter infusion distances reduce processing time, allowing cost savings [34, 36].

As stated above, one of the main drivers for the RFI process is its potential for savings in manufacturing high-performance PMC parts [23–25, 29, 33–40]. The APRICOS and TANGO consortiums of airframes manufacturers reported that RFI using non-crimp reinforcement fabrics is a viable alternative to PMCs made using pre-preg for fuselage skin and stringers, due to the short infusion distances [35]. Bader [37] compared various methods for manufacturing PMCs and developed a cost-performance ratio based on manufacturing cost, mechanical behaviour and monetary savings arising from a reduction in weight. For high-value PMC parts, RFI offered a better cost-performance ratio than both in-autoclave manufacturing using pre-preg and RTM manufacturing. NASA [38] and Qi et al. [39] reported cost savings of 10% to 20% when replacing pre-preg PMC manufacturing with in-autoclave RFI. Booker and Leon [40] from Boeing did a study on replacing pre-preg PMC manufacturing with other processes. Out-of-autoclave RFI using semi-preg materials and VARTM enabled cost savings of 55% and 75% respectively compared with PMC manufacturing using pre-preg.

A summary of RFI process characteristics as mentioned above appears in Table 2.1. Despite some advantages offered by RFI over PMC manufacturing using pre-preg and LCM processes, concerns remain. The two main concerns with RFI are: 1) complete resin impregnation of dry fabric reinforcements and 2) void formation. Both topics will be discussed further in the sections 2.2-2.3.

Table 2.1: Comparison of PMC manufacturing processes

| Characteristic | Process | | |
|---|---|---|---|
| | RTM/VARTM | RFI | Pre-preg |
| Possibility of using stitched preforms | Yes | Yes | No |
| Possibility of using toughened resins | No, low viscosity process requirement | Moderate, depends on infusion distance | Yes |
| Infusion equipment | Expensive | No injection ancillaries | No injection ancillaries |
| Gas removal | Good escape path form dry fabrics | Good escape path form dry fabrics | Low due to absence of dry fabrics |
| Material shelf life | Good, resin and hardener are not pre-mixed | Only resin film is perishable | Fabric and resin combined in a pre-preg are perishable |
| Labour cost | Moderate, less ply stacking | Moderate, less ply stacking | High, long ply stacking and debulking |

## 2.2 Resin flow in resin film infusion

In all LCM processes, including RFI, control of resin flow is critical for maximising saturation of a part before resin gelation. Resin flow can be studied at the macroscopic scale, i.e. at the scale of a part, for preventing dry regions or at the microscopic scale, i.e. at the scale of fibres and yarns to understand how the heterogeneity of the reinforcement structure can affect resin flow and air entrapment. This section first discusses experimental work studying resin flow during RFI, and follows with a discussion of the modelling of RFI processing and resin flow.

### 2.2.1 Experimental work on resin flow

This subsection discusses resin flow during RFI at the macroscopic and microscopic scales, and how processing parameters affect saturation of parts.

#### 2.2.1.1 Macroscopic scale

Most published work on RFI focuses on maximising the resin flow lengths for saturating PMC parts, disregarding the effect that the fibre reinforcement heterogeneity has

on local resin flow. Such work mainly studies RFI parts made with bulk RFI as its stacking configuration features the longest resin flow lengths.

In RFI processing, the driving force for resin infusion consists mainly of applying an external pressure on a stack of fabric reinforcements and resin films through an autoclave or a vacuum. The stack gets compressed and the pressurised resin flows towards zones of low pressure. The low permeability of the fabric reinforcements acts as a resistance to resin flow; greater flow lengths thus necessitate the application of greater pressures. In parts featuring long flow lengths such as in an integrally stiffened part made through the bulk RFI method (Figure 2.2), the use of high pressure autoclaves is mandatory [23, 33, 41–43]. Moreover, since resin flow is driven by a difference in pressure, is it imperative that the external pressure gets transferred effectively to the resin. Improper contact between the fabric reinforcements, resin films, tool and ancillaries will lead to low pressure zones that limit resin flow, resulting in unsaturated fabric zones [33]. Finally, at low applied pressures, capillary forces may become non-negligible, changing resin flow into a capillary flow where resin gets wicked by the fabric reinforcements [32].

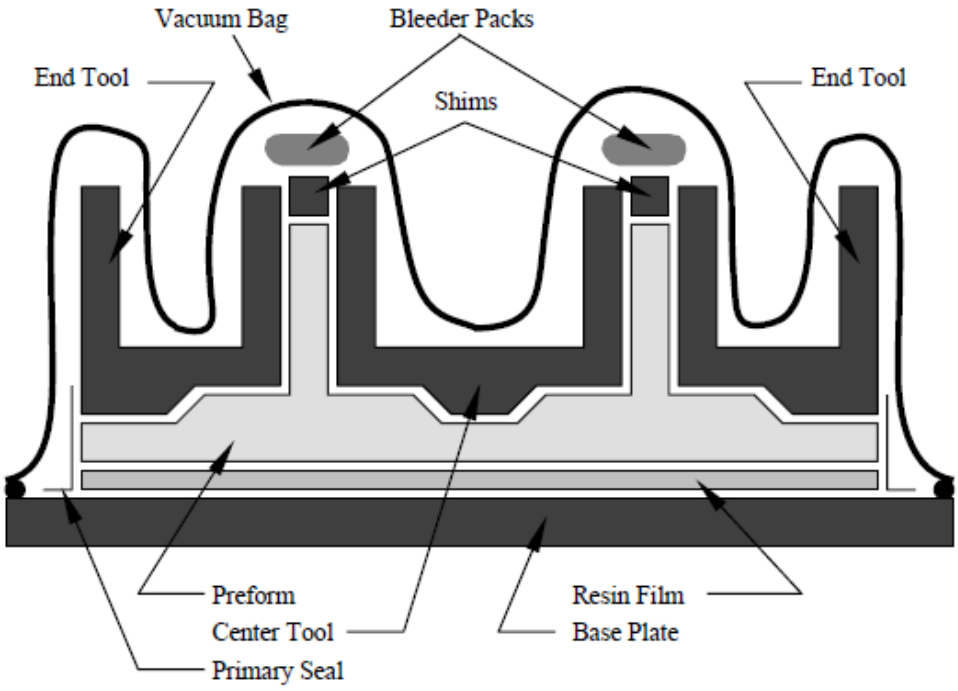


Figure 2.2: RFI processing for an integrally stiffened PMC part [43]

Impregnation is also affected by the resin viscosity, a property that quantifies the resistance of a fluid to continuous deformation resulting from applied shear stresses. Higher viscosity resins require greater applied force for achieving the same flow velocity compared with a lower viscosity resin. In the case of RFI, Letterman identified that resin viscosity should be between 0.1 Pa·s to 8 Pa·s depending on flow length [28]; the greater the flow length, the lower the viscosity has to be due to the limited infusion time prior to resin gelation. The lower bound viscosity values are similar to those of RTM resins which are usually lower than 0.3 Pa·s [44], while the upper bound viscosity values are similar to those of pre-preg resins, which are closer to 10 Pa·s [45, 46]. The higher viscosity limit enabled Hillermeyer et al. [3] to develop and use different types of elastomer-toughened cyanate ester resins formulations for PMC laminates. The toughened resins increased mode 1 and mode 2 interlaminar fracture toughness by 140% and 60% respectively compared to the original lower viscosity RTM resin.

Beyond modifications to resin formulation, viscosity is also affected by process temperatures. Published work [34, 38, 42] suggests that increasing the heating rate can possibly increase the flow length due to the lower viscosities that may be reached. Garschke et al. [34] used the M18 epoxy resin for measuring the effect of cure profiles on the impregnation of a $\pm 46°$, 256 g/m$^2$ non-crimp fabric. Based on a standard cure temperature profile (Figure 2.3), the authors modified the heating rate and the duration of the 1$^{st}$ dwell. Results showed that the requirements for maximising flow lengths were a high heating rate of 10°C/min and short dwell duration of approximately 10 min. Despite significantly shorter gel times, the lower viscosities enabled greater flow lengths. However, such cure conductions resulted in high void contents.

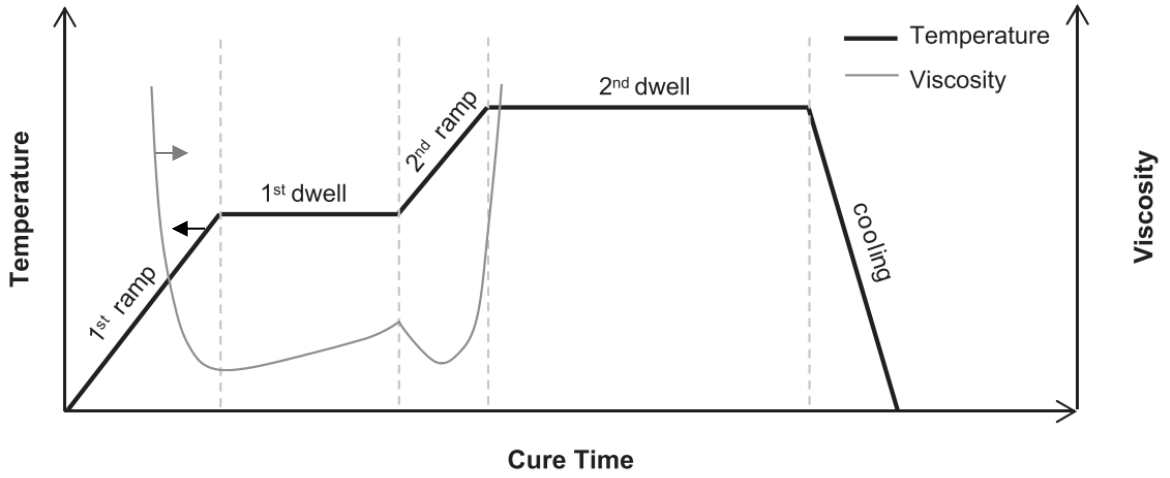


Figure 2.3: Standard cure temperature profile [34]

Resin flow is also affected by the permeability of dry fabric reinforcements, which is affected by the configuration of the fibre network and the fibre volume fraction. The effect of permeability was studied by Kruckenberg et al. [42]. The authors noted that a reduction of the fibre volume fraction from 61.4% to 57.6% increased permeability by 71% and increased infusion distance in a blade stiffened panel by 44% for a 370 g/m$^2$ five harness satin carbon fibre fabric.

Good understanding of resin flow is also vital for maximising resin flow lengths in dry fabric reinforcements. For example, NASA required significant customisation of the resin film distribution for preventing dry areas in a blade stiffened panel due to limited in-plane flow [38]. From this it can also be conjectured that the location of the resin bleeder is critical for impregnation.

Published work on RFI processing focusing on resin impregnation revealed that several parameters must be considered towards maximising the resin flow lengths including the level of external pressure, resin formulation, resin viscosity as a function of cure temperature, fabric permeability and resin distribution (Table 2.2). However, maximising the resin flow lengths into dry reinforcements does not ensure quality of PMC parts because internal voids may remain.

Table 2.2: Summary of parameters affecting resin flow lengths in dry reinforcements for RFI manufacturing based on published work

| Parameter | | Change in parameter | Infusion distance |
|---|---|---|---|
| Applied pressure | | Increase | Increase |
| Fabric: | - Fibre volume fraction | Increase | Decrease |
| | - Permeability | Increase | Increase |
| Resin: | - Viscosity | Increase | Decrease |
| | - Addition of toughening agents | Increase | Decrease |
| Cure: | - Heating rate | Increase | Increase |

#### 2.2.1.2 Microscopic scale

In the case of RFI, publications detailing the effects of resin distribution and reinforcement architecture on local resin saturation within stacks are scarce; available publications [29–33] focus mostly on semi-preg materials. Thomas et al. [29] used ultrasound imaging for measuring resin flow in an interleaved RFI stack consisting of a single layer of plain weave and epoxy resin film. Processing was conducted at a constant temperature of 70°C. In the absence of compaction resin did not flow inside yarns, suggesting minimal capillary forces. Conversely, compaction led to squeezed flow where resin began saturating inter-yarn gaps before saturating yarns. The authors calculated permeability values for yarns from their results, but the low resolution of their imaging technique did not capture the details of microscopic flow well.

Partial impregnation is an alternative method for tracking resin flow whereby a series of panels are produced with various degrees of cure. Taveres et al. [30] used this method for studying resin flow and air permeability in non-crimp stitched fabric (NCF) semi-preg materials during manufacturing of out-of-autoclave sandwich panels. Observation of the surface of the panels showed that resin flow was governed by viscous forces, with zones in the vicinity of stitches being filled first. Permeability to air was also found to be much higher than that of conventional pre-preg materials, potentially lowering the risk of air entrapment. Centea and Hubert [31,32] also used partial impregnation to study the evolution of resin flow and void formation within semi-preg materials during processing

using X-ray microtomography. Observations showed that resin flowed in inter-yarn regions at room temperature but not inside yarns, as this required lower viscosities achieved only at higher processing temperatures. Furthermore, the resin flow front inside yarns was non-uniform which was attributed to the weaving architecture of the semi-preg materials. The authors also suggested that resin viscosity plays an important role in laminate porosity as it controls the start of yarn saturation, leading to closure of air evacuation pathways.

The partial impregnation method is useful to freeze the resin flow front in time, enabling a much wider array of analysis techniques than in-situ observations; however, the method requires several experiments for characterising the process and there may be doubts regarding the accuracy of the method in capturing the precise evolution of resin flow, as the freezing process is not instantaneous. A solution to these issues was proposed by Cender et al. [33]. The authors used a camera to monitor resin flow at the surface of semi-preg materials across a transparent tool. Processing consisted in consolidating 2 different twill-reinforced semi-pregs of different yarn widths under constant pressure and temperature through the use of a heated press. Results showed that resin flow was governed by viscous forces; the higher resolution of the camera enabled capture of the details of resin flow within yarns whereas resin flowed predominantly along the fibers. This enabled the calculation of inter-yarn and intra-yarn permeability values. Resin flow monitoring also showed that the flow front was relatively uniform and that larger spacing between yarn crossings led to longer processing times, due to greater flow lengths.

### 2.2.2 Theory and modelling of resin film infusion

In LCM processes such as RFI, the local behaviour of resin flow is governed by the interaction of viscous and capillary forces [19]. Resin flows mainly in zones of high permeability such as inter-yarn gaps when viscous forces are dominant. This type of flow is often modelled using Darcy's law. Conversely, resin flows primarily from fabric wicking when capillary forces are dominant.

This subsection discusses Darcy's law, capillary flow and then published work on RFI simulations.

#### 2.2.2.1 Darcy's law

Resin flow through dry fabric reinforcements is often modelled using Darcy's law. This is a simplification of the momentum equation for steady flow inside porous media and it is valid only for Re $\ll 1$ [47], but the equation was also used successfully for describing transient infusion problems in LCM processes from the quasi-steady state nature of the flow between time steps [47]. In Darcy's law for LCM processing, resin is modelled as an incompressible fluid while the dry fabric reinforcements are modelled as a porous medium. Darcy's law relates the discharge per unit area $q_i$ along an axis $x_i$ to the pressure gradient in the porous medium, fluid viscosity $\mu$ and directional permeability $K_{ij}$ [48].

$$q_i = \frac{-K_{ij}}{\mu}\frac{\partial P}{\partial x_i} \tag{2.1}$$

where $P$ is the resin pressure. The velocity $v_i$ of the fluid can be obtained from the porosity $\phi$ of the porous medium, i.e. the volume fraction not occupied by the fibres ($\phi = 1 - V_f$):

$$v_i = \frac{q_i}{\phi} = \frac{-K_{ij}}{\phi\mu}\frac{\partial P}{\partial x_i} \tag{2.2}$$

When using Darcy's law, reinforcements are modelled as uniform porous media characterised by a single permeability tensor that varies with compaction pressure. A method for measuring the out-of-plane permeability of fabrics under various compaction pressures was presented by Ouagne and Bréard [15]. Despite substantial simplifications made regarding reinforcement architectures whereby their dual-scale architecture is not considered, models based on Darcy's law can provide reasonable predictions of global flow front locations as discussed below in section 2.2.2.3.

#### 2.2.2.2 Capillary flow

During RFI processing, the driving force for resin flow into fabrics is mostly attributable to applied pressure. However, resin flow can also be driven by capillary action, causing fabrics to wick resin. For any porous medium including dry fabrics, the capillary pressure driving a flow in yarns is governed by both the liquid surface tension $\gamma$ and

contact angle $\theta_C$ between a solid surface and a liquid, here the fibres and the epoxy resin respectively.

The surface tension, or surface energy of a liquid, corresponds to the energy required for creating a new surface of said liquid, and it is governed by the cohesion of atoms within a phase and the adhesion of atoms from dissimilar phases. Physically, it occurs because surface atoms of a phase have fewer and/or weaker bonds beyond the phase surface compared to bulk atoms which are pulled equally from all sides (Figure 2.4). This results in the attraction of the high energy surface towards the bulk. In the absence of external forces, a liquid will take the shape of a sphere so as to reduce its surface area and achieve a state of minimal energy.

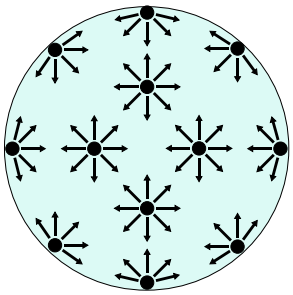

Figure 2.4: Atomic attraction inside a liquid drop

A list of surface tension values for epoxy resins and surface energy values for carbon fibres that were retrieved from literature appears in Appendix A. In the case of epoxy resins, reported surface tension values are in the range of 35 mJ/m$^2$ to 47 mJ/m$^2$ depending on the resin formulation, testing method and testing conditions [49–54]. Moreover, carbon fibres using an epoxy sizing also have similar surface energy values as epoxy resins [49]. The surface tension of epoxy is affected slightly by temperature, as Page et al. [50] and Cheng et al. [54] observed a reduction of -0.05 mJ/°C·m$^2$ to -0.11 mJ/°C·m$^2$ for various types of epoxy resins. Furthermore, it was shown that gases at pressures lower than a few atmospheres have a limited effect on the surface tension of a liquid [55], which means that the vacuum environment of RFI should have limited effect on this property.

The contact angle $\theta_c$ corresponds to the angle between a liquid phase and a contacting solid phase. Shallower angles imply that the liquid and solid phases are more attracted to each other and that there is greater wettability. The contact angle results from the interaction of various phases, usually a solid-liquid-gas interaction (Figure 2.5).

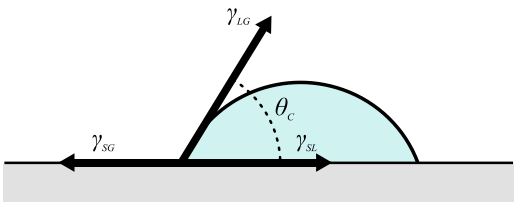


Figure 2.5: Liquid drop on a solid surface showing solid-liquid-gas interactions

The force balance at the interface of the phases can be described by the Young equation [56]:

$$\gamma_{SL} + \gamma_{LG} \cos\theta_c = \gamma_{SG} \tag{2.3}$$

where $\gamma_{SL}$ is the surface energy of the solid-liquid interaction, $\gamma_{LG}$ is the surface tension of the liquid, and $\gamma_{SG}$ is the surface energy of the solid-gas interaction.

A list of reported values for the contact angle of epoxy resins on single carbon fibres appears in Appendix A. Average contact angle values vary from 15° to 50° [49, 51, 52, 54, 57]. The contact angle can be reduced by using an epoxy-based sizing on the fibres [51, 52]. Cheng et al. [54] also noticed that an increase in temperature from 20°C to 120°C decreased the contact angle from 15° to 5°. Finally, Oroojalian et al. [57] showed that the contact angle could be altered by loading epoxy resins with CNTs. A small addition of CNTs, less than 1%, reduced the contact angle by up to 30%, but any further addition resulted in an increase in contact angle due to the increase in resin viscosity.

In the case of RFI, the combined capillary effect of surface tension and contact angle on resin flow into the fabrics can be defined as a positive pressure that forces the resin into yarns. The equation for the capillary pressure $P_C$ is as follows [47]:

$$P_c = \frac{F_S}{d_f}\frac{V_f}{\left(1-V_f\right)}\gamma\cos\theta_C \tag{2.4}$$

where $F_S$ is the flow shape factor and $d_f$ is the fibre diameter. The shape factor is a tensor that varies depending on the fibre orientation respective to resin flow. For flow in an aligned fibre bundle in the longitudinal direction the shape factor is approximately 4 while for transverse flow the shape factor is approximately 2 [47].

#### 2.2.2.3 Resin flow simulations

Optimisation of the resin flow lengths and porosity levels in RFI can be done experimentally by trial and error. However, this can be time consuming and may require significant investment, especially for producing large complex parts. An alternative solution is to use computational modelling for simulating the RFI process.

Published work for RFI part manufacturing consists of resin flow models at the macroscopic scale using Darcy's law, where no detailed modelling of the fabric architecture is made, for both bulk [42, 43, 58–66] and interleaved [36, 67] processing methods. In this section, a summary of these models is presented.

In simple cases, Darcy's law can easily be solved analytically for evaluating the time-dependent resin flow length. The analytical solution is particularly well-suited for unidirectional flow in cases such as flat laminates or blade-stiffened panels, i.e. a skin reinforced by T-section profiles as depicted previously in Figure 2.2. Kruckenberg et al. [42] used a 1D analytical model for predicting impregnation time in a blade-stiffened PMC panel made using the bulk RFI method. The model used assumptions for reducing the complexity of the analytical formulation, such as neglecting fabric compaction and heat transfer. For achieving a 1D analytical solution, the authors also modelled the skin of the panel as having an equivalent width to the stiffener. They nonetheless used experimental permeability and viscosity values based on their specific cure cycle for predicting flow. Compared with experimental data their simulation results showed some discrepancies; in some cases the simulations over-predicted infusion distances by as much as 8% whereas in other cases it under-predicted infusion distances by as much as 22%. Park and Saouab [59]

also proposed an analytical model for solving infusion problems in RFI for a blade-stiffened panel but their model included compaction of the porous medium. However, no comparison with experimental results was performed.

Numerical methods are often desirable for solving Darcy's equation in more complex cases for predicting resin flow lengths. For example, Blest et al. [67] used finite differences for modelling the 1D flow in an interleaved RFI process. They neglected compaction, but nonetheless incorporated heat transfer and cure kinetics models for predicting temperature rises resulting from the cure reaction. Thompson [36] used the same finite differences method for modelling the interleaved RFI process, but his model included compaction of the porous medium and resin viscosity based on a cure kinetics model. Simulations performed were compared with experiments for estimating resin bleed and final thickness of a PMC part. Depending on the case tested, simulations overestimated the mass of resin bleed by 22.6% to 91.6% while discrepancies for the final part thickness were between 0% and 7.8%.

Increased complexity in part geometry requires 2D and 3D modelling for predicting multi-axial flow. Moreover, a numerical method more robust than finite differences is often required for ensuring accuracy of the predicted resin flow lengths. The conventional method for solving resin infusion in LCM processes, including RFI, is the control volume finite element method (CVFEM) [47, 60, 61, 64, 65]. The method uses finite elements in which control volumes are discretised and each control volume is associated to a single element node (Figure 2.6). Simply, CVFEM consists in separating the mechanical deformation from the flow calculations. At the beginning of each time step, the finite element mesh is deformed due to a change in pressure distribution within fabrics. After mesh deformation, control volumes are discretised around nodes of finite elements for calculating resin flow.

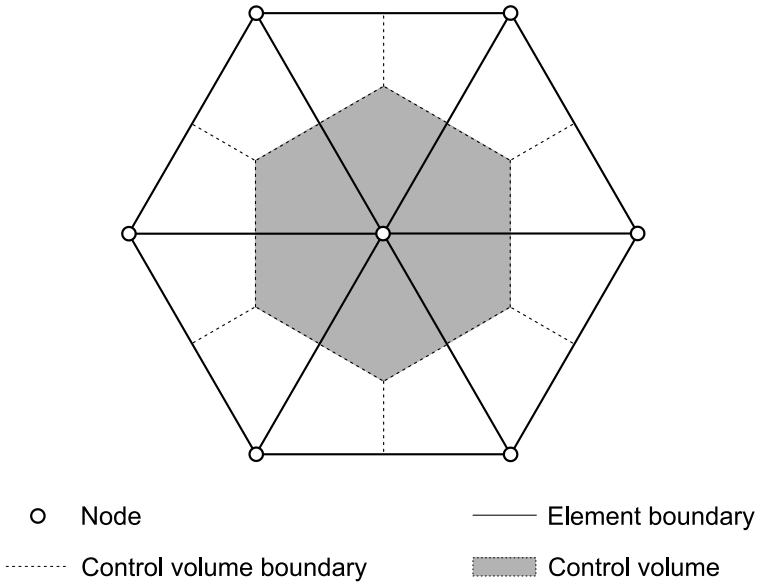


Figure 2.6: Discretisation of the CVFEM domain with triangular elements

Loos and MacRae [61] used CVFEM for modelling bulk RFI processing of a blade-stiffened panel manufactured in-autoclave at 689 kPa, using Hercules 3501-6 resin (Figure 2.7). The authors created a 2D model incorporating cure kinetics and viscosity models but they did not account for compaction of the reinforcement.

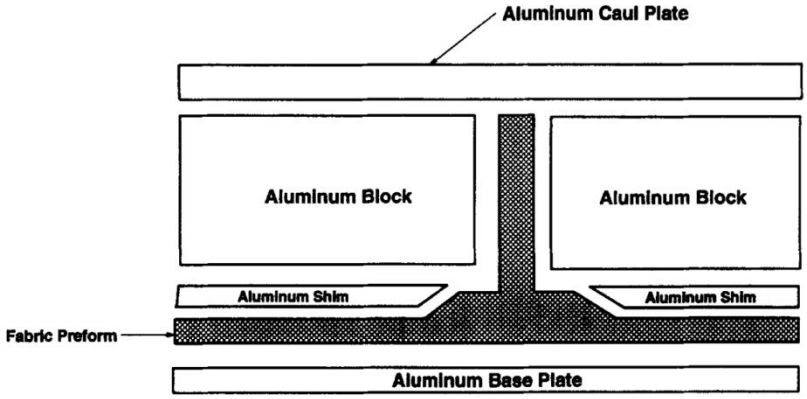


Figure 2.7: Exploded view of a blade-stiffened panel [61]

Caba et al. [43, 58] expanded the same model to 3D and also modelled bulk RFI processing of a stepped panel. The error between experimental and simulated infusion times at various part locations was 4% to 12% for a blade-stiffened panel and 9% to 23%

for the stepped panel (Figure 2.8). It was also shown that the models were more accurate with increasing resin flow lengths. It was conjectured that the reason is that the viscosity model was not accurate for low temperatures at the onset of resin flow. Loos et al. [62] further improved the blade-stiffened panel model by adding elastic deformation. The model featured compaction of the reinforcement and thermal expansion. Simulation results showed that thermal expansion in the tool affected the compaction of the preform locally. Simulations also predicted warpage as seen in the actual manufactured part. The new model features increased the predicted infusion time compared with previous models. This led to moderate overestimation of the infusion time by 5% to 17%.

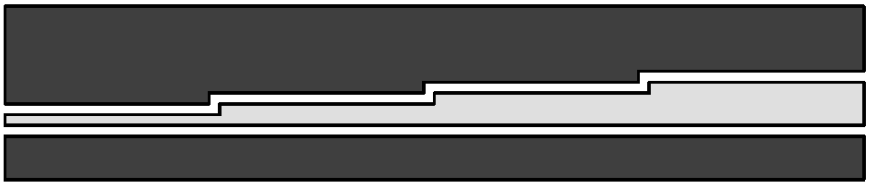

Figure 2.8: Stepped panel placed between tools [43]

As seen, CVFEM was used for modelling flow in RFI effectively; however, the combined use of finite element and finite volume methods with CVFEM requires great computational power and time. This led to simpler modelling efforts using solely the finite element method (FEM) [41, 63]. For a simple case of a blade-stiffened panel without any cure kinetics, viscosity or compaction models, Mei et al. [63] reduced computational time by 87% when using FEM compared to CVFEM for identical infusion results. However, the accuracy of the method was not verified based on experimental data.

Computational models were also used for understanding and optimising process parameters. Park and Kang [64] produced a 2D model using CVFEM for simulating bulk RFI in a blade-stiffened panel. It featured cure kinetics, reinforcement compaction, and viscosity models. The simulation results showed that lower cure temperature enabled greater resin flow lengths due to slower cure reaction and that the level of external pressure significantly affects flow lengths.

Another modelling aspect that is often overlooked is the capillary action [41, 68]. Han et al. [41] showed through simulations that capillary forces could increase the resin flow length in RFI processing and act as a supplement to the external pressure. However, their results showed that the capillary action is only noticeable when the absolute resin pressure falls below 300 kPa.

All published work on RFI process simulation revealed that several models must be combined to predict resin flow lengths effectively. A summary of these models appear in Table 2.3. The scale at which published RFI simulations were made also prevented the modelling of a detailed fabric reinforcement architecture that could be used for assessing resin flow separation around and into yarns due to fabric heterogeneity and variability. Hence, a multi-scale modelling approach specifically for RFI is missing for characterising void formation in processed parts.

Table 2.3: Lists of design considerations based on published work in RFI process modelling

| Inputs | Simulation models | Outputs |
|---|---|---|
| Pressure: - External | Flow | Flow location |
| - Capillary | Compaction | Infusion time |
| Heat sources/temperature profile | Cure kinetics | Internal fabric/resin pressure |
| Part geometry | Viscosity | Fabric: - Deformation |
| | Void formation | - Fibre volume fraction |
| | Residual stresses | - Permeability |
| | | Resin: - Viscosity |
| | | - Degree of cure |

## 2.3 Void formation

RFI processing can lead to the creation of voids in PMC parts that have a detrimental effect on the mechanical properties of PMCs. Despite the importance of understanding mechanisms for void formation, published work studying voids in RFI processing is scarce

[23, 34, 36, 38, 39, 69, 70]. This section will first describe the types of voids that can be observed in RFI processed parts. Then it will discuss the effects that process parameters have on void contents in PMCs. Finally, it will present process simulations of void formation during RFI.

### 2.3.1 Type of voids

Two major types of voids can be found in PMCs made with RFI: flow-induced voids [67, 71–76] and gas-induced voids [34, 77–80].

Flow-induced voids result from out-of-solution gases that are trapped in the resin matrix by the coalescence of multiple resin flow fronts. This is caused by the dual-scale architecture of fibre reinforcements at fibre and yarn scales which leads to different resin velocities inside and around yarns. Hence, the formation of these voids can be understood through a better understanding of resin flow at the microscopic scale.

The formation of flow-induced voids depends on the ratio of viscous forces to capillary forces, which can be quantified by the capillary number *Ca*. A modified capillary number *Ca** was defined by Patel and Lee [28] that considers the interactions between the resin and fibres:

$$Ca^* = \frac{\mu v_z}{\gamma \cos\theta} \tag{2.5}$$

From Darcy's law and the Capillary number, equations 2.1 and 2.5, it follows that void content can be minimised through control of the ratio of capillary to viscous forces by modulating the injection pressure to achieve uniform resin flow. Empirical data suggests that the critical *Ca** for minimising micro- and macro voids, i.e. when resin flow velocities inside and around yarns are equivalent, is in the order of $10^{-3}$ [20].

Gas-induced voids are caused by gases present in resin films or RFI stacks prior to processing. The main sources of gases are by-products of the polymerisation reaction, moisture and air entrapped between layers of resin film or semi-pregs during collation [77, 81, 82]. Gases that remain out of solution during RFI form bubbles that leave holes in PMC

parts. This occurs when their vapour pressure exceeds that of the resin [78]. Thus, the best solution to mitigate gas-induced voids is to ensure that gases are dissolved in the resin by using a manufacturing process that leads to high resin pressures, such as the use of an autoclave [34, 69, 77, 83]. However, this solution is not always available and alternatives are required for controlling the amount of gases that come out of solution during processing.

Out-of-solution gas within a bubble behaves as an ideal gas [84, 85]. From this, it follows that the volume $V$ of a bubble can grow with increasing temperature $T$ and decreasing pressure $P$, but also from a change in the amount of matter $n$:

$$V = \frac{nRT}{P} \tag{2.6}$$

where $R$ is the ideal gas constant. Gas diffusing into bubbles is a major source of gas-induced voids. Grunenfelder and Nutt [77] showed that moisture inside the resin tends to diffuse into bubbles, increasing bubble size, and that diffusion rates increase with the process temperature.

### 2.3.2 Processing parameters affecting voids

Resin bleed affects strongly the surface finish of a PMC part [23]. Pinholes on the surface of a PMC part are foretelling the presence of internal voids due to excessive resin bleed. During resin bleed, the compression pressure within the stacks of fabric reinforcement and resin film gets transferred towards the fabrics as resin viscosity reduces and resin is displaced, leading to a reduction in resin pressure. If the resin pressure drops too much, two issues arise. Firstly, capillary forces may become sufficiently strong to wick the resin into the fabrics and out of low pressure zones. Secondly, volatiles may be expelled if resin pressure reduces below the vapour pressure. In RFI, these issues were mitigated by Qi et al. [39] who controlled resin bleed using a perforated caul plate for bulk RFI performed in-autoclave. The amount of resin bleed was optimised by varying the size of the holes in the caul plate and the quantity of resin. The use of optimised parameters permitted a void content of approximately 1% and a fibre volume fraction of 55%.

Margueres et al. [69] also investigated the effects of resin bleed in RFI, as well as those of laminate thickness and fabric architecture. They used commercial semi-preg material E-glass/M9.6F HexFIT® in manufacturing flat laminates through out-of-autoclave vacuum bagging, and tested two different processing configurations. Configuration #1 featured an inner permeable bag around the stack and bleeder plies. The amount of bleeder plies was controlled for providing very limited resin bleed. Configuration #2 featured a stack covered in perforated film which exposed one surface of the stack to multiple bleeder and breather plies. The authors tested 3 different glass reinforcements: 1) ± 45° non-crimp stitched fabric, 2) twill 2×2 and 3) twill 2×2 combined with a ± 45° non-crimp stitched fabric. Porosity and fibre volume fraction values of the laminates varied between 0.88% and 4.63% and between 35% and 41% respectively. Limited bleeding in configuration #1 enabled a reduction of porosity by 50% to 70% compared with configuration #2, depending on the fabric reinforcement used. However, configuration #1 reduced the fibre volume fraction by 5% to 10% compared with configuration #2. The thickness of the semi-preg stack also affected the porosity and fibre volume fraction of the laminates. Increases in the number of semi-preg plies from 3 to 15 resulted in an increase in porosity from 2.7% to 4.5% and a slight reduction of fibre volume fraction from 39.3% to 37.5%. Finally, the authors noted an effect of fabric architecture on porosity, as laminates made with non-crimp stitched fabrics featured much greater porosity than those made from twill fabrics; however, no mention of the size or location of the voids was made.

Higher porosity levels observed with non-crimp stitched fabrics were also reported by Shim et al. [70] who observed that low pressure zones in stitching areas were predisposed to void formation. Heterogeneity in pressure distribution created by the stitches also produced more micro-cracking during thermal cycling due to thermal expansion differences between the fabric and stitches.

The cure cycle also affects laminate porosity in RFI. Margueres et al. [69] compared a cure cycle recommended by the manufacturer having a single 60 min dwell at 120°C to a longer cure cycle having a 60 min dwell at 80°C plus a 60 min dwell at 120°C. The latter enabled a reduction in porosity of more than 55% compared to the prior. Conversely, Thompson [36] investigated the effect of cure temperature (70°C to 80°C) and compaction

pressure (17 kPa to 93 kPa) on the porosity and fibre volume fraction of out-of-autoclave RFI laminates made with semi-preg material Cycom™ 754 / E-QX 3600-5. The author showed that greater applied pressure increased the fibre volume fraction and usually yielded lower porosity levels. No clear trend of the effect of cure temperature was found, but this may be due to the small range of temperatures tested.

Garschke et al. [34] provided a more thorough analysis of the effect of the cure cycle on porosity and fibre volume fraction in out-of-autoclave RFI parts. The authors manufactured flat panels using the bulk RFI method with bi-directional non-crimp stitched fabrics and M18 epoxy resin. Consolidation and cure were achieved using the Quickstep process. The authors probed the effects of various heating rates (2.8°C/min and 13°C/min) and cure dwell time (0 min to 60 min). The porosity of the flat panels varied from 2.8% to 4.8% while the fibre volume fraction varied from 53% to 55%. Most voids were located around stitches in the fabrics.

Another solution for lowering porosity lies in removing gas dissolved in the resin before consolidation. Garschke et al. [34] investigated the effect of resin film degassing on porosity and fibre volume fraction. Resin film degassing at room temperature and at 40°C had marginal impact on porosity. However, degassing at 80$^{o}$C for 30 min enabled lowering the porosity from 4.8% to 0.98% and increasing the fibre volume fraction from 53% to 56%. Since degassing at elevated temperature affects cure, the authors tested other degassing methods. The authors tried to debulk the stack prior to cure, aiming at removing gas entrapped between resin plies, but the method only provided a marginal reduction in porosity and small increase in fibre volume fraction. Conversely, the use of a solid release film under the resin film stack during manufacturing reduced porosity to 2.49% compared to 4.8% in a baseline panel, and increased fibre volume fraction to 56% compared to 53%. It was conjectured that the lower porosity resulted from the gas permeability of the release film that provided an additional escape path for the gases within the stack. Porosity was then reduced further to 0.37% by adding a peel ply under the solid release film beneath the resin film stack, which allowed greater gas removal. The use of the peel ply enabled reaching porosity values comparable to the 0.44% value that was achieved with an

autoclave RFI panel that the authors manufactured using the same parameters as the baseline panel.

Finally, the last method for reducing porosity consists in pressurising the resin using external pressure to collapse voids, as permitted by autoclaves or presses. Margueres et al. [69] reduced porosity from 3.58% to 1.57% by using an autoclave pressurised at 3 bars instead of a vacuum bag in an oven for manufacturing RFI laminates.

### 2.3.3 Void formation simulations

Most simulations of the RFI process focused on resin flow and part saturation while limited studies investigated mechanisms of void formation.

Li et al. [65] used a 2D model using CVFEM for simulating the RFI processing of flat plates. The authors investigated the resin pressure and fabric volume fraction distributions inside laminates for assessing the risk of the formation of gas-induced voids based on the resin pressure. From their results, the authors suggested that the amount of bleeder placed above the PMC plate should be controlled for preventing vaporisation of gases dissolved in the resin. Moreover, based on the results of Trochu et al. [86] the authors suggested that the external pressure should be adjusted during the cycle for controlling the ratio of viscous to capillary forces, aiming at minimising porosity levels through the resin flow velocity. However, they did not provide any models or critical values for the pressure or resin velocity that could lead to void formation.

In contrast, Sevostianov et al. [78] provided an analytical model for estimating void formation in RFI parts made using the bulk RFI method due to vaporisation of gases dissolved in the resin. Their model was based on the temperature and applied pressure, and used a 2D CVFEM. From their results, they proposed an optimised temperature profile for curing a PMC part.

## 2.4 Carbon nanotube reinforced composites

This thesis investigates the fabrication of multi-scale PMCs reinforced by both carbon fibres and carbon nanotubes (CNTs). Here, carbon fibres provide in-plane

reinforcement while CNTs are used as a toughening agent for reinforcing the relatively weak matrix and improving the interlaminar mechanical properties of PMCs. It should be noted that another way of using CNTs in multi-scale PMCs is to graft them directly on the carbon fibre instead of mixing them with the matrix [87, 88]. Even though the grafting method shows potential for multi-scale PMCs due to the transverse alignment of CNTs, it was not investigated in this work because it is not currently applicable to large-scale processing due to high costs and low rates of fabrication.

This section is divided in three parts. Firstly, a description of CNTs is provided. Secondly, the fabrication and properties of nano-modified polymers is discussed. Thirdly, the properties and processing of multi-scale composites featuring continuous fibres embedded in a nano-modified polymer is presented.

### 2.4.1 Carbon nanotubes

Carbon nanotubes are an allotrope of carbon with a hollowed cylindrical crystalline structure where the walls feature a hexagonal lattice of carbon atoms. More specifically, CNTs consists of a folded sheet of graphene (Figure 2.9). CNTs appear as slender tubes that have diameters in the nanometre range and large aspect ratios in the order of 30-1000 [89]. CNTs can feature a single wall (SWCNT) with a typical diameter of 1nm to 2nm or multiple concentric walls (MWCNTs) with an interlayer spacing of 0.34 nm resulting in an outside diameter ranging from 2 nm to 25 nm [18, 89].

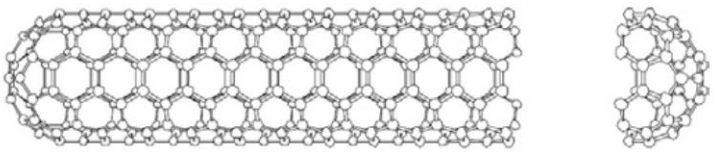

Figure 2.9: Schematic of a CNT[7]

The great interest towards CNTs comes from their outstanding mechanical and electrical properties (Table 2.4). For example, some studies [90–95] have showed that

CNTs can be 5 times stiffer than steel and 100 times stronger for an equivalent volume. In addition, CNTs have great electrical and thermal conductivities, contrasting with that of polymers used in PMCs. However, individual CNTs cannot be used in macroscopic applications due to their small size and must therefore be embedded inside a matrix, limiting the performance that can be achieved. This is similar to technical fibres such as carbon fibres that must also be embedded in a matrix for creating rigid structures.

Table 2.4: CNT properties along the axial direction

| Property | Value | References |
|---|---|---|
| Elastic modulus [GPa] | 20 - 1300 | [90–92, 94, 96] |
| Tensile strength [GPa] | 15 - 150 | [90–95] |
| Thermal conductivity [W/m·K] | 50 - 600 | [97, 98] |
| Electrical conductivity [S/m] | $1\times10^{4}$ - $3\times10^{6}$ | [99–107] |

Optimising the interaction of CNTs with the matrix is critical for realising the full potential of CNTs. Compared with other geometries, the high aspect ratio of CNTs is beneficial for load transfer. However, pristine CNTs do not form covalent bonds with surrounding matrix, hence they must rely on relatively weak physical van der Waals interactions for transferring load. Therefore, CNTs are often pulled out of the matrix during loading instead of breaking [108]. The weak van der Waals forces also limit the inherent strength of multi-walled CNTs because the outer wall can debond and unsheathe from the inner walls [90].

The interaction between CNTs and the matrix can be improved by functionalising CNTs. Functionalisation is a chemical process that alters the surface of the CNTs to enable the formation of covalent bonds with the polymer matrix, improving load-transfer [21, 109]. This can be achieved by strong acid oxidation of the CNTs. For example, Qiu et al. [21] functionalised MWCNTs by putting them in baths of nitric and sulphuric acids that were shaken with ultrasound. Functionalisation disrupts the structure of CNTs, resulting in surface defects that weaken CNTs. Wang et al. [95] showed through experiments that surface defects could reduce the strength of CNTs by a factor of at least 4. In addition,

functionalised CNTs were shown to decrease the cross-linking of the polymer matrix as they participate in the cure by bonding themselves to the polymer matrix [21]. This can result in a decrease of the glass transition temperature $T_g$.

### 2.4.2 Nano-modified polymers

Properties of polymers can be modified through the addition of nano-particles. CNTs provide significant improvements to the electrical conductivity of polymers [110, 111]. Qiu et al. [21] observed that a concentration of less than 1 wt% of CNTs increases electrical conductivity of polymers by 11 orders of magnitude. CNTs can also be used for increasing the modulus and strength of polymers [112]. Reported values vary widely. For example, a concentration of 0.5 wt% of CNTs may increase the modulus of polymers by less than 10% [19, 108] but a similar concentration may increase modulus by more than 50% [19, 113]. This variability is attributed to different distribution states of CNTs in polymers [89], and is affected by 1) dispersion uniformity, 2) concentration, 3) aspect ratio and 4) alignment [18].

#### 2.4.2.1 Dispersion

Dispersion refers to the distribution of nano-particles in polymers. In general, greater mechanical properties are achieved if there is homogenous dispersion of nano-particles, i.e. when CNTs are not agglomerated [108, 114]. This ensures that the polymer is reinforced uniformly, preventing any weaker regions that could initiate or propagate failure. Achieving a homogenous dispersion of CNTs in polymers can be quite challenging. Relatively strong van der Waals forces between CNTs result in entanglement and clustering [16, 19, 21, 89]. The strong attraction forces are caused by the high surface area of CNTs relative to their size.

There are different methods for exfoliating i.e. separating nano-particles, including the use of shear stresses [16, 18, 19, 111], ultra-sonication [16, 109, 113, 115, 116], surfactants [16, 113, 114] and functionalisation [16, 109, 117]. In general, multiple methods are combined for achieving good uniformity of dispersion.

Relatively high shear stresses are required for exfoliating nano-particles. For example, Fan and Advani [89] found that the shear stresses produced by a magnetic stirrer were too low for achieving good exfoliation of CNTs dispersed in an acetone solvent and epoxy resin. A more effective exfoliation method consists in using a twin-screw extruder [18, 19]. The twin-screw extruder can also be used for orientating nano-particles in the shear direction [18, 19]. Even though the use of shear stresses is highly effective for achieving a homogeneous dispersion of nano-particles, the process has some issues. First, nano-particles are not in a stable state and they can re-agglomerate once shear stresses are removed. In the case of thermosetting polymers, shear stresses must be maintained until polymer gelation occurs, to prevent motion and re-agglomeration of nano-particles [18]. Second, the dispersion process tends to sever nano-particles [16]. Fan and Advani [89] found that the length of their MWNTs reduced to less than 1 μm due to the treatment compared to their original length of 10 μm to 15 μm.

Ultra-sonication is another method for exfoliating nano-particles [16, 18, 89, 113, 116]. It consists in using ultrasound for agitating nano-particles and disrupting inter-molecular interactions. Ultra-sonication is usually performed in a solvent, such as acetone, ethanol or dimethylformamide. Fan and Advani [89] observed that ultra-sonication was particularly effective for dispersing CNTs in epoxy. The authors managed to reduce the diameter of clusters from 500 μm to less than 3 μm. It is also worth noting that the solvent used for ultra-sonication affects the properties of nano-modified polymers. Lau et al. [116] found that acetone was a particularly effective solvent as it did not affect the cure kinetics of epoxy.

Surfactants are also used for exfoliating nano-particles [16, 113, 114]. They can disrupt the surface tension of the polymer matrix, enabling better compatibility between the nano-particles and polymer. However, they enable limited exfoliation compared with other methods [113]. In addition, surfactants can be difficult to remove from the polymer matrix following exfoliation.

As discussed above, functionalisation of nano-particles can be used for improving the interfacial strength between polymers and nano-particles by enabling covalent bonds. This

also enhances compatibility between polymers and nano-particles, improving attraction between nano-particles and homogeneity of the dispersion [16, 18, 21, 109, 117]. This results from functionalisation generating negative charges that counteract van der Waals forces [16]. Ma et al. [109] showed that amino-functionalisation could prevent re-agglomeration of CNTs in epoxy during cure as opposed to pristine CNTs. The improved dispersion resulted in much higher flexural modulus and strength. Functionalisation can even result in a dispersion that remains stable for months in very low viscosity liquids [117]. However, functionalisation can reduce greatly the electrical conductivity of CNTs as it induces defects in CNTs and disrupts their electrical structure [21]. In addition, electrical conductivity is reduced by a uniform dispersion because CNTs must be interconnected to create conduits in which electricity can flow [118].

The various methods presented above do not have the same efficacy for exfoliating CNTs. Fan et al. [16] tested three dispersion methods: 1) mechanical stirring, 2) ultra-sonication and use of a surfactant, and 3) CNT functionalisation and ultra-sonication. The authors found that only CNT functionalisation coupled with ultra-sonication resulted in well dispersed and non-aggregated CNTs.

Even though effective methods exist for dispersing CNTs in polymers, it is important to note that manufacturing processes using nano-modified polymers can result in a reduction of the uniformity of the dispersion. As mentioned above, CNTs can re-agglomerate if they have too much mobility. This can be an issue with hot-melt nano-modified epoxies where processing at elevated temperatures leads to a reduction in viscosity and re-agglomeration of CNTs [15].

#### 2.4.2.2 Concentration

The concentration of nano-particles affects the properties of polymers. At low concentrations, the modulus of nano-modified polymers increases with higher concentrations of nano-particles [9]. However, at high concentrations, nano-particles can have a negative effect. An important issue is that the viscosity of polymers or solvents increases with the concentration of nano-particles [119]. This can have a significant effect on processing. Schaffer et al. [117] dispersed MWCNTs in water and found that at a

concentration of 0.5 vol%, MWCNTs increased the viscosity of the solution considerably. This was attributed to the entanglement of MWCNTs. At a concentration of 4 vol%, the suspension would gel, and at a concentration of 50 vol%, the suspension became a porous semisolid. Hence, only a minute quantity of nano-particles can be added to polymers before processing issues arise.

Another issue is that relatively high concentrations of nano-particles can hinder the homogeneity of the dispersion (Figure 2.10). Higher concentrations result in greater attraction forces between nano-particles as the inter-particle distances are statistically shorter, which increases the amount of agglomeration [109]. In such cases, Rahman et al. [120] noted that the addition of CNTs improved the modulus and strength of epoxy up to a concentration of 0.3 wt%.

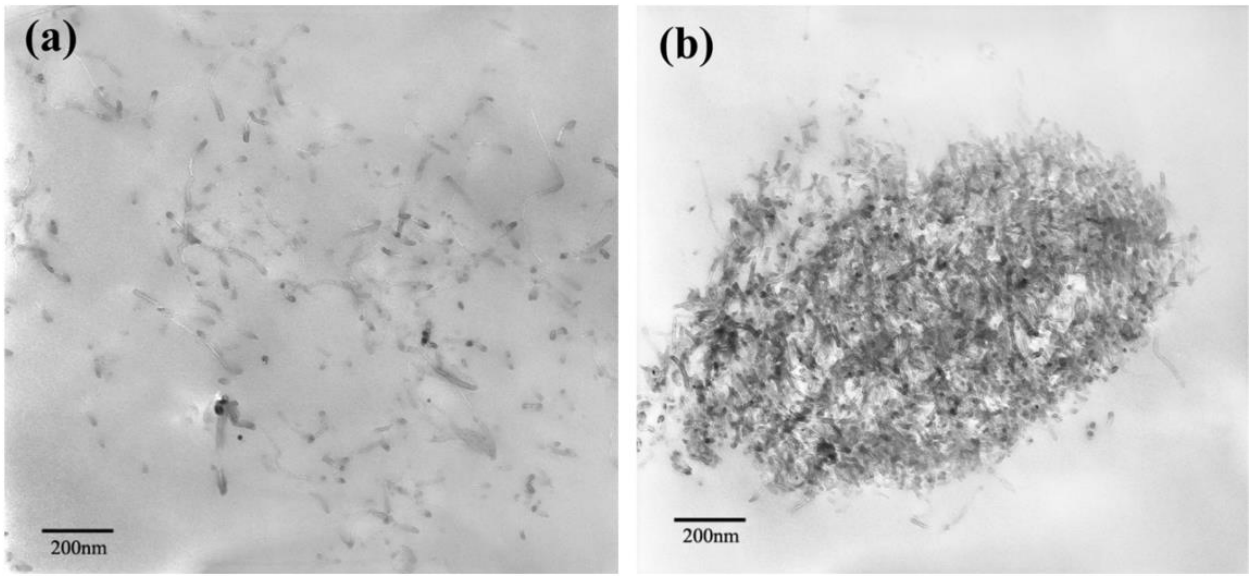


Figure 2.10: Dispersion of CNTs in epoxy at a loading of a) 0.3 wt% and b) 0.5 wt% [121]

#### 2.4.2.3 Aspect ratio

Greater CNT aspect ratios increase the strength and stiffness of nano-modified polymers. Ayatollahi et al. [122] noted improvements of 6% and 3.5% in stiffness and tensile strength of the polymer, respectively, by using CNTs with double the aspect ratio. Guo et al. [123] noted that longer CNTs resulted in greater storage modulus, but that the percolation threshold for electrical conduction was reduced.

The aspect ratio also affects the rheology of nano-modified polymers. Potschke et al. [119] showed that in polycarbonate, the incorporation of CNTs increased viscosity more than adding the same concentration of lower aspect ratio nano-fibres or carbon black.

It follows that the targeted aspect ratio for CNTs must be a compromise optimised for mechanical and electrical properties, and processability of the nano-modified polymer.

#### 2.4.2.4 Alignment

Similar to polymers reinforced with continuous fibres, nano-modified polymers are strengthened when nano-particles are aligned in the load direction [19]. An effective way to align CNTs is to subject them to shear stresses [18, 19].

Thostenson and Chou [19] used a micro-scale twin-screw extruder to disperse 5 wt% of MWCNTs into a polystyrene polymer. The high shear forces involved in the process disentangled MWCNTs and aligned them in the direction of the shear flow. The authors observed that the storage modulus of polystyrene increased by 49% when aligning MWCNTs compared to neat polystyrene. This was markedly more than the 10% improvement obtained from randomly oriented MWCNTs.

Fan and Advani [18] investigated the effect of the shear rate on the alignment of CNTs. They noted that a minimum shear rate of $10^3$ $s^{-1}$ was required for achieving significant levels amount of CNT alignment. Conversely, a shear rate of $10^5$ $s^{-1}$ was found to be much more effective for aligning CNTs.

### 2.4.3 Multi-scale composites

CNT nano-modified polymers can be used in the manufacturing of continuous fibre composites for improving mechanical and electrical properties. However, several processing issues can arise when manufacturing PMCs with nano-modified polymers, making it difficult to harness the full potential of nano-modification. This section first discusses the mechanical and electrical properties granted to PMCs by nano-modification, and then discusses processing of multi-scale PMCs.

#### 2.4.3.1 Properties

For mechanical properties, the addition of CNTs has very little influence on the tensile or flexural properties of PMCs as these are governed mainly by the fibre reinforcements [124–127]. Most of the benefits of CNTs are the improvements of interlaminar properties. The addition of 0.3 wt% CNTs can improve ILSS by 10% to 15% [124–126]. In a more optimistic case, Zhou et al. [128] observed a 77% improvement in ILSS from a CNT loading of 0.5 wt%. CNTs can also improve the fracture toughness of PMCs under mode I loading $G_I$, but these improvements are generally lower than those observed for ILSS [126, 129–131]. Improvements in interlaminar properties translate to greater impact strengths; an improvement of approximately 8% from a CNT loading of 3.0 wt% was noted by Song et al. [132]. Benefits from CNTs are attributed to their ability to delay damage, increase crack density, bridge cracks, and dissipate energy through CNT pull-out [130, 133–135].

Improvements to mechanical properties depend greatly on a uniform dispersion of CNTs, and good interfacial adhesion between the CNTs and polymer matrix [124]. The agglomeration of CNTs is undesirable as it yields heterogeneous matrix properties and because agglomerates act as stress concentrators, reducing strength [125]. Agglomeration becomes a significant issue at higher CNT loadings [135]. Conversely, a good interfacial adhesion is critical for maximising load transfer from the matrix to CNTs. Both dispersion and adhesion can be improved by functionalisation of CNTs, improving mechanical properties [124]. Mechanical properties can also be improved by adding CNTs not only in

the polymer matrix, but also in the fibre sizing to improve interfacial shear strength between matrix and fibres [128, 136].

The alignment of CNTs in the through-thickness direction is also highly beneficial to mechanical properties. Aldajah and Haik [137] observed that the flexural modulus and strength improved by 20% and 15% respectively by aligning CNTs as opposed to having a random orientation of CNTs.

CNTs are particularly effective at improving the electrical conductivity of PMCs [126]. Contrary to mechanical properties, the electrical conductivity benefits from CNT agglomeration [124]. This is because agglomerates create connected conduits in which electricity can flow. The improved electrical conductivity can be used for diverse applications. For example, this allows for conductive heating of PMCs which is useful for de-icing applications [138]. The higher conductivity can also be used for monitoring damage in PMCs by measuring changes in electrical resistance [139]. Additionally, CNTs can improve lightning protection of PMCs, reducing damage from a lightning strike and improving residual strength [138].

#### 2.4.3.2 Processing

Several processing difficulties arise when manufacturing PMCs with resins nano-modified with CNTs. The main issue is that CNTs increase resin viscosity significantly, reducing the maximum infusion length that can be achieved compared with neat resins [140]. Viscosity increases with the loading of CNTs [134]; at a certain CNT loading, the viscosity increases sharply [141], preventing any practical infusion. The CNT loading threshold for infusion was found to be equal to 0.3 wt% [124, 125, 140]. The sharp increase in viscosity is attributed to the agglomeration of CNTs. A solution to minimise the viscosity increase consists in functionalising CNTs to reduce agglomeration [125, 140].

Despite the use of resins featuring well dispersed CNTs, the processing of PMCs can result in the re-agglomeration of CNTs which increases resin viscosity and reduces mechanical properties [124, 135]. Re-agglomeration can occur during degassing [124] or

during consolidation [130]. The low viscosities required for resin flow grants great mobility to CNTs which agglomerate due to strong van der Waals forces.

Another issue of processing multi-scale PMCs is the filtration of CNTs. Information regarding the filtration of CNTs during PMC manufacturing is scarce, filtration is discussed mostly for in-plane infusion [16, 124, 126, 127, 129]. Filtration is not affected by the morphology of CNTs [129], but it is affected by their agglomeration [16, 127]. Large CNT clusters are easily filtered by fibre reinforcements while small CNT clusters can flow readily between yarns. This results in strong filtration of large CNT clusters at the injection inlet and moderate filtration of the remaining CNTs away from the inlet [16, 129]. Filtered CNT clusters can restrict resin flow in yarns significantly [16, 21]. Hence, a key solution consists in using nano-modified resins with well dispersed CNTs. Alternatively, filtration can be reduced by using processes that feature very short resin flow lengths such as wet lay-up [131, 137], use of pre-pregs [130], or through-thickness infusion methods [21] including RFI [5]. Despite the reduced filtration of CNT in inter-yarn gaps, it is not clear whether these processes allow for good infiltration of CNTs inside yarns.

Currently, even though filtration of CNTs was observed in PMCs, no studies investigating in detail the effect of filtration media or the effect of through-thickness filtration are available in the open literature. The development of such knowledge is needed for designing good multi-scale PMCs. In addition, even though RFI was used for manufacturing multi-scale PMCs [5], no study of the filtration or dispersion of CNTs was made. Hence, the detailed analysis of RFI processing and CNT filtration presented in this work provides a valuable contribution to the processing of multi-scale PMCs.

The improvement in interlaminar properties of PMCs from the addition of CNTs also depends on the orientation of the nano-particles. As discussed above, greater interlaminar shear strength is achieved when CNTs are aligned in the through-thickness direction. The most reliable method for alignment CNTs is through an electromagnetic field [137]. However, this method is not yet applicable for industrial scale manufacturing. CNTs can also align with the resin flow direction if the shear rate is sufficiently high. Fan and Advani [18] investigated the possibility of aligning CNTs from shear rates during infusion. They

studied the alignment of CNTs in micro- and nano-size channels. Micro-size channels were representative of inter-yarn gaps in fabrics. A relatively high resin velocity of 20 mm/s was required for aligning CNTs with the flow direction. Conversely, a flow rate of less than 2 mm/s was required for aligning CNTs inside nano-size channels which are representative of the dense fibre network of yarns (Figure 2.11). Based on these observations, it is not expected that the resin flow rates achievable in RFI are sufficient fast to yield any alignment of CNTs.

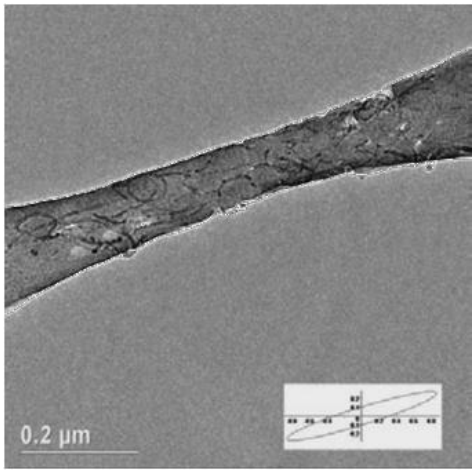


Figure 2.11: TEM image of MWCNT alignment due to a shear flow in a nano-size channel [18]

## 2.5 Concluding remarks

The literature review identified three main topics in RFI manufacturing that are still not well understood and that the thesis research work seeks to address. They are the effects that the processing parameters and dual-scale architecture of fibre reinforcements have on 1) resin flow at the microscopic scale, 2) void formation, and 3) CNT distribution in multi-scale PMCs.

### 2.5.1 Resin flow

Resin flow during RFI processing is well characterised at the macroscopic scale through experimental work and computer modelling. However, limited information is available in the literature describing thoroughly resin flow and the effect that processing

parameters have of resin flow at the microscopic scale. As discussed in section 2.3, understanding how process parameters and material selection affect flow inside and around the yarns is critical for understanding, quantifying and controlling voids in PMCs.

### 2.5.2 Void formation

A summary of published work on the methods used for reducing porosity in PMC parts processed with RFI appears in Table 2.5. It can be seen that published work investigated mostly the curing conditions, vacuum bagging configuration and resin system. However, despite the greater porosity observed in PMC laminates produced with non-crimp stitched fabrics, limited information is available about the effect of fabric architecture and variability on the porosity levels within laminates processed through RFI. This requires further research. In addition, studies of the effect of fabric heterogeneity in RFI processing would be even more valuable for particle filtering, such as for CNT nano-reinforcements used in this present work. Another area of interest is the effect of dry fabric reinforcements and resin film stacking configuration, as no published work compared the bulk and interleaved RFI processing methods, nor quantified differences between them in terms of processing or laminate quality. This is particularly of interest as Blest et al. [67] noted defects in an intermediate layer during infusion, resulting from the merging resin flow.

Table 2.5: Summary of RFI processing factors affecting quality a PMC parts based on published work

| Factor | Change in factor | Porosity | Fibre volume fraction |
|---|---|---|---|
| Bleeding | Increase | Increase | Increase |
| Stack thickness | Increase | Increase | Decrease |
| Fabric stitching | Yes | Increase | Increase |
| Applied pressure | Increase | Decrease | Increase |
| Debulking | Yes | Slight decrease | Slight increase |
| Peel ply | Yes | Increase | Increase |
| Resin flowability | Increase | Decrease | Increase |

### 2.5.3 Multi-scale composites

CNTs have a clear potential for improving mechanical properties of polymers, and the interlaminar shear strength and toughness of PMCs. The benefits provided by CNTs depend on the 1) dispersion uniformity, 2) concentration, 3) aspect ratio and 4) alignment of CNTs. In this work, the integration of CNTs into epoxy was not studied as this was performed by project collaborator Nanoledge who supplied raw materials. However, the contribution of this work lies in the in-depth characterisation of the effect that RFI processing has on CNT distribution in multi-scale PMCs. More particularly, the work is the first to study re-agglomeration of CNTs during RFI and filtration of CNTs due to transverse resin flow across fibre reinforcement.

# Chapter 3

## Experimental plan and methods

This chapter presents the methodology that was followed for achieving the objectives of the thesis. It is divided into five sections.

Section 1 details the research plan that was followed throughout the work. Section 2 describes the RFI process and presents all variations tested in this work. Sections 3 to 5 discuss experiments that were carried out during the work. These were divided into three types: physical characterisation of materials, mechanical characterisation and computer modelling.

### 3.1 Research plan

The main objective of the thesis was to validate the viability of out-of-autoclave RFI processing for fabricating multi-scale carbon fibre PMCs featuring epoxy modified with CNTs, following a methodology that may be used at industrial scale. This can only be achieved through a thorough understanding of the RFI process. Based on the review of literature presented in Chapter 2, prior knowledge of RFI was lacking for achieving the objectives. Thus, in addition to studying the fabrication of multi-scale PMCs, the work required an exhaustive study of the RFI process.

The methodology followed towards the completion of the thesis is described in Figure 3.1. It is a progressive process featuring 4 main strategic focus areas.

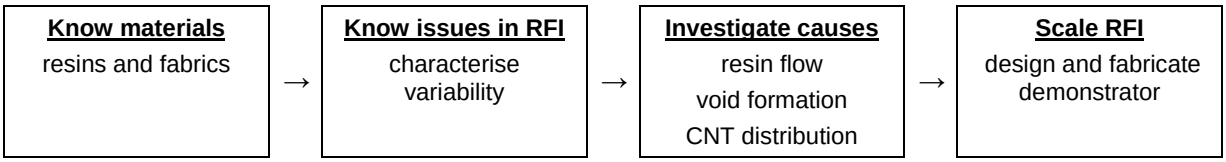


Figure 3.1: Process followed for the fabrication of multi-scale PMCs through RFI

The first focus area consisted of selecting different grades of resins and fabrics that are representative of those used in RFI applications. It is essential that their properties be quantified extensively as they have a direct effect on RFI processing. In the case of the resins, the first focus area involved characterising properties including the film geometry, density, viscosity, surface tension and contact angle. Fabrics characterisation included the geometry, surface density and compaction behaviour. This strategic focus area is discussed in chapters 4 and 5.

The second focus area consisted in understanding processing issues that can arise during the fabrication of PMC parts made using RFI. This was achieved by performing a preliminary study of the fabrication of flat laminates. Numerous parameters were investigated including material selection, bagging configuration, level of interleaving and use of CNTs. The quality of laminates was then characterised in terms of porosity, fibre volume fraction and interlaminar strength in selected cases. The identification of defects and processing issues contributed to the planning of follow-up experiments. This strategic focus area is discussed in Chapter 6.

The third focus area consisted of understanding the sources of processing issues previously identified. It enabled detailed analysis of three core elements namely resin flow, void formation and CNT distribution, and was achieved by studying the influence that the materials and level of stack interleaving have on RFI processing. In the case of resin flow, the work describes how processing parameters affect resin saturation of fabric layers, locally and globally. This is done through in-situ observation of resin flow at the surface of the RFI stack, coupled with computer simulations for gaining better understanding of flow inside the stack. Void formation was characterised through in-situ observations. Several types of voids were studied, but greater effort was put towards the study of volatile voids formed by out-of-solution gases because they were the most important source of PMC

defects in this work. The loss of a uniform distribution of CNTs in the resin during RFI processing was characterised by studying CNT filtration and CNT clustering. These mechanisms were linked to fabric architecture and resin viscosity. The knowledge developed in this third strategic focus area enabled a better understanding of the sources of defects and how they may be mitigated, contributing to the development of guidelines for the reliable manufacturing of parts using RFI. This strategic focus area is discussed in chapters 7, 8 and 9.

Finally, the fourth focus area consisted in evaluating the scalability of the process. The work consisted in designing and fabricating a part that is representative of an industrial part. For this work, the part selected was a delta-stringer panel designed in collaboration with Bombardier Aerospace. The work sought to identify potential issues with the scaling-up process, leading ultimately to the fabrication and comparison of demonstrator panels made of neat PMCs and multi-scale PMCs. Two types of delta-stringer panels were fabricated, small-scale panels for preliminary work and large-scale demonstrator panels for the proof of concept. This strategic focus area is discussed in Chapter 10.

Ultimately, the progressive approach to the work ensured that it provided clear understanding of the feasibility and issues in using RFI for manufacturing multi-scale PMCs.

## 3.2 Fabrication

This section describes the method used for producing PMCs through RFI. The presentation of the process is divided in four categories: 1) description of materials, 2) stacking of fabric reinforcements and resin films, 3) PMC cure and 4) vacuum bagging.

### 3.2.1 Materials

#### 3.2.1.1 Resins films

Hot-melt epoxy-based resin films were prepared by Axson (formerly Nanoledge) and Gurit Ltd. They were B-staged pre-catalysed resin films that are semi-solid at room

temperature due to partial curing. The films differ in resin formulation and CNT loading. Their characteristics appear in Table 3.1.

Table 3.1: Specifications of resin films as reported by suppliers [142–144]

| Resin system | Manufacturer | Resin formulation | CNT loading (wt%) | Surface density ($g/m^2$) | $T_g$ (°C) | Viscosity (Pa·s) |
|---|---|---|---|---|---|---|
| LEO 2376 | Axson | L7 | 0 | 120 | 160 | 190 at 60°C |
| LEO 2377 | Axson | L7 | 0.3 | 100 | 160 | 260 at 60°C |
| LEO 2396 | Axson | L9 | 0 | 120 | 180 | 61 at 60°C<br>18.5 at 70°C<br>8.6 at 80°C |
| LEO 2397 | Axson | L9 | 0.3 | 100 | N/A | N/A |
| SA 70 | Gurit | SA 70 | 0 | 150[a] | 120 | N/A |

Note: [a] SA 70 features a 25 $g/m^2$ glass fibre carrier

Axson supplied four resin films: LEO 2376, LEO 2377, LEO 2396 and LEO 2397. The films were supplied in two batches at different times over the project duration and in different thicknesses. Resin films were made from two resin formulations referred to as formulations L7 and L9. Both formulations were made from mixtures of bisphenol A epoxy resin and dicyane diamide (DICY) based hardener [145]. The major differences between them are their viscosities and glass transition temperatures of 160°C and 180°C after cure for formulations L7 and L9 respectively. Resin films of both formulations were also loaded with 0.3 wt% of Baytubes® C 150 P multi-walled carbon nanotubes (MWCNTs) from Bayer MaterialScience AG and their properties appear in Table 3.2.

Table 3.2: Specifications of Baytubes® C 150 P MWCNTs as reported by the supplier [146]

| Property | Value |
|---|---|
| Purity | >95 wt% |
| Number of walls | 3 to 15 |
| Outer diameter | 13 nm |
| Inner diameter | 4 nm |
| Length: -before dispersion | >1 μm |
| -after dispersion | 0.2 μm to 1 μm |
| Bulk density (ISO 60) | 0.13 g/cm$^3$ to 0.15 g/cm$^3$ |
| Loose aggregate size | 0.1 mm to 1 mm |

In addition to the LEO resin film series, epoxy-based resin film SA 70 from Gurit was used for assessing the effect of resin formulation. It features a neat prepreg resin formulation that has lesser flowabilty than the LEO infusion resins. It should be noted that SA 70 resin film features a light glass fibre support carrier which remains in PMC parts following RFI processing.

The characterisation of resin films is reported in Chapter 4.

#### 3.2.1.2 Fabric reinforcements

A total of 7 carbon fibre fabrics and 1 glass fibre fabric were used for assessing the effect of fabric architecture on PMC processing and laminate quality. The fabrics have different surface densities and architectures including plain weaves, twills 2×2, bidirectional non-crimp stitched fabrics and unidirectional non-crimp fabrics. A complete list of fabrics appears in Table 3.3. The codes given to each fabric identify the architecture followed by a distinct characteristic; for example, *L* is for a low surface density, *H* is a high surface density, *P* is for the use of powder binder, *D* identifies the fabric used for the demonstrator and *G* stands for glass fibres.

It should be noted that most work towards studying the effect of fabrics is performed using fabrics PW-L, Twill-L, Twill-H, NCF-L and NCF-H because they enable direct

comparisons for the cover factor, surface density and architecture. Photographs of these fabrics appear in Figure 3.2. Characterisation of these fabrics is reported in Chapter 5. Fabrics NCF-HP and NCF-HD were supplied by Bombardier Aerospace. They featured similar architectures and surface densities as fabric NCF-H, and were used as replacement of other carbon fabrics in less critical work due to limited availability. Finally, fabric Twill-G was used in Chapter 9 for assessing CNT filtration because glass fibres enabled sharp contrast imaging of dark CNTs.

Table 3.3: Specifications of fabric reinforcements as reported by suppliers

| Fabric | Manufacturer | Style | Orientation | Surface density ($g/m^2$) | Fibre | Yarn |
|---|---|---|---|---|---|---|
| PW-L | Texonic | Plain weave | (0/90) | 197 | HTS40 | 3K |
| Twill-L | Texonic | Twill 2×2 | (0/90) | 215 | HTS40 | 3K |
| Twill-H | Texonic | Twill 2×2 | (0/90) | 429 | HTS40 | 6K |
| NCF-L | Saertex | NCF, tricot-warp knitted | (-45/+45) | 250 | HTS40 | 12K |
| NCF-H | Saertex | NCF, chain stitched | (-45/+45) | 534 | HTS40 | 12K |
| NCF-HP | Saertex | NCF, chain stitched, powder binder | (-45/+45) | N/A | N/A | N/A |
| NCF-HD | Saertex | NCF, tricot-warp knitted | (-45/+45) | N/A | N/A | N/A |
| Twill-G | N/A | Twill 2×2 | (0/90) | N/A | E-glass | N/A |

Notes: - no datasheet were provided for fabrics NCF-HP, NCF-HD and Twill-G

Nomenclature:
- L: Low surface density
- H: High surface density
- P: Powder binder
- D: Fabric for technical demonstrator
- G: Glass fibres

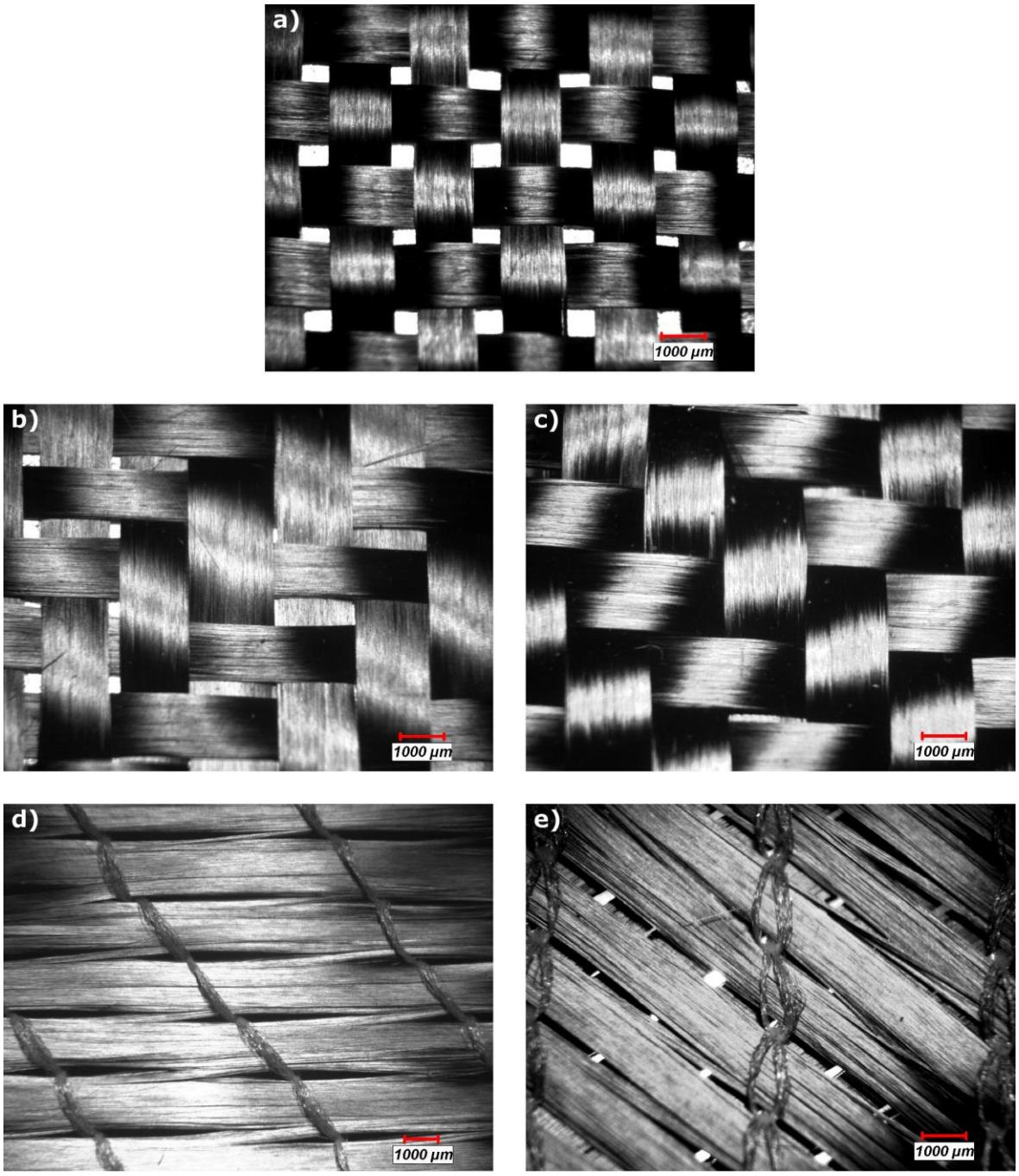


Figure 3.2: Fabric a) PW-L, b) Twill-L, c) Twill-H, d) NCF-L and e) NCF-H

Most fabrics were made from untwisted poly-acrylonitrile (PAN) HTS40 (Toho Tenax) carbon fibre yarn. Specifications of the carbon fibres obtained from Toho Tenax appear in Table 3.4. The exact nature of the fibre sizing was not specified by the fibre or fabric suppliers but they can be of two types: epoxy-based or polyurethane-based.

Table 3.4: Specifications of HTS40 fibres as reported by the supplier [147, 148]

| Property | Value |
|---|---|
| Density | 1.76 g/cm$^3$ |
| Diameter | 7.0 μm |
| Thermal expansion, longitudinal | -0.1 μm/m |
| Specific heat capacity | 710 J/kg·K |
| Thermal conductivity, longitudinal | 10 W/m·K |
| Tensile strength | 4200-4600 MPa |
| Tensile modulus | 240 GPa |
| Elongation at break | 1.8% |
| Electrical resistivity | $1.6 \times 10^{-3}$ Ω·cm |
| Sizing level | |
| - E23 sizing (epoxy-based) | 1.3% |
| - F13 sizing (polyurethane-based) | 1.0% |

### 3.2.2 Lay-ups

The RFI stacking process consists in laying fabric and resin film plies in a specific sequence, producing a stack that is consolidated into a PMC afterwards. The stacking sequence, or configuration, depends mostly on the desired level of interleaving. In the thesis, two stacking configurations were tested, bulk and interleaved stacking. The number of resin films was selected towards targeting a conservative $V_f$ value of 55% in consolidated PMC laminates; an extra 10% of resin was added for bleeding and limiting risks of resin starvation.

In bulk RFI (Figure 3.3), separate stacks of fabric reinforcements and resin films were prepared and then superimposed, resulting in stacks devoid of interleaving. For fabric reinforcement stacks, plies were layered for obtaining balanced stacks. Laminates consisted in square symmetric lay-ups with orthogonal fibre directions of $[0/90]_{NS}$ or $[+45/-45]_{NS}$. For the resin film stacks, thin plies were stacked together using a laminating roller, forming thick single layer resin films. The laminating roller was used for removing air pockets that formed between collated plies. Finally, the two stacks of fabric and resin were assembled

together by laying the dry fabric reinforcement stack over the resin film stack, forming the final PMC stack.

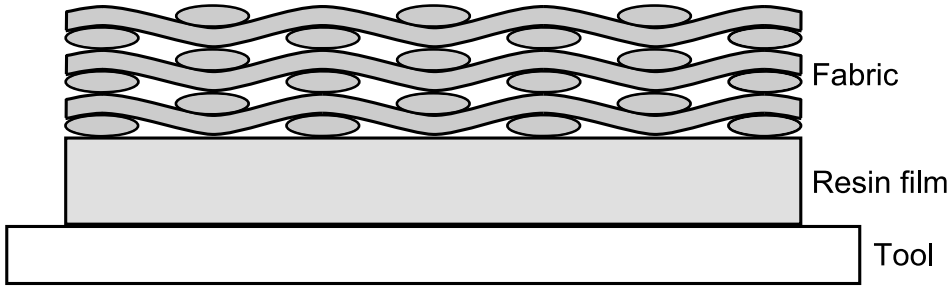


Figure 3.3: Bulk RFI stacking configuration

In interleaved RFI (Figure 3.4), a single stack was made from layering fabric reinforcement plies and resin films alternatively, resulting in complete interleaving. The fabric reinforcement plies and resin films were compacted together using a laminating roller. Fabric orientations for flat laminates were selected to create square symmetric PMC lay-ups as for bulk RFI. The interleaved method was also used for fabricating the technological demonstrator discussed in Chapter 10 which features a quasi-isotropic lay-up.

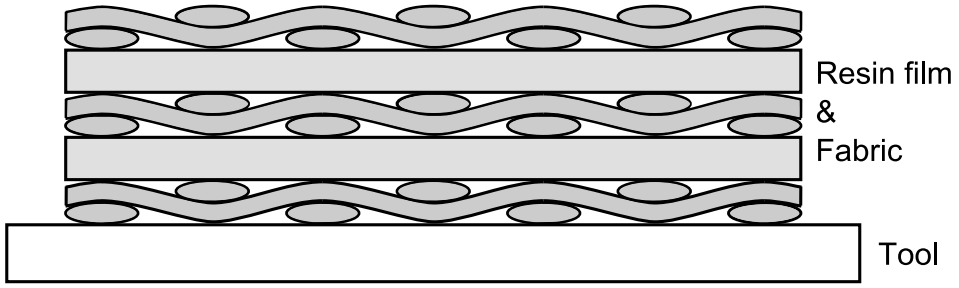


Figure 3.4: Interleaved RFI stacking configuration

In the case of flat laminates, bulk and interleaved RFI result predominantly in through-thickness resin flow. However, some part geometries may lead to in-plane flow. This is the case, for example, of the fabrication of stiffened panels made with bulk RFI. In this work, the influence of in-plane flow on the filtration of CNTs is presented in Chapter 9. In-plane flow was achieved by using an unconventional RFI method, in-plane RFI, which consisted in using parallel stacks of fabric reinforcements and resin films. Instead of layering stacks on top of each other, they were positioned side by side (Figure 3.5).

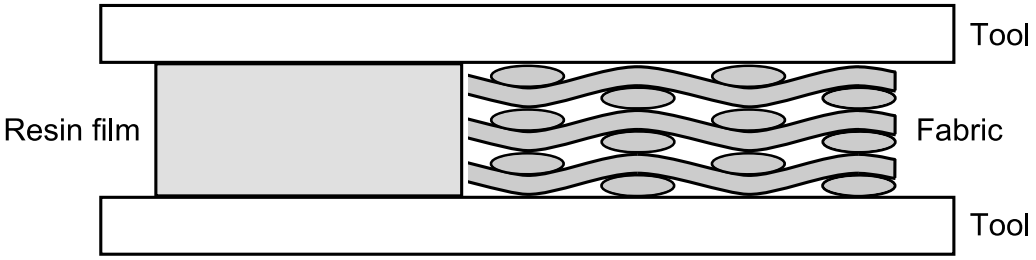


Figure 3.5: In-plane RFI stacking configuration

### 3.2.3 Cure cycles

PMC stacks were cured in a convective oven (PF120, Carbolite Inc.). Most cures were made following the recommended cure temperature profile (Figure 3.6). In-situ studies of RFI presented in chapters 7-9 used conductive heating method for cure. This used a 7 mm thick aluminium caul plate featuring a HR5466 flexible electric heater from MINCO supplied with 70 W. Heater power was controlled through a hysteresis controller programmed in LabVIEW with a ±1°C threshold. The control thermocouple was located on the dry side of the caul plate, 10 mm away from the heater.

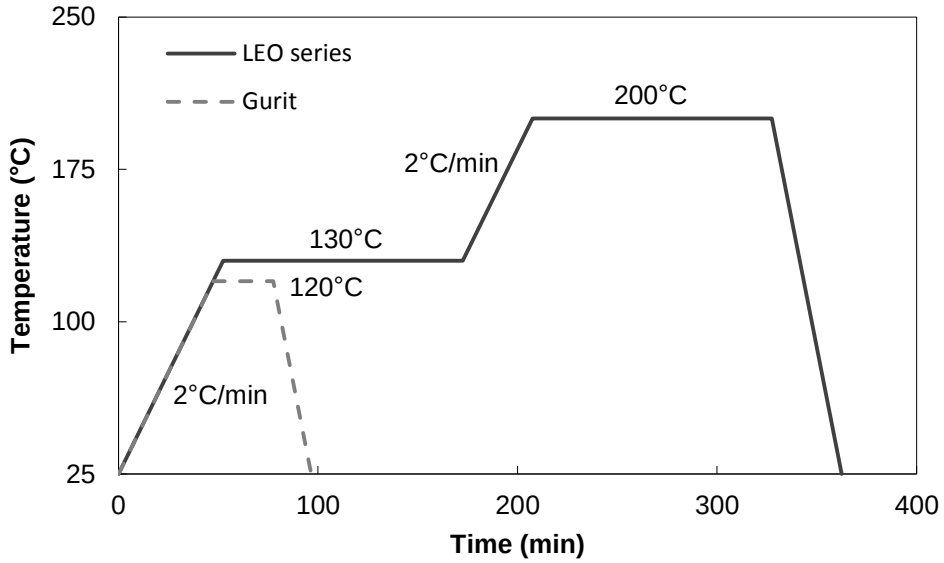


Figure 3.6: Manufacturer cure cycle (L-STD and S-STD) for the LEO series and Gurit SA 70 resin films

Stacks made with any type of LEO resin film require the same cure conditions. They are heated at a rate of 2°C/min up to a temperature of 130°C which is held for 2 hours. Afterwards, they are heated at a rate of 2°C/min up to a temperature of 200°C for a post-cure lasting 2 hours. The consolidated PMCs are then left to cool back to room temperature. This cure cycle is referred to as L-STD.

Stacks made with the SA 70 resin film are heated at a rate of 2°C/min up to a temperature of 120°C which is held for 30 min. The resin film does not require any post-cure. Once consolidated the PMC is left to cool back slowly down to room temperature. This cure cycle is referred to as S-STD.

In certain experiments featuring the LEO resin films presented in chapters 6 and 9, cure cycles different to those proposed by the manufacturer are used for evaluating their effect on the processing of PMCs. A complete list of cure cycles appears in Table 3.5. Cure cycle L-MON was used during experiments designed for monitoring resin flow. It followed the same cure as L-STD but did not use any post-cure. Cure cycle L-LCT was used in Chapter 9 for studying CNT clustering and it featured a low cure temperature for controlling resin viscosity.

Table 3.5: Cure cycles used in this work

| Resin film | Name | Cure | | | Post-cure | | |
|---|---|---|---|---|---|---|---|
| | | Ramp (°C/min) | Temperature (°C) | Duration (hr) | Ramp (°C/min) | Temperature (°C) | Duration (hr) |
| LEO series | L-STD | 2 | 130 | 2 | 2 | 200 | 2 |
| | L-MON | 2 | 130 | 2 | | | |
| | L-LCT | 2 | 60 | 72 | 2 | 200 | 2 |
| SA 70 | S-STD | 2 | 120 | 0.5 | | | |

### 3.2.4 Bagging configurations

Fabric and resin film stacks were consolidated under a vacuum bag. The various bagging configurations and vacuum ancillaries used are described in this section. Bagging configurations were divided based on the type of RFI processing: bulk RFI, interleaved RFI and in-plane RFI. Additionally, this section also describes the double vacuum bagging method that was used in Chapter 8 for studying void formation.

#### 3.2.4.1 Vacuum equipment and bagging ancillaries

Consolidation was achieved by pulling a vacuum of 0.98 bar under a vacuum bag, applied using a diaphragm vacuum pump (DAA-V715A-EB, Gast). In all experiments other than those featuring the double vacuum bagging method, the vacuum was pulled for the entire cure duration.

Ancillaries for vacuuming and consolidating PMCs were:

- Flat aluminium tool, 6 mm thick
- Flat glass tool, 15 mm thick
- Flat aluminium caul plate, 6 mm thick
- Flexible silicone rubber caul sheet, 1.5 mm thick
- Bag material (Securlon® L-1000, Airtech)
- Release film (Wrightlon® 5200B, Airtech)

- Perforated release film with 0.14% open area (Wrightlon® 5200B-P3, Airtech)
- Breather material (UltraWeave® 606, Airtech)
- Sealant tape and dam material (SM5126, Schnee-Morehead)
- Glass weave (3M)
- Release agent (Chemlease, Chemtrend)

#### 3.2.4.2 Bulk RFI bagging methods

Three different bagging methods were used for investigating bulk RFI (Table 3.6). The methods were selected based on previous expertise and knowledge developed during the work. They differed based on the type of bleeding configuration and use of a sacrificial bleeder ply.

**Table 3.6: Differences between the bulk RFI bagging methods**

| Bagging method | Bleeding | Sacrificial breather ply | Comment |
|---|---|---|---|
| B-1 | Surface | Yes | Standard approach |
| B-2 | Edge | No | |
| B-3 | Mostly surface | No | Method B-1 adapted for in-situ observations |

Bagging method B-1 was the standard approach developed during the project for bulk stacks (Figure 3.7) and consisted of placing the stack on a tool that was protected with a release film. The stack was positioned in such manner that the resin was facing the tool. The edges of the stack were sealed with a sealant tape dam, ensuring that resin flows in the through-thickness direction. The stack was covered with perforated release film and with a glass fibre weave for extracting air and volatiles. A caul plate was used for ensuring uniform compaction. Two layers of breather connected to a vacuum port were placed over the entire assembly. Finally, a vacuum bag was installed and sealed with the same sealant tape as the dam of the stack.

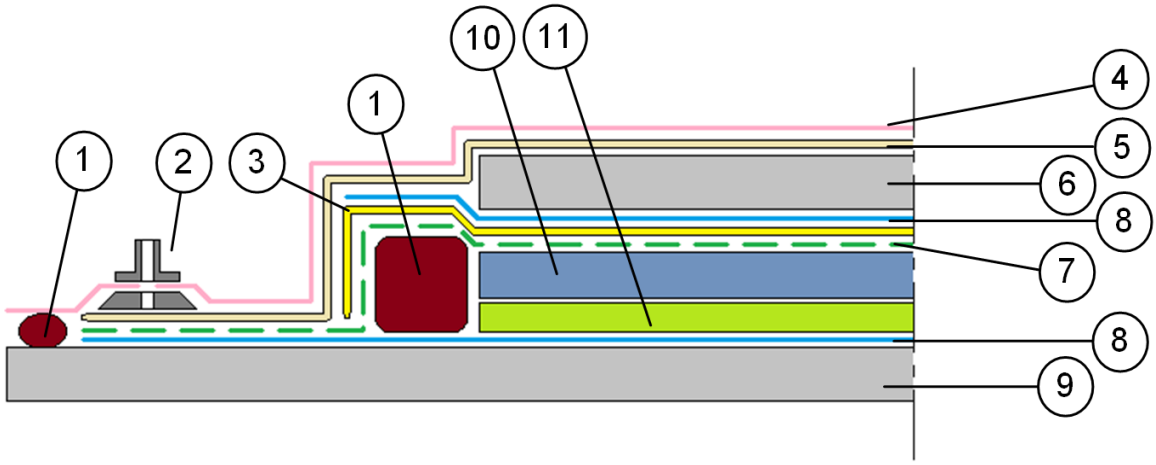


1) Sealant tape 2) Vacuum valve 3) Glass fabric 4) Bag 5) Breather
6) Caul plate 7) Perforated film 8) Release film 9) Tool 10) Fabric
11) Resin

Figure 3.7: Bagging method B-1 for bulk RFI

Bagging method B-2 for bulk stacks (Figure 3.8) featured edge breathing instead of surface breathing like method B-1. Bleeding and breathing was performed by a layer of glass fabric wrapped around the sealant tape edge dam.

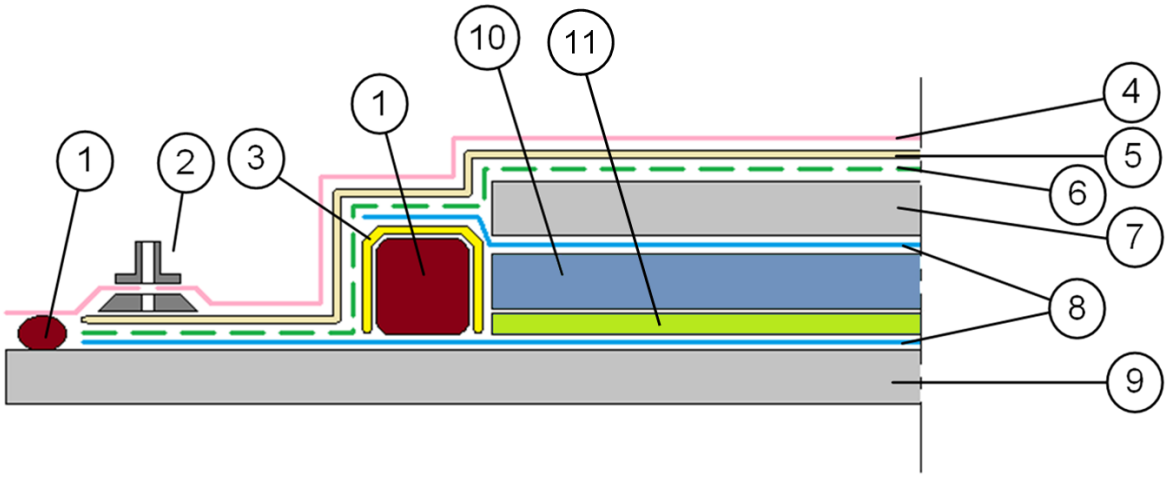


1) Sealant tape 2) Vacuum valve 3) Glass fabric 4) Bag 5) Breather
6) Perforated film 7) Caul plate 8) Release film 9) Tool 10) Fabric
11) Resin

Figure 3.8: Bagging method B-2 for bulk RFI

Bagging method B-3 for bulk stacks (Figure 3.9) was the method used for in-situ monitoring of resin flow performed over a glass tool. It is equivalent to method B-1 but in an inverted sequence, i.e. the dry fabric stack is laid directly on the tool instead of the resin stack. Additionally, bleeding and breathing were achieved using the first ply of the stack as opposed to having a dedicated glass fibre layer on the surface of the stack. This enabled direct monitoring of resin flow at the surface of the stack through the glass tool. No release film was used on the surface of the tool to help with the observation of resin flow at the surface of the fabric stack; instead the glass tool was coated with a release agent.

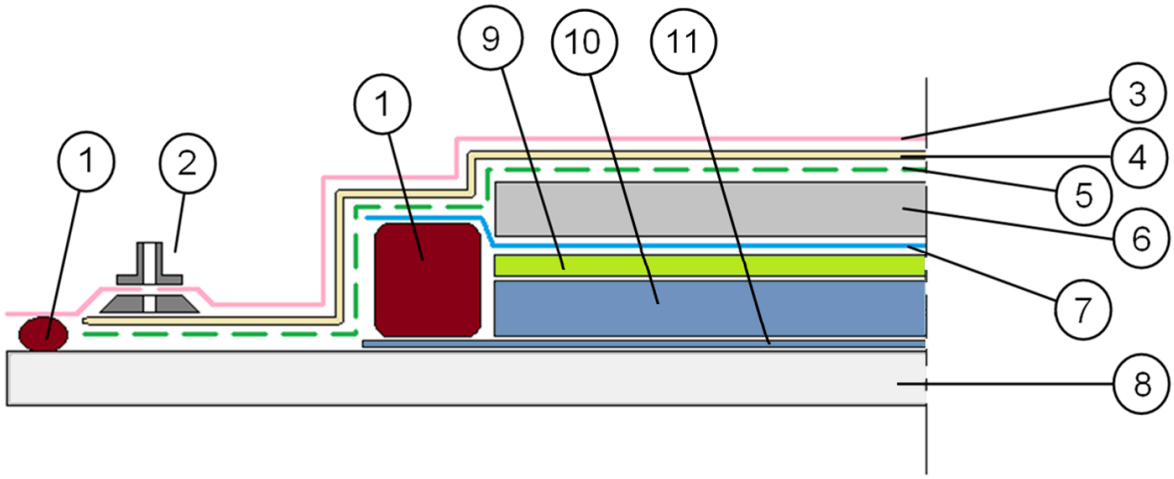


1) Sealant tape 2) Vacuum valve 3) Bag 4) Breather 5) Perforated film
6) Heated caul plate 7) Release film 8) Glass tool 9) Resin 10) Fabric
11) Surface fabric ply

Figure 3.9: Bagging method B-3 for bulk RFI

#### 3.2.4.3 Interleaved RFI bagging methods

Six different bagging configurations were tested for interleaved RFI (Table 3.7). The methods were selected based on previous expertise and knowledge developed during the work. They differed based on the use of a caul plate, type of bleeding configuration, use of a release film on the surface of stacks and restriction of the bleeding.

**Table 3.7: Differences between the interleaved RFI bagging methods**

| Bagging method | Caul plate | Bleeding | Surface release film | Restricted bleeding | Comment |
|---|---|---|---|---|---|
| I-1 | Yes | Edge | Yes | No | Standard approach |
| I-2 | Yes | Surface | No | No | |
| I-3 | Yes | Edge | No | No | |
| I-4 | No | Edge | Yes | No | |
| I-5 | Yes | Edge | Yes | Yes | |
| I-6 | Yes | Edge | Yes | No | Method I-1 adapted for in-situ observations |

Bagging method I-1 for interleaved stacks (Figure 3.10) was the standard approach developed during the project for performing interleaved RFI. In this case, the stack of fabric reinforcements and resin films was placed over a tool that was protected with a release film. Edge breathing was used for extracting air and volatiles out of the stack. This consisted of a glass fibre weave covering a sealant tape dam that was in contact with the edges of the stack. The stack was covered in release film and a caul plate was used for providing uniform compaction. The assembly was covered with perforated release film and two layers of breather connected to a vacuum port.

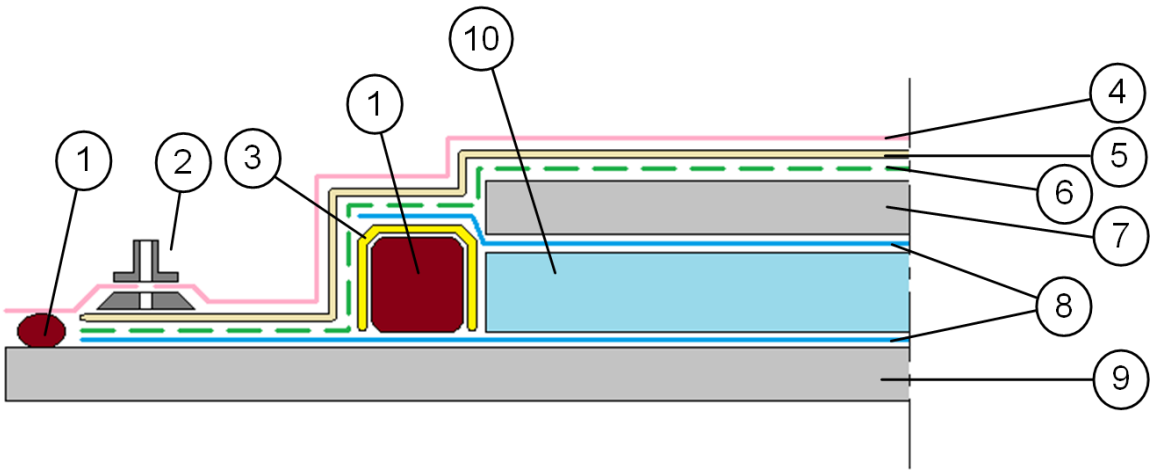


1) Sealant tape 2) Vacuum valve 3) Glass fabric 4) Bag 5) Breather
6) Perforated film 7) Caul plate 8) Release film 9) Tool 10) Stack

Figure 3.10: Bagging method I-1 for interleaved RFI

Bagging method I-2 for interleaved stacks (Figure 3.11) was the first method used in the project for performing interleaved RFI. It used a metallic frame around the edges of the stack and a caul plate on the surface of the stack for controlling resin bleeding. Breathing was ensured through a bleeder ply positioned between the caul plate and stack. The method was not retained due to difficulties in removing the cured parts from the metallic frame and excessive bleeding.

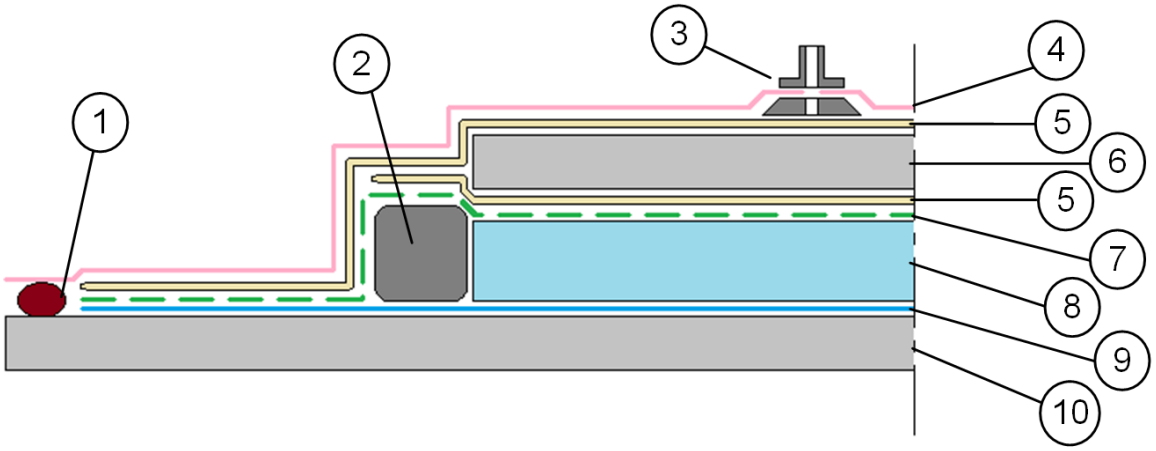


1) Sealant tape 2) Metal frame 3) Vacuum valve 4) Bag 5) Breather
6) Caul plate 7) Perforated film 8) Stack 9) Release film 10) Tool

Figure 3.11: Bagging method I-2 for interleaved RFI

Bagging method I-3 for interleaved stacks (Figure 3.12) was the precursor of method I-1. It differed only by the absence of the non-perforated release film covering both the stack and dam. The method can lead to important bleeding due to a gap between the dam and the caul plate.

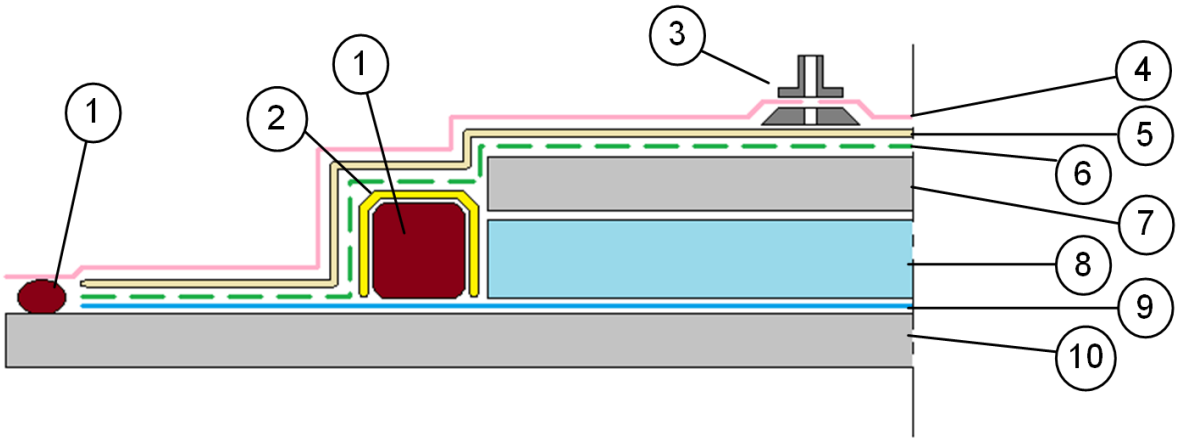


1) Sealant tape 2) Glass fabric 3) Vacuum valve 4) Bag 5) Breather
6) Caul plate 7) Perforated film 8) Stack 9) Release film 10) Tool

Figure 3.12: Bagging method I-3 for interleaved RFI

Bagging method I-4 for interleaved stacks (Figure 3.19) was very similar to method I-1 except that it did not feature a caul plate.

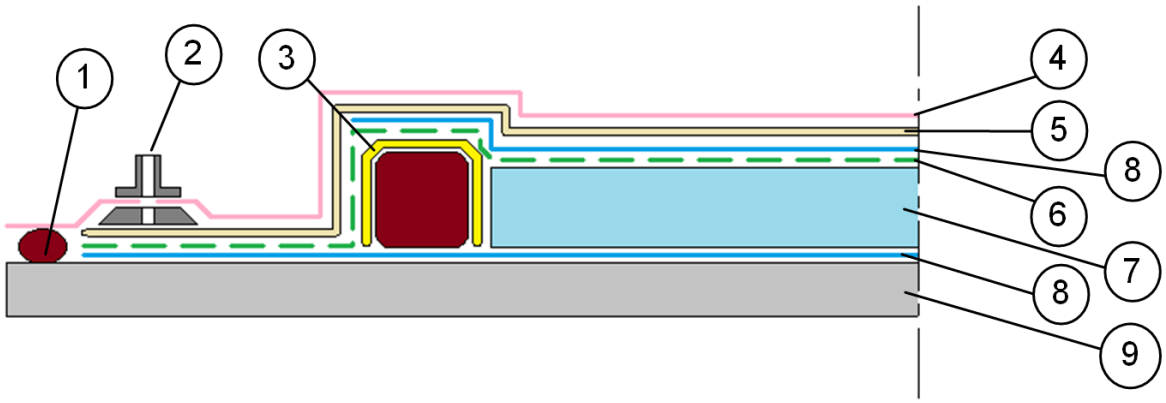


1) Sealant tape 2) Vacuum valve 3) Glass fabric 4) Bag 5) Breather
6) Perforated film 7) Stack 8) Release film 9) Tool

Figure 3.13: Bagging method I-4 for interleaved RFI

Bagging method I-5 for interleaved stacks features the exact same ancillaries as method I-1. The only difference is that edge bleeding was restricted by reducing the coverage of the glass fabric weave above the sealant tape dam surrounding the RFI stack. Instead of full coverage, the glass fabric only covered 5% of the edge dam (Figure 3.14).

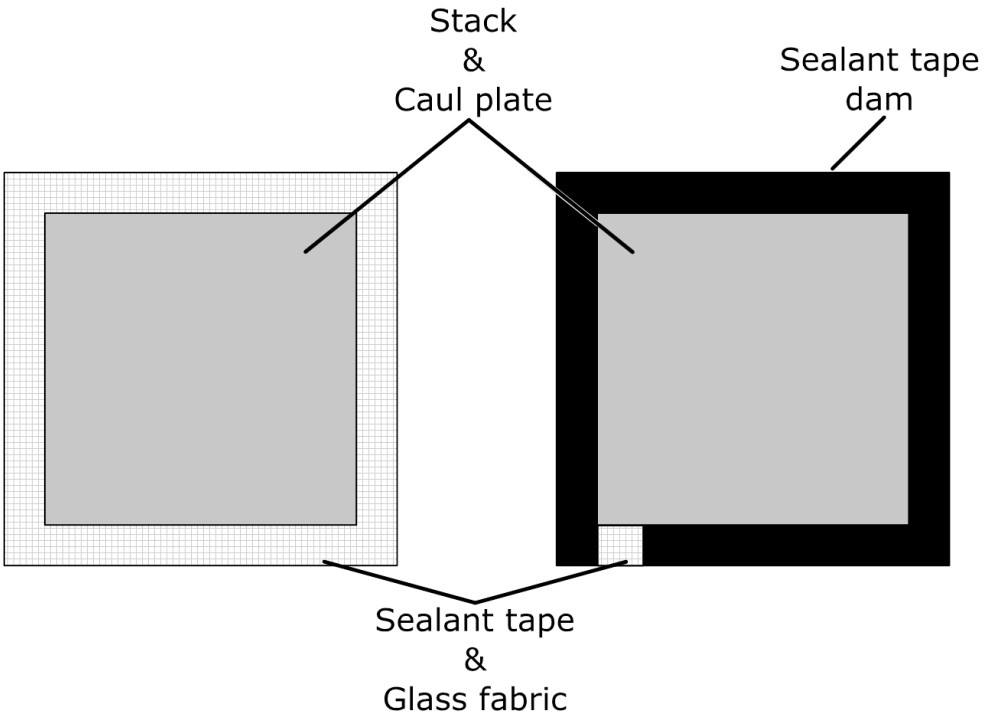


Figure 3.14: Top view comparing the edge bleeding coverage for bagging methods I-1 (left) and I-5 (right)

Bagging method I-6 for interleaved stacks (Figure 3.15) is the method that was used for in-situ monitoring of resin flow. It is very similar to method I-1 except that consolidation is performed over a glass tool. Additionally, to ensure good visibility of the stack, no release film was added on the tool; instead a liquid release agent was applied to ensure debonding of the cured stack.

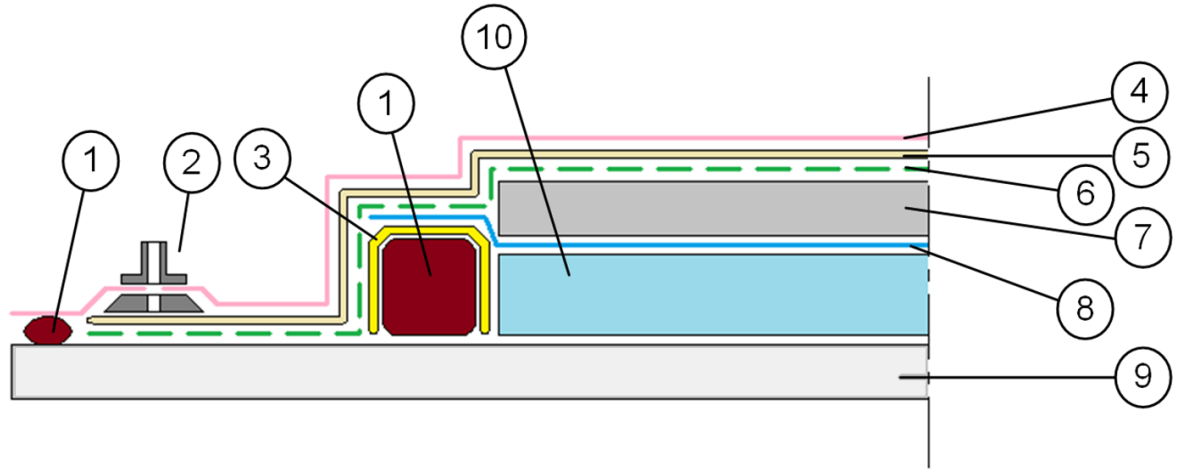


Figure 3.15: Bagging method I-6 for interleaved RFI

#### 3.2.4.4 In-plane RFI bagging configuration

In this work, a single bagging configuration was used for in-plane RFI: bagging method P-1 (Figure 3.16). Stacks of resin films and dry fabrics were laid adjacent to each other inside an inner bag made of release film. The opening of the inner bag was at the edge of the fabric stack, forcing resin flow through the fabric stack. The inner bag was laid over a tool that featured an open and closed section. The fabric stack was laid in the closed section, ensuring a constant stack thickness during processing. The resin film stack was laid in the open section and compression of the resin was achieved through a caul plate. Edge breathing was used for controlling resin bleeding. It consisted of a sealant tape dam wrapped in a glass fabric weave. The assembly was covered with perforated release film and two layers of breather. It was then sealed in a bag and connected to a vacuum pump.

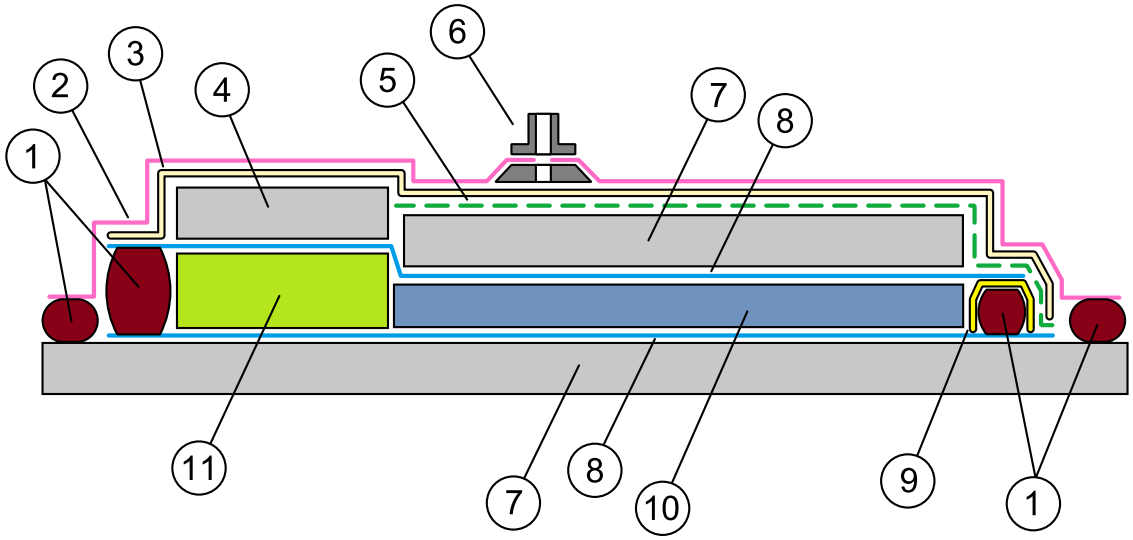


1) Sealant tape 2) Bag 3) Breather 4) Caul plate 5) Perforated film
6) Vacuum valve 7) Closed tool 8) Release film 9) Glass fabric 10) Fabric
11) Resin

Figure 3.16: Bagging method P-1 for in-plane RFI

#### 3.2.4.5 Double vacuum bagging method

The double vacuum bagging method was used for investigating void formation in Chapter 8. The method consisted of performing PMC consolidation of interleaved RFI stacks inside a rigid chamber, providing independent control over ambient pressure and pressure inside an inner vacuum bag. The term double vacuum bagging refers to the use of an outer bag that sealed the chamber and inner bag in which stacks were consolidated (Figure 3.17).

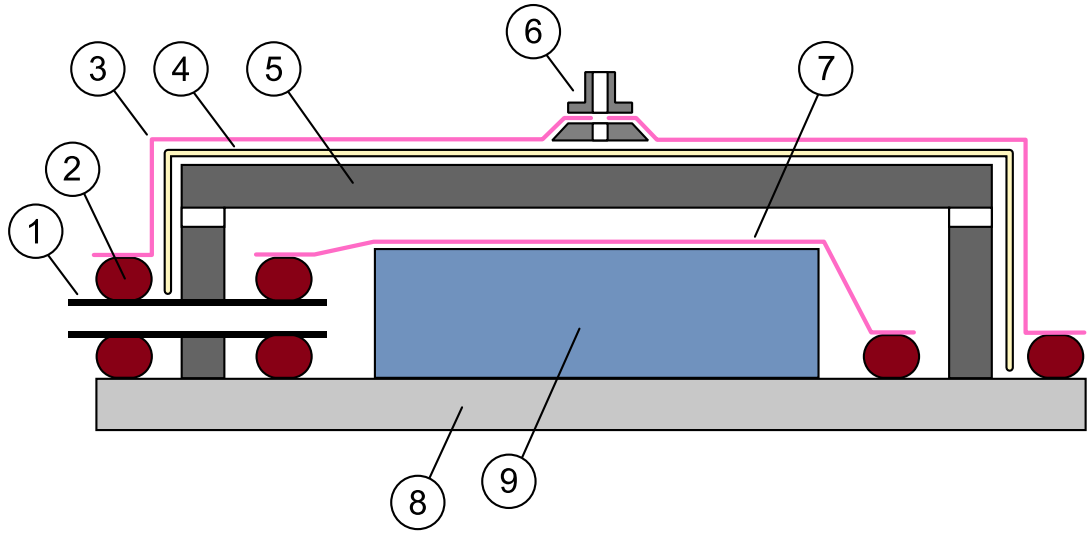


1) Vacuum tube 2) Sealant tape 3) Outer bag 4) Breather 5) Chamber
6) Vacuum valve 7) Inner bag 8) Tool 9) Stack and ancillaries

Figure 3.17: Double vacuum bagging method

The double vacuum bagging method enables four different pressure conditions that are described in Table 3.8. Mode OH-IH occurs when both the inner and outer bags are at ambient pressure. This mode is equivalent to using no bags. Mode OH-IL occurs when vacuum is pulled only in the inner bag. This is equivalent to using a single vacuum bag, leading to compaction of the fabric/resin stack. Mode OL-IL occurs when vacuum is pulled under both the inner and outer bags. This does not cause any compaction of the RFI stack, but it subjects the resin to a low pressure. Mode OL-IH occurs when vacuum is pulled only in the outer bag. There is no use for this mode as it leads to the same pressure conditions as mode OH-IH with the exception that the inner bag inflates. The other important aspect of the double vacuum bagging method is that pressure conditions can be changed at any time during consolidation.

Table 3.8: Pressure conditions achievable with double vacuum bagging method

| | | Outer bag pressure | |
|---|---|---|---|
| | | Low | High |
| Inner bag pressure | Low | OL-IL: Degassing<br>No compaction<br>Low resin pressure | OH-IL: Resin flow<br>Compaction<br>High resin pressure |
| | High | OL-IH: Bag inflation<br>No compaction<br>High resin pressure | OH-IH: Ambient conditions<br>No compaction<br>High resin pressure |

The double vacuum bagging method was implemented by first making a vacuum bag over a tool using bagging method I-6. This vacuum bag was termed the inner bag. Then a rigid vacuum chamber made of wood and aluminium was installed over the inner bag. The chamber was sealed with a vacuum bag, termed the outer bag. Each bag was connected to independent vacuum ports, providing control over the pressure of the bags.

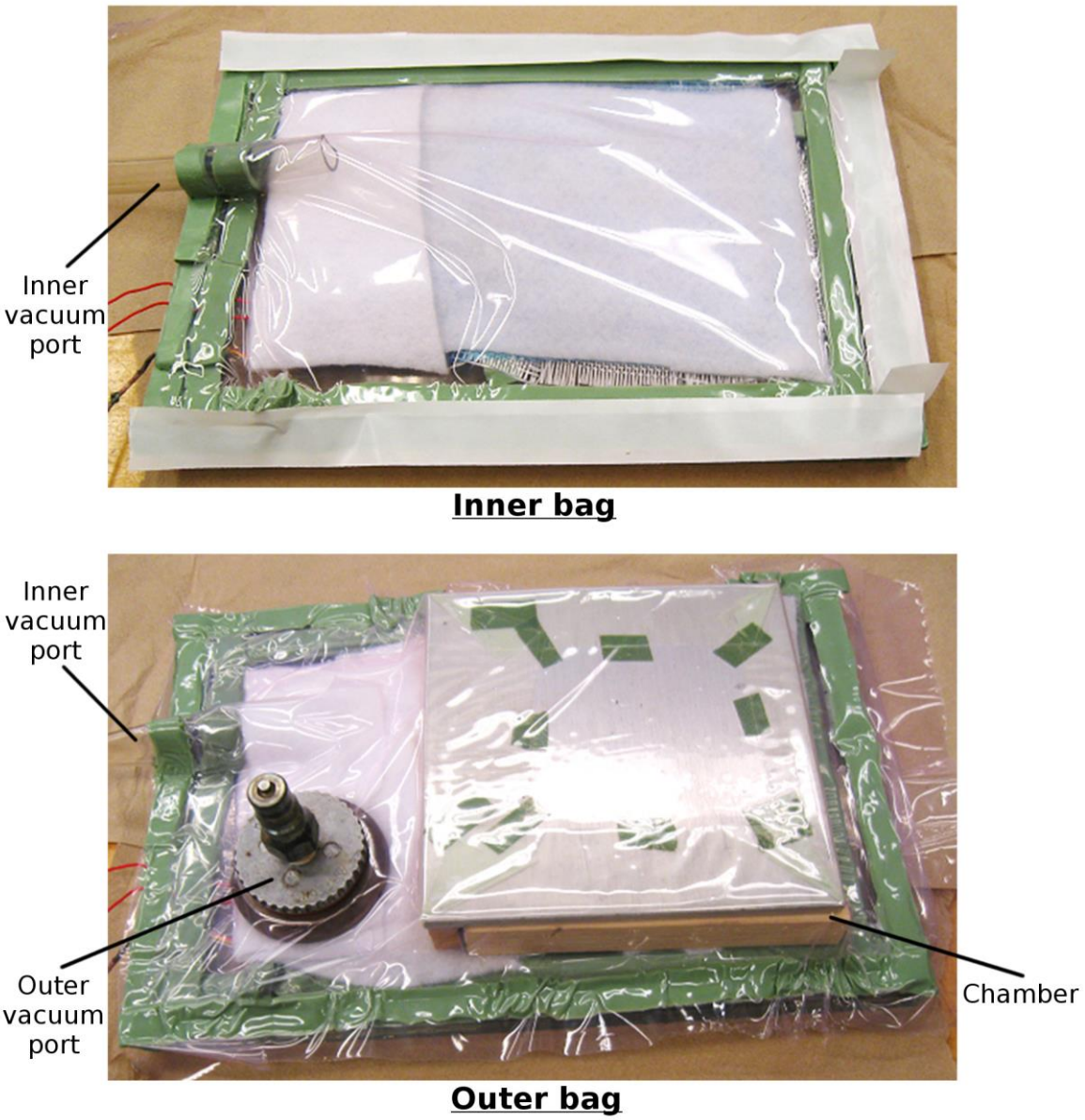


Figure 3.18: Double vacuum bagging experimental set-up showing the inner (top) and outer (bottom) bags

## 3.3 Physical characterisation

This section describes characterisation methods used for investigating the physical properties of materials. A list of methods and chapters in which they are used appears in Table 3.9.

Table 3.9: Physical characterisation methods

| Group | Characterisation | Ref. chapter |
|---|---|---|
| Resin films | Surface density | 4 |
| | Resin density & film thickness | 4 |
| | Resin viscosity & gelation | 4 |
| | Resin surface tension | 4 |
| | Contact angle | 4 |
| | Volatile content | 4 |
| Fabric reinforcements | Surface density | 5 |
| | Transverse permeability | 5 |
| | Pressure distribution in stacks | 5 |
| | Surface geometry of fabrics | 5 |
| | Fabric cover factor | 5 |
| Microscopy | Sample preparation | 4, 6, 8, 9, 10 |
| | Fibre volume fraction & porosity | 6, 8, 9, 10 |
| | CNT distribution | 4, 9 |

Resin films are characterised in Chapter 4. Surface density, density and thickness measurements are performed to assess manufacturing variability of resin films. These measurements also enable the calculation of the amount of resin films required for RFI stacks in chapters 6 through 10. Resin viscosity, gelation, surface tension and contact angle values are measured for enabling characterisation of the resin flow in Chapter 7. The volatile content is measured for describing void formation in PMCs in Chapter 8.

Fabric reinforcements are characterised in Chapter 5. Surface density measurements are used for assessing the manufacturing variability of the reinforcements and determining the number of fabric plies used in RFI stacks. Transverse permeability measurements are

used for describing resin flow in Chapter 7. Pressure distribution experiments enable the characterisation of the pressure state within RFI stacks prior to resin flow. It is used for understanding resin flow in Chapter 7. Surface geometry and cover factor measurements provide valuable information for characterising resin flow, void formation and CNT filtration in chapters 7-9.

Microscopy is also performed for assessing the fibre volume fraction, porosity and CNT distribution within PMCs. It is used throughout the thesis.

### 3.3.1 Resin films

#### 3.3.1.1 Resin film surface density

Surface density values for the LEO resin films were obtained by weighing plies using a high precision balance (Sartorius Extend ED124S, ±0.1 mg) and dividing the mass by the total area of the plies. Each surface density value was obtained by weighing at least 0.08 $m^2$. A minimum of 4 measurements were performed, providing an average value and standard deviation. No values were obtained for resin film SA 70 due to its limited use in this thesis for fabricating PMCs. Results appear in Section 4.1.

#### 3.3.1.2 Resin density and film thickness

Resin density and film thickness of LEO films were measured on resin film stacks featuring at least 10 plies. Density values were obtained by dividing the mass by the stack volume. The mass was measured using a high precision balance (Sartorius Extend ED124S, ±0.1 mg) while the volume was calculated from the stack dimensions measured using a calliper (Mitutoyo, ±0.01 mm). Due to limited availability of the materials only 2 to 10 density measurements were made per resin film. No values were obtained for resin film SA 70 due to its limited use in this thesis for fabricating PMCs. Results appear in sections 4.1 and 4.2.

#### 3.3.1.3 Resin viscosity and gelation

Dynamic viscosity profiles of all resin films were characterized using an oscillatory rheometer (AR 2000, TA Instruments). The equipment was operated by Hugo Laurin at NRC Aerospace. Testing was performed between parallel plates using a frequency of 1 Hz and a contact pressure of 400 Pa. Resin films were subjected to a temperature ramp of 2°C/min followed by an isothermal dwell at cure temperature. The selected temperature profiles were the same as those recommended by the manufacturers.

In addition to the providing viscosity curves, the experiments provided gelation times. They were defined as the time at which the storage modulus surpasses the loss modulus.

Viscosity and gelation results appear in Section 4.5.

#### 3.3.1.4 Resin surface tension

Surface tension measurements were made on all resin films. Measurements were performed at room temperature using the sessile drop technique with a goniometer (VCA Optima EX, AST Products Inc.). The experiment consisted in using the resins as the solid surface because they are semi-solid at room temperature, and depositing a probing water drop of 1 µL on their surface. The contact angle between the water and resin, as well as the shape of the water drop, were recorded with a camera.

Afterwards, SE-2500 Surface Energy software from AST Products Inc. was used for calculating the surface energy of the resins using the geometric mean method, which uses the known properties of water and the estimated free energy of the probing water drop based on its geometry.

Surface tension values were obtained from a series of 10 measurements. The surface tensions of the resins were measured on uncured, partially cured and fully cured resin films. Results appear in Section 4.6.

#### 3.3.1.5 Resin contact angle on a single fibre

Contact angles were measured for all resin films contacting HTS40 fibres. Measurement of the contact angle had to be performed on a resin drop contacting a single fibre. This was achieved by tensioning a yarn. Fibres were removed manually from the yarn for obtaining single fibres. Afterwards, solid resin pellets made from the films were placed on top of the tensioned fibres and the resin-fibre system was cured partially in the oven at 130°C for 2 hours. During cure, the resin pellets became liquid and some droplets formed on the fibres. The hardened resin droplets on the fibres were analysed using a digital microscope (Section 3.3.3). A typical image of the resin droplets on a single carbon fibre appears in Figure 3.19.

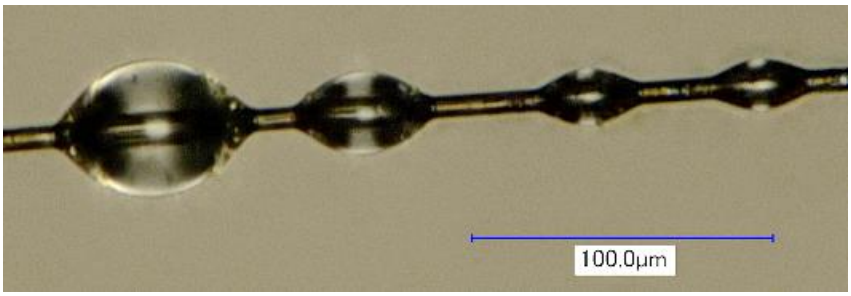


Figure 3.19: Resin droplets on a single fibre

The contact angle was taken as the smallest angle at the liquid to fibre interface, as described by Rebouillat et al. [149]. Measurement is delicate because the liquid droplets are non-spherical, and strong adhesion at the contact point of the fibre and droplet changes the shape of the droplet (Figure 3.20). In this work, the angle was measured through direct measurement, i.e. measuring the smallest angle discernible. Contact angle values were obtained from a minimum of 15 droplets for each resin. Results appear in Section 4.7.

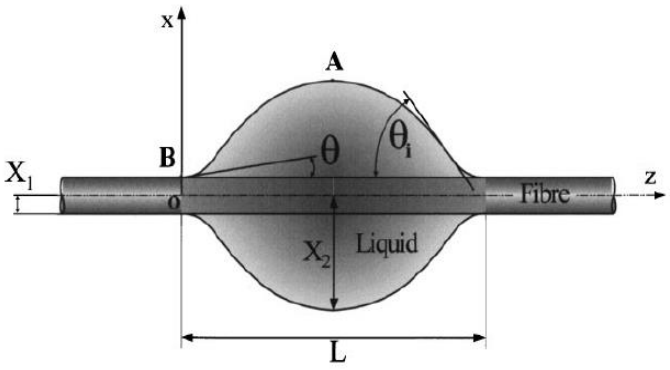


Figure 3.20: Geometric description of a liquid droplet on a single fibre where $\theta$ represents the contact angle [149]

#### 3.3.1.6 Resin film volatile contents

The initial volatile content of LEO resin films was measured using the methodology presented in ASTM D1259-06 [150] for measuring non-volatile contents of resin solutions. Test method B for heat-reactive resin solutions was followed. The method consists of weighing resin before and after a drying period of 2 hours at 105°C in ambient air. Each sample consisted of a single 75 mm by 75 mm layer of resin film weighing approximately 1 g. Mass measurements were made with a balance (Sartorius Extend ED124S, ±0.1 mg). The volatile content was defined as the ratio of the mass loss during drying to the initial mass of the resin film. No measurements were made for resin film SA 70 because it was not used in the assessment of void formation. Results appear in Section 3.3.1.6.

### 3.3.2 Fabrics

#### 3.3.2.1 Fabric surface density

Surface density values were obtained for all fabrics. Measurements were made following the same procedure as that of resin films and the method is presented in Section 3.3.1.1. Results appear in Section 5.1.

#### 3.3.2.2 Fabric permeability

An apparatus was fabricated for measuring the transverse permeability of fabrics (Figures 3.21 and 3.22). It consists of a cylindrical tube, 100 mm in diameter, through which a test fluid is pumped using a piston controlled by a universal testing machine (Instron 4482). The inside of the cylinder features three sections (Figure 3.22). The top and bottom sections are regions for stabilizing the flow rate and are free of anything that could provide significant obstruction to flow. The middle section consists of a pair of 25 mm thick honeycomb layers between which a fabric stack is positioned. Supports were added behind the honeycombs layers for reducing bending, but it is worth noting that for clarity, they are not shown in Figure 3.22. In addition, spacers were used for controlling the thickness of the fabric stack.


Figure 3.21: System for transverse permeability measurements

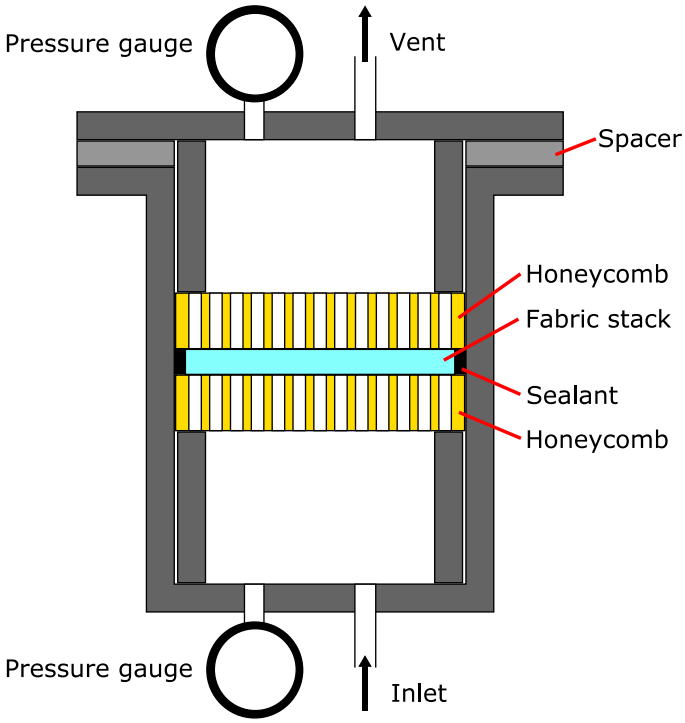


Figure 3.22: Transverse permeability apparatus

Saturated transverse permeability values of fabric stacks were measured using the modified Darcy's law (Eqn. 2.1). Results were obtained by measuring the pressure drop across a 3.6 mm thick stack having a 10 cm diameter subjected to a constant fluid flow rate. The edges of the stacks were sealed using sealant tape. A single stack was tested per type of fabric and pressure drop measurements were taken at 4 different flow rates for each stack. Pressure measurements were made using analogue gauges with a precision of ± 1 kPa in a range of 0 kPa to 100 kPa. Values were recorded for several minutes following pressure stabilization. The test fluid was pure silicone oil with a viscosity of 0.5 Pa·s. The number of fabric plies per stack was based on a targeted fiber volume fraction of 0.55. It is worth noting that permeability values were only obtained for comparing fabrics together and not for modelling resin flow. This would have required permeability values for different fiber volume fractions due to local change in fabric compaction during processing. Transverse permeability results appear in Section 5.4.

#### 3.3.2.3 Pressure distribution in stacks

Resin flow is driven by resin pressure which originates from the compaction of the dry fabric reinforcement and resin film stack. The work sought to characterise pressure distribution in stacks and see whether it has a significant effect on resin flow.

Pressure distributions inside the stacks were obtained from $2\text{ in} \times 1\text{ in}$ pressure measurement films (Prescale extreme low pressure, Fujifilm Corp.) that were interleaved between each ply of the stack. The prescale system was composed of two sheets, a sheet with micro-encapsulated colour-forming material and a colour-developing sheet. Under specific pressure, capsules burst and colour the developing sheet.

Two sets of experiments were conducted for characterising the pressure distribution in a RFI stack. The first set aimed at characterising the pressure distribution between two plies of fabric, to understand force distribution between contacting yarns. The second set aimed at characterising the interaction between the dry fibre reinforcement and resin film. This set featured complete interleaving, where the stack featured a resin film for every fabric ply.

In both sets of experiments, stacks were made of 8 fabric plies with or without resin film interleaving; each set of plies was interleaved with a pressure measurement film (Figure 3.23). The stacks were placed on a tool and were bagged using the same configuration as in RFI; they were covered with a release film, two plies of breather and a vacuum bag. The bag was vacuumed for 2 minutes at approximately -0.98 bar. Afterwards, the bag was removed and the pressure measurement films were extracted from the stacks for analysis. The films are analysed qualitatively to observe the general pattern of pressure distribution and quantitatively to assess the coverage of high pressure zones. Quantitative analysis was done through contrast image analysis using software ImageJ (version 1.49). The coverage was obtained by the ratio of the number of coloured pixels, as opposed to those that remained white, to the total number of pixels in the image.

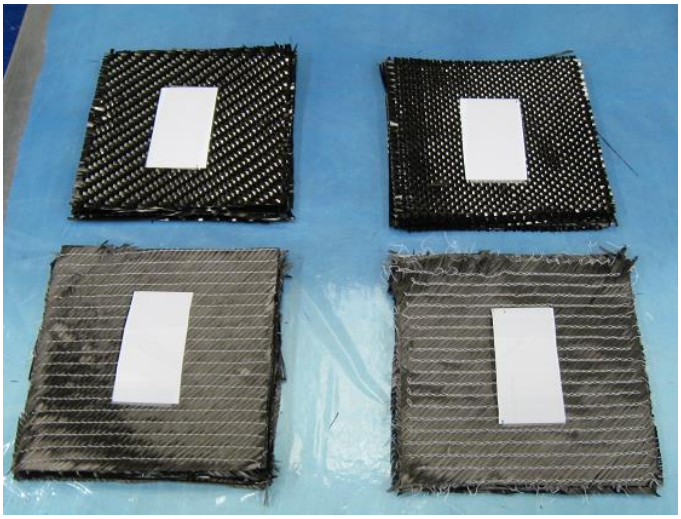

Figure 3.23: Pressure measurement films atop fabric stacks

Five specific cases were analysed for assessing the pressure distribution at various locations within a fabric stack (Figure 3.24). These cases are:

- Fabric-to-tool
- Fabric-to-breather
- Fabric-to-fabric with contiguous parallel yarns
- Fabric-to-fabric with contiguous perpendicular yarns
- Fabric-to-fabric with contiguous yarns at 45°

Results appear in Section 5.6.

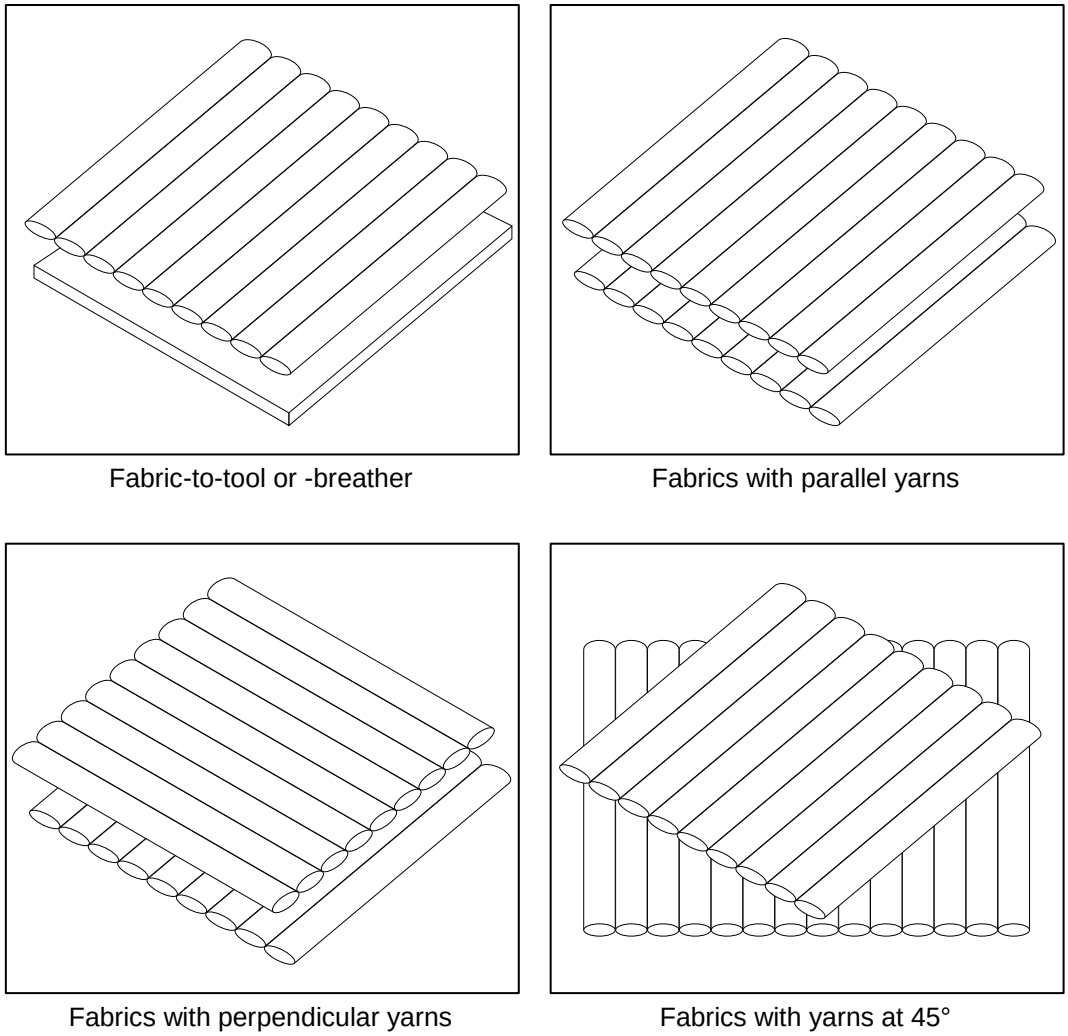


Figure 3.24: Selected cases for the investigation of pressure distribution within fabric stacks

The pressure distribution within stacks of fabrics and resin films was also investigated. The experiments explored cases similar to those used for the fabric stacks:

- Resin-to-tool
- Resin-to-breather
- Interleaved resin film between fabric plies with parallel yarns
- Interleaved resin film between fabric plies with perpendicular yarns
- Interleaved resin films between fabric plies with yarns at 45°

Results appear in Section 5.7.

#### 3.3.2.4 Surface geometry of the fabric architecture

Different geometric parameters were investigated for describing the surface of fabrics (Figure 3.25):

- yarn width, $w_y$
- yarn spacing, $d_s$
- yarn float length
- spacing of stitches

Values were measured from optical microscopy images of the surface of fabrics that were not subjected to compaction. Each geometric parameter was evaluated from at least 30 measurements. Results appear in 5.2.

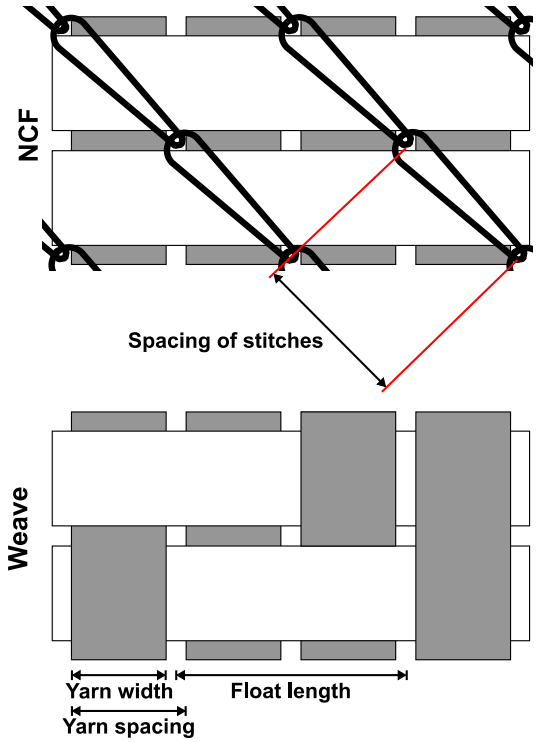


Figure 3.25: Surface geometrical parameters of fabrics

#### 3.3.2.5 Cover factor

The linear cover factor $CF_x$ and the total cover factor $CF$ were used for characterising yarn gaps in fabrics. Measurements were performed through optical microscopy of the surface of the fabrics. Each cover factor value was obtained through the analysis of five distinct fabric photographs containing three to five yarns each.

The linear cover factor $CF_x$ is defined as the percentage of the projected area of a fabric that is covered by one set of yarns, either a set of warp or weft yarns, and was calculated by taking the ratio of the yarn width $w_y$ to the yarn spacing $d_s$:

$$CF_x = \frac{w_y}{d_s} \tag{3.1}$$

The total cover factor is defined as the percentage of the projected area of a fabric that is covered by either warp or weft yarns. It was calculated from the linear cover factors as:

$$CF = CF_{x,\mathrm{a}} + CF_{x,\mathrm{e}} - CF_{x,\mathrm{a}} \times CF_{x,\mathrm{e}} \tag{3.2}$$

where subscripts "a" and "e" represent warp and weft directions respectively. Results appear in Section 5.3.

### 3.3.3 Microscopy

#### 3.3.3.1 Sample preparation for microscopy

Sample preparation for microscopy consisted of three steps, namely 1) sectioning, 2) mounting and 3) grinding and polishing.

The sectioning process consisted in acquiring representative sample cross-sections by cutting samples including fabric reinforcements, resin films, or PMC parts. In the cases of fabric reinforcements and resin films sectioning was performed using a utility knife while for PMCs it was performed using a water-cooled circular saw equipped with a diamond blade (Brutus, Q.E.P. Co.).

Representative PMC samples were obtained by sectioning and analysing four cross-sections, 20 mm in width, taken at various locations inside a part. Sections cut perpendicular to the fibre direction were used for measuring fibre and yarn geometrical parameters, and CNT distribution; sections cut at 45° from the fibre direction were used for measuring the porosity $V_v$ and global fibre volume fraction $V_f$, due to lower fibre pull-out during polishing.

The mounting process consisted in encapsulating the samples inside a polymer matrix that provided a stable base for polishing, improving focus during microscopy. Samples were mounted at room temperature using a two part epoxy (Anamet Inc.). The epoxy was cast around samples inside a 25 mm mounting cup and they were put inside a vacuum chamber for removing out-of-solution gases. The epoxy was then cured for 24 hours at room temperature.

The grinding and polishing processes aimed at improving the surface finish of the mounted samples, limiting artefacts that could hinder microscopic measurements. A series

of grinding and polishing operations were performed using sequentially finer abrasives, up to 0.04 μm colloidal silica suspension. The steps used for the grinding and polishing are presented in Table 3.10.

Table 3.10: Polishing procedure for PMC samples

| Step | Polishing surface | Abrasive | Lubricant | Polishing time (min) |
|---|---|---|---|---|
| 1) | MD-Piano #220 (Struers) | None | Water | 1 |
| 2) | #500 SiC-Paper | None | Water | 1 |
| 3) | MD-Largo (Struers) | 9μm diamond suspension | None | 4 |
| 4) | MD-Mol (Struers) | 1μm diamond suspension | None | 3 |
| 5) | MD-Chem (Struers) | 0.04μm silica suspension | None | 2 |
| 6) | MD-Chem (Struers) | None | Water | 1 |

#### 3.3.3.2 Microscopic observations

Microscopy was performed using two different microscopes: 1) high-magnification materialographic optical microscope (Olympus XJP-3A) and 2) digital optical microscope (VHX-2000, Keyence) capable of greater depth-of-field through image stacking. The materialographic microscope was used for quantitative measurements on flat sample cross-sections including $V_v$ and $V_f$ of PMCs, dimensions of reinforcements and resin films, and CNT cluster distribution. The digital microscope was used for its great depth-of-field that improved observations of CNT clusters compared to the materialographic microscope. A scanning electron microscope, SEM (EVO MA-10, Carl Zeiss NTS GmbH) was also tested for observing individual CNTs but the high beam intensity damaged samples which prevented its use.

Optical microscopy using either microscope was performed using two methods. First, the reflected light method was used for obtaining surface images of sample cross-sections and for measuring volume fractions and dimensions of the reinforcements and voids. Second, the transmitted light microscopy method was used for looking through thin sample

slices, less than 50 µm in thickness, for assessing the distribution and size of CNT clusters. The thickness was reached through extended grinding and polishing operations.

#### 3.3.3.3 Fibre volume fractions and porosity contents

A series of representative images of the sample cross-sections were taken using optical microscopy. These images were used for measuring the global fibre volume fraction $V_f$ and porosity content $V_v$ with image analysis software Clemex Vision Lite. Quantitative values for $V_f$ and $V_v$ were obtained through contrast image analysis.

The dual scale architecture of the reinforcements resulted in the quantification of $V_f$ through a two steps approach. $V_f$ was approximated from the volume fraction of yarns $V_y$ in the sample cross-section and the fibre volume fraction $V_{fy}$ inside yarns (Figure 3.26).

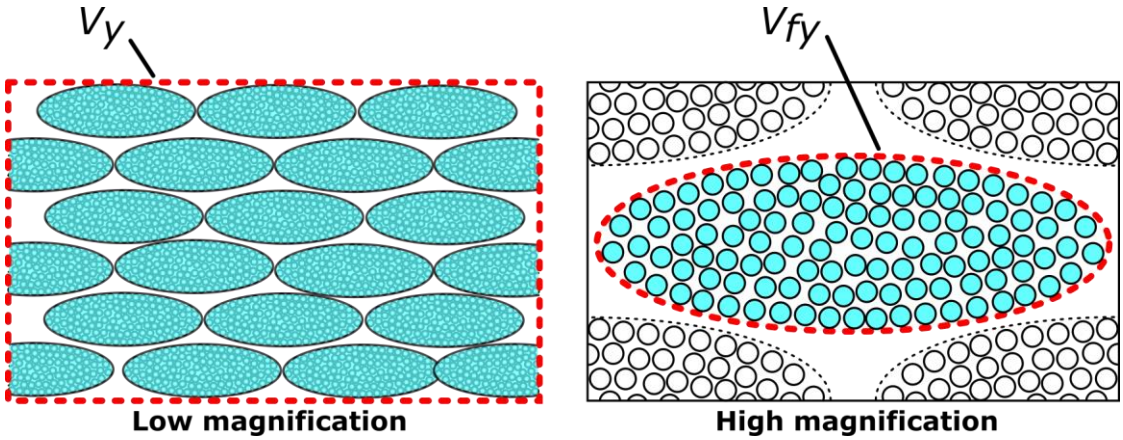


Figure 3.26: Fraction area used for calculating of $V_y$ (left) and $V_{fy}$ (right)

$V_y$ was measured at 50X magnification and was obtained by scanning the entire surface of the sample cross-section, whereas $V_{fy}$ was measured at 1000X magnification and was obtained by taking at least 100 random measurements of fibre volume fraction inside yarns. The global fibre volume fraction $V_f$ was obtained by multiplying the $V_{fy}$ by $V_y$ of the:

$$V_f = V_y \cdot V_{fy} \tag{3.1}$$

In the case of $V_v$ the porosity was measured at 50X magnification by scanning the entire surface of the sample cross-section, similar to $V_y$.

#### 3.3.3.4 CNT distribution

CNTs agglomerated into clusters during RFI processing. This resulted into matrix regions with low CNT content that were clear, and matrix regions with high CNT content that were pitch black. The distribution of CNTs was obtained by taking the ratio of black regions to the total area of analysis. Measurements were achieved through contrast analysis using software ImageJ (Version 1.49).

CNT distribution was quantified for PMC cross-sections or PMC surfaces depending on the fibre type. Cross-sections were used for glass fibre PMCs because the fibres offer good contrast against CNT clusters, which is not the case for opaque carbon fibres. Conversely, PMC surfaces were used for carbon fibre PMCs because light reflection on the round surface of the fibers enables sufficient contrast between CNTs and the carbon fibres. Results appear in Chapter 9.

### 3.3.4 In-situ RFI characterisation

#### 3.3.4.1 Resin flow monitoring system

In-situ characterisation of resin flow during RFI was performed through visual observation. Experiments consisted of consolidating fabric plies and resin film stacks in a vacuum bag, and observing resin flow at the surface of the stack through a glass tool using a D5100 DSLR camera from Nikon (Figure 3.27). Images were taken every 20 seconds for the entire cure duration. A ring light was used for non-directional lighting, limiting yarn shadows. After the experiments, fill factors, void contents, bubble contents and CNT cluster contents at the surface of stacks were measured through image analysis.

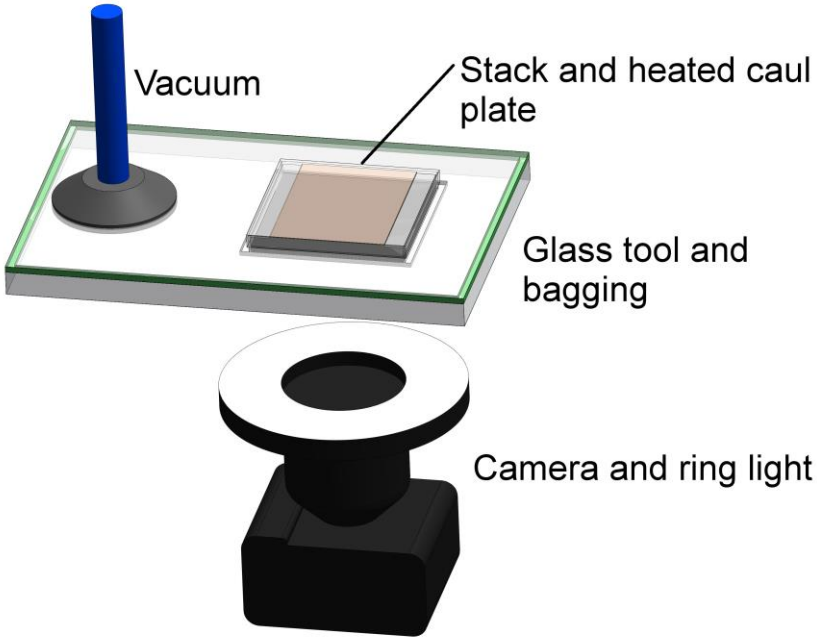


Figure 3.27: Setup for monitoring resin flow

#### 3.3.4.2 Fill factors

The resin saturation process of RFI stacks was characterised by fill factor *FF* values that were defined as the fraction of yarns and inter-yarn gaps at the surface of stacks that is saturated with resin. *FF* was quantified for selected images throughout RFI consolidation. *FF* was measured through image contrast analysis using ImageJ software (Version 1.49). In several cases, resin boundaries had to be defined manually to limit errors caused by non-uniform brightness levels resulting from vignetting and light reflecting off of the fibres.

The resin saturation process was identical for all experiments. First, resin saturated inter-yarn gaps and then proceeded to the saturation of yarns; this discussed further in Chapter 7. The absence of any depth perception from images recorded by the camera prevented a clear identification of the *FF* at which complete saturation of inter-yarns gaps occurred. However, from observations it was clear that *FF* values below 0.50 were related to the saturation of inter-yarn gaps and that values above 0.80 were related to the saturation of yarns. It follows that the transition from the saturation of inter-yarn gaps to the saturation of yarns occurred at *FF* values between 0.50 and 0.80.

From the general resin saturation process, four indicators based on *FF* values were used for comparing resin kinematics between experiments. These indicators are: #1 total saturation time, #2 inter-yarn saturation time, #3 yarn saturation time and #4 surface ply saturation time (Figure 3.28).

The total saturation time was defined as the time required for progressing *FF* from 0 to 0.98, i.e. time elapsed between the start of the experiment, before any heating and compaction, and the moment when near complete resin saturation was reached. A *FF* of 1.00 was not used because of possible air entrapment in yarns and/or incomplete infusion leading to partial saturation, although such events were mostly limited to experiments featuring the combination of SA 70 resin and NCF-H fabric.

The inter-yarn saturation time was an indicator for the saturation of inter-yarn gaps of the surface fabric layer. It was defined as the time required for *FF* to progress from 0.02 to 050. A minimum *FF* value of 0.02 was used for ensuring that the inter-yarn saturation only accounted for flow occurring in the surface layer.

The yarn saturation time was an indicator for the saturation of yarns. It was defined as the time required for *FF* to progress from 0.80 to 0.98.

Finally, the surface ply saturation time was an indicator for the saturation of the last fabric ply in bulk RFI stacks, i.e. the saturation of the fabric ply in direct contact with the glass tool. It was defined as the time required for progressing *FF* from 0.02 to 0.98, i.e. from the moment resin was first observed at the surface ply to the moment when near complete saturation of the ply was reached. This indicator was only used for bulk RFI experiments because it is only with the bulk RFI stacking configuration that fabric stacks were used. It is worth noting that despite similar progression of *FF*, the total saturation time refers to the saturation of all fabric layers in a stack while the surface ply saturation time refers only to the saturation of a single ply within a stack.

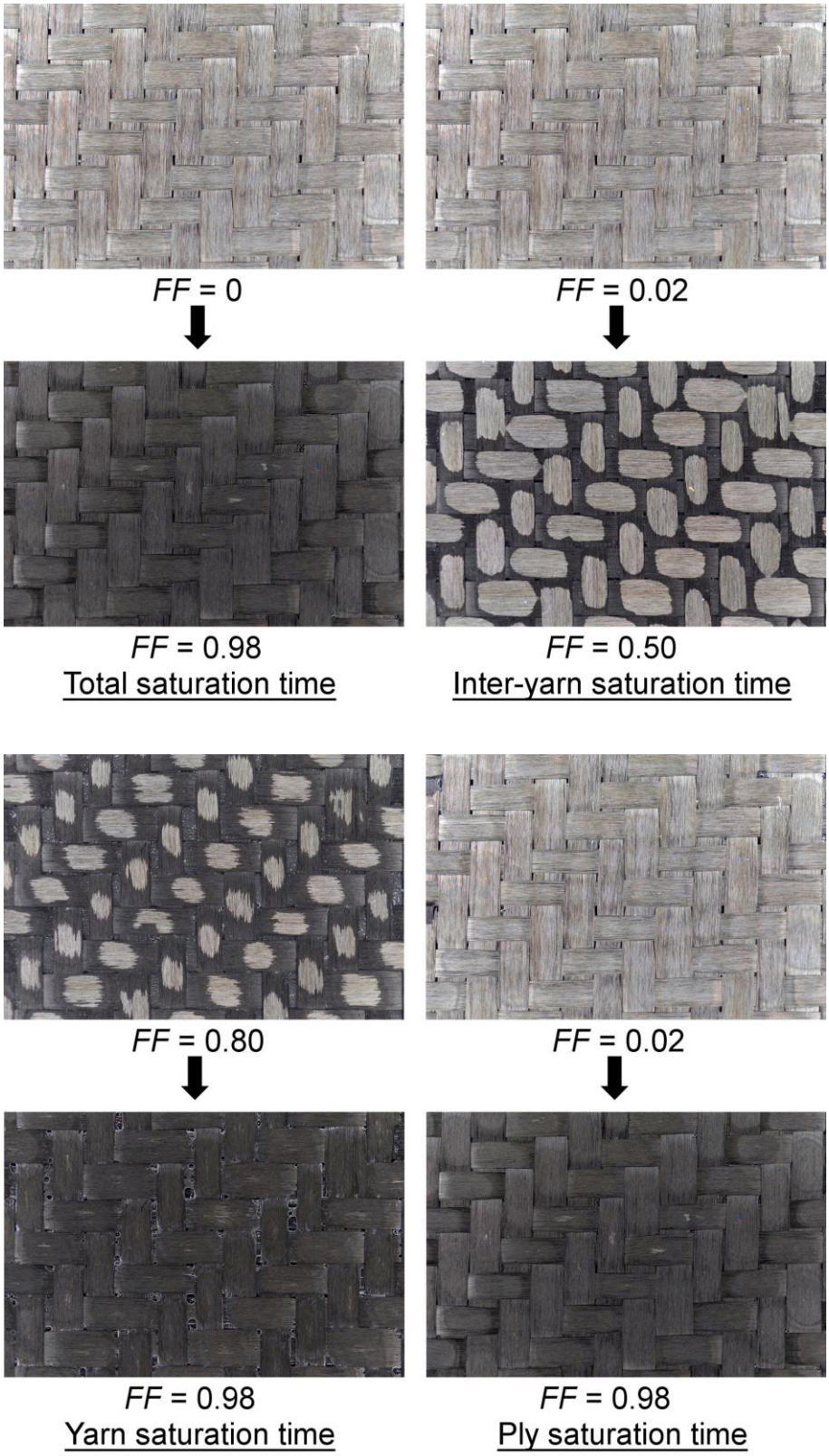


Figure 3.28: Description of saturation times for fill factor analysis

#### 3.3.4.3 Surface bubble and surface void contents

In this work, out-of-solution gases, i.e. bubbles, remaining in the resin after cure were found to be the greatest source of porosity in PMCs. The amount and size of bubbles in the resin varied greatly during RFI processing; bubbles nucleated, were dragged by resin flow, merged, expanded, contracted and collapsed. A qualitative description of bubble kinematics throughout the entire cure cycle was created from surface images of RFI stacks.

During RFI, bubbles grew in size until reaching the isothermal dwell of the cure cycle. Afterwards, bubbles contracted and in some cases, complete gas dissolution was achieved. The aim of the work was to understand how material selection could affect bubble contraction and gas dissolution during RFI. This was done by quantifying the change in bubble content and bubble radii at the surface of stacks during the isothermal dwell, using image analysis software ImageJ (Version 1.49).

The bubble content was defined as the fraction area of the surface of the stack that was covered by bubbles. It was measured at the beginning of the isothermal dwell and after resin gelation. In this work, the term surface void content was used for bubble content values measured after gelation because the resin was no longer in liquid phase. Bubble radii were obtained by taking the average of the minor and major radii of the projected bubble dimensions. Radii were quantified for interleaved RFI only because resin flow in bulk RFI resulted in important degassing and gas dissolution, preventing bubble analysis. A total of 5 bubbles per experiment were tracked and only bubbles featuring near-circular cross-sections were analysed. Results appear in Chapter 8.

## 3.4 Mechanical characterisation

This section describes characterisation methods used for investigating the mechanical behaviour of materials. A list of methods and chapters in which they are used appears in Table 3.11.

Table 3.11: Mechanical characterisation methods

| Group | Characterisation | Ref. chapter |
|---|---|---|
| Resin films | Relaxation and creep | 4 |
| Fabric reinforcements | Compaction | 5 |
| PMCs | ILSS | 6, 9 |
| | Stringer pull-out | 10 |

The viscoelastic behaviour of resin films is characterised in Chapter 4. Relaxation and creep experiments were performed to understand whether resin films at room temperature behave more like solids or viscous fluids. The type of behaviour has a direct effect on resin flow at the beginning of the RFI process.

The compaction behaviour of fabric reinforcements is characterised in Chapter 5. The aim was to understand how the fabric architecture affects compaction. Results were used in Chapter 6 for discussing the effects of fabric selection on the fibre volume fraction within flat PMCs.

Mechanical experiments were also performed for characterising the interlaminar properties of PMCs. The effect of material selection on the interlaminar shear strength (ILSS) of flat PMCs is discussed in chapters 6 and 9. Additionally, pull-out experiments were performed on delta-stringer panels to characterise their interlaminar properties. Results are discussed in Chapter 10.

### 3.4.1 Resin film relaxation and creep

The viscoelastic behaviour of semi-solid resin films at room temperature was characterised through two types of experiments, 1) relaxation experiments and 2) compressive creep experiments.

Both types of experiments were performed by compacting resin film stacks between 2 platens using an Instron 4482 load frame (Figure 3.29). Before testing, square resin films

having a width of 10.6 cm were stacked to approximately 1.6 mm and compressed using a laminating roller for reducing voids. In the case of relaxation experiments, stacks were compacted at a rate of 0.5 mm/min until a desired compaction pressure was reached, and strain was held constant for at least 5 min. Conversely, in the case of creep experiments, stacks were compacted under constant pressure that was controlled via a hysteresis controller. The load frame deformation that was obtained from compaction experiments performed without resin films was subtracted from all measurements. Results appear in Section 4.8.

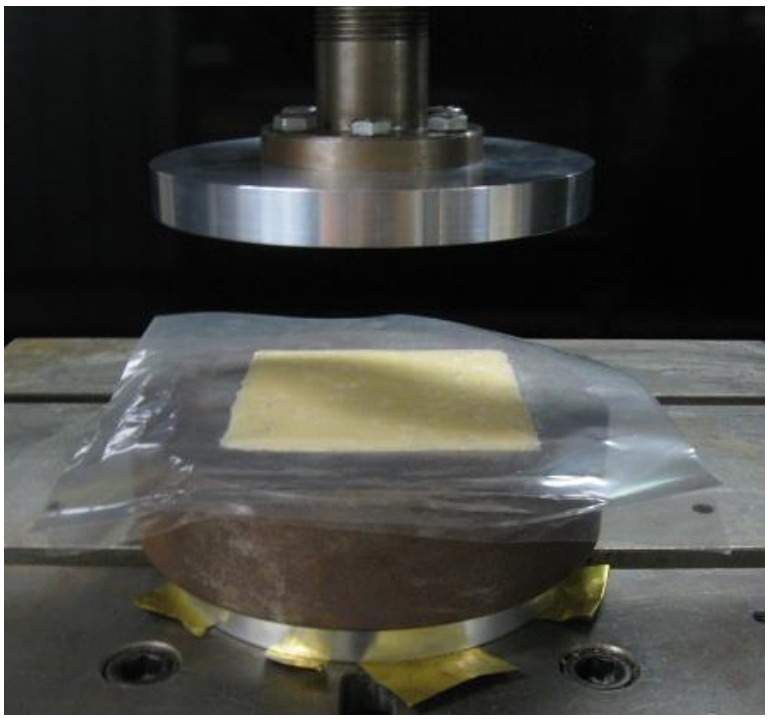

Figure 3.29: Compaction set-up for relaxation and creep tests on resin films

### 3.4.2 Fabric compaction

Fabrics undergo fibre-to-fibre network reorganisation during compaction, enabling a more compact structure and lower fabric thickness. At the onset of compaction, the yarns and fibres within fabrics are all undulated to various extents. As compaction force is applied, fibres undergo bending and fibre-to-fibre contact points start sliding, leading to fibre straightening and an increase in fibre volume fraction.

The relationship between the global fibre volume fraction $V_f$ of the fabrics and the compaction pressure was characterised by compacting fabrics between two circular platens (Figure 3.30).

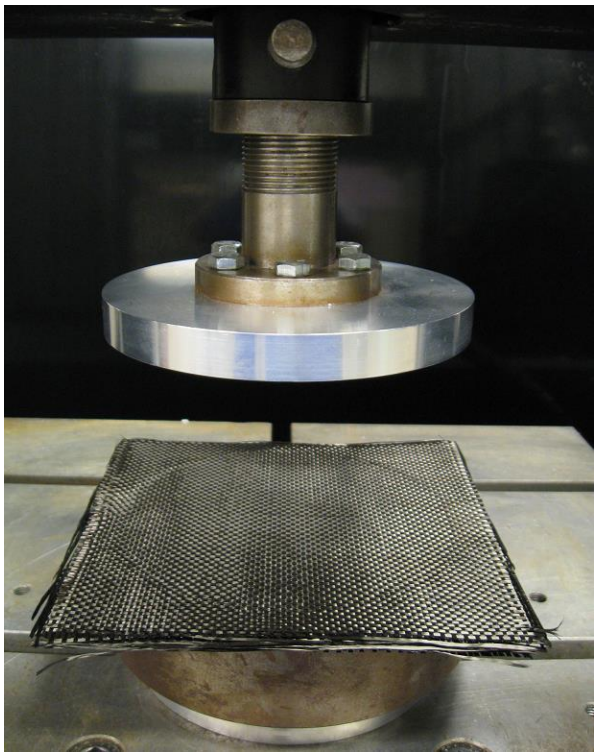

Figure 3.30: Set-up for compacting fabric stacks

Fabrics were cut into a 175 mm square shape using a utility knife. Sample size exceeded that of the 150 mm diameter platens, minimising the effect of cutting artefacts.

Compaction was performed on an Instron 4482 load frame at a rate of 0.5 mm/min until a compaction pressure of 1 MPa was reached. The load was measured through a 100 kN load cell and the displacement was monitored through the cross-head motion. The deformation of the load frame resulting from loading was measured and subtracted from the raw data of cross-head position. The actual displacement measurements were taken relative to the contacting point between platens, leading to stack thickness measurements. From stack thickness, the fibre volume fraction was obtained based on the volume between the platens ($V_{stack}$) and the volume taken by the fibres ($V_{fabric}$) using the following equation:

$$V_f = \frac{V_{\text{fabric}}}{V_{\text{stack}}} = \frac{\left( A\frac{N_{\text{plies}}\rho_s}{\rho_{\text{fibre}}} \right)}{\left( At_{\text{stack}} \right)} = \frac{N_{\text{plies}}\rho_s}{\rho_{\text{fibre}}t_{\text{stack}}} \tag{5.1}$$

where $A$ is the compacted surface, $N_{\text{plies}}$ is the number of fabric plies, $\rho_s$ is the surface density of a single fabric ply, $\rho_{\text{fibre}}$ is the density of the fibres (~1800 kg/m$^3$) and $t_{\text{stack}}$ is the measured distance between platens after correcting for frame deformation.

A total of 51 repetitive compactions cycles were applied on each fabric stack for assessing the extent of fibre reorganisation due to each successive compaction. Stacks were made from 12 fabric plies. A single compaction experiment was performed per fabric reinforcement. No repeats were made due to limited availability of the fabrics, except for fabric NCF-HP that showed that the fibre volume fraction deviates little between repeats, ± 1% (Appendix B). Results appear in Section 5.5.

### 3.4.3 ILSS

PMC interlaminar shear strength (ILSS) values were compared using the short-beam strength method, ASTM standard D2344 [151]. ILSS was calculated as:

$$ILSS = \frac{3}{4}\frac{P_m}{bh} \tag{3.2}$$

where $P_{\text{m}}$ is the maximum load, $b$ is the specimen width and $h$ is the specimen thickness.

Testing was performed on an Instron 4482 load frame at a rate of 1 mm/min until failure. Loads were measured by the load cell and displacements were obtained from cross-head motion. The test fixture and loading of the specimens appear in Figures 3.31 and 3.32. Specimens were 4 mm thick, 12 mm wide and 38 mm long. A span of 25 mm was used and the radii of the loading nose and supports were 3.0 mm and 1.5 mm respectively. A total of three specimens were tested per PMC. Results appear in Section 6.6.

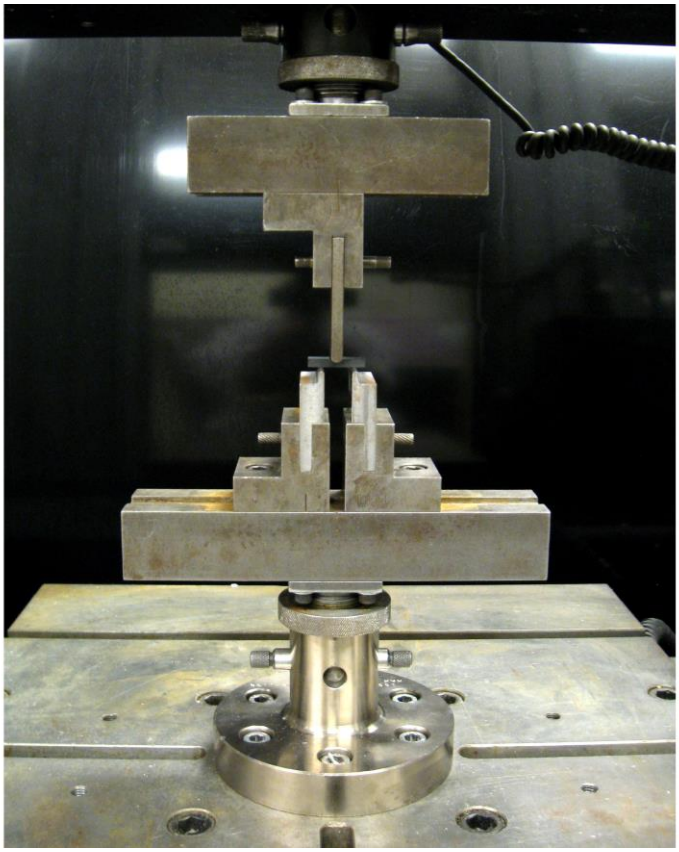

Figure 3.31: 3-point bending fixtures for short-beam interlaminar shear strength test

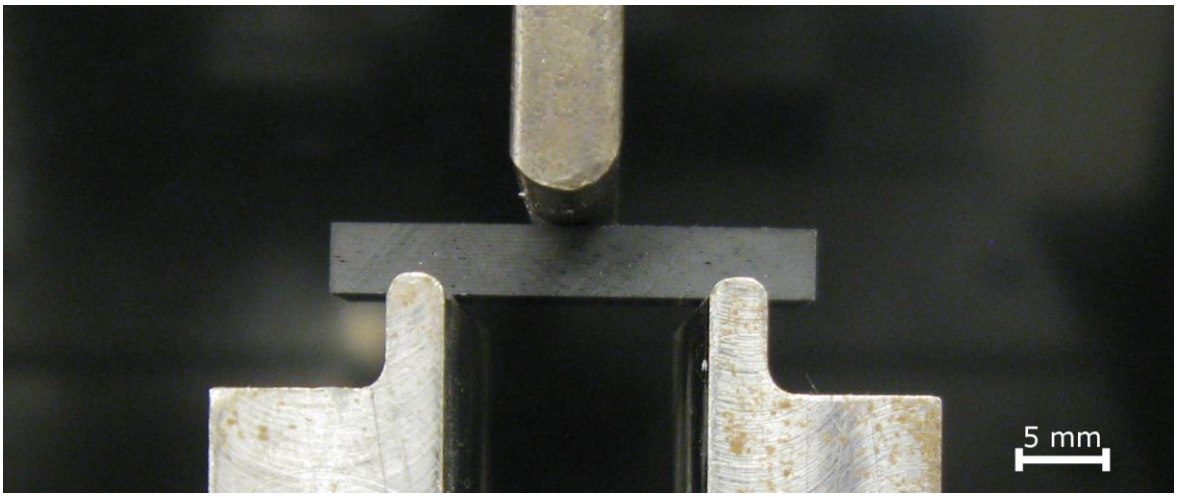


Figure 3.32: Short-beam under 3-point bending

### 3.4.4 Stringer pull-out

Pull-out experiments were performed in Chapter 10 with delta-stringers, i.e. a skin and delta stiffener structure. Experiments consisted of pulling on specimens from the inside of the hollowed section, at the centre of the skin and top of the delta stiffener (Figure 3.33). Testing was performed on an Instron 4482 load frame at a rate of 1 mm/min until complete delamination between a side of the delta-stiffener and skin. Loads were measured by the load cell and displacements were obtained from cross-head motion. After testing, the total crack length was measured using a millimetric ruler. A single pull-out test was performed per small-scale preliminary delta-stringers, while 3 specimens were tested per large-scale delta-stringers demonstrator panels.

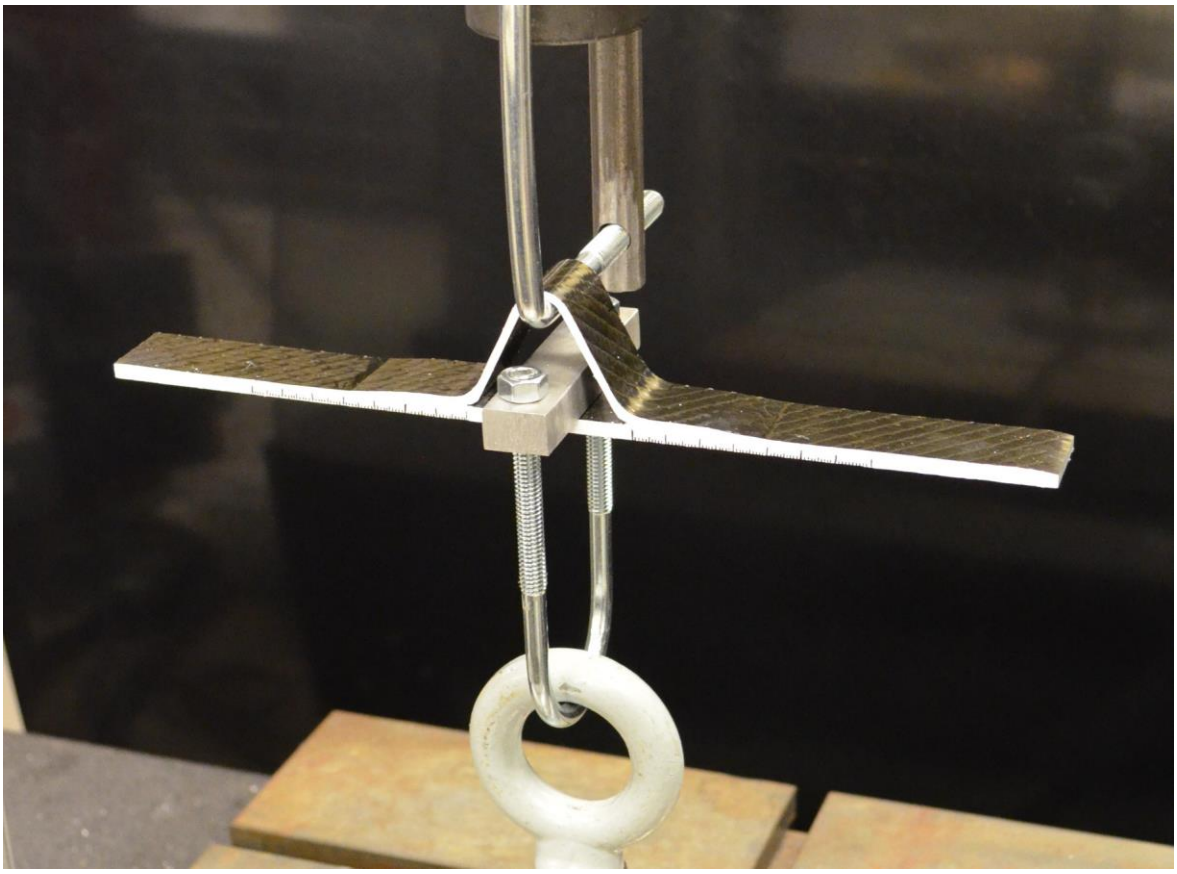

Figure 3.33: Set-up for pull-out testing on delta stringers

Average energy release rate values for mode 1 loading ($G_I$) were calculated from the load-displacement curves of pull-out experiments. $G_I$ is defined as the energy per surface

area that is dissipated during the creation of a new crack surface. The energy dissipated $U_{\text{Dissipated}}$ consists of the total energy $U_{\text{Total}}$, i.e. area under a load-displacement curve, minus the remaining elastic energy $U_{\text{Elastic}}$ in the beams following crack growth (Figure 3.34).

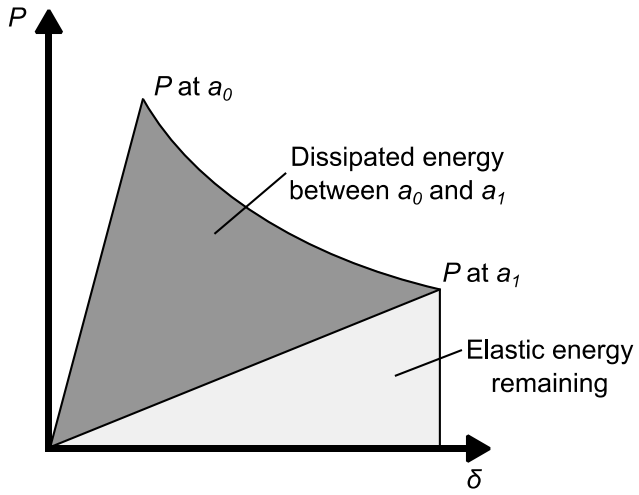


Figure 3.34: Load-displacement curve ($P/\delta$) for a DCB test showing the energy dissipated during crack growth from crack length $a_0$ to $a_1$

In this work, the elastic energy $U_{\text{Elastic}}$ was assumed to be linear elastic while the total energy $U_{\text{Total}}$ was calculated by a Riemann sum. From this, the dissipated energy was equal to:

$$U_{\text{Dissipated}} = \underbrace{\sum_{i=1}^{n} P_i \Delta\delta_i}_{U_{\text{Total}}} - \underbrace{\frac{P_n \delta_n}{2}}_{U_{\text{Elastic}}} \tag{3.3}$$

where $P_i$ is the load at increment $i$, $\Delta\delta_i$ is the change in displacement between two increments, and $P_n$ and $\delta_n$ are the load and displacement at final crack length. A $G_{\text{I}}$ value was then obtained by dividing the dissipated energy by the newly generated crack area $A$:

$$G_{\text{I}} = \frac{U_{\text{Dissipated}}}{A} \tag{3.4}$$

## 3.5 Flow simulations

Simulations of resin flow inside stacks were performed in Chapter 7 for complementing in-situ observations of resin flow at the surface of RFI stacks. All fabric models were developed from the geometry of the unit cell of fabric PW-L as consolidated in PMCs.

3D computer models of fabrics represented as interlaced yarns featuring an elliptic cross-section were created using TexGen software [152]. TexGen models were imported into ANSYS Workbench (V 12) for producing the final models and control volume meshes of fabrics. Two types of models were used (Figure 3.35): 3D and 2D models. 3D models consisted of a single or multiple layers of fabric, and were used for steady-state flow simulations and fabric/stack permeability analyses. Conversely, 2D models consisted of a cross-section of a fabric unit cell, and were used for multi-phase flow simulations and saturation analyses. It is worth noting that a complete 3D model could not be used for multi-phase flow simulations due to limitations in computational power. Nonetheless, results with the 2D model were still effective at confirming experimental observations regarding resin flow in RFI.

Resin flow simulations were performed with ANSYS Fluent (V12). Details regarding simulation parameters are given below.

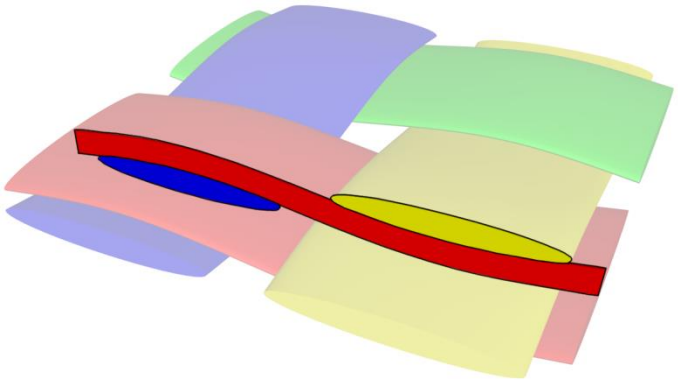

Figure 3.35: Representations of a 3D model for a plain weave and its associated cross-section for 2D modelling

### 3.5.1 Transverse permeability simulation

Steady-state flow simulations solving for the conservation of mass and Navier-Stokes equations were performed for calculating transverse permeability values using 3D models consisting of a unit cell of a single fabric layer or fabric stack. The domain of the model extended well beyond that of the thickness of the fabric layer or fabric stack to ensure that flow before and after the fabric was fully developed, i.e. the domain thickness before and after the fabric was equivalent to more than the thickness of 4 fabric layers. In the case of fabric stacks, the through-thickness ply offset was set at 20 μm, a value sufficient to prevent mesh distortion and enable convergence yet small enough to prevent significant in-plane flow between layers. A 50 μm mesh element size was used around yarns and yarns were modelled as non-porous solid volumes to reduce computational load. It is worth noting that yarns were modelled initially as porous media with permeability values ranging from $10^{-12}$ m/s to $10^{-14}$ $m^2$, which are typical values for flow along and across an array of carbon fibres as used in PMCs [153]. However, the pressure response was not affected by the change in permeability because inter-yarn gaps were much more permeable than yarns, which meant that there was minimal flow inside yarns.

During the simulations, the outlet pressure was set as 0 Pa and flow velocity at the inlet was set at 100 μm/s. Upon reaching steady state conditions, the pressure that was developed at the inlet was calculated from the average values of the pressure on surface elements. The transverse permeability $K_z$ was calculated from 1D Darcy's law (Eqn. 2.2):

$$K_z = v\mu \frac{\Delta z}{\Delta P} \tag{3.5}$$

where $v$ is the fluid velocity, $\mu$ is the fluid viscosity, $\Delta z$ is the fabric/stack thickness and $\Delta P$ is the pressure drop.

The parameters used for 3D simulations appear in Table 3.10. Results appear in Section 7.5.

Table 3.12: Parameters for transverse permeability simulations

| **Parameter** | **Value** |
|---|---|
| Time | Steady-state |
| Element size | 200 µm far and 50 µm close to yarns |
| Viscous model | Laminar |
| Solution methods | |
| - Pressure-velocity coupling | Coupled scheme |
| - Spatial discretization | Gradient: Least squares cell<br>Pressure: Second order<br>Momentum: Third-order |
| Yarns | Solid |
| Resin | |
| - Density | 1200 kg/m$^3$ |
| - Viscosity | 10 Pa·s |
| Boundary conditions (sidewalls) | Symmetry |
| Velocity at inlet | 100 µm/s |
| Pressure at outlet | 0 kPa |

### 3.5.2 Multi-phase flow

2D transient simulations of multi-phase flow were performed for characterising resin saturation of yarns. The simulations solved for the conservation of mass, and Darcy's Law inside the yarns and Navier-Stokes equations between the yarns. Simulations featured an air and resin phase. Initially, the inter-yarn gap regions were all filled with resin while the yarns were filled with air. This assumption was based on experimental results (Chapter 7). Resin was driven inside yarns by an external pressure of 100 kPa. The ratio of resin saturation in yarns was monitored throughout the simulations. Two configurations were tested, interleaved RFI and bulk RFI. The interleaved RFI configuration consisted of a 2D yarn model where resin flow into yarns from all external surfaces (Figure 3.36a). Conversely, bulk RFI models accounted for yarn contact across plies by sectioning the top and bottom regions of the models by 10 µm (Figure 3.36b). The sectioning resulted in a contact region that was 60% of yarn spacing. This value was estimated from observations

made during resin flow experiments (Chapter 7). Permeability values for the longitudinal and transverse yarn directions were taken as $1.04 \times 10^{-12}$ m$^2$ and $5.18 \times 10^{-14}$ m$^2$ respectively. These values were obtained from the Kozeny-Carman equation for resin flow along and across an array of aligned fibres using a yarn fibre volume fraction of 0.65, and longitudinal and transverse Kozeny constants of 6 and 0.3 respectively [154]. Yarn saturation times were obtained from the flow simulations by taking the time required to fill 95% of either the longitudinal or transverse yarns, whichever occurred first. The reasoning behind this was that yarns are also filled from the out-of-plane axis which is not modelled in 2D, i.e. because resin also fills the transverse yarns along their longitudinal axis. It should be noted that an incomplete saturation value of 95% was used for mitigating the effects of phase mixing and backflow at the model boundaries that prevented complete saturation.

The parameters used for 2D simulations appear in Table 3.13. Results appear in Section 7.5.

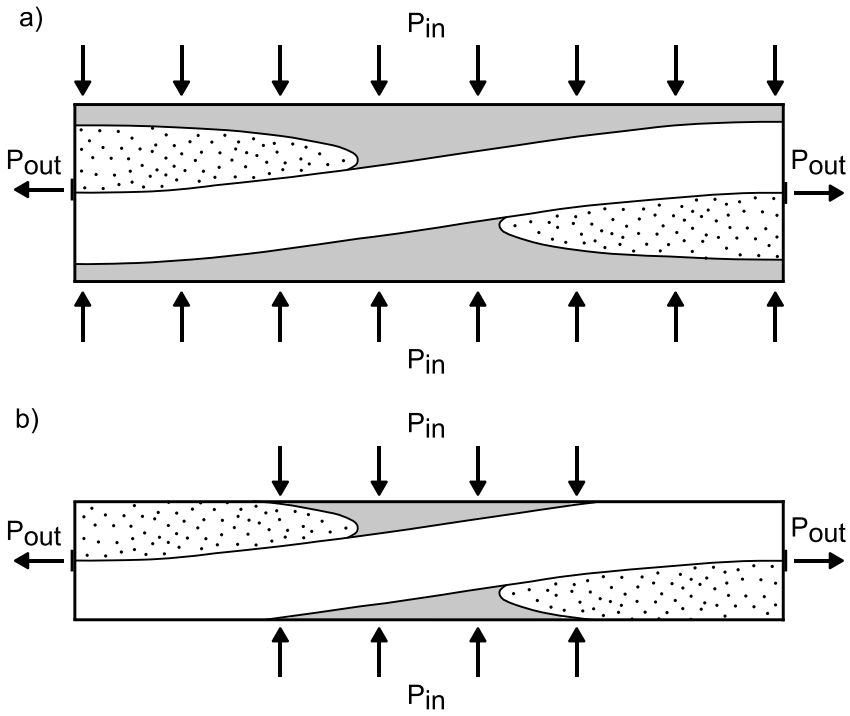


Figure 3.36: Boundary conditions for multi-phase flow simulations, a) interleaved RFI and b) bulk RFI

Table 3.13: Parameters for multi-phase flow simulations

| **Parameter** | **Value** |
|---|---|
| Time | Transient |
| Element size | 10 µm |
| Viscous model | Laminar |
| Multiphase model | Volume of fluid |
| Solution methods | |
| - Pressure-velocity coupling | SIMPLE scheme |
| - Spatial discretization | Gradient: Least squares cell<br>Pressure: PRESTO!<br>Momentum: Second Order Upwind<br>Volume fraction: Geo-Reconstruct |
| Yarns | |
| - Porosity | 0.35 |
| - Transverse permeability | $5.18 \times 10^{-14}$ m$^2$ |
| - Longitudinal permeability | $1.04 \times 10^{-14}$ m$^2$ |
| Resin | |
| - Density | 1200 kg/m$^3$ |
| - Viscosity | 10 Pa·s |
| Air | |
| - Density | 1.225 kg/m$^3$ |
| - Viscosity | $1.79 \times 10^{-5}$ Pa·s |
| Boundary conditions (excl. inlet and outlet) | No shear-stresses |
| Pressure at inlet | 100 kPa |
| Pressure at outlet | 0 kPa |

# Chapter 4

## Resin films

This chapter describes the characterisation of neat and nano-modified resins used in this work, focusing mostly on LEO resins. Results are used in later chapters understanding resin flow, void formation and CNT distribution during RFI processing. Characterised features include:

1. Resin film thickness, surface density and bulk density
2. Resin film morphology
3. CNT distribution
4. Resin viscosity and gelation
5. Resin surface tension
6. Resin contact angle
7. Resin viscoelastic behaviour

### 4.1 Resin film thickness, surface density and bulk density

Resin film thickness, surface density and bulk density values for LEO resin films appear in Table 4.1. Resin films used in the work were obtained in two batches and results are reported accordingly. It should be noted that few measurements were made on the first batch of materials due to limited resin quantities. Results show that in general there is little variation within a resin film roll, with the exception of the second batch of LEO 2376. The addition of 0.3 wt% of CNTs did not have any statistical significance on the density of the resins. Results were used for calculating the amount of resin required in RFI stacks for producing PMCs in chapters 6 and 10.

Table 4.1: Thickness, surface density and bulk density values of LEO resin films

| Resin | Batch | Film thickness (μm) | Surface density ($g/m^2$) | Bulk density ($g/m^3$) |
|---|---|---|---|---|
| LEO 2376 | #1 | – | 145 ± 3 | – |
| | #2 | 190 ± 56 | 222 ± 76 | 1188 ± 14 |
| LEO 2377 | #1 | – | 119 ± 3 | – |
| | #2 | 217 ± 3 | 255 ± 9 | 1222 ± 31 |
| LEO 2396 | #1 | – | 146 ± 2 | – |
| | #2 | 191 ± 3 | 228 ± 5 | 1212 ± 54 |
| LEO 2397 | #1 | – | – | – |
| | #2 | 221 ± 7 | 228 ± 5 | 1168 ± 63 |

## 4.2 Resin film morphology

A qualitative evaluation of thickness consistency and inner void distribution was performed for characterising the morphology of the LEO resin film series. During evaluation, resin films were placed on clear PMMA supports for surface analysis using optical microscopy, and were cast in epoxy and cured partially for cross-sectional analysis.

The thickness consistency was investigated through optical microscopy of the uncured resin film surface using transmitted light and of the resin film cross-section using reflective light on cast samples (Figure 4.1). The surface investigation of resin films revealed that the intensity of transmitted light varied greatly across the samples, indicating variability in the resin film thickness. The thinner regions were structured in channels that ran along the rolling direction of the resin films. Investigation of resin film cross-sections revealed that the channels varied in depth while the thickest regions all appear to have a similar height. It should be noted that no local thickness measurements were made due to difficulties in polishing the soft and uncured resin film, preventing clear identification of resin film boundaries. Nevertheless, variations in resin film thickness are relatively constant throughout the films, suggesting that they should not have any major effect on resin flow or saturation. However, the stacking of resin films might result in important trapping of air within the channels of the films.

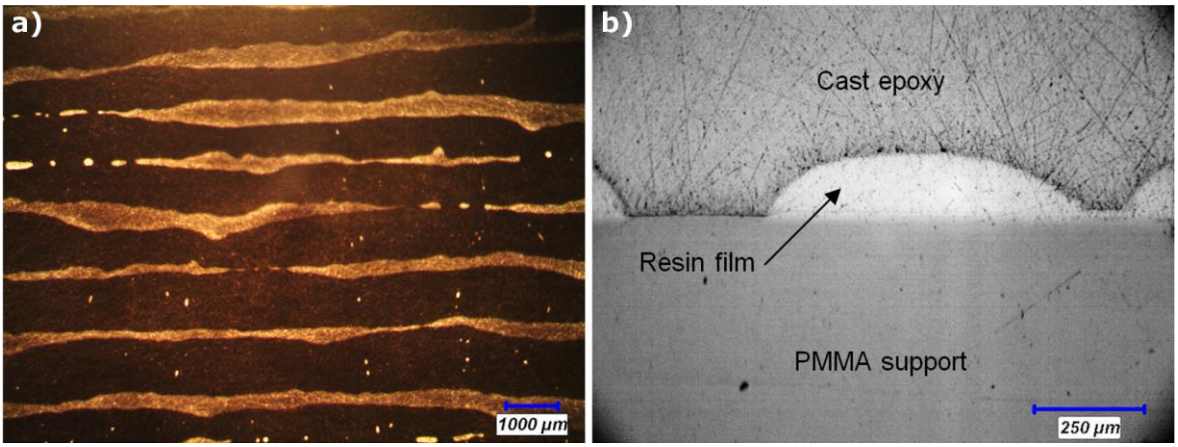


Figure 4.1: Optical microscopy of a) the surface of LEO 2377 resin film and b) cross-section of LEO 2396 resin film

Initial void distribution in resin films was investigated through optical microscopy of the surface of the films. Figures 4.2 and 4.3 show that using reflected light, the surfaces of the resin films appear to be relatively smooth; however, transmitted light revealed that the inside of all resin films was filled with large quantities of micro-bubbles.

Results showed that resin films are a great source of volatiles because they feature large quantities of micro-bubbles and the stacking of films can trap air due to uneven film thicknesses. These volatiles were found to be a major source of voids in PMCs (Chapter 8). Hence, this suggests that the resin films require extensive degassing prior to PMC consolidation, or using manufacturing processes that provide sufficient resin pressure for collapsing these bubbles, i.e. using an autoclave.

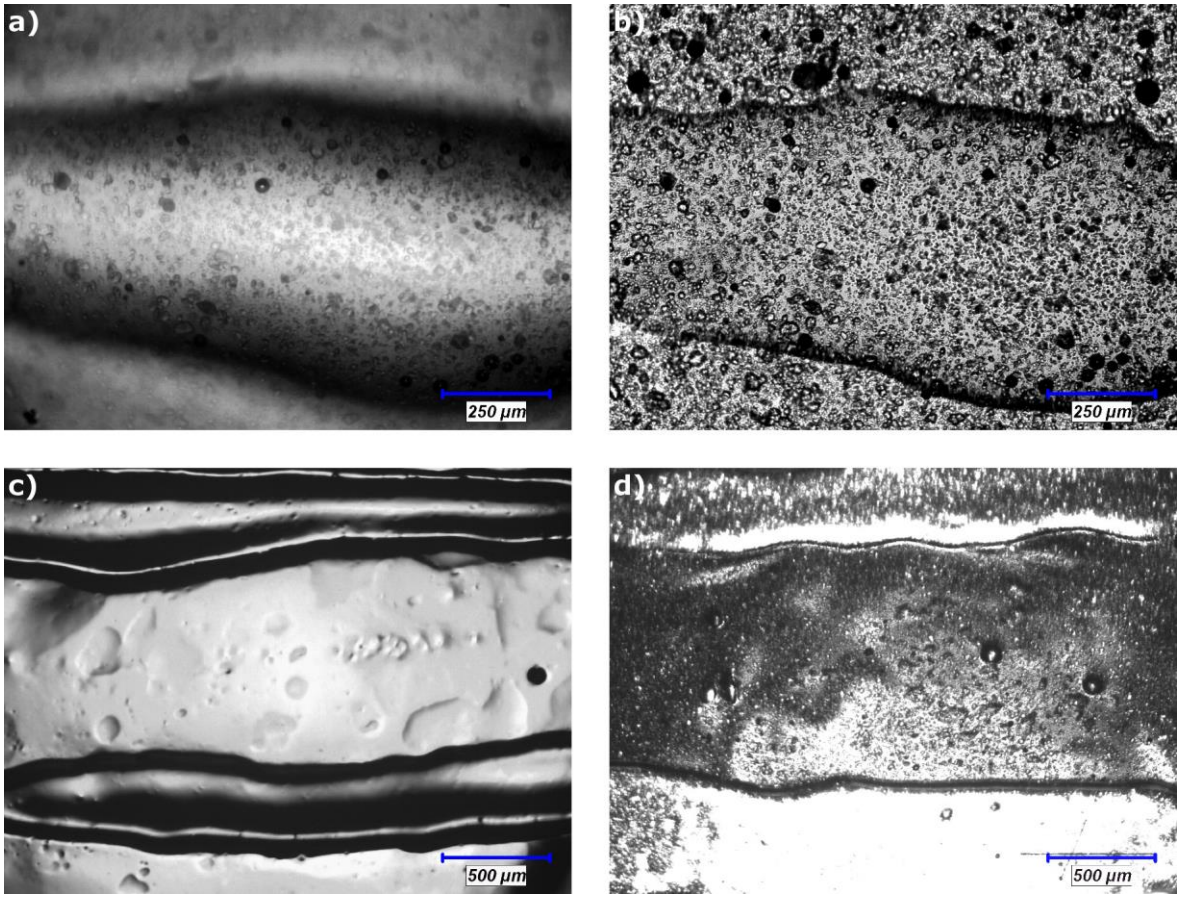


Figure 4.2: Surfaces of resin films: a) reflected light and b) transmitted light microscopy of LEO 2376, and c) reflected light and d) transmitted light microscopy of LEO 2377

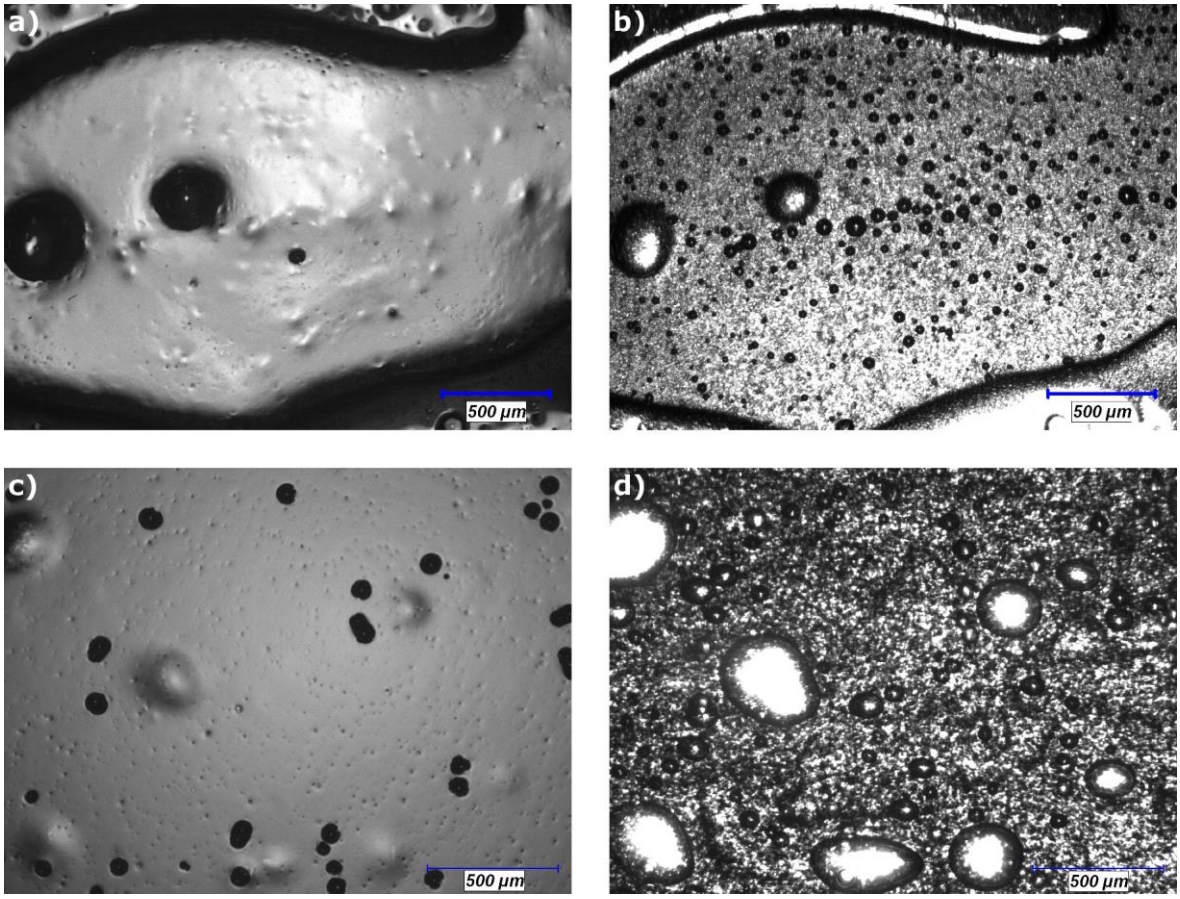


Figure 4.3: Surfaces of resin films: a) reflected light and b) transmitted light microscopy of LEO 2396, and c) reflected light and d) transmitted light microscopy of LEO 2397

## 4.3 Resin film volatile content

Volatile contents for as-received LEO resin films appear in Table 4.2. Results show that there are no major statistical differences in volatile contents between resin films, irrespectively of the epoxy formulation and CNT loading. Hence, any differences in void contents that can be observed in laminates made with the LEO resins are not due to the initial volatile content of the resins. It follows that the mixing process of the resin has a bigger impact on the volatile content than the properties of the resin itself. These results are used in the analysis of void formation in Chapter 8.

Table 4.2: Volatile content of LEO resin films

| Resin | Volatile content (wt%) |
|---|---|
| LEO 2376 | 0.38 ± 0.02 |
| LEO 2377 | 043 ± 0.05 |
| LEO 2396 | 0.44 ± 0.05 |
| LEO 2397 | 0.40 ± 0.06 |

## 4.4 CNT distribution within resin films

CNT distribution in the resin films was investigated qualitatively using transmitted light optical microscopy. Observations were made on uncured resin films and also on cured resin plates made by Yang [155].

Characterisation of uncured resin films (Figure 4.4) showed that neat resins were clear in regions devoid of bubbles. The addition of 0.3 wt% CNTs reduced transmitted light significantly, but the effect was not uniform; there were regions where the resin was clear but most regions were populated with dark clusters, representing regions of higher CNT density. The distribution of the clusters was uniform throughout the resin films.

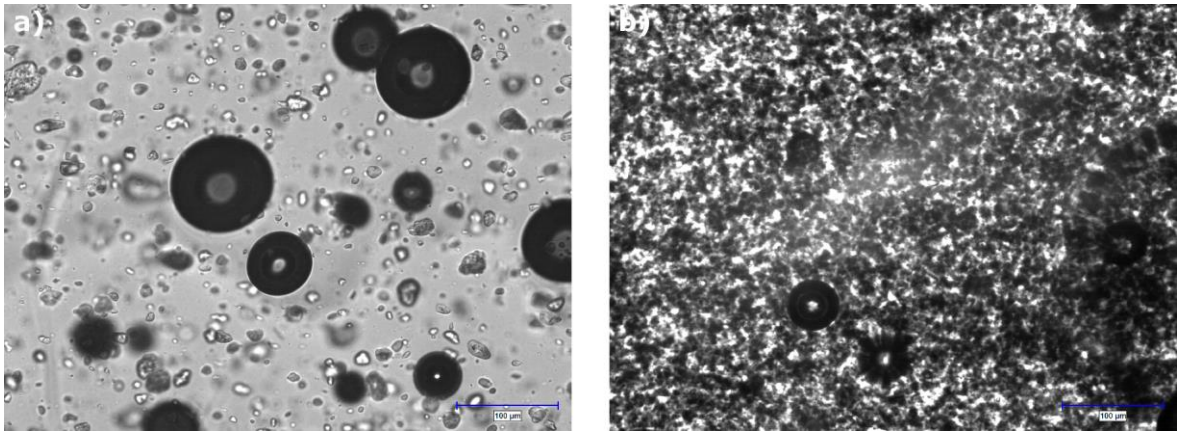


Figure 4.4: Transmitted light microscopy of a) neat resin film LEO 2376 and b) CNT-modified resin film LEO 2377

Thin cross-sections of resin plates (Figure 4.5) showed high void contents and CNT clusters. Some neat resin regions were seen around voids but generally, CNT distribution was relatively uniform. Hence, for unreinforced plates, resin cure did not affect CNT distribution significantly. These results were used for discussing CNT distribution in multi-scale PMCs in Chapter 9.

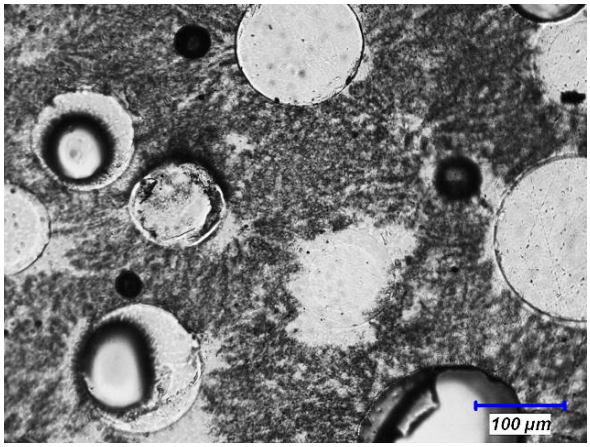


Figure 4.5: Transmitted light microscopy of a thin cross-section of LEO 2377 cured plate with lighter regions representing voids

## 4.5 Resin viscosity and gelation

Viscosity curves appear in Figure 4.6. Values are in agreements with those presented by the suppliers (Table 3.1). Based on the results, three major distinctions were made between the resins: 1) LEO resins reached much lower viscosity values than the SA 70 pre-preg resin, 2) the minimal viscosity of resin formulation L7 was higher than that of resin formulation L9 and 3) the presence of 0.3 wt% of CNTs increased resin viscosity. These results were useful for analysing resin flow kinematics in Chapter 7 and CNT clustering in Chapter 9. In addition, rheology data was used for obtaining gelation times (Table 4.3). Results showed that gelation was affected by the resin formulation but not the CNT loading. In Chapter 8, gelation times were used for discussing gas dissolution during RFI processing and void contents in PMCs.

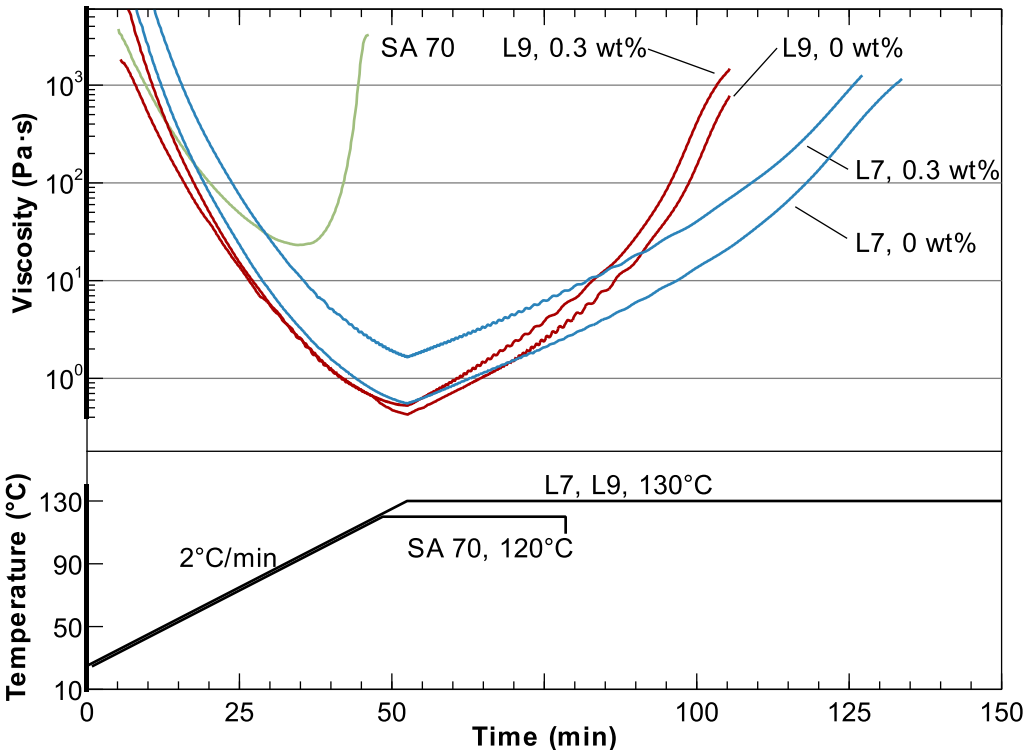


Figure 4.6: Resin viscosity curves when subjected to recommended cure temperature profiles

Table 4.3: Gelation time for resins

| Resin | Cure cycle | Gelation time (min) |
|---|---|---|
| LEO 2376 | L-STD | 136 |
| LEO 2377 | L-STD | 135 |
| LEO 2396 | L-STD | 106 |
| LEO 2397 | L-STD | 104 |
| SA 70 | S-STD | 46 |

## 4.6 Resin surface tension

Surface tension values for resin films that are uncured, cured and post-cured appear in Table 4.4. All values are within the range of values reported in the literature for various types of epoxies (Appendix A).

LEO resin films showed similar surface tension throughout the entire curing process. No significant effect of the addition of 0.3 wt% CNT was observed. Cumulative cross-linking after 2 hours at 130°C resulted in a reduction of surface tension by approximately 8 $mJ/m^2$. Uncured SA 70 resin featured a much lower surface tension than LEO resin films. However, its cross-linking resulted in a slight increase in surface tension. These results, when combined with the resin contact angle (Section 4.7) show that LEO resins are affected equally by capillary forces. Hence, any differences in resin flow between the LEO resins observed in Chapter 7 are caused by differences in viscosity. The higher surface tension of LEO resin films compared to SA 70 resin film suggests that LEO resins are affected more by capillary forces.

Table 4.4: Surface tension values for resin films

| Resin | Surface tension ($mJ/m^2$) | | |
|---|---|---|---|
| | Before cure | After cure | After post-cure |
| LEO 2376 | 42.0 ± 1.8 | 34.3 ± 1.2 | 34.0 ± 0.9 |
| LEO 2377 | 42.1 ± 2.0 | 35.2 ± 0.9 | 33.6 ± 1.2 |
| LEO 2396 | 42.5 ± 1.9 | 34.4 ± 0.7 | 34.4 ± 1.1 |
| LEO 2397 | 41.9 ± 1.6 | 36.5 ± 0.9 | 34.0 ± 1.3 |
| SA 70 | 34.6 ± 1.6 | 38.5 ± 2.4 | – |

## 4.7 Resin contact angles with fibres

Measured contact angles appear in Table 4.5. Results show that all resins have a similar contact angle of approximately 23°. Resin SA 70 has a slightly higher contact angle than the LEO resins, but the difference is statistically insignificant. Hence, the type of formulation and CNT loading had a marginal effect on the contact angle. It can be

concluded that the capillary forces during RFI processing were mostly affected by the surface tension (Section 4.6).

Table 4.5: Contact angle between resins and a single HTS40 fibre obtained by direct measurement

| Resin | Contact angle (°) |
|---|---|
| LEO 2376 | 22.9 ± 3.0 |
| LEO 2377 | 22.7 ± 2.7 |
| LEO 2396 | 23.1 ± 2.8 |
| LEO 2397 | 22.0 ± 3.8 |
| SA 70 | 25.9 ± 5.0 |

The values obtained fall within the lower range of those reported in the literature (Appendix A). It is conjectured that the low values were obtained due to epoxy sizing on the fibres that improved adhesion, and to the droplets being cured, i.e. geometrically frozen, at 130°C which reduced the surface energy and contact angle. More accurate values would require direct quantification of the contact angle throughout cure, which was not warranted here because surface tension values (Section 4.6) provided sufficient information regarding the extent of capillary forces between resins.

## 4.8 Resin viscoelastic behaviour

#### 4.8.1.1 Relaxation of resin films

Compressive relaxation experiments were performed on resin films with epoxy formulation L7 (LEO 2376 and LEO 2377) under pressures of 100 kPa (Figure 4.8) and 1 MPa (Figure 4.7).

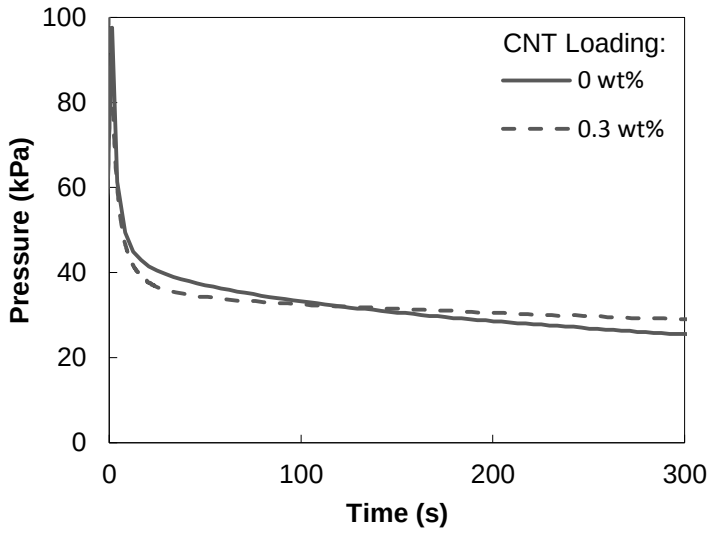


Figure 4.7: Stress relaxation of LEO 2376 and LEO 2377 resin films after 100 kPa loading

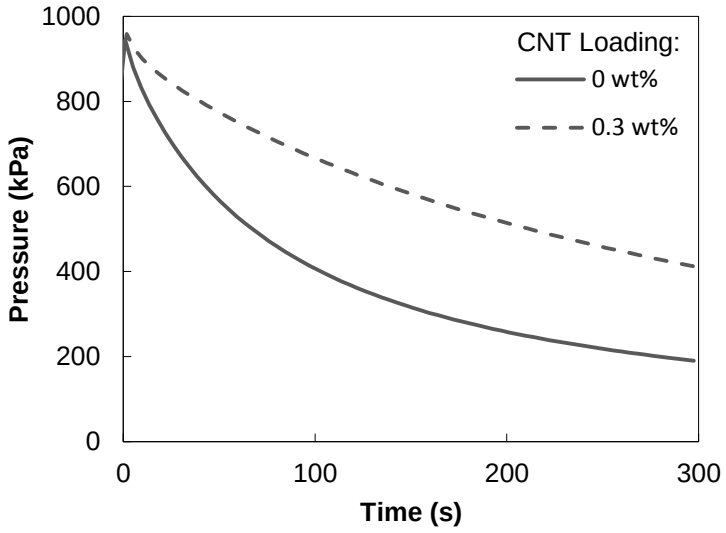


Figure 4.8: Stress relaxation of LEO 2376 and LEO 2377 resin films after 1 MPa loading

All relaxation curves showed a non-linear stress reduction with time and a rate of stress reduction that decreased with time. After an extended relaxation period during 100 kPa relaxation experiments, stress appears to reach a plateau, suggesting that a minimum stress level is required for plastic deformation of the resin films to occur. This minimum flow stress was less than 30 kPa.

Results also showed that the resin films have marked viscoelastic behaviour. The LEO 2376 was mostly viscous as it underwent 74 % and 80 % stress reductions following 300 s relaxation from 100 kPa and 1 MPa respectively. Added CNTs in LEO 2377 had minimal effect on the viscoelasticity at 100 kPa as stress reduction was 77% after 300 s. Conversely, at a higher pressure of 1 MPa the stress reduction was 57%, suggesting a reduction of resin mobility under higher stresses compared with the neat resin. Relaxation was not studied with resin films of formulation L9 as they showed similar viscous behaviour as those of formulation L7 (Figure 4.6). From these relaxation experiments, it can be assumed that films behave as viscous fluids from the onset of RFI processing. This is further confirmed by compressive creep experiments (Section 4.8.1.2) and it has direct implications on resin flow (Chapter 7).

#### 4.8.1.2 Compressive creep of resin films

Compressive creep experiments have been performed on resin films with epoxy formulation L7 (LEO 2376 and LEO 2377). The hysteresis control system assessed the compression load every 2.5 s and increased it if the stress relaxed by more than 5 kPa from target level. It should be noted that a single experiment was performed for each testing condition.

The evolution of pressure and compressive strain through time for both resin films under out-of-autoclave conditions appear in Figure 4.9. The control system took approximately one minute for stabilising the pressure at 95 kPa. Afterwards, it can be seen that under a relatively constant load, strain varied approximately linearly with time. Such behaviour is typical of viscous flow. In this case, the resin films were deformed at a very slow rate of 3.8 µm/min and 3.1 µm/min for the LEO 2376 and LEO 2377 resin films respectively. The lower strain rate of the LEO 2377 is likely attributable to the increase in viscosity due to the added CNTs. Nonetheless, this behaviour suggests that at room temperature the resin films act as a viscous fluid when sufficient pressure is applied. It is expected that resins featuring formulation L9 (LEO 2396 and LEO 2397) would behave similarly due to comparable viscosities (Figure 4.6).

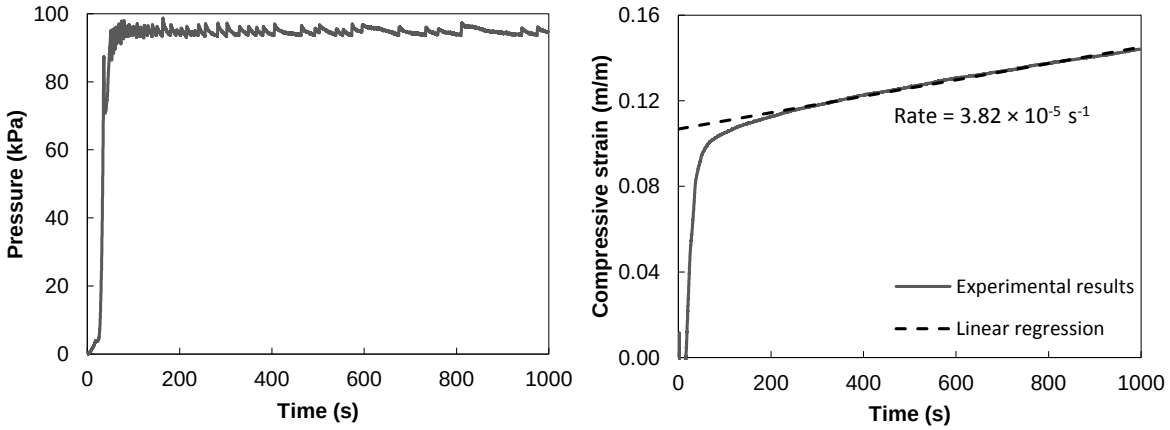


LEO 2376: L7, 0 wt% CNT

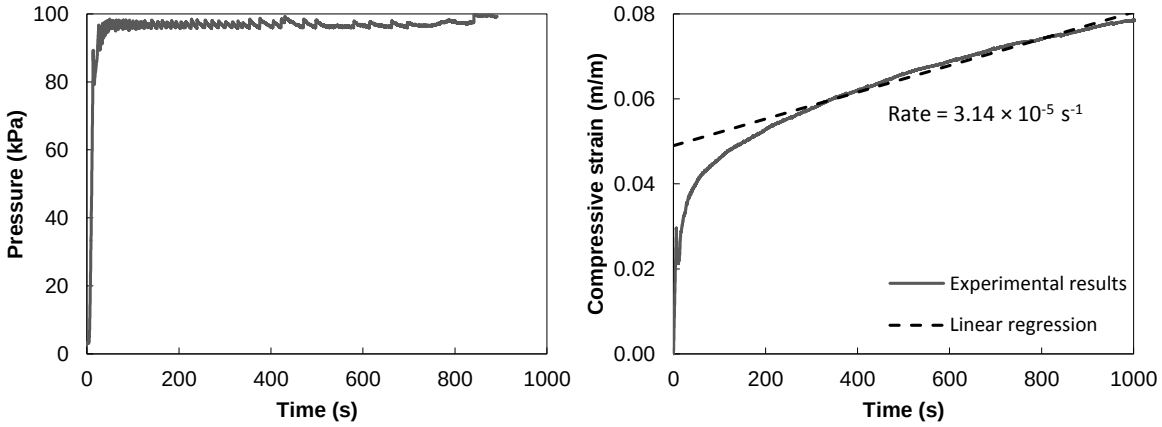


LEO 2377: L7, 0.3 wt% CNT

Figure 4.9: LEO 2376 and LEO 2377 pressure (left) and compressive strain (right) during a creep experiment at 95 kPa

The relaxation experiments suggested that the resin films require a minimum amount of pressure to initiate flow, which prompted the probing of the effect of pressure on the creep rate. Additional creep experiments were performed at 10 kPa, 50 kPa and 900 kPa for the LEO 2377 resin film (Figure 4.10), the LEO resin featuring the highest viscosity. Results showed that once compaction pressure is stabilised, the strain rate is constant with time and that it increases with compaction pressure. Moreover, no flow is observed at the lower pressure of 10.6 kPa, confirming that the resin film behaves as a Bingham rheological fluid.

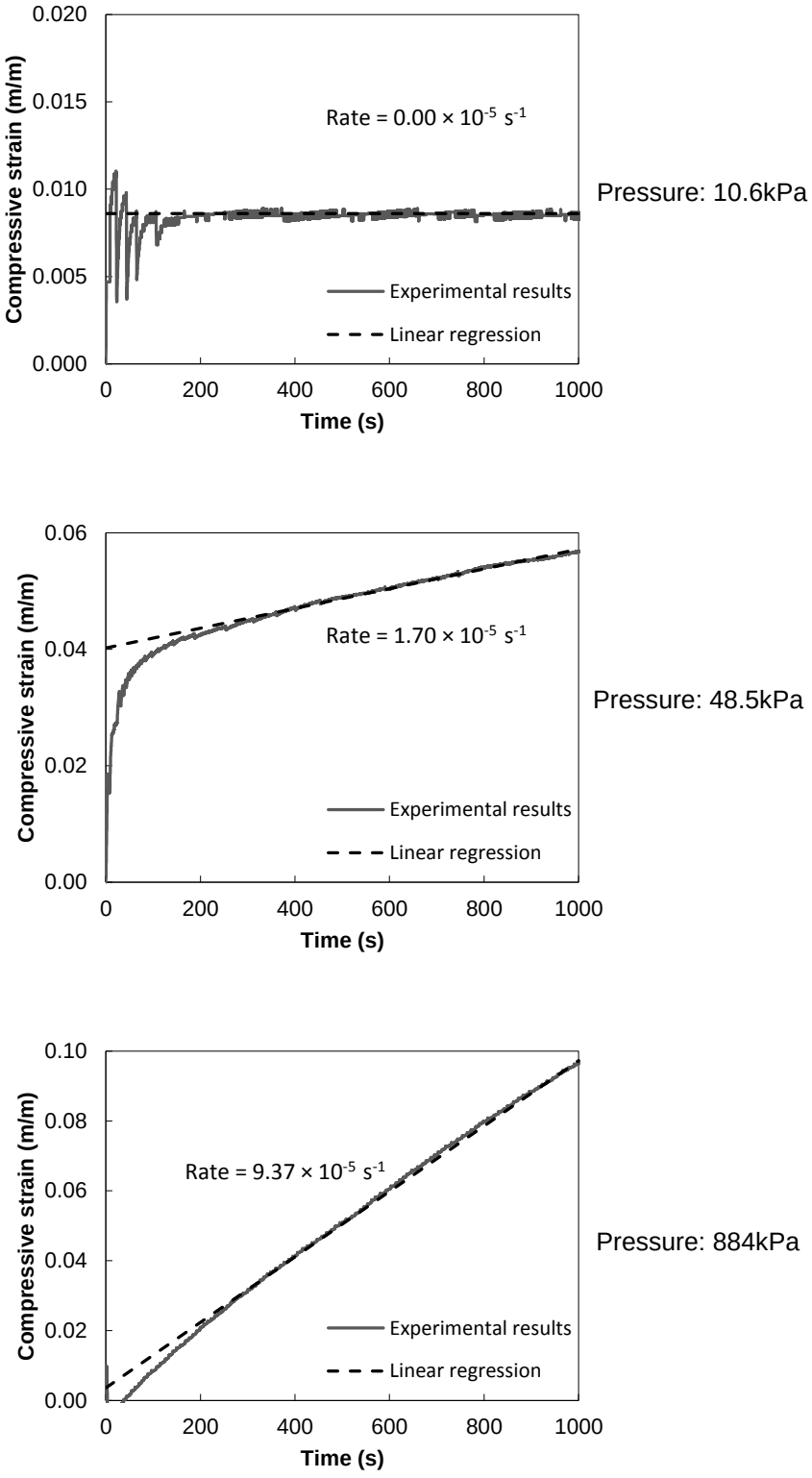


Figure 4.10: LEO 2377 compressive strain during creep experiments at 10 kPa, 50 kPa and 900 kPa

Strain rates for the LEO 2377 resin film were plotted as a function of the compaction pressure and they were used for estimating the minimum stress required for initiating flow (Figure 4.11). Results suggested that stress increases exponentially with the strain rate. Hence, at very low strain rates the LEO 2377 resin film loaded with CNTs undergoes shear thickening. Due to the lack of data for other resin films it is impossible to determine whether the shear thickening at very low strain rates is attributable to the CNTs or the resin formulation.

An exponential curve fitting was used for predicting the minimum stress allowing resin flow. For resin LEO 2377 it was estimated that a compaction pressure of only 27.8 kPa was required, which is in the same range as stress levels observed after relaxation. Considering that LEO 2377 is the LEO resin film with the highest viscosity, that the flow stress is low and that viscosity reduces significantly with temperature, it is expected that for most RFI processing conditions the resin films will behave as viscous fluids having negligible elasticity. Hence, this further confirms that resin films can be treated as viscous fluids from the onset of RFI processing. This information contributes to the understanding of resin flow in Chapter 7.

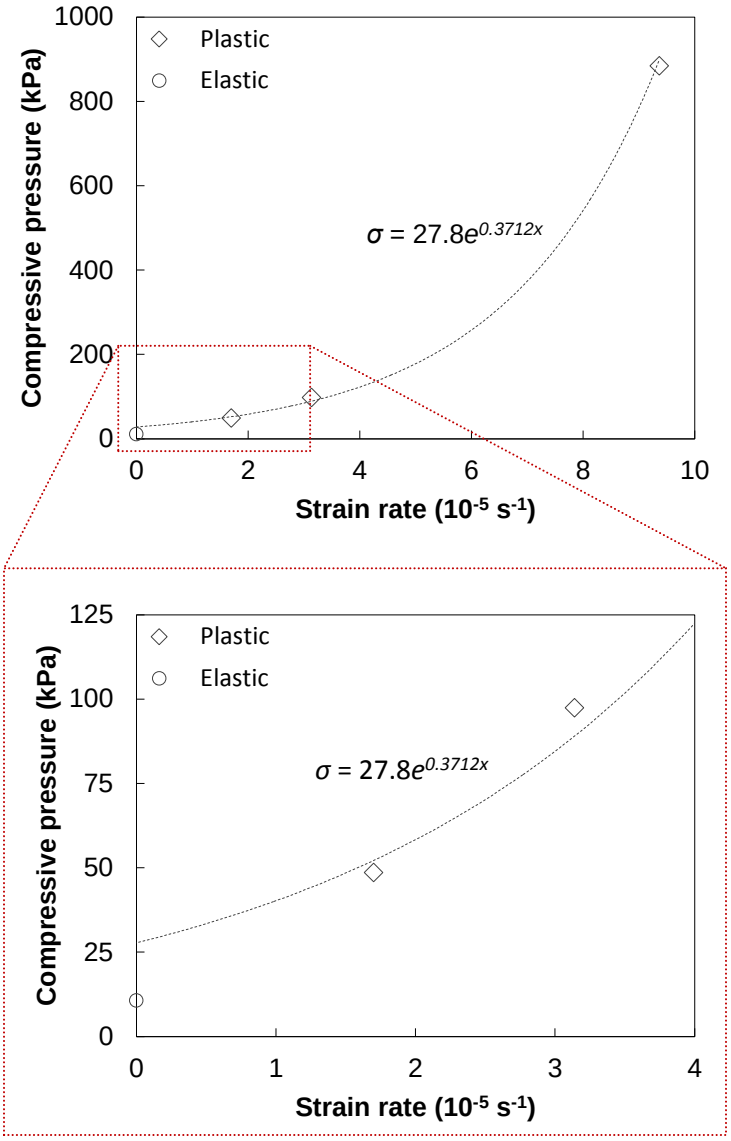


Figure 4.11: LEO 2377 compressive pressure as a function of the strain rate

## 4.9 Remarks

Resin films used for RFI were characterised. Important viscous and capillary properties driving resin flow were obtained, as well as morphological characteristics of resin films. Key observations and findings for future chapters are:

- As-received resin films do not have consistent thickness and they contain numerous bubbles.
- LEO resin films all have a similar initial volatile content.
- CNTs are evenly distributed in the resin films as-received.
- CNTs affect viscosity, but not capillary properties.
- It is expected that resins behave mostly as purely viscous fluids under RFI processing conditions. Even though resins behave like Bingham rheological fluids at room temperature, the force required for driving resin flow is low and resins showed a sharp drop in viscosity with increasing temperature.

# Chapter 5

## Fabrics

This chapter characterises the carbon fibre fabrics used in this work and how they behaved when stacked. Results contribute to the analysis of resin flow, void formation and CNT distribution in future chapters. Characterised feature include:

1. Fabric surface density
2. Fabric surface geometry
3. Fabric cover factor
4. Fabric compaction
5. Pressure distribution within fabric stacks
6. Pressure distribution within fabric/resin film stacks

### 5.1 Fabric surface density

Measured surface density values for all fabrics appear in Table 5.1. The values are consistent and show a maximum standard deviation of ± 7.0 g/m$^2$. Data suggests that variability is independent of surface density as light and heavy fabrics show comparable standard deviations. Furthermore, with the exception of fabric Twill-H, the measured surface densities are in general agreement with supplier data. Surface density values are used for calculating the quantity of fabric plies required in PMC parts for chapters 6, 9 and 10. More importantly, values are used for understanding the effects of the fabric and yarn

thicknesses on inter-yarn and intra-yarn resin flow (Chapter 7), gas dissolution and void formation (Chapter 8), and CNT filtration (Chapter 9).

Table 5.1: Surface density of fabrics

| Fabric | Manufacturer surface density data ($g/m^2$) | Measured surface density ($g/m^2$) | |
|---|---|---|---|
| | | Average | Standard deviation |
| PW-L | 197 | 192.4 | ± 5.4 |
| Twill-L | 215 | 205.2 | ± 6.8 |
| Twill-H | 429 | 403.2 | ± 3.5 |
| NCF-L | 250 | 254.1 | ± 4.6 |
| NCF-H | 534 | 537.8 | ± 5.9 |
| NCF-HP | N/A | 535.0 | ± 4.5 |
| NCF-HB | N/A | 533.7 | ± 3.3 |
| Twill-G | N/A | 315.3 | ± 4.2 |

## 5.2 Fabric surface geometry

Geometrical values describing the surface of fabrics appear in Table 5.2. All values were obtained from fabrics as-received. The measured yarn widths and spacings were relatively similar between fabrics. The float length and stitches were similarly unaffected by the surface density of fabrics. Values were used in Chapter 7 for analysing resin flow and producing fabric models for flow simulations.

Table 5.2: Geometrical parameters for describing the surface of fabrics

| Fabric | Yarn width (mm) | Yarn spacing (mm) | Float length /spacing of stitches (mm) |
|---|---|---|---|
| PW-L | 1.55 ± 0.10 | 2.11 ± 0.11 | 2.11 ± 0.22 |
| Twill-L | 1.70 ± 0.21 | 1.99 ± 0.18 | 3.98 ± 0.25 |
| Twill-L | 1.89 ± 0.16 | 2.01 ± 0.15 | 4.02 ± 0.21 |
| NCF-L | 1.70 ± 0.19 | 1.81 ± 0.20 | 7.34 ± 0.08 |
| NCF-H | 1.60 ± 0.15 | 1.76 ± 0.16 | 7.04 ± 0.22 |

## 5.3 Fabric cover factor

Cover factor values for fabrics as-received appear in Table 5.3. All fabrics had similar total cover factors with the exception of PW-L which featured large gaps between yarns. In twills the cover factor increased slightly with the surface density; this was not the case with NCFs. In addition, measurements indicate that linear cover factors for PW-L, NCF-L and NCF-H are independent of orientation while Twill-L and Twill-H featured greater linear cover factors in the warp direction.

Table 5.3: Measured cover factors for warp and weft yarns in non-compressed fabrics

| Fabric | $CF_x$, Warp | | $CF_x$, Weft | | $CF$ |
|---|---|---|---|---|---|
| | Average | Standard deviation | Average | Standard deviation | |
| PW-L | 0.728 | ± 0.045 | 0.738 | ± 0.067 | 0.928 |
| Twill-L | 0.913 | ± 0.080 | 0.800 | ± 0.078 | 0.982 |
| Twill-L | 0.978 | ± 0.035 | 0.899 | ± 0.058 | 0.998 |
| NCF-L | 0.939 | ± 0.042 | 0.935 | ± 0.055 | 0.996 |
| NCF-H | 0.911 | ± 0.047 | 0.912 | ± 0.058 | 0.992 |

Cover factor values were also obtained for fabrics during a single compaction at 1 bar using the in-situ flow monitoring system. It should be noted that no differentiations were made between the linear cover factor in the warp and weft directions. Values are presented in Table 5.4. In general, fabric compaction provided a small increase in cover factor. The spreading of fibres and increase in cover factor were more noticeable in fabrics featuring a more open structure, but they were still very limited. Hence, cover factors measured on non-compressed samples are representative of values for fabric plies in compressed stacks.

Results for the cover factors were used for explaining inter-yarn resin flow (Chapter 7) and CNT filtration (Chapter 9).

Table 5.4: Measured fabric cover factors during compaction at 1 bar

| Fabric | $CF_x$ | | $CF$ |
|---|---|---|---|
| | Average | Standard deviation | |
| PW-L | 0.761 | ± 0.053 | 0.943 |
| Twill-L | 0.912 | ± 0.078 | 0.992 |
| Twill-L | 0.979 | ± 0.030 | 1.000 |
| NCF-L | 0.926 | ± 0.066 | 0.995 |
| NCF-H | 0.954 | ± 0.045 | 0.998 |

## 5.4 Fabric permeability

Saturated transverse permeability values for 3.6 mm thick stacks at a global fibre volume fraction $V_f$ of approximately 55% were obtained for the six fabrics that were used in studying bulk RFI. Results appear in Table 5.5. Three observations were made: 1) weaves were more permeable than NCFs, 2) stacks featuring higher surface density fabrics were more permeable and 3) lower fabric cover factors increased permeability. Transverse permeability values were used for discussing resin flow in RFI (Chapter 7) and CNT filtration (Chapter 9).

Table 5.5: Measured values for saturated transverse permeability

| Fabric code | Number of plies | $V_f$ | Permeability ($10^{-13}$ m$^2$) |
|---|---|---|---|
| PW-L | 19 | 0.56 | 24.3 ± 1.4 |
| Twill-L | 18 | 0.57 | 5.3 ± 0.2 |
| Twill-H | 9 | 0.56 | 26.8 ± 1.6 |
| NCF-L | 14 | 0.55 | 2.6 ± 0.2 |
| NCF-H | 7 | 0.58 | 10.8 ± 1.0 |
| Twill-G | 16 | 0.54 | 17.3 ± 1.2 |

## 5.5 Fabric compaction

Compaction curves showed that dry fabrics returned a non-linear response in compaction, wherein the compaction pressure rose exponentially with an increase in fibre volume fraction. Fabric deformation was mostly elastic but some permanent deformation occurred between compaction cycles, signs of fibre network reorganisation resulting in greater fibre volume fractions. As shown in Figure 5.1 for fabric Twill-H, the extent of fibre reorganisation reduced as the number of compaction cycles increased. For all fabrics, all deformation had become essentially elastic before 51 compaction cycles at 1 MPa.

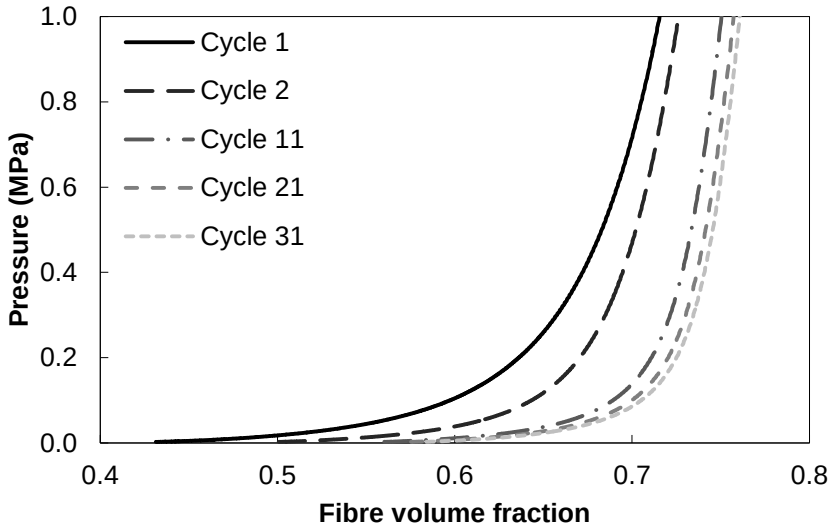


Figure 5.1: Compaction pressure as a function of fibre volume fraction and compaction cycle for fabric Twill-H

A comparison of fibre volume fraction for all dry fabrics compacted to 1 MPa is presented in Figure 5.2. Improvement in fibre volume fraction gained from repetitive compaction occurred in the first 10 compaction cycles. Furthermore, notable differences existed between curves for different fabrics. However, the absence of repeated testing due to lack of sufficient material prevents the confirmation of any of the trends that are discussed next.

From current results, the twills (Twill-L and Twill-H) could be compacted further than the plain weave (PW-L). It is conjectured that this may be attributed to the lower number yarn crossovers that limit fibre straightening. Conversely, even with the absence of crossovers, fabrics NCF-L and NCF-H did not reach greater fibre volume fractions than the weaves, likely due to the presence of stitches.

The increase of fibre volume fraction observed with the twills (Twill-L and Twill-H) and the non-crimp fabrics (NCF-L and NCF-H) suggests that it was related to an increase in fabric surface density. This may be attributed to inter-yarn gaps getting smaller relative to the fabric ply thickness as the surface density increases between different fabrics. In the case of the non-crimp fabrics, the difference was much more noticeable; it might also have been caused by the difference in stitching configuration, i.e., chain stitching (NCF-H) and knitting (NCF-L).

Lastly, comparing similar fabrics NCF-H and NCF-HP it can be seen that the effect of adding a powder binder to fabric NCF-HP greatly reduced the fibre volume fraction. This was expected as the powder is intrusive and takes-up space between fibres.

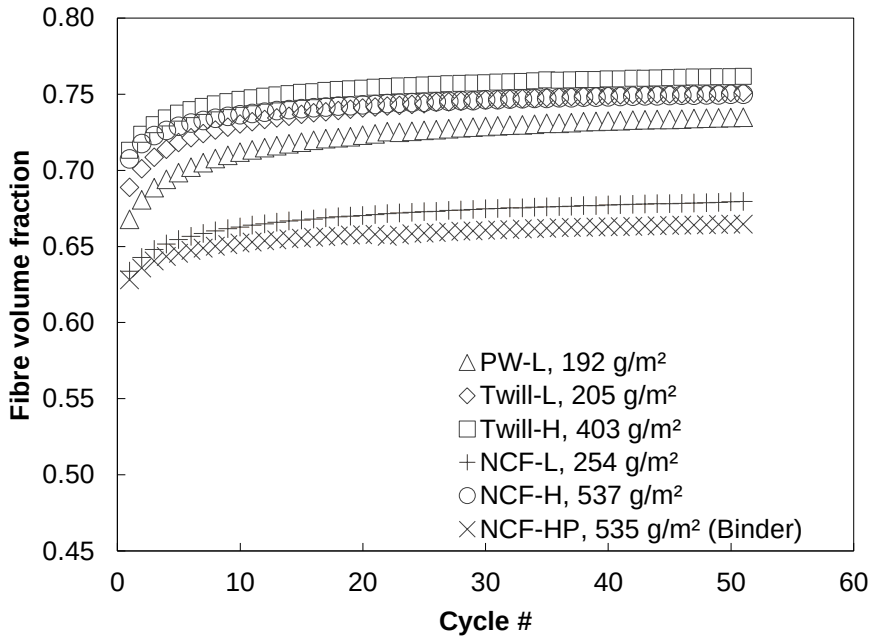


Figure 5.2: Fibre volume fraction of various dry fabrics after repetitive compaction tests to 1 MPa

Fibre volume fraction values at 1 MPa after the 1st and 51st cycles, as well as the increase from repetitive compactions are presented in Table 5.6 for each fabric. These values were compared for investigating compaction in possible autoclave processing. Based on current results, the fibre volume fraction is expected to lie between the lower 60% values and lower 70% values in an autoclave, before heating and without any previous compaction. Repetitive pre-compaction done until no further improvement in fibre network can be detected increased the fibre volume fraction by approximately 5%. The effect was slightly stronger with lighter weaves (PW-L and Twill-L).

Table 5.6: Increase in dry fabric fibre volume fraction due to repetitive compaction at 10 bar

| Compaction cycle (#) | Fabric fibre volume fraction (%) | | | | | |
|---|---|---|---|---|---|---|
| | PW-L | Twill-L | Twill-H | NCF-L | NCF-H | NCF-HP |
| 1 | 66.8 | 68.9 | 71.3 | 63.4 | 70.7 | 62.8 |
| 50 | 73.5 | 75.1 | 76.2 | 67.9 | 75.0 | 66.5 |
| Difference | +6.7 | +6.2 | +4.9 | +4.5 | +4.3 | +3.7 |

Conversely, fibre volume fraction values recorded at 100 kPa under repetitive compaction to 1 MPa are depicted in Figure 5.3, aiming at investigating out-of-autoclave processing. The lower pressure reduced the fibre volume fraction at the first compaction cycle, to roughly 50% to 60%. The same trends seen for the fibre volume fraction values recorded at 1 MPa remain. However, the effect of repetitive compaction on the fibre volume fraction that may be reached was greater. Improvements were up to 10% in fibre volume fraction, resulting in a fibre volume fraction that is comparable to that of fabrics compacted at 1 MPa for a single compaction cycle.

The compaction of dry fabric was used for discussing variations in fibre volume fraction $V_f$ in flat PMCs (Chapter 6).

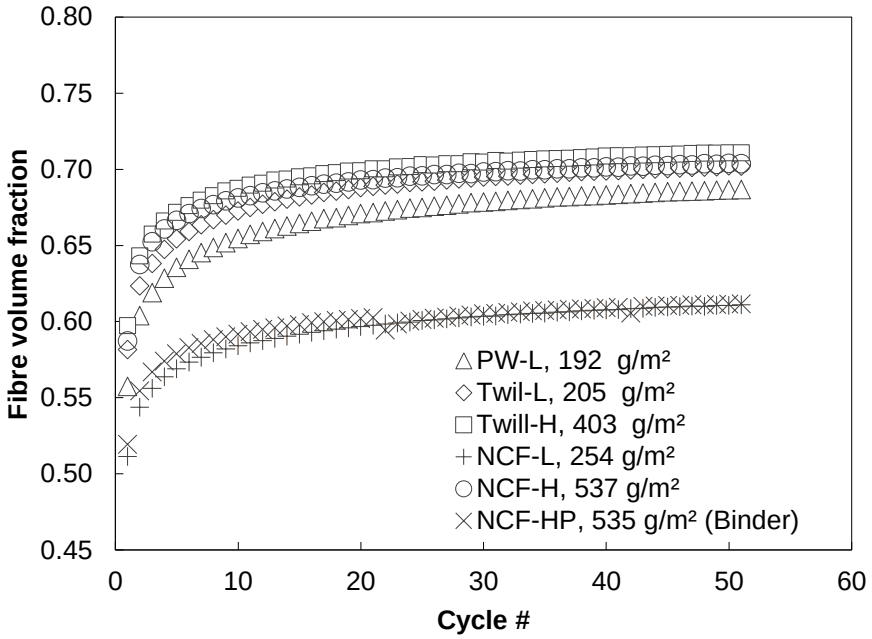


Figure 5.3: Fibre volume fraction of various dry fabrics at 100 kPa after repetitive compaction to 1 MPa

## 5.6 Pressure distribution within fabric stacks

The interaction of fibres and local pressure distribution within fabric stacks during compaction was studied for five fabrics, namely PW-L, Twill-L, Twill-H, NCF-L and NCF-H using pressure mesaurement films. The aim was to understand how pressure distribution varies between fabrics and whether the pressure distribution has an effect on resin flow during RFI processing (Chapter 7).

The stacking sequence for each stack appears in Table 5.7. The sequence was selected because it provides the types of fabric-to-fabric contacts that occur in quasi-isotropic lay-ups such as what is used in delta-stringer demonstrators (chapter 10). In the case of fabric NCF-L, the top and bottom sides of the fabric differed due to the knitting pattern; the side in contact with the pressure sensitive film was accounted for in the analysis of the pressure distribution.

The section presents first the qualitative analysis of the pressure measurement films, followed by quantification of the pressure distribution through image analysis.

Table 5.7: Stacking sequences for the pressure distribution experiments

| Fabric | PW-L/Twill-L/Twill-H | NCF-L | NCF-H |
|---|---|---|---|
| Stacking sequence | $[(0/90)_3, (+45/-45)]_S$ | $[(0/90), (90/0)_2 (+45/-45)]_S$ | $[(0/90), (90/0)_2 (+45/-45)]_S$ |
| Layer #1 | (0/90) | ($0^T$/$90^B$) | ($0^B$/$90^T$) |
| Layer #2 | (0/90) | ($90^T$/$0^B$) | ($90^B$/$0^T$) |
| Layer #3 | (0/90) | ($90^T$/$0^B$) | ($90^B$/$0^T$) |
| Layer #4 | (+45/-45) | ($+45^B$/$-45^T$) | ($+45^B$/$-45^T$) |
| Layer #5 | (-45/+45) | ($-45^T$/$+45^B$) | ($-45^T$/$+45^B$) |
| Layer #6 | (90/0) | ($0^T$/$90^B$) | ($0^B$/$90^T$) |
| Layer #7 | (90/0) | ($0^B$/$90^T$) | ($0^T$/$90^B$) |
| Layer #8 | (90/0) | ($90^T$/$0^B$) | ($90^T$/$0^B$) |

Notes: - ($\theta_1$/ $\theta_2$) format denotes the orientation of a bidirectional fabric, where $\theta_1$ and $\theta_2$ represent the warp and weft yarns respectively

- Superscripts T and B represent the top and bottom side of the fabric which is determined by the stitching/knitting pattern

### 5.6.1 Qualitative pressure distribution in fabric stacks

#### 5.1.1.1 Fabric against tool

Pressure distributions on fabrics pressing against a hard tool are presented in Figure 5.4. In the case of weaves, pressure was distributed over an array of points that was caused by the overlapping of warp and weft yarns. In non-crimp fabrics, some pressure was conveyed through the overlapping of yarns but most of the pressure was distributed along stitches that cross yarns.

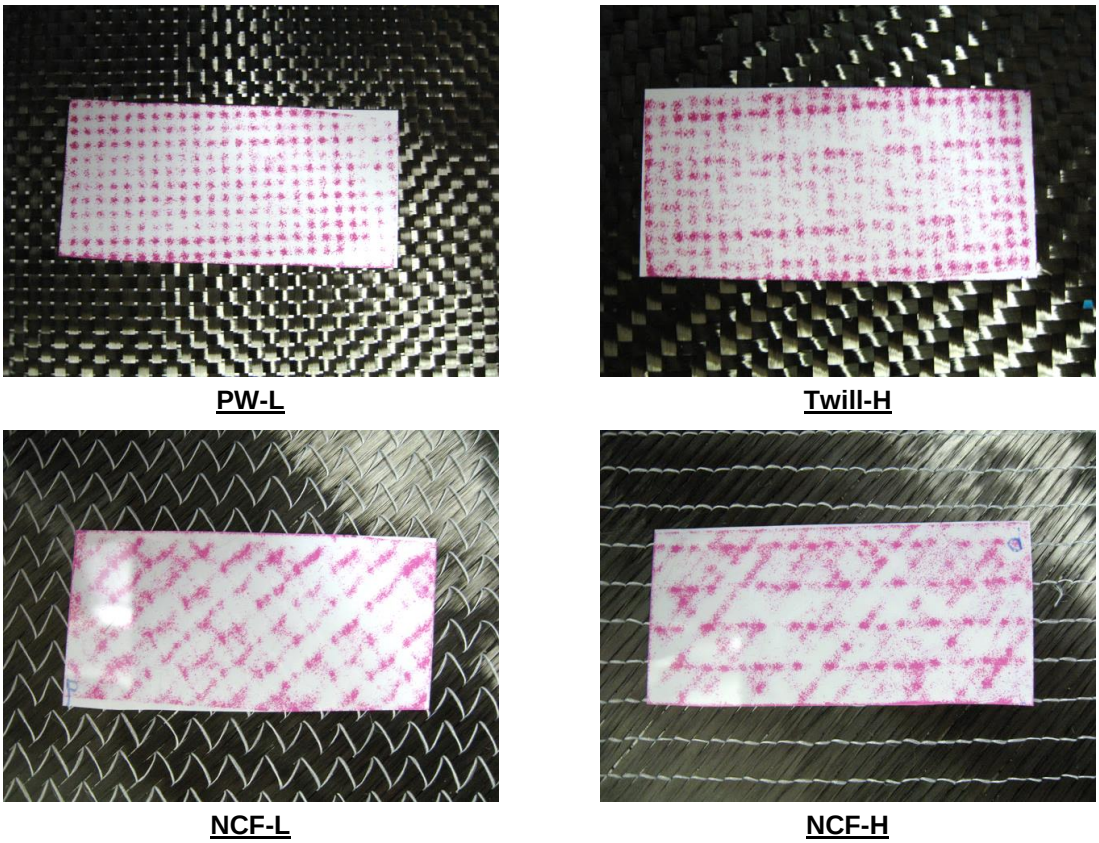


Figure 5.4: Pressure distributions at fabric-to-tool interface

#### 5.1.1.2 Fabric against breather

Pressure distributions on fabric pressing against the breather (Figure 5.5) were similar to the fabric-to-tool pressure distributions; however, the pliable nature of the breather enabled more uniform pressure distributions as indicated by fine pink dots on the pressure measurement films in inter-yarn regions.

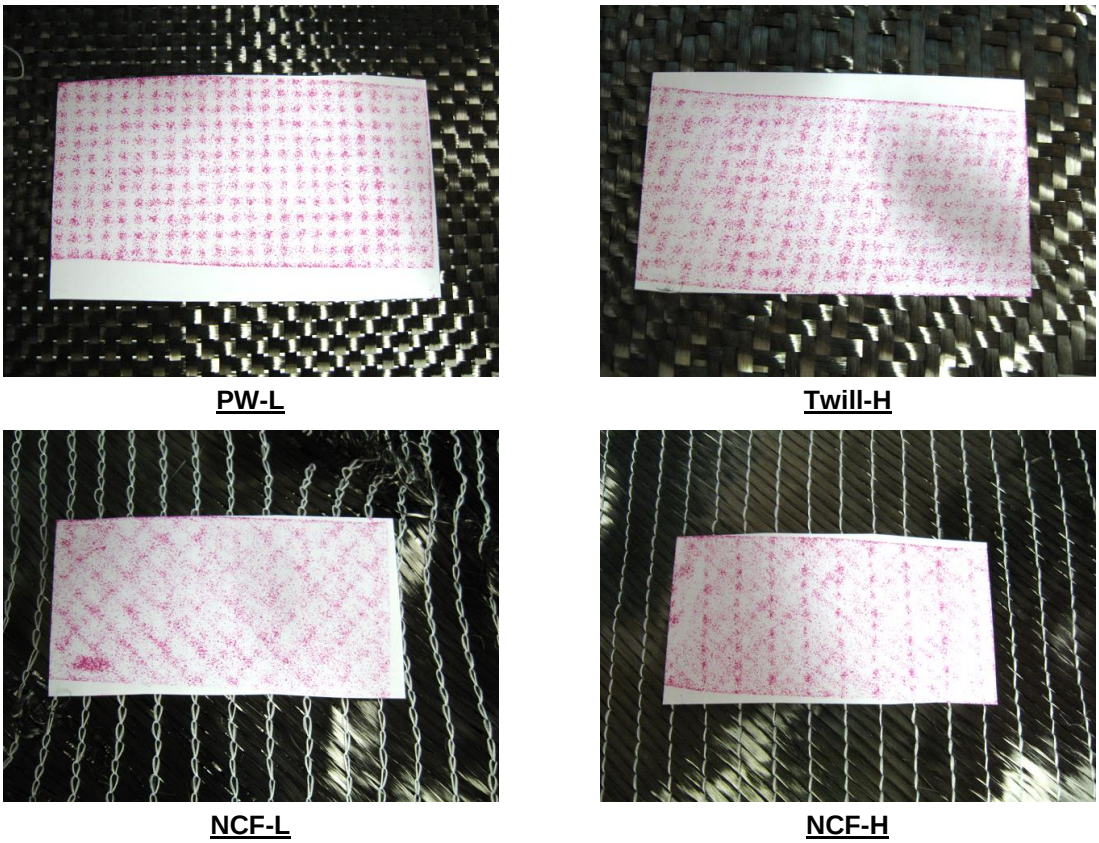


Figure 5.5: Pressure distributions at fabric-to-breather interface

#### 5.1.1.3 Contiguous plies with parallel yarns

Pressure distributions between contiguous fabric plies with parallel yarns appear in Figure 5.6. Pressure distribution patterns were more complex than those seen with the tool and breather because they depend on nesting of the contiguous fabrics.

In the case of weaves, the pressure was distributed along an array of points if contiguous yarns were aligned. Conversely, if two contiguous fabric plies were offset, the increase in nesting results in more uniform pressure distributions in the form of a denser array of pressure points.

In the case of non-crimp fabrics, the alignment of fabric plies was of lower importance as the pressure was mostly distributed along the stitches. For the chain stitched fabric NCF-H, contiguous fabric plies having parallel yarns resulted in stitch threads running in perpendicular directions, giving a grid-like pattern of pressure distribution. The

pressure appeared slightly greater at the crossing of stitches. For the tricot warp-knitted fabric NCF-L, the pressure distribution depended on the contacting fabric surfaces because the fabric top side has stitch threads running in a linear direction whereas on the bottom side has stitch threads running in a zigzag pattern. When top sides were contiguous, unlike fabric NCF-H, the linear running stitching threads did not explicitly produce a grid-like pattern. The pressure distributions appeared more uniform and seemed to be affected by the bottom side of the fabrics. In the case of fabrics with contiguous top and bottom sides, the pressure distribution appeared even more uniform as stitch threads covered a greater surface. Nonetheless, slightly greater pressures were observed at the crossing of stitch threads. It should be noted that no data was recorded for fabrics with contiguous bottom sides but it is conjectured that the greater coverage of the knitting thread would lead to more uniform pressure distributions.

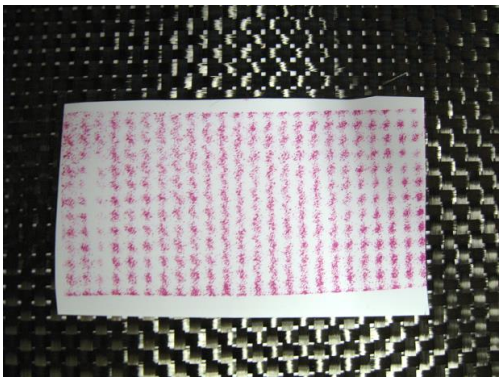

**PW-L: minimal offset**

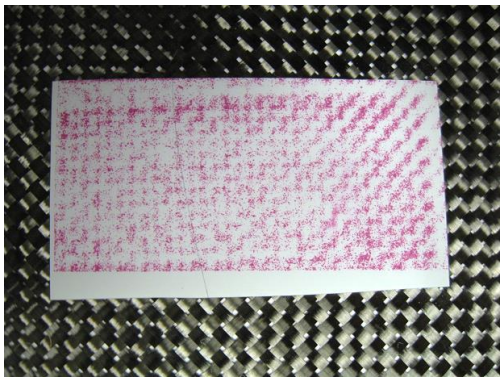

**PW-L: high offset**

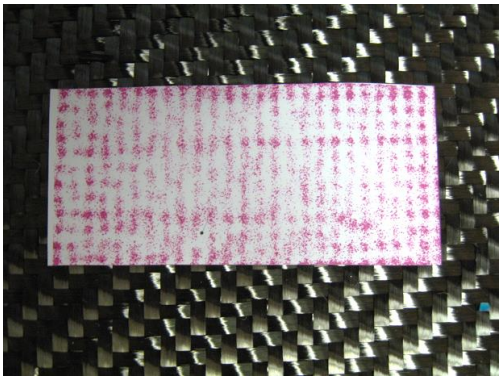

**Twill-H: minimal offset**

**NCF-L: tricot, bottom-top contiguous sides**

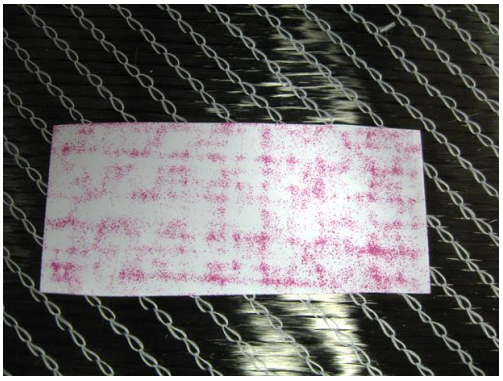

**NCF-L: tricot, top-top contiguous sides**

**NCF-H: chain stitch**

Figure 5.6: Pressure distributions at fabric-to-fabric interface with parallel yarns

#### 5.1.1.4 Contiguous plies with perpendicular yarns

Pressure distributions between contiguous fabric plies with perpendicular yarns appear in Figure 5.7. It should be noted that for weaves, the symmetry of the fabrics provided identical results to those presented in the case of contiguous fabrics with parallel yarns, and therefore they will not be discussed further.

In the case of non-crimp fabrics, pressure distributions were again mostly affected by the stitches. For the chain stitched fabric NCF-H, contiguous fabric plies having perpendicular yarns resulted in stitch threads running in a parallel direction. Most of the pressure was distributed along stitches but also along fibre orientation, as hinted by the light colour grid pattern. For the tricot warp-knitted fabric NCF-L the pressure distribution appeared more uniform than for NCF-H. Fabric plies with contiguous top and bottom sides offered the same pressure distributions as the case having parallel yarns, suggesting limited impact of yarn orientation. This configuration provided the most homogeneous fabric-to-fabric pressure distribution that was observed. Fabric plies having contiguous bottom side resulted in a zigzag pattern following the stitch threads, with no indication of fibre orientation. Hence, fibre orientation appears of lower importance for tricot warp-knitted fabrics than for the other fabrics tested.

**NCF-L: tricot, bottom-top contiguous sides**

**NCF-L: tricot, bottom-bottom contiguous sides**

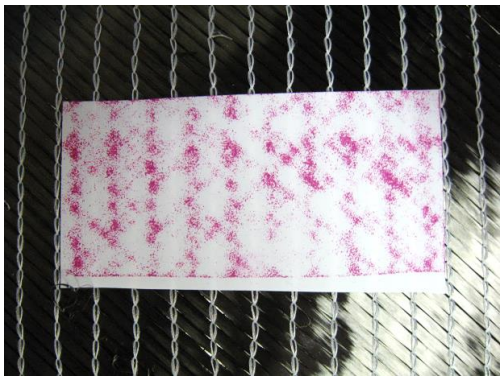

**NCF-H: chain stitch**

Figure 5.7: Pressure distributions at fabric-to-fabric interface with perpendicular yarns

#### 5.1.1.5 Contiguous plies with 45 degree yarns

Pressure distributions caused by contiguous fabric plies with yarns oriented at 45° from each other appear in Figure 5.8.

In the case of weaves the pressure distribution took the shape of a specific pattern of crosses and circles. The pattern was more visible with the plain weave than the twills, again showing greater pressure uniformity provided by the latter type of fabric.

In the case of non-crimp fabrics, pressure distribution was governed again by the stitching thread location. For the chain stitched fabric NCF-H pressure was mostly distributed along the running path of the stitching threads which are offset by 45°, resulting is a diamond pattern. For the tricot warp-knitted fabric NCF-L pressure distribution seemed more uniform as the stitching thread covered a greater surface of the fabric. The most uniform pressure distribution appears when NCF-L fabric plies have contiguous bottom sides.

**PW-L**

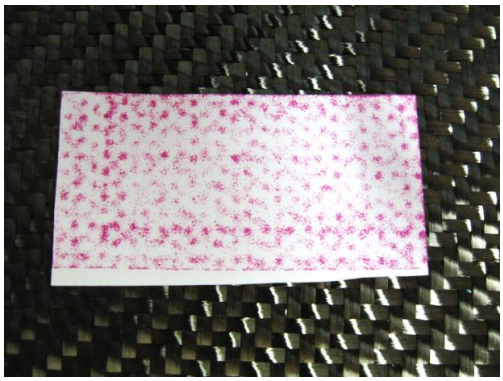

**Twill-H**

**NCF-L: tricot, bottom-bottom contiguous sides**

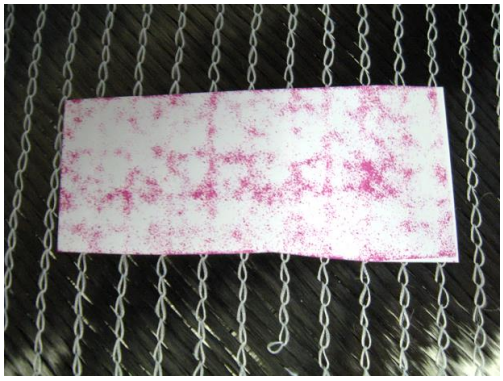

**NCF-L: tricot, bottom-top contiguous sides**

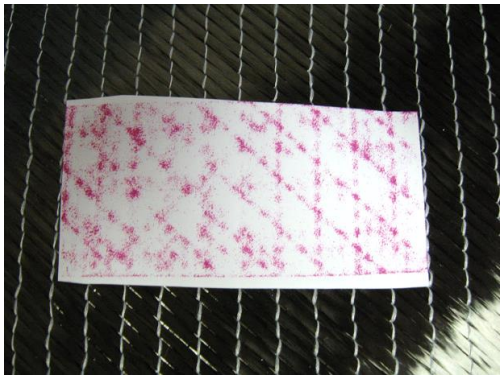

**NCF-H: chain stitch**

Figure 5.8: Pressure distributions at fabric-to-fabric interface with yarns at 45°

### 5.6.2 Coverage of high pressure regions

Qualitative analysis of the pressure measurement films showed that pressure distribution is heterogeneous in stacks due to the architecture of the fabrics that lead to localised high pressure zones. The coverage of these high pressure zones was compared for different locations within the stacks and for different fabric architectures.

Results show that the coverage of high pressure zones is greater at the breather/stack interface compared with that seen within stacks and at the tool/stack interface (Figure 5.9); however, this is not statistically significant. In addition, the coverage of high pressure zones varied for different fabric architectures and fabric-to-fabric stacking orientations (Figure 5.10). Considering variability within the measurements it can be concluded that the architecture of fabrics and stacking sequence that were tested did not affect pressure distribution significantly. Hence, even though the pressure distribution patterns are quite different within stacks, the coverage of pressure high pressure zones remains largely constant. This suggests that the fibre volume fraction $V_f$ in PMCs depends solely on the compaction behaviour of fabrics (Section 5.5) and little on the stacking sequence. In addition, it is shown in Section 5.8 that the heterogeneous distribution of pressure caused by the fabric architecture has a direct effect on the local distribution of resin in interleaved RFI stacks.

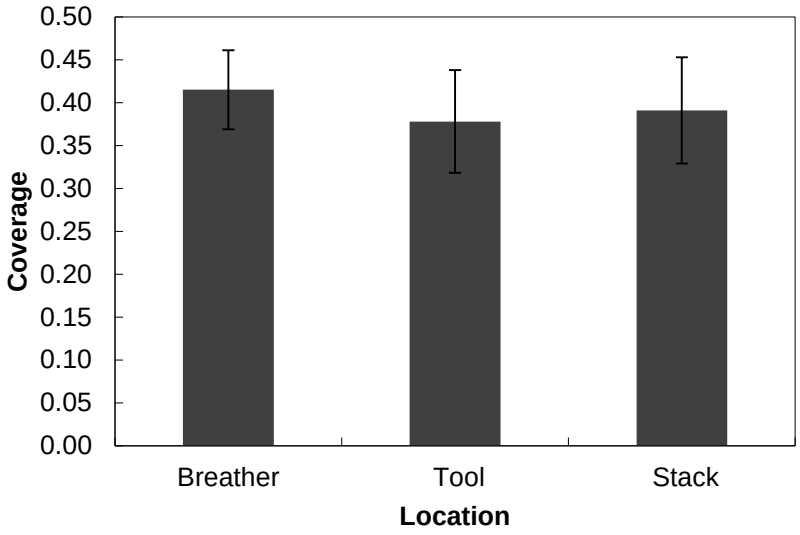


Figure 5.9: Coverage of high pressure zones at different locations within neat fabric stacks

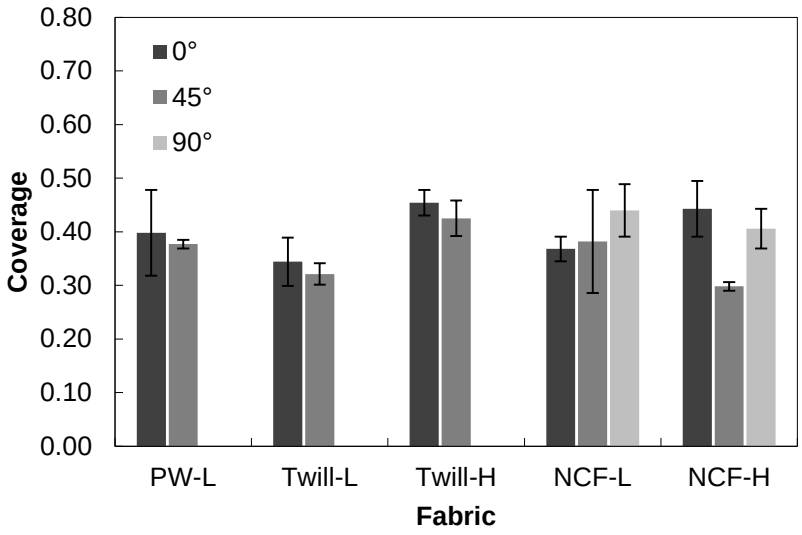


Figure 5.10: Coverage of high pressure zones in neat fabric stacks for different fabric architectures and fabric-to-fabric orientations

## 5.7 Pressure distribution within fabric/resin film stacks

The effect of resin films on the local pressure distribution within fabric/resin film interleaved RFI stacks during compaction was studied for five fabrics, namely PW-L, Twill-H, NCF-L and NCF-H using pressure measurement films. No measurements could be taken for fabric Twill-L due to technical issues preventing the extraction of the measurement films. The stacking sequence for each stack was the same as those described fabric for stacks used in Section 5.7 (Table 5.7). Again, in the case of fabric NCF-L, the top and bottom sides of the fabric differed due to the knitting pattern; the side in contact with the pressure measurement film was accounted for in the pressure distribution analysis.

The section presents first the qualitative analysis of pressure measurement films, followed by quantification of the pressure distribution through image analysis.

### 5.7.1 Qualitative pressure distribution in fabric/resin film stacks

#### 5.1.1.6 Resin against tool

The presence of resin films led to marginal improvements in pressure homogeneity at the tool interface (Figure 5.11). However, pressure distribution patterns similar to those observed with neat fabric stacks were seen, with pressure concentrating at yarn crossovers and stitches.

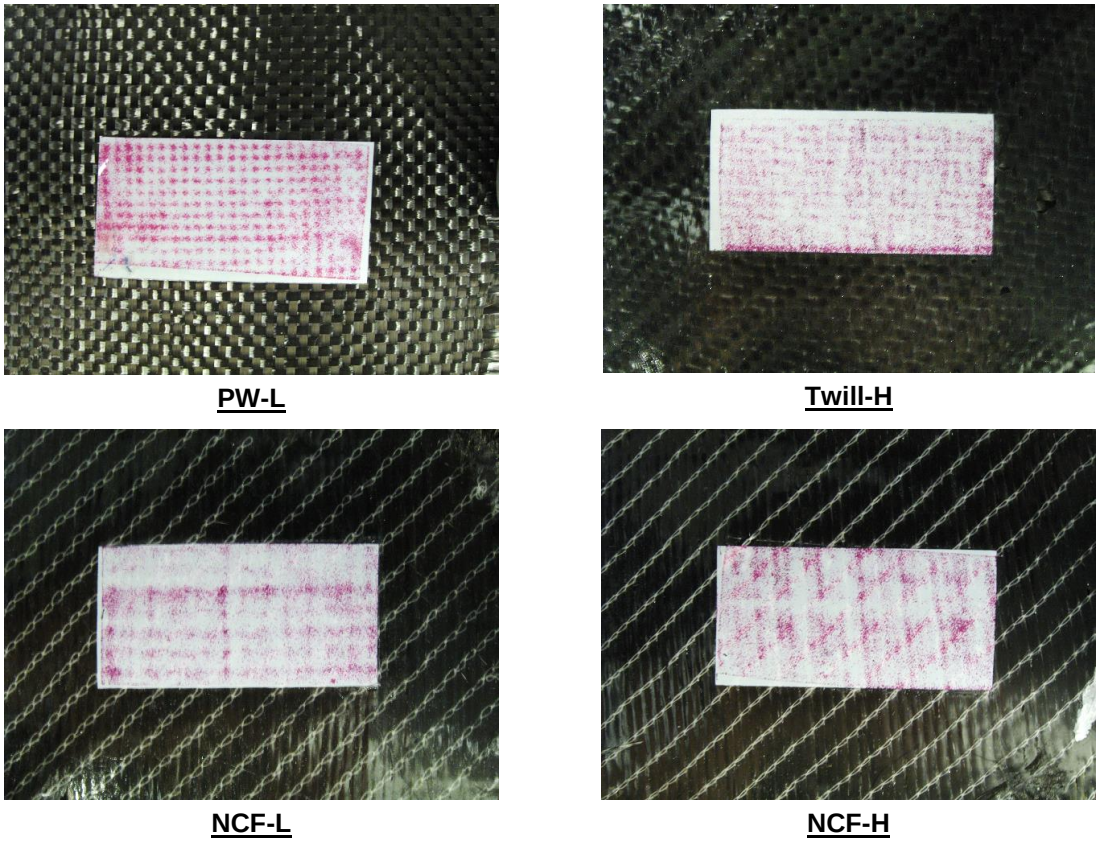


Figure 5.11: Pressure distributions at resin-to-tool interface

#### 5.1.1.7 Resin against breather

Pressure distributions at the resin film and breather interface appear in Figure 5.12. The combined conformability of the breather and resin film around the yarns improved the homogeneity of the pressure distributions significantly compared with those

seen with fabric stacks. For most fabrics, the yarn or stitch locations were not readily apparent.

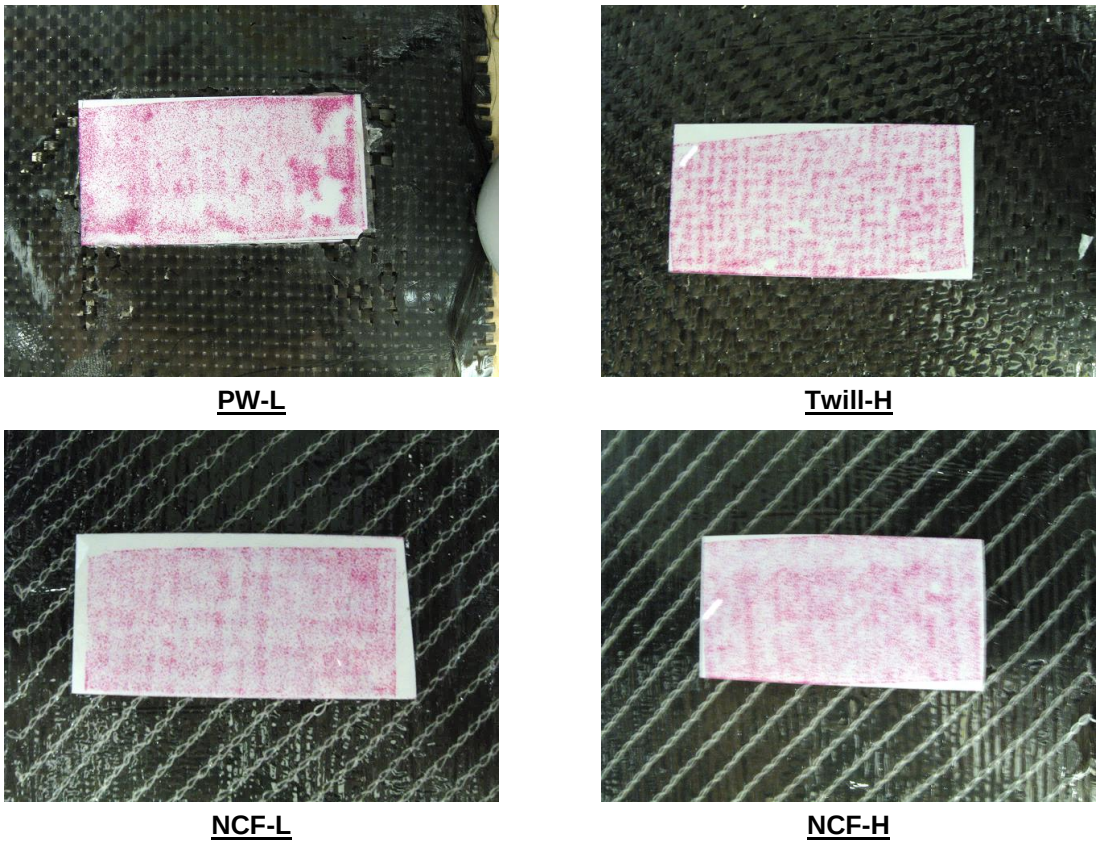


Figure 5.12: Pressure distributions at resin-to-breather interface

#### 5.1.1.8 Interleaved resin film between fabric plies with parallel yarns

Pressure distributions between neighbouring fabrics having parallel yarns appear in Figure 5.13. The presence of the resin film improved the homogeneity of the pressure distribution slightly, but in most cases pressure still concentrated at the same locations. The most notable change occurred with fabric Twill-H where the pressure distribution pattern took the diagonal shape of the twill 2×2 instead of the dotted patterns resembling that of fabric PW-L. Moreover, in non-crimp fabrics it can be seen that the effect of the stitches on the pressure concentration was lessened in favour of yarn crossovers.

**PW-L**

**Twill-H**

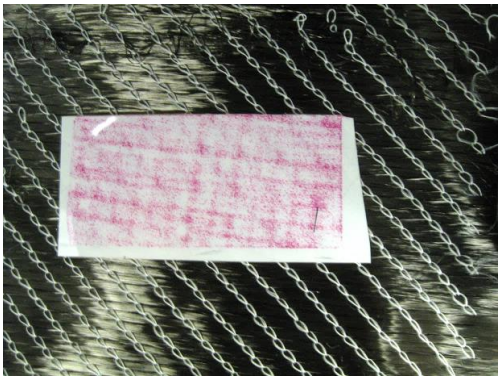

**NCF-L: tricot, bottom-top contiguous sides**

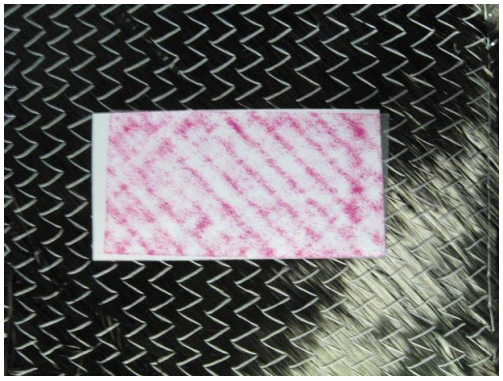

**NCF-L: tricot, bottom-bottom contiguous sides**

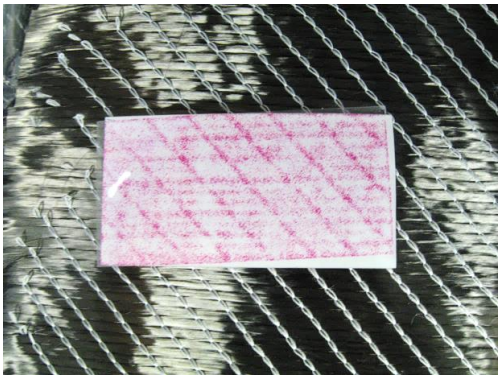

**NCF-H: chain stitch**

Figure 5.13: Pressure distributions at the resin film interleaved between fabric plies with parallel yarns

#### 5.1.1.9 Interleaved resin film between fabric plies with perpendicular yarns

Pressure distributions due to neighbouring non-crimp fabrics having perpendicular yarns appear in Figure 5.14. As for the case with parallel yarns, the presence of the resin film enhanced pressure uniformity; the effect of yarns on the pressure distribution became greater while the effect of stitches was lessened.

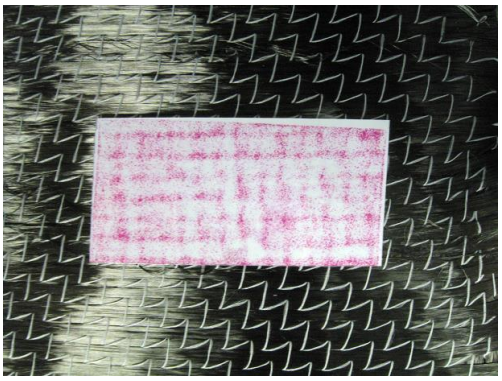

**NCF-L: tricot, bottom-top contiguous sides**

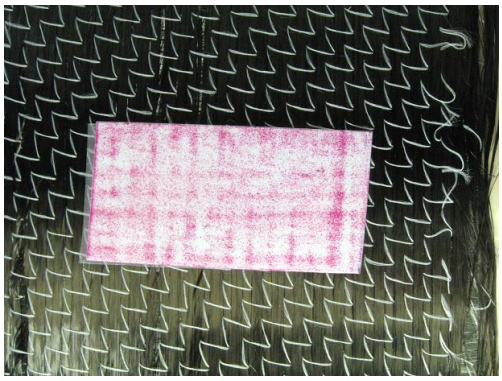

**NCF-L: tricot, bottom-bottom contiguous sides**

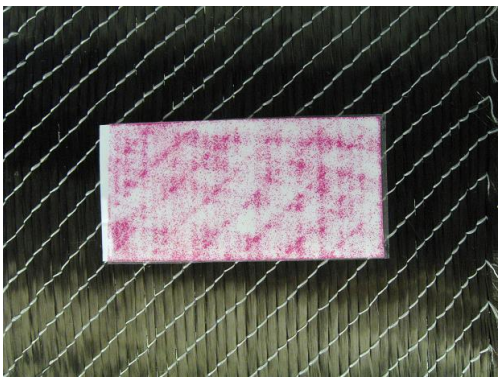

**NCF-H: chain stitch**

Figure 5.14: Pressure distributions at the resin film interleaved between fabric plies with perpendicular yarns

#### 5.1.1.10 Interleaved resin film between fabric plies with 45 degree yarns

Pressure distributions between neighbouring fabrics having yarns at 45° appear in Figure 5.15. The improved uniformity of the pressure distribution lessened but did not eliminate the repeating patterns of the 45° offset.

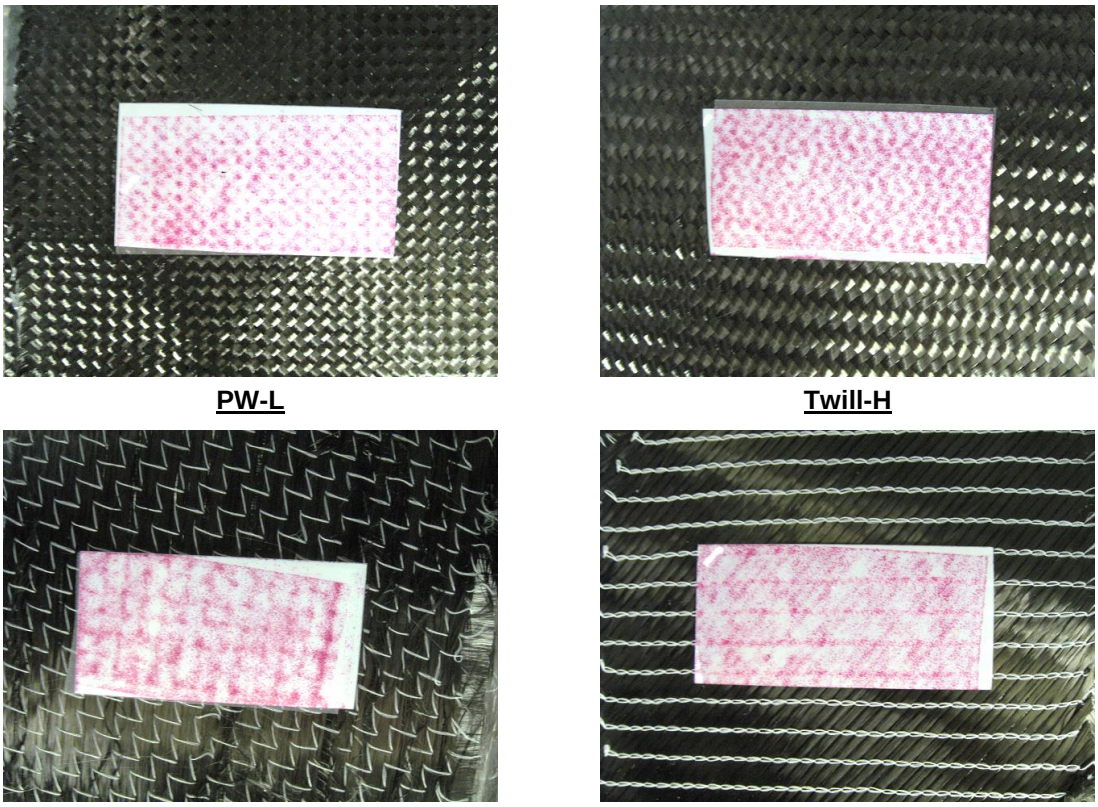


Figure 5.15: Pressure distribution at the resin film interleaved between fabric plies with yarns at 45°

### 5.7.2 Coverage of high pressure regions

Qualitative analysis of the pressure measurement films showed that similarly to fabric stacks, pressure distribution is heterogeneous due to the architecture of the fabrics that lead to localised high pressure zones. However, the presence of the highly compliant resin film resulted in more uniform pressure distributions. This was confirmed quantitatively by the greater coverage of high pressure zones that was measured at approximately 55% of the surface area, as opposed to the 40% coverage for the fabric stacks (Section 5.6.2).

The presence of the resin films reduced the surface effect of the tool and breather material (Figure 5.16). Also, there also was less variation in pressure coverage due to different fabric architectures and fabric-to-fabric stacking orientations (Figure 5.17); all combinations of fabrics and orientation led to a pressure coverage of approximately 55%.

Hence, resin films in interleaved RFI greatly influences the distribution of pressure by attenuating the effects of the stacking sequence and fabric architecture. Nevertheless, the heterogeneous pressure distribution had a direct effect on local resin distribution in compacted stacks (Section 5.8).

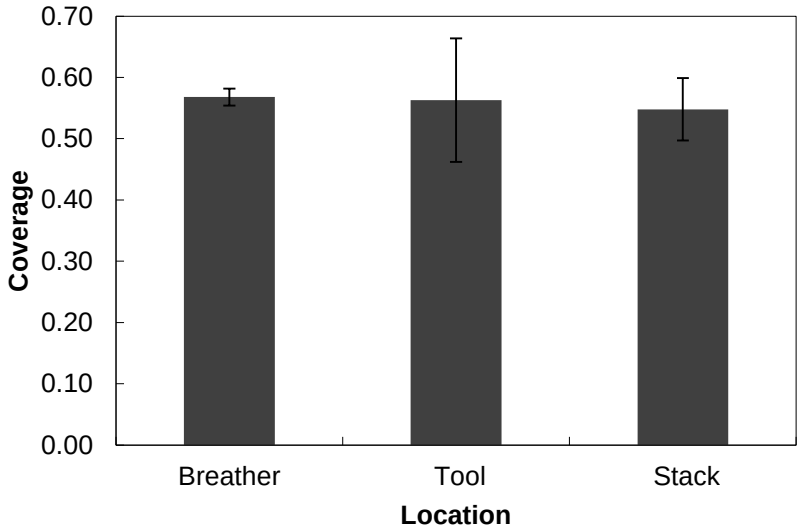


Figure 5.16: Coverage of high pressure zones at different locations within fabric/resin film stacks

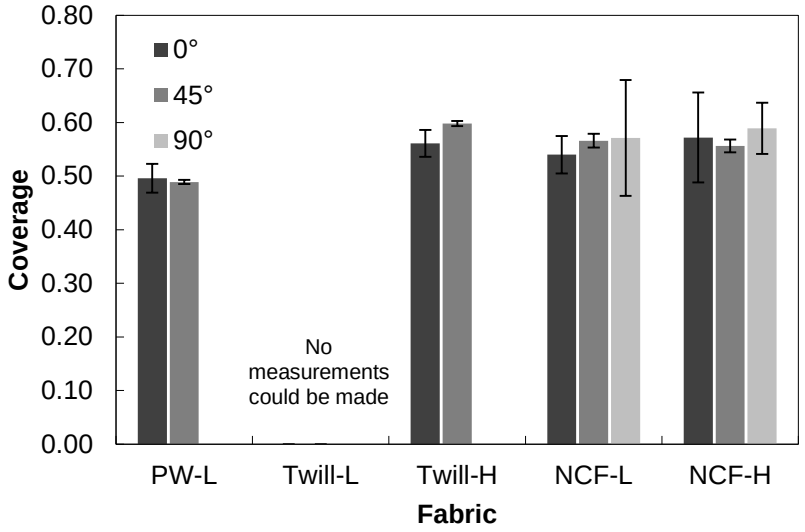


Figure 5.17: Coverage of high pressure zones in fabric/resin film stacks for different fabric architectures and fabric-to-fabric orientations

## 5.8 Resin distribution in stacks following compaction

In interleaved RFI the fabric/resin films stacks are compacted before infusion by a compaction roller and/or vacuum bag. In this section, the initial resin distribution was investigated within two stacks of fabrics and resin films; one stack was compacted with a laminating roller only while the other stack was also vacuumed. All stacks were made by interleaving non-crimp fabric NCF-H plies with LEO 2376 resin films.

After compaction, the stacks were cast in epoxy and prepared for microscopic inspection. The cast samples were heated in an oven at 130°C for curing the resin. Due to the low thermal stability of the cast epoxy, the LEO resin film could not be post-cured. This resulted in relatively soft LEO resin films that hindered the polishing of the samples, leaving artefacts that included scratches and most notably, resin pull out. Finally, the resin distribution was assessed through optical microscopy.

Microscopic inspection revealed that pre-compaction from either the laminating roller or the vacuum bagging failed to force the resin effectively between the yarns (Figure 5.18). Despite a surplus of resin, the film of resin tended to stay between fabric plies. This is attributable in most parts to low pressure zones within stacks (sections 5.6 and 5.7) that limit resin flow because of the heterogeneous fabric architecture. Thus, it is expected that many inter-yarn regions remain devoid of resin before infusion. This has a direct effect on resin flow (Chapter 7).

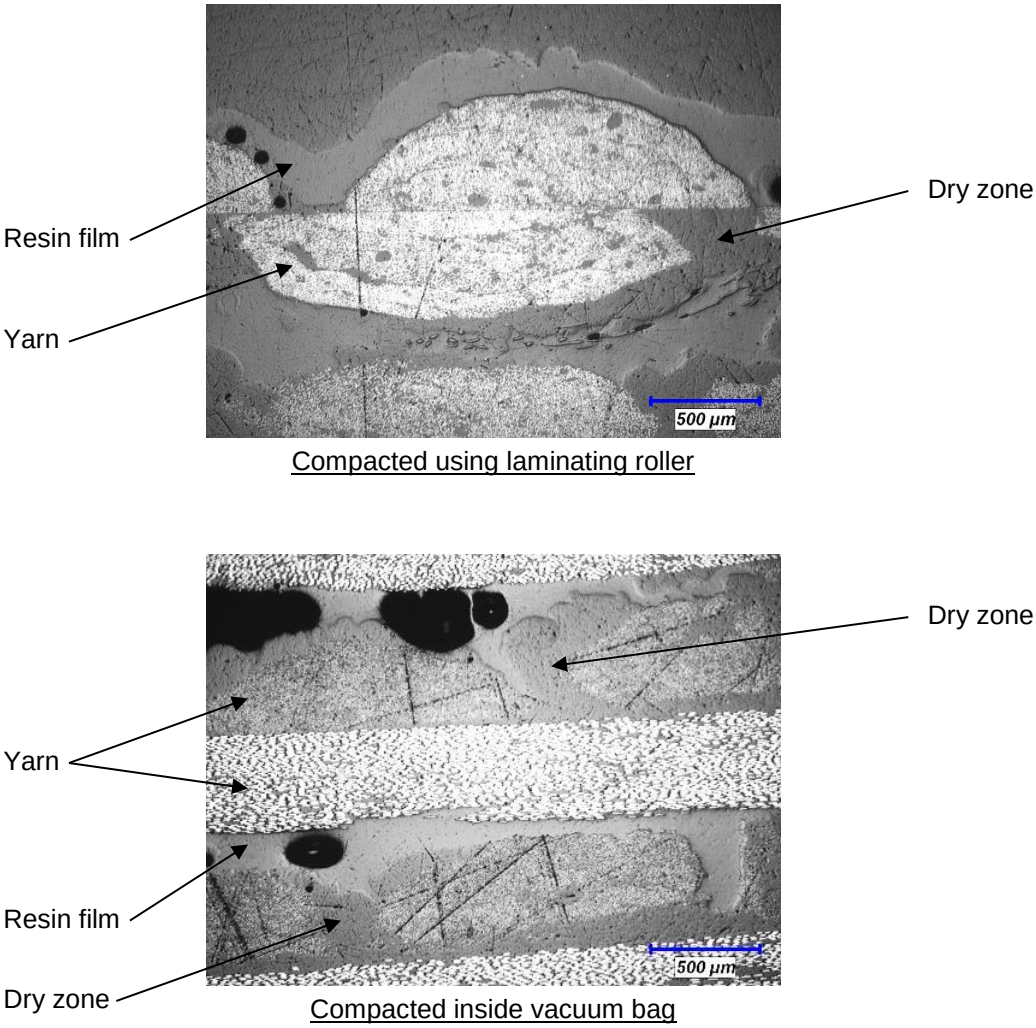


Figure 5.18: Resin distribution within stacks compacted using a laminating roller (top) and a vacuum bag (bottom)

## 5.9 Remarks

Fabrics used for RFI were characterised. Various parameters were investigated, including surface density, fabric geometry, permeability, compaction behaviour of stacks and pressure distribution within stacks. Key observations and findings for future chapters are:

- Fabrics have unique geometries that affect their permeability. Permeability is linked in part to the fabric surface density and cover factor.
- Permeability increases with lower cover factor and higher surface density.

- Fabric types affect the compaction of stacks and how pressure is distributed.
- The distribution of pressure affects the distribution of resin within stacks.
- Despite compaction, inter-yarn gaps can remain devoid of resin before RFI processing.

This section provided the initial state of fabric/resin film stacks at the beginning of RFI processing which is critical for understanding resin flow. In addition, surface density, cover factor and transverse permeability values are used in chapters 7 to 9 for describing resin flow, void formation and CNT filtration.

# Chapter 6

## Fabrication and analysis of flat PMCs

The first step taken towards the evaluation of the RFI process for fabricating multi-scale composites was the assessment of the quality of PMC obtained using RFI, defined here in terms of porosity, fibre volume fraction, CNT distribution and in some cases ILSS. Towards this aim, flat PMCs were fabricated under different processing conditions and characterised for developing knowledge on how to produce high quality PMC parts. More importantly, inspection of these PMCs helped identify key processing concerns that are investigated in greater details in chapters 7-9.

Several experimental programmes listed in Table 6.1 were undertaken for identifying potential hurdles in manufacturing PMCs having a minimum amount of defects. In this chapter, PMCs used in these programmes are presented first, followed by the results obtained in each programme.

Table 6.1: List of experimental programmes for PMC part manufacturing

| Experimental programme | Description |
|---|---|
| M-VC | Effect of viscous and capillary forces |
| M-SC | Effect of stacking configuration |
| M-BL | Effect of bleeding configuration |
| M-PC | Effect of pre-compaction |
| M-FR | Effect of fabric, resin formulation and CNTs |

## 6.1 List of PMC parts

All PMC parts fabricated in the context of this chapter were flat laminates approximately 4 mm in thickness and featuring a symmetric, balanced and orthogonal lay-up. A complete list the processing conditions appears in Tables 6.2-6.4. It should be noted that various bagging configurations were used in this work due to continuous refinement of the method.

Table 6.2: Description of flat PMCs for programmes M-VC and M-SC

| Experimental programme | Laminate | Fabric | Resin | Resin formulation | CNT loading (wt%) | Stacking | Cure | Bagging | Width (mm) |
|---|---|---|---|---|---|---|---|---|---|
| M-VC | M-VC-01[a] | NCF-HP | SA 70 | SA 70 | 0 | Interleaved | S-STD | I-2 | 200 |
| | M-VC-02[a] | NCF-HP | LEO 2396 | L9 | 0 | Interleaved | L-STD | I-3 | 200 |
| | M-VC-03[b] | NCF-HP | SA 70 | SA 70 | 0 | Interleaved | S-STD | I-2 | 200 |
| | M-VC-04[b] | NCF-HP | LEO 2396 | L9 | 0 | Interleaved | L-STD | I-3 | 200 |
| M-BL | M-BL-01 | NCF-H | LEO 2396 | L9 | 0 | Interleaved | L-STD | I-4 | 100 |
| | M-BL-02 | NCF-H | LEO 2396 | L9 | 0 | Interleaved | L-STD | I-3 | 100 |
| | M-BL-03 | NCF-H | LEO 2396 | L9 | 0 | Interleaved | L-STD | I-1 | 100 |
| | M-BL-04 | NCF-H | LEO 2396 | L9 | 0 | Interleaved | L-STD | I-5 | 100 |

Note: [a] resin starved laminate
[b] resin rich laminate

Table 6.3: Description of flat PMCs for programmes M-SC and M-PC

| Experimental programme | Laminate | Fabric | Resin | Resin formulation | CNT loading (wt%) | Stacking | Cure | Bagging | Width (mm) |
|---|---|---|---|---|---|---|---|---|---|
| M-SC | M-SC-01 | NCF-H | LEO 2396 | L9 | 0 | Bulk | L-STD | B-2 | 100 |
| | M-SC-02 | NCF-H | LEO 2377 | L7 | 0.3 | Bulk | L-STD | B-2 | 100 |
| | M-SC-03 | NCF-H | LEO 2396 | L9 | 0 | Interleaved | L-STD | I-1 | 100 |
| | M-SC-04 | NCF-H | LEO 2377 | L7 | 0.3 | Interleaved | L-STD | I-1 | 200 |
| | M-SC-5 | NCF-H | LEO 2396 | L9 | 0 | Bulk | L-STD | B-1 | 100 |
| M-PC | M-PC-01 | NCF-H | LEO 2396 | L9 | 0 | Interleaved | L-STD | I-1 | 100 |
| | M-PC-02 | NCF-H[a] | LEO 2396 | L9 | 0 | Interleaved | L-STD | I-1 | 100 |

Note: [a] For M-PC-02, the fabric stack was pre-compacted to 1 MPa

Table 6.4: Description of flat PMCs for programme M-FR

| Experimental programme | Laminate | Fabric | Resin | Resin formulation | CNT loading (wt%) | Stacking | Cure | Bagging | Width (mm) |
|---|---|---|---|---|---|---|---|---|---|
| M-FR | M-FR-01 | NCF-H | LEO 2377 | L7 | 0.3 | Interleaved | L-STD | I-1 | 200 |
| | M-FR-02 | NCF-H | LEO 2376 | L7 | 0 | Interleaved | L-STD | I-1 | 200 |
| | M-FR-03 | NCF-L | LEO 2377 | L7 | 0.3 | Interleaved | L-STD | I-1 | 200 |
| | M-FR-04 | NCF-L | LEO 2376 | L7 | 0 | Interleaved | L-STD | I-1 | 200 |
| | M-FR-05 | Twill-H | LEO 2377 | L7 | 0.3 | Interleaved | L-STD | I-1 | 200 |
| | M-FR-06 | Twill-L | LEO 2377 | L7 | 0.3 | Interleaved | L-STD | I-1 | 200 |
| | M-FR-07 | Twill-H | LEO 2376 | L7 | 0 | Interleaved | L-STD | I-1 | 200 |
| | M-FR-08 | Twill-L | LEO 2376 | L7 | 0 | Interleaved | L-STD | I-1 | 200 |
| | M-FR-09 | NCF-H | LEO 2396 | L9 | 0 | Interleaved | L-STD | I-1 | 200 |
| | M-FR-10 | NCF-L | LEO 2396 | L9 | 0 | Interleaved | L-STD | I-1 | 200 |
| | M-FR-11 | Twill-L | LEO 2396 | L9 | 0 | Interleaved | L-STD | I-1 | 200 |
| | M-FR-12 | Twill-H | LEO 2396 | L9 | 0 | Interleaved | L-STD | I-1 | 200 |
| | M-FR-13 | NCF-H | LEO 2397 | L9 | 0.3 | Interleaved | L-STD | I-1 | 200 |
| | M-FR-14 | Twill-H | LEO 2397 | L9 | 0.3 | Interleaved | L-STD | I-1 | 200 |
| | M-FR-15 | Twill-L | LEO 2397 | L9 | 0.3 | Interleaved | L-STD | I-1 | 200 |
| | M-FR-16 | NCF-L | LEO 2397 | L9 | 0.3 | Interleaved | L-STD | I-1 | 200 |

## 6.2 Experimental programme M-VC: effect of viscous and capillary forces

### 6.2.1 Description

Four laminates were fabricated to evaluate the effect of viscous and capillary forces on the fabrication of PMCs; details appear in Table 6.2. Laminates were made with resins SA70 and LEO 2396, resins with the highest and lowest ratio of viscosity to surface tension, respectively. Laminate M-VC-01 and M-VC-02 were resin starved, while laminates M-VC-03 and M-VC-04 were resin rich, featuring 50% more resin than required for a laminate with a fibre volume fraction $V_f$ of 0.55.

### 6.2.2 Results

Starved laminate M-VC-01 was made with resin SA 70. Its cross-section showed that resin fills inter-yarn gaps before filling yarns, as indicated by dry regions at the centre of yarns (Figure 6.1). It follows that for resin SA 70, flow is governed by the permeability of the reinforcement and that viscous forces dominate over capillary forces.

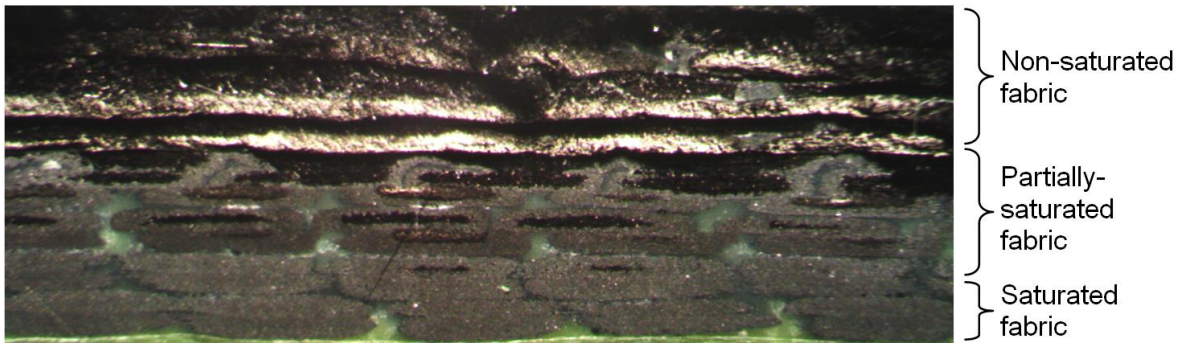


Figure 6.1: Starved laminate M-VC-01 featuring resin SA 70

Starved laminate M-VC-02 was made with resin LEO 2396 and its cross-section showed that resin was wicked by the yarns, leaving inter-yarn gaps free of resin (Figure 6.2). This typical case of over-bleeding suggests that capillary forces can be very strong in the resin compared with viscous forces, and that special care must be taken to prevent excessive bleeding when fabricating laminates.

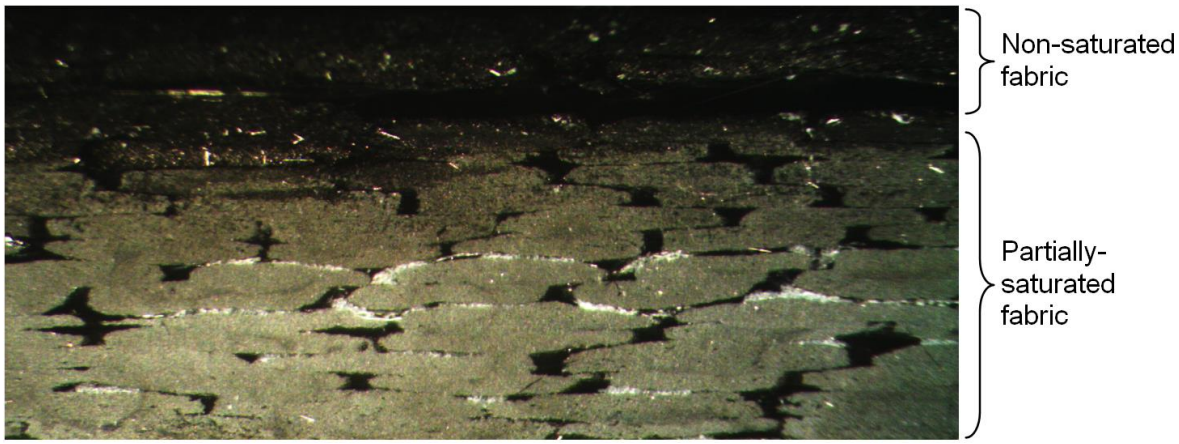


Figure 6.2: Starved laminate M-VC-02 featuring resin LEO 2396

Resin rich laminate M-VC-03 made with SA 70 resin appears in Figure 6.3. It featured a smooth resin rich surface on the bottom tool side. Resin rich zones were distributed along yarns and were more frequent in the centre of the laminate. Conversely, the top surface contacting the bleeder ply featured a rough surface with a resin distribution that appeared uniform. The thickness of the laminate was 5.28 mm ± 0.10 mm, with a thicker region in the centre of the laminate due to lesser bleeding.

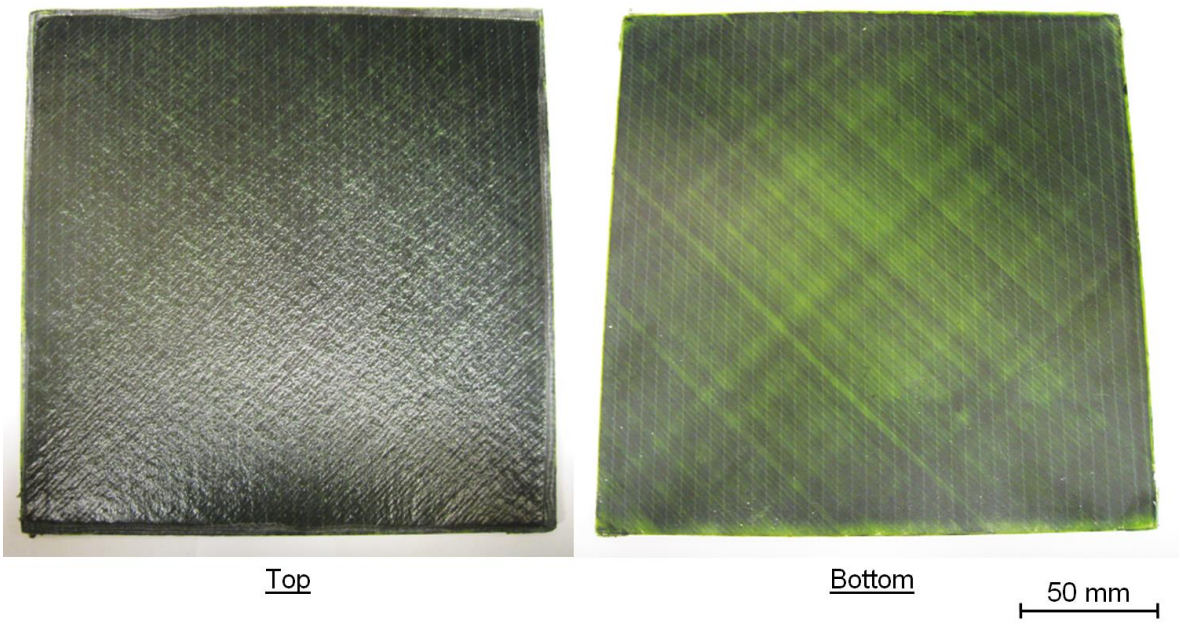


Figure 6.3: Top and bottom surfaces of laminate M-VC-03 after cure

The cross-section (Figure 6.4) of the laminate revealed resin rich zones between fabric plies, caused in part by the glass carrier in the SA 70 resin film. Closer inspection of the laminate cross-section using optical microscopy (Figure 6.5) revealed that the inter-yarn gaps were well saturated with resin, but that some yarns had internal micro-voids. Hence, as noted with starved laminate M-VC-03, resin flow was affected strongly by the low permeability of yarns, indicating that viscous forces dominated over capillary forces.

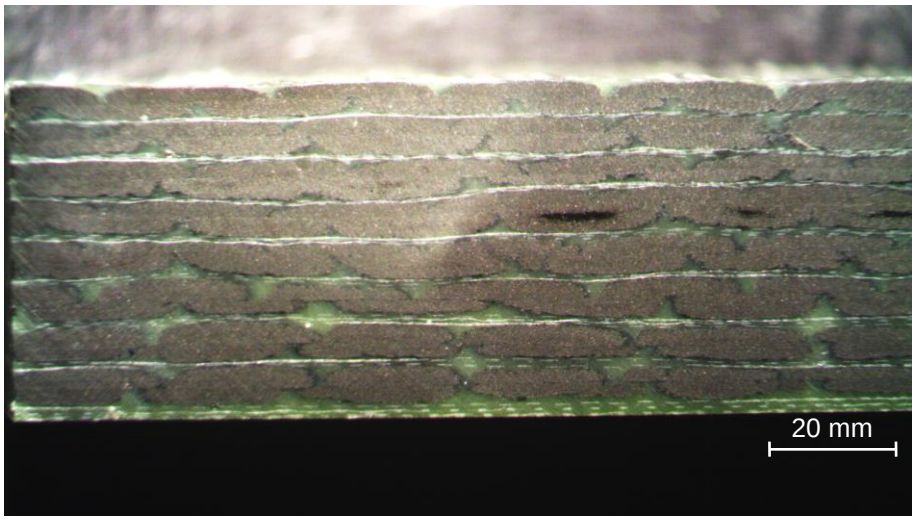


Figure 6.4: Cross-section of laminate M-VC-03 under stereo-microscope

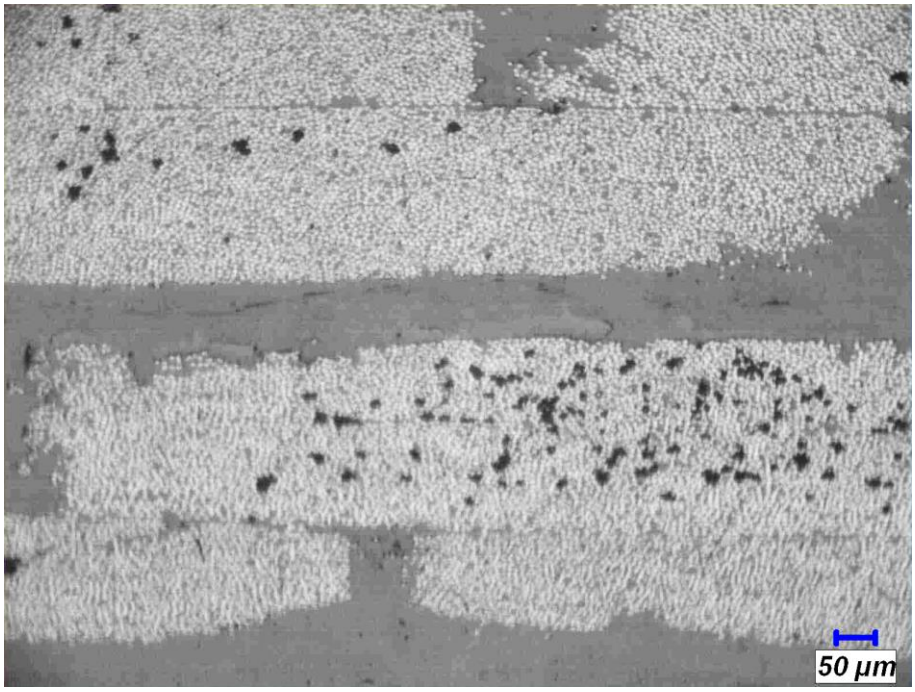


Figure 6.5: Optical micrograph of laminate M-VC-03, where voids (pitch black) are mostly distributed inside yarns

Unlike for laminate M-VC-03, the fabrication of laminate M-VC-04 resulted in a significant amount of resin flow in the breather material that clogged the vacuum port (Figure 6.6). This event showed that resin LEO 2396 flows much more easily than resin SA 70.

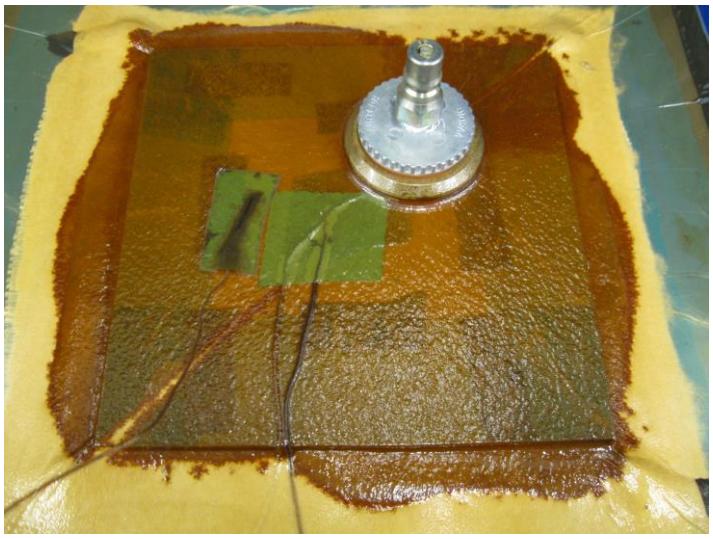

Figure 6.6: Breather material and vacuum port of laminate M-VC-04 filled with resin

Inspection of laminate M-VC-04 showed that it had a thickness of 4.10 mm ± 0.05 mm and that greater resin flow led to a more uniform thickness than laminate M-VC-03. Despite a clear excess of resin, both surfaces of the laminate featured pinholes aligned with the inter-yarn gaps (Figure 6.7).

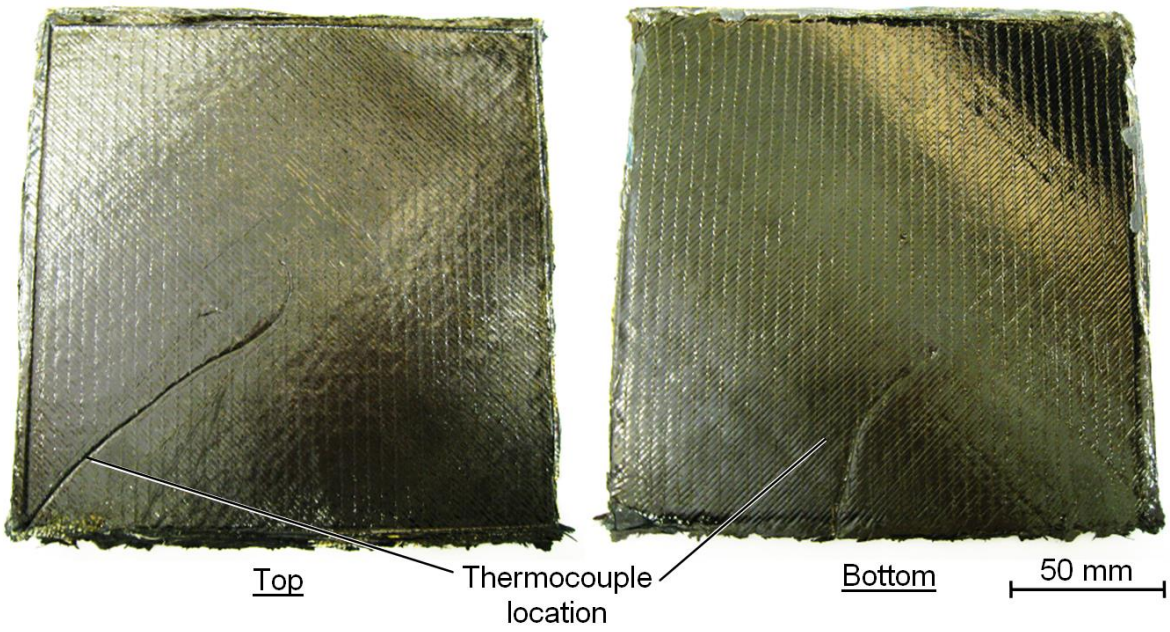


Figure 6.7: Top and bottom surfaces of laminate M-VC-04

The cross-section of laminate M-VC-04 revealed a significant amount of large macro-voids located in inter-yarn gaps (Figure 6.8). These voids are highly reminiscent of those observed in starved laminate M-VC-02. This suggests that despite the resin rich nature of this RFI stack, excessive wicking of resin was present nonetheless. Hence, the use of LOE 2396 resin requires rigorous control of the bleeding, which was not achieved with bagging method I-3.

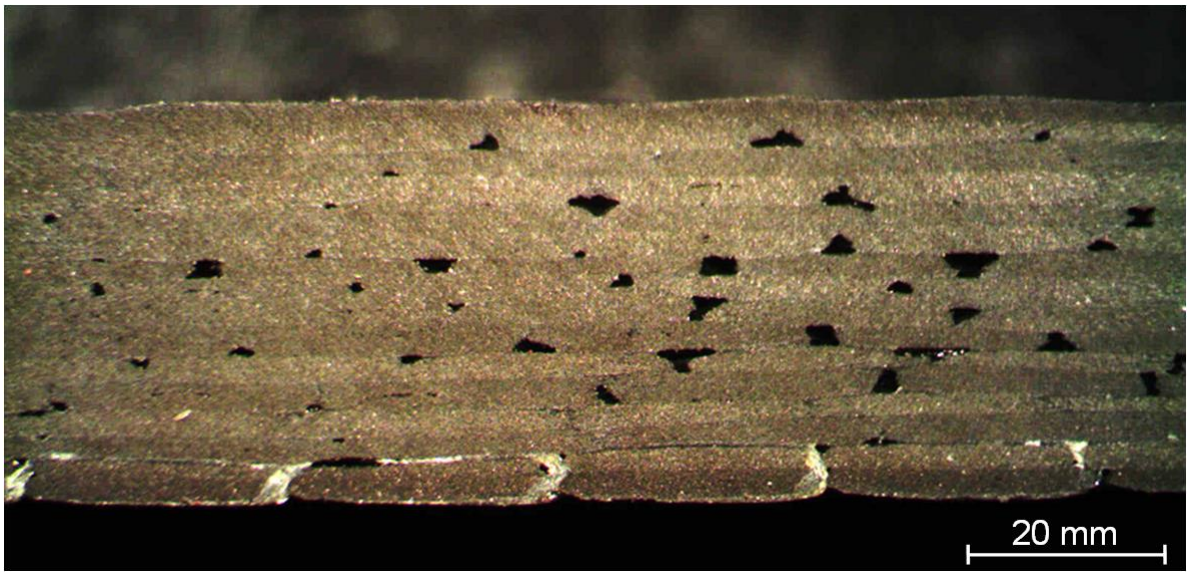


Figure 6.8: Cross-section of laminate M-VC-04 under stereo-microscope

### 6.2.3 Findings

The four laminates of experimental programme M-VC showed that resins can behave very differently in RFI, depending on their material properties. This can lead to resin flowing predominantly either inside or around yarns depending of the relative strengths of viscous and capillary forces, resulting in different void formation mechanisms. For example, flow of resin SA 70 was governed mostly by the permeability of the fabric, leaving micro-voids within yarns, whereas flow of resin LEO 2396 was governed mostly by capillary forces leaving macro-voids in inter-yarn gaps. Thus, upon designing an RFI processing operation it is crucially important to select a resin formulation that can limit void formation, as well as a suitable bleeding method for controlling breathing and bleeding. Moreover, from the results it is expected that all LEO resins pose a risk for over-bleeding due to their similar viscosities and surface tensions.

## 6.3 Experimental programme M-BL: effect of bleeding configuration

### 6.3.1 Description

Experimental programme M-VC showed that high flowability resins such as the LEO series are susceptible to excessive wicking. To address this issue, experimental programme M-BL was devised for evaluating the effectiveness of various bleeding configurations.

Four laminates were fabricated using unique bleeding configurations, all of which used edge bleeding for minimising resin loss; details appear in Table 6.2. For comparison purposes, all laminates featured the same materials and were fabricated concurrently inside the same vacuum bag. A picture of the stacks and bagging method taken prior to processing appears in Figure 6.9.

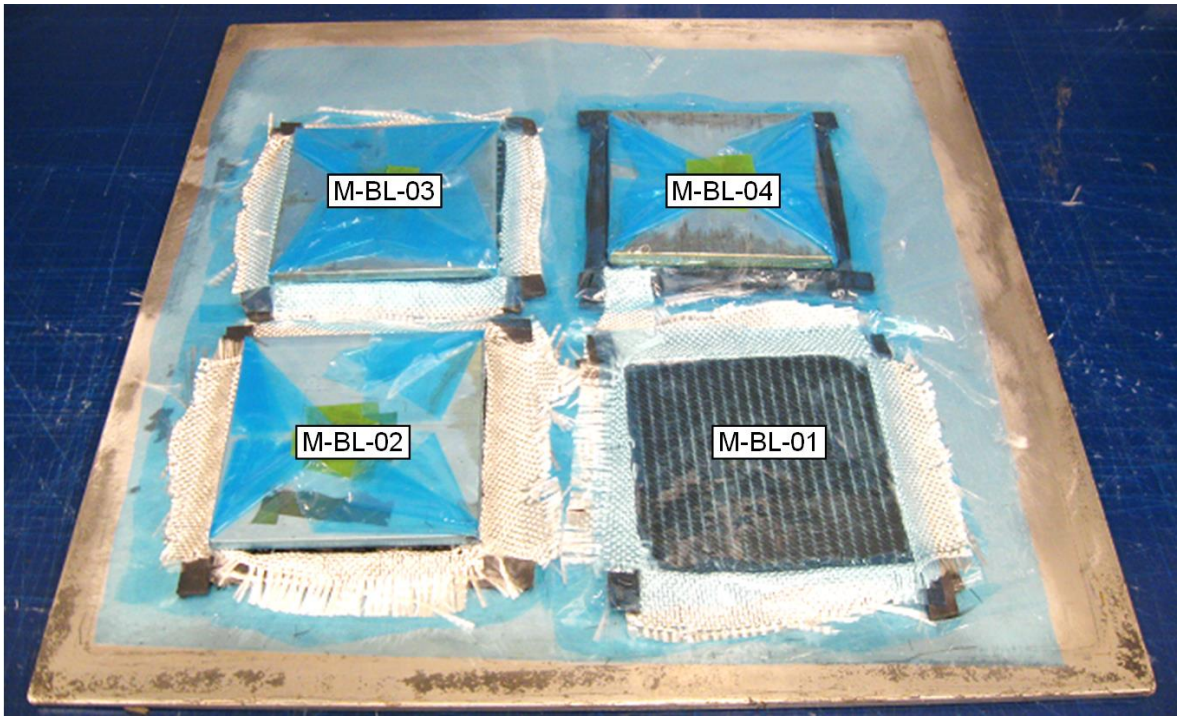


Figure 6.9: Bleeding configurations for experimental programme M-BL

### 6.3.2 Results

Traces of resin were observed in the breather plies after cure (Figure 6.10). Inspection revealed that the amount of resin bleed varied depending on bleeding configuration. M-BL-02 showed the most bleeding of all laminates. This was caused by the gap between the small caul plate and edge dam that enabled resin to flow directly into the breather plies, bypassing the glass fabric bleeder ply of the resin dam. It is worth noting that M-BL-02 used the same bleeding method used in experimental programme M-VC, which also featured strong bleeding. M-BL-03 showed the second-most abundant bleeding, slightly more abundant than M-BL-01 but much less than M-BL-02. M-BL-04 showed the least amount of resin bleed. This was expected due to the smaller resin escape path, resulting from the glass fabric bleeder covering only 5% of the total perimeter of the laminate.

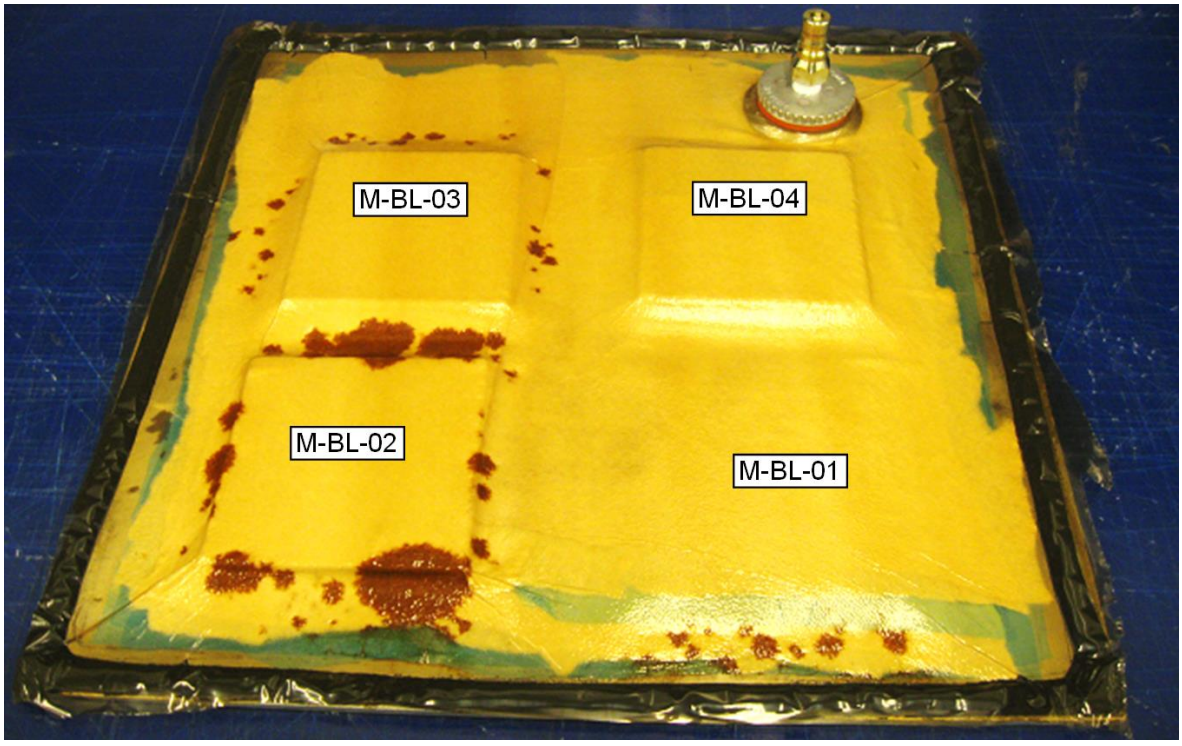


Figure 6.10: Resin bleed during experimental programme M-BL

The removal of the vacuum bag revealed that all faces of the laminates in direct contact with the tool or a caul plate featured smooth surfaces. Only the face of laminate M-BL-01 in contact with the breather ply featured a rough surface.

Measurements of laminate thickness were made. Thickness values along the length of the laminates are plotted in Figure 6.11. It can be seen that all laminates except M-BL-01 had a relatively uniform thickness. For M-BL-01, the lack of caul plate prevented uniform compaction which resulted in resin accumulating at the centre of the laminate, a region less subjected to edge bleeding. The use of a caul plate also increased resin bleeding significantly as seen by the much lower thicknesses for laminates M-BL-02, M-BL-03 and M-BL-04 compared with laminate M-BL-01.

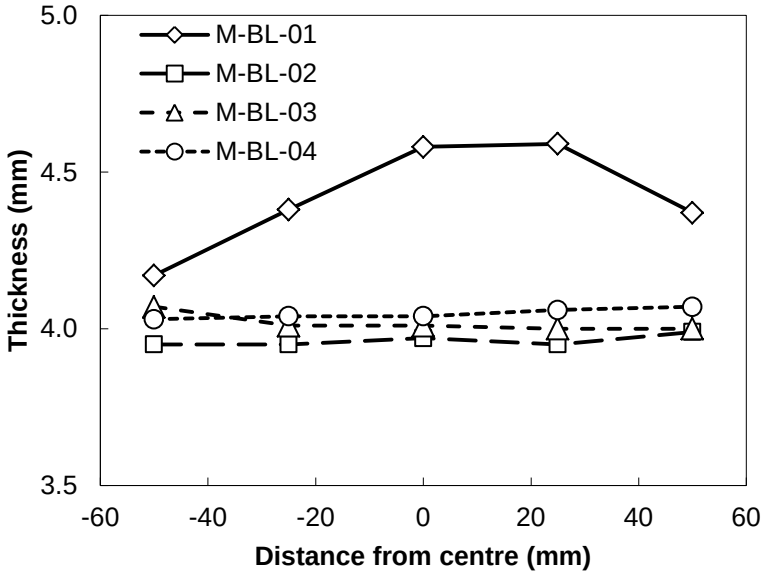


Figure 6.11: Thickness measurements along the length of M-BL laminates

Fibre volume fraction $V_f$ values for the laminates appear in Figure 6.12. As expected, the trends follow those obtained from the thickness measurements, wherein the absence of a caul plate results in a much lower $V_f$. In addition, the reduction of the bleeding in laminate M-BL-04 also resulted in a lower fibre volume fraction compared with the other laminates featuring a caul plate.

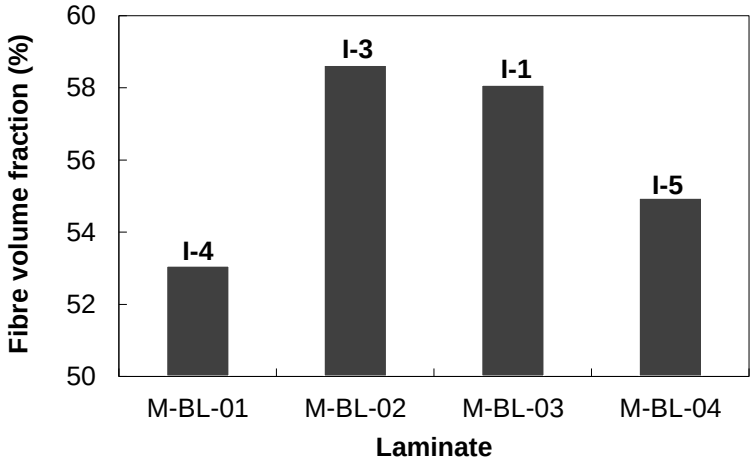


Figure 6.12: Fibre volume fraction values for M-BL laminates and bagging methods I-1, I-3, I-4 and I-5

Porosity values for the laminates appear in Figure 6.13. Unsurprisingly, the highest level of porosity was obtained in laminate M-BL-02 which featured the highest amount of bleeding. However, laminate M-BL-04 showed that excessive restriction of bleeding can also lead to high porosity. In this case, porosity was not caused by excessive wicking but by insufficient breathing of the stack which limited extraction of gasses such as air and volatiles. Laminates M-BL-01 and M-BL-03 featured the lowest levels of porosity because they achieved a good balance between restricting bleeding and enabling gas extraction. Additionally, it is worth noting that bagging methods used for making these two laminates differ only by the use of a caul plate. Hence, the use of a caul plate is not the dominant factor for controlling porosity.

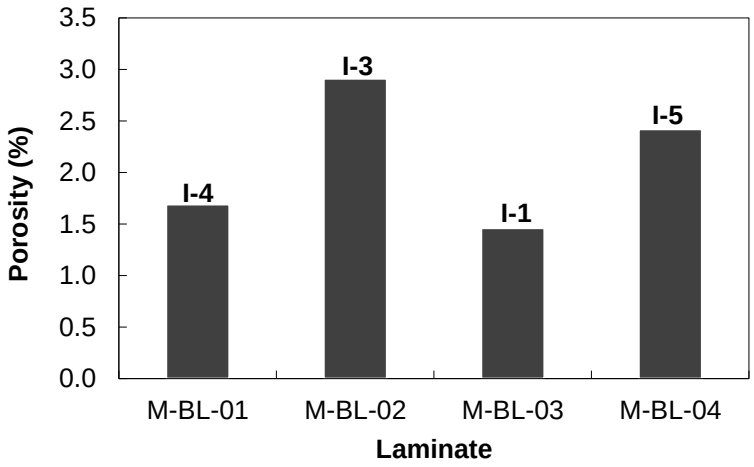


Figure 6.13: Porosity values for M-BL laminates and bagging methods I-1, I-3, I-4 and I-5

### 6.3.3 Findings

Experimental programme M-BL showed that the bleeding configuration has a strong influence on the consolidation of laminates. First of all, results showed that the use of a caul plate not only enhances the surface finish of laminates, but also improves their thickness uniformity by increasing bleeding. More importantly, the bleeding configuration has a direct effect over the porosity of laminates. Limited restriction of bleeding can result in excessive wicking of resins subjected to strong capillary forces, while excessive restriction of bleeding can prevent effective extraction of gases within laminates. In this work, bagging method I-1 was found to be the best bleeding configuration.

## 6.4 Experimental programme M-SC: effect of the stacking configuration

### 6.4.1 Description

A comparison between bulk and interleaved RFI methods was performed in experimental programme M-SC. The objective was to identify any potential differences in fabricated laminates due to varying levels of resin film interleaving in the stacking sequence.

Five laminates were fabricated; a list appears in Table 6.3. They were made with the LEO resins featuring the highest and lowest viscosities. Laminates M-SC-01 through M-SC-04 were made with highly similar bagging methods (methods I-1 and B-2) using edge bleeding. This was done to minimise the number of variables affecting processing. Conversely, laminate M-SC-05 featured a bagging method designed specifically for the through-thickness flow of bulk RFI.

### 6.4.2 Results

In the case of laminates featuring edge bleeding (M-SC-01 to M-SC-04), the interleaved RFI laminates featured smooth surfaces with occasional pinholes. The same was observed for bulk RFI laminate M-SC-02 that was made with the higher viscosity resin. However, the use of a lower viscosity resin in laminate M-SC-01 resulted in a laminate that featured a large non-saturated region on its face that was in contact with the caul plate (Figure 6.14).

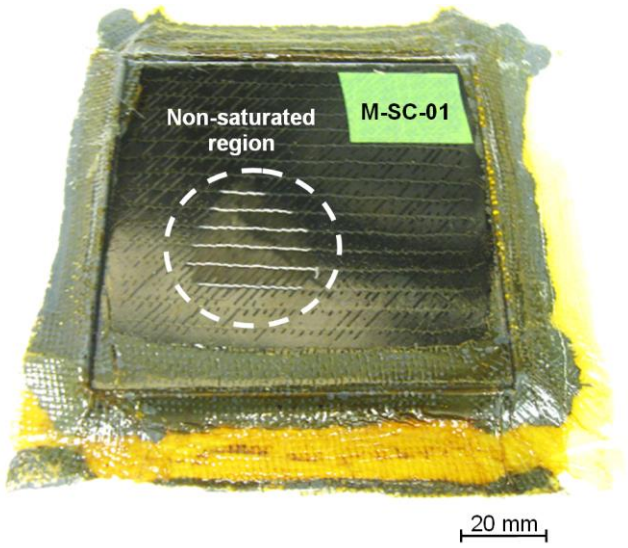


Figure 6.14: Non-saturated region in bulk RFI laminate M-SC-01 due to edge bleeding

The non-saturated region was caused by the resin flowing in the through-thickness direction faster at the edges than at the centre of the stack due to a difference in local permeability arising from the glass fabric used for edge bleeding. This closed the air evacuation channels at the edges of the stack before sufficient saturation could be achieved, entrapping a large quantity of air under the caul plate. As mentioned above, this behaviour was not observed with the nano-modified resin LEO 2377 and was attributed to a more uniform resin flow front which minimised air entrapment.

Bagging method B-1 was designed specifically for preventing non-saturated regions in bulk RFI. Instead of relying on edge bleeding, the bagging method seals the edges of the stack with sealant tape and bleeding is achieved through a bleeder ply at the surface of the stack. This method is highly effective in preventing non-saturated regions from occurring at the surface of the stack, but the absence of direct contact between the laminate and caul plate results in a rough laminate surface (Figure 6.15).

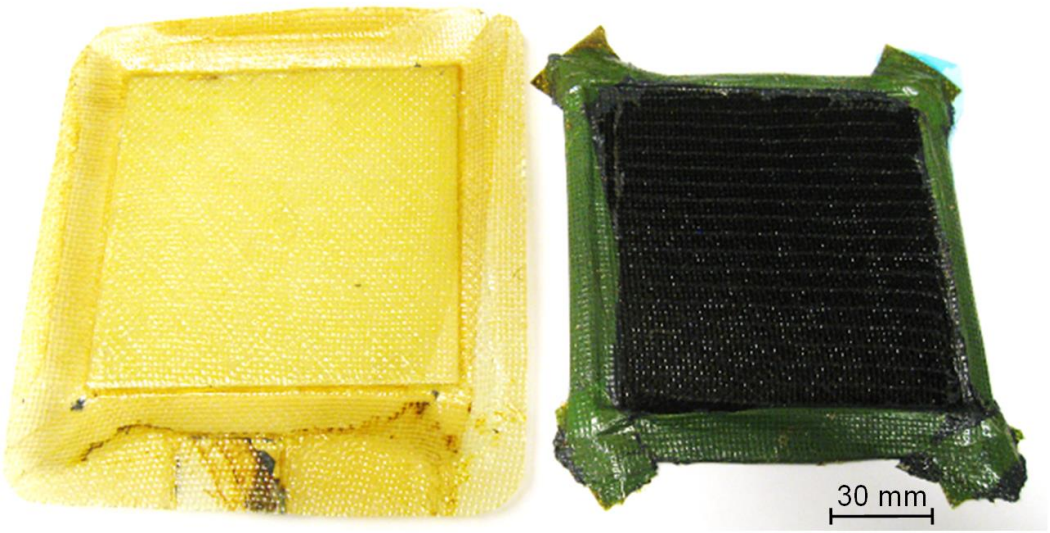


Figure 6.15: Bleeder ply (left) and laminate (right) for M-SC-05

All laminates were analysed for fibre volume fraction and porosity in saturated regions; results appear in Table 6.5. In the case of fibre volume fraction $V_f$, no clear trends were found. Edge bleeding had no effect on the fibre volume fraction compared with surface bleeding, while the level of resin film interleaving affected the fibre volume fraction within yarns slightly. However, laminates differed greatly in terms of porosity. Results showed that the use of a higher viscosity resin filled with CNTs decreased the void content significantly compared with a low viscosity resin. This will be investigated further in Section 6.6.

The level of interleaving also had a strong effect on the porosity of laminates fabricated with edge bleeding, whereas bulk RFI led to an important reduction in porosity compared with interleaved RFI. However, edge bleeding cannot be used reliably with bulk RFI due to risks of air entrapment. Unfortunately, the use of surface bleeding (laminate M-SC-05) resulted in an increase in porosity that negated most of the benefits of bulk RFI. However, it is worth noting that the analysis of void formation in Chapter 8 suggests that bulk RFI still has potential for reducing the porosity in laminates despite surface bleeding.

Table 6.5: Laminate fibre volume fraction and porosity for experimental programme M-SC

| Laminate | Resin | Level of interleaving | Bagging method | Volume fraction (%) | | | Porosity (%) |
|---|---|---|---|---|---|---|---|
| | | | | $V_{fy}$ | $V_y$ | $V_f$ | |
| M-SC-01 | LEO 2396 | None | B-2 | 64.6 | 90.1 | 58.2 | 1.8 |
| M-SC-02 | LEO 2377 | None | B-2 | 65.2 | 87.0 | 56.7 | 0.1 |
| M-SC-03 | LEO 2396 | Full | I-1 | 66.3 | 86.0 | 57.0 | 2.8 |
| M-SC-04 | LEO 2377 | Full | I-1 | 71.6 | 85.7 | 61.4 | 1.2 |
| M-SC-05 | LEO 2396 | None | B-1 | 64.2 | 90.3 | 58.0 | 2.5 |

### 6.4.3 Findings

Experimental programme M-SC showed that the level of interleaving of resin films within stacks has a strong effect on the quality of laminates. Results showed that in certain cases, the absence of resin film interleaving in bulk RFI reduces porosity in laminates compared to the full interleaving of interleaved RFI. However, it was shown that bulk RFI requires surface bleeding for limiting risks of air entrapment, leading to surface roughness.

## 6.5 Experimental programme M-PC: effect of pre-compaction

### 6.5.1 Description

Debulking is an important step in manufacturing PMC parts made of pre-preg material. It consists of applying external pressure and vacuum to a stack before cure for removing air entrapped between pre-preg plies, minimising void formation during consolidation. Experimental programme M-PC sought to investigate any advantages that this procedure could bring in RFI.

Theoretically, debulking should have minimal impact in RFI as the presence of dry fabric reinforcements provides air evacuation channels for reducing air entrapment. Moreover, as seen in Section 5.8, pre-compaction does not assist significantly the distribution of resin within inter-yarn gaps of tight fabrics.

For experimental programme M-PC, two laminates were fabricated (Table 6.3). Before cure, stack M-PC-01 did not undergo any pre-compaction whereas stack M-PC-02 was vacuumed while being compacted to 1 MPa between platens, using an Instron 4482 load frame (Figure 6.16). Compaction was performed at a rate of 1 mm/min and was repeated 3 times. Vacuum was applied during the entire duration of compaction, contributing to air removal.


Figure 6.16: Pre-compaction to 1 MPa of stack M-PC-02 under a load frame and vacuum bag

### 6.5.2 Results

Both laminates featured smooth surfaces. Laminates M-PC-01 and M-PC-02 had similar thicknesses of 4.11 mm ± 0.04 mm and 4.13 mm ± 0.02 mm respectively. The analysis of cross-sections revealed that pre-compaction still resulted in voids in inter-yarn gaps (Figure 6.17). Moreover, materialographic inspection measurements presented in Table 6.6 revealed that pre-compaction did not affect the fibre volume fraction. It may also be argued that pre-compaction to 1 MPa may reduce porosity slightly, 0.3% in this case, but this may also be attributed to variability in the process. Hence, pre-compaction does not appear to be worthwhile for RFI manufacturing.

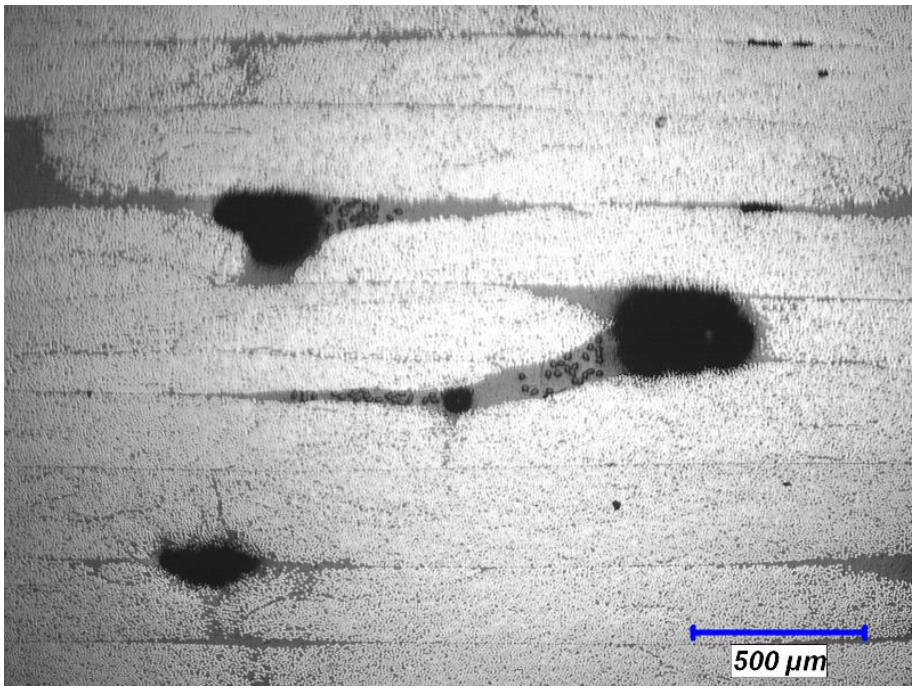


Figure 6.17: Micrograph of macro-voids in inter-yarn gaps for pre-compacted laminate M-PC-02

Table 6.6: Laminate fibre volume fraction and porosity for experimental programme M-PC

| Laminate | Pre-compaction | Fibre volume fraction (%) | | | Porosity (%) |
|---|---|---|---|---|---|
| | | $V_{fy}$ | $V_y$ | $V_f$ | |
| M-PC-01 | No | 66.5 | 89.5 | 59.5 | 2.4 |
| M-PC-02 | 1 MPa | 65.8 | 89.5 | 58.9 | 2.1 |

### 6.5.3 Findings

Results suggest that despite the use of large compaction pressures of 1 MPa, pre-compaction is not a viable procedure for improving the quality of RFI parts. The procedure does not provide an increase in fibre volume fraction nor does it reduce porosity considerably. The absence of an effect on porosity was already expected because it was shown in Section 5.8 that pre-compaction does not force resin effectively into narrow inter-yarn gaps, where laminate voids appear.

## 6.6 Experimental programme M-FR: effect of fabric, resin formulation and CNTs

### 6.6.1 Description

Experimental programme M-FR is a multivariate series of experiments that sought to identify the effect of four factors on the fibre volume fraction, porosity and ILSS of laminates, namely the fabric architecture, fabric surface density, resin formulation and CNT loading. A 2-level, full factorial design of experiments was performed, resulting in the fabrication of 16 laminates (Table 6.4). The full factorial design (Table 6.7) also enabled the investigation of interactions between factors, named contrasts.

Table 6.7: Full factorial design for experimental programme M-FR

| Factor | Level | |
|---|---|---|
| | Low | High |
| A: Fabric architecture | Twill | NCF |
| B: Fabric surface density ($g/m^2$) | <260 | >400 |
| C: Resin formulation | L7 | L9 |
| D: CNT loading (wt%) | 0 | 0.3 |

### 6.6.2 Results

All laminates were fabricated successfully. They featured flat surfaces due to the combination of the interleaving RFI method and the use of a caul plate, but the amount of surface defects varied between them. For example, laminates featuring CNTs had smoother surfaces while those featuring NCF fabrics had more pin holes.

Differences between the laminates also affected the fibre volume fraction, porosity and ILSS (Table 6.8). The total fibre volume fraction was relatively constant between laminates, lying in the mid-50s. Conversely, porosity and ILSS varied significantly between laminates. Laminate M-FR-06 had the lowest porosity value at 0.1%, and highest

ILSS value at 78.8 MPa. These values were obtained with a low surface density twill and LEO 2377 resin film. On the other hand, laminate M-FR-09 had the highest porosity value at 2.8%, and lowest ILSS value at 45.0 MPa. These values were obtained with a high surface density NCF and LEO 2396 resin film.

Table 6.8: Laminate yarn and fibre volume fraction, porosity and ILSS responses for experimental programme M-FR

| Laminate | Volume fraction (%) | | | Porosity (%) | ILSS (MPa) |
|---|---|---|---|---|---|
| | $V_{fy}$ | $V_y$ | $V_f$ | | |
| M-FR-01 | 63.5 | 87.4 | 55.5 | 0.9 | 55.4 |
| M-FR-02 | 66.4 | 86.6 | 57.5 | 1.5 | 53.5 |
| M-FR-03 | 62.9 | 88.6 | 55.7 | 1.3 | 75.0 |
| M-FR-04 | 64.2 | 89.9 | 57.7 | 1.8 | 67.8 |
| M-FR-05 | 68.6 | 83.8 | 57.5 | 0.5 | 63.4 |
| M-FR-06 | 65.0 | 85.6 | 55.6 | 0.1 | 78.8 |
| M-FR-07 | 64.3 | 83.6 | 53.8 | 2.4 | 59.9 |
| M-FR-08 | 62.4 | 85.8 | 53.5 | 0.7 | 72.7 |
| M-FR-09 | 66.3 | 86.0 | 57.0 | 2.8 | 45.0 |
| M-FR-10 | 62.1 | 86.0 | 53.4 | 2.2 | 61.3 |
| M-FR-11 | 66.6 | 87.7 | 58.4 | 1.8 | 67.8 |
| M-FR-12 | 66.0 | 83.9 | 55.4 | 1.7 | 54.8 |
| M-FR-13 | 63.6 | 83.7 | 53.3 | 2.3 | 49.9 |
| M-FR-14 | 61.5 | 82.0 | 50.4 | 2.0 | 58.1 |
| M-FR-15 | 65.9 | 86.1 | 56.8 | 1.2 | 74.6 |
| M-FR-16 | 61.4 | 84.8 | 52.1 | 1.8 | 70.7 |

In addition, results showed a fairly strong correlation between the ILSS of laminates and porosity (Figure 6.18). As expected, laminates featuring more voids tended to have weaker interlaminar strength. However, ILSS is affected by more than porosity alone, and from the raw data it is difficult to identify the role of each of the 4 factors and their interactions. Hence, the large amount of data that was obtained from the experiments was

analysed more thoroughly using statistical tools for design of experiments, more specifically by examining the effect of each contrast [156] i.e. how each contrast changes the response.

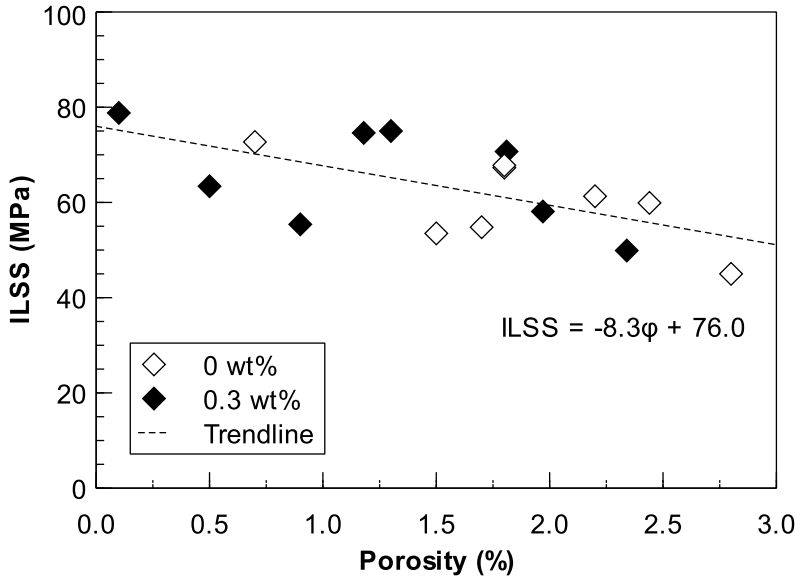


Figure 6.18: Variation of ILSS with porosity for laminates featuring different CNT loadings in experimental programme M-FR

For a 2-level run, the effect of a contrast can be calculated as:

$$Effect = \frac{2}{N}\left[\sum\left(y^{+}\right) - \sum\left(y^{-}\right)\right] \tag{6.1}$$

where $N$ is the number of experiments, $y^{+}$ is a response for a contrast at its high level and $y^{-}$ is a response for a contrast at its low level. For example, the effect of contrast A on porosity is obtained by taking the average porosity of laminates made with NCFs and subtracting the average porosity of laminates made with twills. This procedure was done for every contrast, i.e. factors and interactions, and every response.

The effects of contrasts on the fibre volume fraction inside yarns, $V_{fy}$, appear in Figure 6.19. Several contrasts had comparable contributions to $V_{fy}$, including main factors and interactions between factors. This suggests that the variability that was observed is likely inherent to the out-of-autoclave RFI process and not to the investigated factors, i.e. selection of materials. However, little variation of $V_{fy}$ was observed, less than ± 2%.

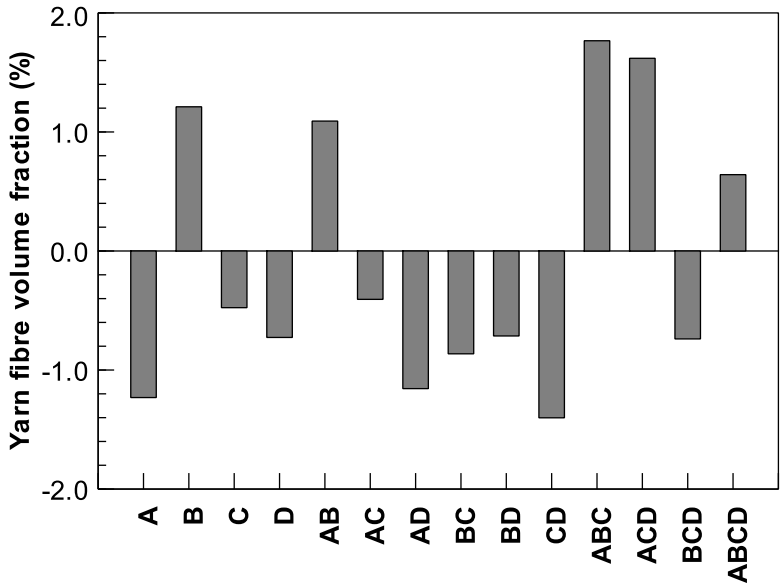


Figure 6.19: Effect of contrasts on the fibre volume fraction $V_{fy}$ in yarns for laminates of experimental programme M-FR

The effects of contrasts on the yarn fraction $V_y$ appear in Figure 6.20. Results showed that factors A and B were the greatest contributors to $V_y$. The use NCFs increased $V_y$ by 1.8% compared with twills, and higher surface density fabrics reduced $V_y$ by 2.2%. These differences are directly related to the geometry of fabrics. For example, undulated yarns in weaves reduce the packing of yarns compared with NCFs. Additionally, in the case of weaves, thinner yarns result in more straight fibres and better packing. However, similarly to $V_{fy}$ the difference in $V_y$ between laminates is small.

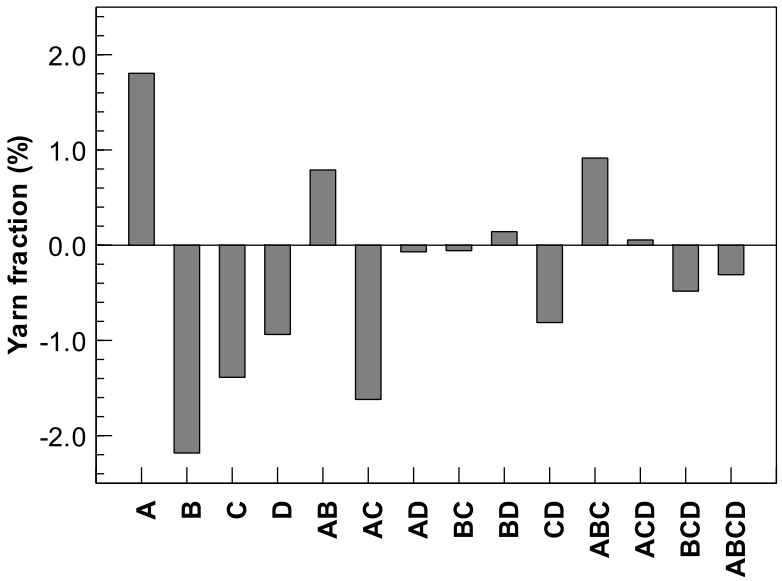


Figure 6.20: Effect of contrasts on the yarn fraction $V_y$ for laminates of experimental programme M-FR

The effects of contrasts on the global fibre volume fraction of laminates $V_f$ appear in Figure 6.21. Considering that $V_f$ was calculated from $V_{fy}$ it is expected that there would be little correlation with any of the main factors. The strongest variations resulted from contrasts composed of the interactions of multiple factors, suggesting that differences are caused likely by the out-of-autoclave RFI process and not the material selection. This is interesting, considering that the type of fabric had a fairly strong influence on the compaction of stacks (Section 5.5). Hence, the presence the resin plays a significant role in the reorganization of the fibre networks in fabrics during RFI.

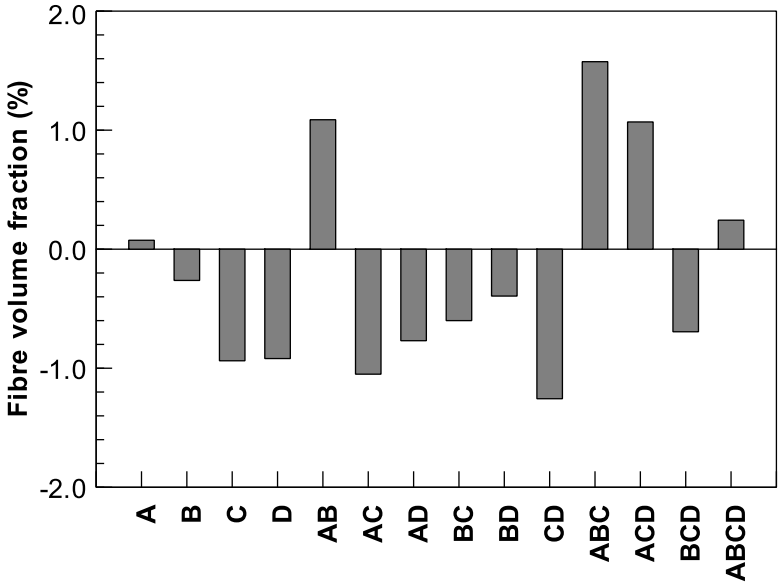


Figure 6.21: Effect of contrasts on the global fibre volume fraction $V_f$ for laminates of experimental programme M-FR

The effects of contrasts on the porosity $V_v$ of laminates appear in Figure 6.22. Results showed that the main factors are the strongest contributor to porosity levels. The greatest source of porosity was the use of resin formulation L9 instead of L7. Potentially, this may be caused by the lower viscosity of formulation L9 which can increase the likelihood of over-bleeding. The CNT loading, fabric architecture and surface density all had a similar contribution to porosity. The addition of CNTs reduced porosity, and this behaviour appears to be attributable to the increase in viscosity. NCFs increased porosity compared to twills while higher surface density fabrics increased porosity. The reasons behind these observations will be investigated in greater details in Chapter 8.

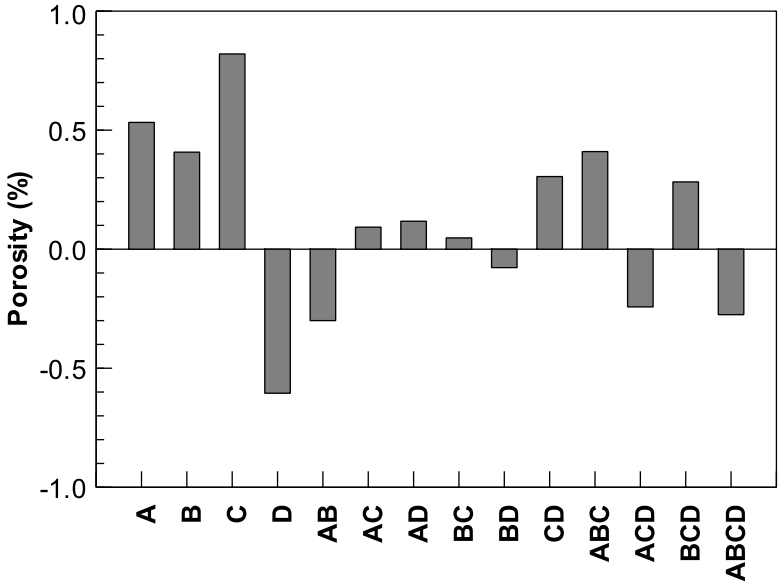


Figure 6.22: Effect of contrasts on the porosity $V_v$ for laminates of experimental programme M-FR

The effects of contrasts on the ILSS of laminates appear in Figure 6.23. Results showed that ILSS was predominantly affected by the main factors. Most importantly, the use of low surface density fabrics brought a clear benefit to the ILSS. This can be linked in part to the lower porosity resulting from such fabrics, but it is not the sole factor given the extent of the improvement. Advantages of thin-ply laminates are discussed in the literature [157, 158] and relate to delayed micro-cracking of the matrix. Weaves improved the ILSS compared with NCFs; this may be due to the higher delamination resistance of woven laminates compared with UD laminates [159]. Resin formulation L7 improved ILSS; this is likely attributable with the lower porosity levels. Finally, the addition of CNTs improved the ILSS slightly. Part of the improvement was linked to the lower porosity, but there was also a small but direct contribution of CNTs as will be discussed in Chapter 9.

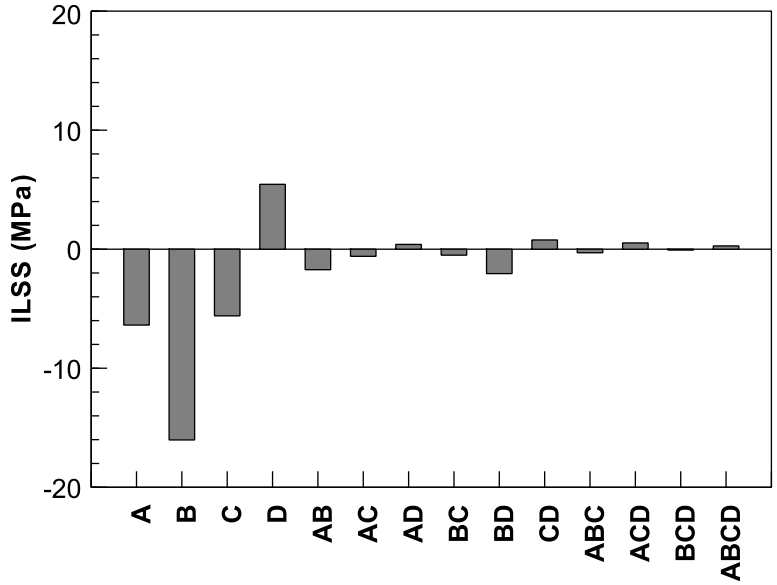


Figure 6.23: Effect of contrasts on the ILSS for laminates of experimental programme M-FR

### 6.6.3 Findings

The multivariate experimental programme M-FR investigated the effect that fabrics, resin formulation and CNT loading have on the fibre volume fraction, porosity and ILSS of laminates. Results showed that material selection played a major role over the porosity and ILSS of laminates but less on their fibre volume fraction. Additionally, porosity was found to be a relatively good metric for the ILSS of laminates. The best combination of materials for low porosity PMCs was a low surface density fabric and a resin having a viscosity that is not too low to prevent over-bleeding. Regarding multi-scale PMCs, results showed that on average the addition of 0.3 wt% of CNTs improved the ILSS by 8.5%.

## 6.7 Remarks

The fabrication and characterisation of flat laminates revealed that PMCs of very different quality can be obtained using out-of-autoclave RFI, depending on processing conditions. It was shown that porosity is a good metric for the interlaminar resistance of PMCs and that it is affected by the:

- Level of resin film interleaving in stacks
- Bagging method
- Selection of resin film and fabric

More specifically, porosity was related to resin viscosity, fabric surface density, CNT loading, level of breathing and bleeding, and the direction of resin flow. Guidelines for making high quality PMC parts can be proposed from these results. For example, PMC parts with low porosity should be made with a relatively high viscosity resin, a low surface density fabric and use of CNTs. However, the inspection of flat laminates did not improve knowledge pertaining to the reasons why these parameters affect quality. Hence, a thorough study of resin flow, void formation and CNT distribution is presented in chapters 7-9 to improve knowledge of RFI processing. Nevertheless, the study of flat laminates was critical for identifying key issues of RFI processing which led to the more focused work of the next chapters.

# Chapter 7

## Kinematics of resin saturation

In Chapter 6, the analysis of flat laminates showed that materials and fabrication methods influence the quality of PMC parts. However the observations did not provide much insight into physical explanation of differences in part quality. It follows that the first step towards improving parts processed using RFI is to understand precisely what happens during material consolidation. This chapter focuses on describing resin saturation kinematics during interleaved and bulk RFI processing, and how fabrics and resins affect infusion. Infusion kinematics are characterised by experimental monitoring of resin flow at the surface of stacks as described in Section 3.3.4. Following experimental results, resin flow is studied further using computer simulations.

The chapter opens on a description of resin flow at room temperature. Then it proceeds with the description of resin flow in interleaved RFI, followed by the description of resin flow in bulk RFI. A discussion of experimental observations is presented before discussing computer simulations. Physical experiments are introduced in Table 7.1. Stacks in experiments made with interleaved RFI bagging configuration I-6 featured a central resin layer and outer fabric layers made of a single fabric ply. Conversely, stacks in experiments made with bulk RFI bagging configuration B-3 featured a resin layer laid over a fabric stack made of several fabric plies resulting in a 4 mm thick laminate upon consolidation.

Table 7.1: List of experiments for the study of kinematics of resin flow

| Experiments | Bagging configuration | Cure Cycle | Resin | Fabric |
|---|---|---|---|---|
| Resin flow at room temperature | I-6 | N/A | SA 70 and LEO 2376 | PW-L |
| Interleaved RFI | I-6 | L-MON | All | All |
| Bulk RFI | B-3 | L-MON | L9 neat and CNTs | All |

## 7.1 Resin flow at room temperature

Under a compaction pressure of 100 kPa, resin squeeze flow was observed with both resins as depicted in Figure 7.1. These results confirm the results of compressive creep experiments presented in Section 4.8, which suggested that resin films behave mostly as viscous fluids at room temperature.


Figure 7.1: Evolution of the resin squeeze flow around fabric PW-L at room temperature for LEO 2376 resin

The evolution of the fill factor *FF* (Figure 7.2) showed that the resins impregnated the inter-yarn regions very slowly and that the filling rates decreased significantly with time, preventing any significant intra-yarn infusion. Moreover, increase in *FF* slowed

markedly in the range of *FF* of 0.4 to 0.5, highlighting the higher resistance to viscous flow of yarns compared to inter-yarn gaps. Results also showed that at room temperature, pre-preg resin SA 70 displayed lower viscosity than infusion resin LEO 2376, which is consistent with viscosity data (Section 3.3.1.3). Despite viscous flow, high resin viscosity prevents any practical infusion without any heating and may explain the absence of significant resin flow during the pre-compaction experiments in Section 5.8, which featured short compaction cycles.

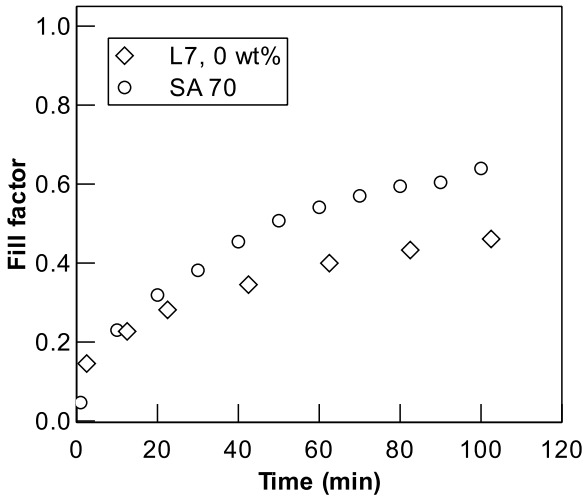


Figure 7.2: Fill factor progression for resins LEO 2376 and SA 70 through fabric PW-L at room temperature

## 7.2 Resin flow in interleaved RFI laminates

### 7.2.1 Observations

Experiments conducted on interleaved stacks showed that all tested combinations of fabrics and resins followed similar infusion kinematics when subjected to a standard cure temperature profile (Figure 7.3). Resin flowed first in gaps around yarns and stitches where permeability was greatest. Flow fronts were generally uniform. After saturating inter-yarn regions, resin began filling yarns predominantly along the fibre direction in accordance

with observations made by Cender et al. [73] who tested semi-preg materials at constant temperatures.

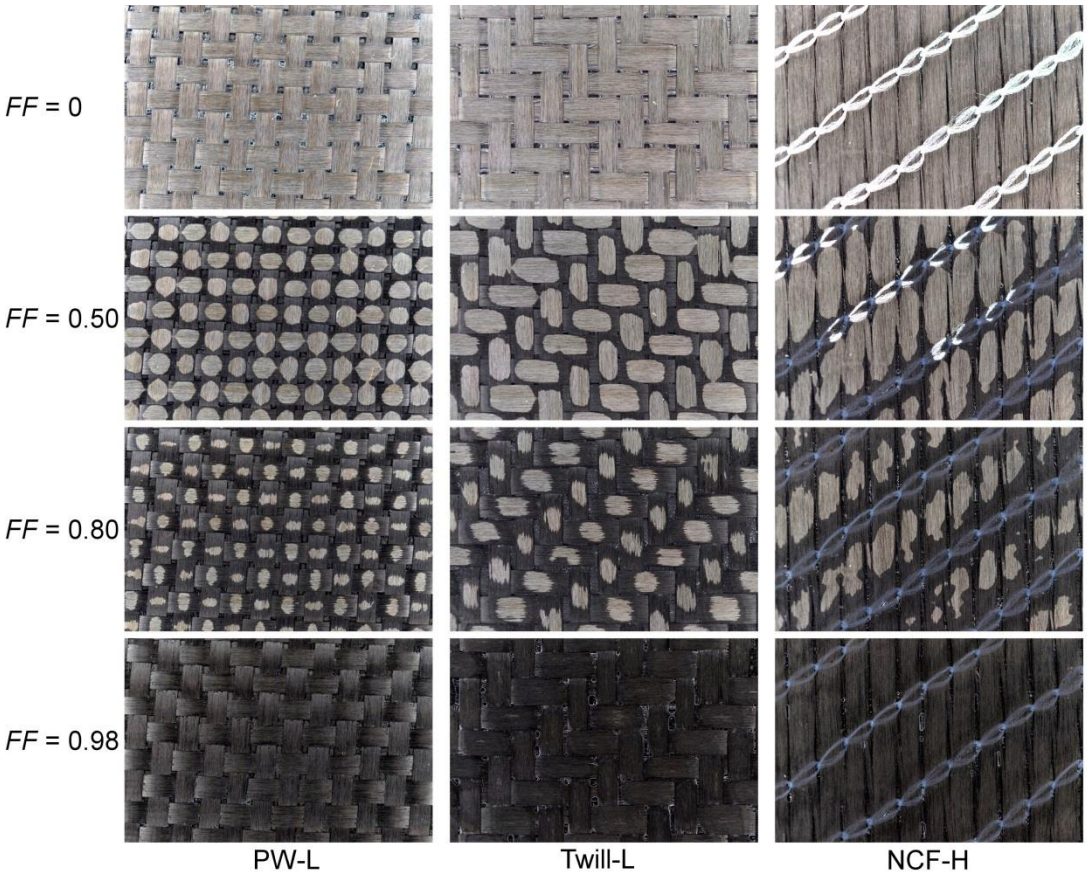


Figure 7.3: Typical resin flow through plain weave, twill and non-crimp fabrics for interleaved RFI

Evolution of *FF* was qualitatively similar for the various combinations of fabrics and resins tested. A typical *FF* curve appears in Figure 7.4. At the beginning of the cure cycle, high resin viscosity limited flow. As the temperature increased resin viscosity lowered, enabling rapid filling of inter-yarn gaps, and then of yarns. *FF* increased at a mostly constant rate up to a value of at least 0.90. It is conjectured that the absence of strong transitions in filling rates observed, despite significant differences in permeability between

yarns and surrounding regions, is attributable to ever-decreasing resin viscosity during the heating phase which promoted resin flow.

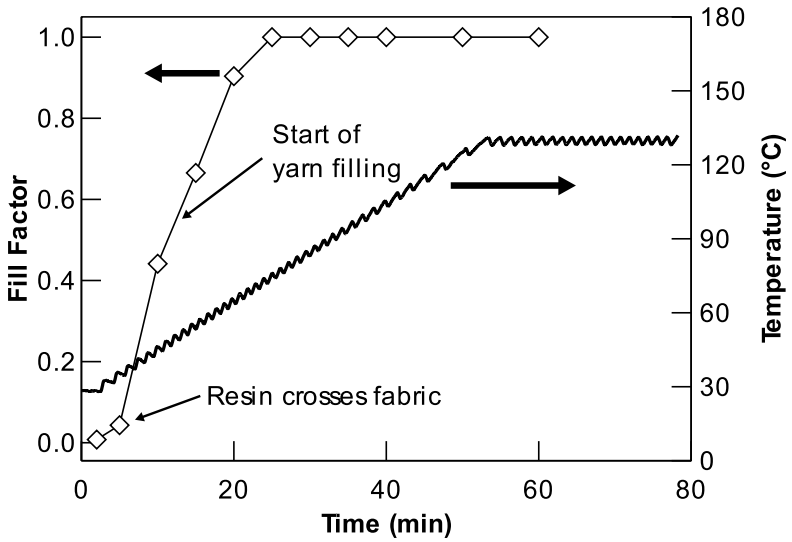


Figure 7.4: Typical fill factor and temperature progression during a standard cure cycle using interleaved RFI (depiction of Twill-H, LEO 2376)

### 7.2.2 Saturation times

Results for total saturation time are presented, followed by those for inter-yarn saturation and yarn saturation.

#### 7.2.2.1 Total saturation times

Total saturation times within a single fabric layer varied from 18 min to more than 50 min for all combinations of fabrics and resin films tested (Figure 7.5). In most cases, saturation was achieved well before dwell temperatures were reached. Resin type had the greatest effect on the total saturation time. Pre-preg resin SA 70 led to the longest saturation times and complete yarn saturation of the thickest fabric (NCF-H) could not be achieved before gelation: infusion stopped at *FF* of 0.93. The addition of 0.3 wt% of CNTs to resin formulations L7 and L9 increased saturation times. These results were consistent with measured resin viscosity profiles. Fabrics also affected the total saturation time. The

lower cover factor of fabric PW-L led to lower saturation times than observed with fabric Twill-L of similar surface density (Figure 7.5a). Total saturation times increased with fabric surface density (Figure 7.5b).

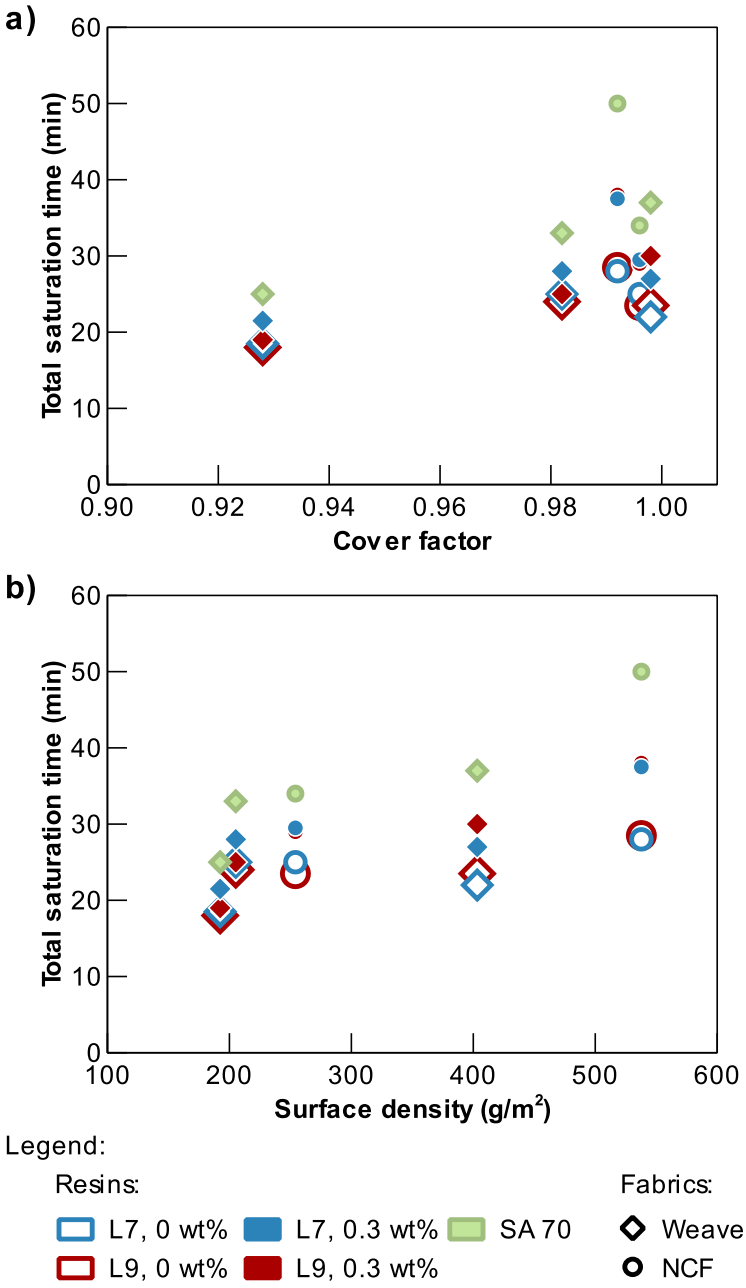


Figure 7.5: Total saturation time for interleaved RFI based on a) cover factor and b) surface density

#### 7.2.2.2 Inter-yarn saturation times

Inter-yarn saturation times (Figure 7.6) varied between 7 min and 19 min. Here again, resin formulation affected saturation times and the addition of CNTs lengthened saturation times. Pre-preg resin SA 70 led to saturation times comparable with those of neat infusion resins because its viscosity (Section 4.5) near room temperature is similar to that of LEO resins. This behavior is also consistent with flow experiments performed at room temperature (Section 7.1).

Figure 7.6a shows that saturation times of inter-yarn gaps increased with a reduction in cover factor, as depicted by the noticeably lower saturation times achieved with fabric PW-L compared with other woven fabrics. Hence, having a tighter yarn network increased flow resistance and delayed infusion. No notable effect of the fabric surface density on inter-yarn saturation time was observed (Figure 7.6b). Both NCFs led to similar inter-yarn saturation times whereas saturation of Twill-H was marginally faster than for Twill-L. These results also showed that saturation times were not linearly proportional to permeability values. However, when factoring the increased flow lengths associated with thicker fabrics based on the modified Darcy's law (Eqn. 2.2), results followed the trends of permeability values. It follows that the size and number of inter-yarn gaps were much more important than through-thickness infusion distances for controlling the saturation of inter-yarn gaps in interleaved RFI.

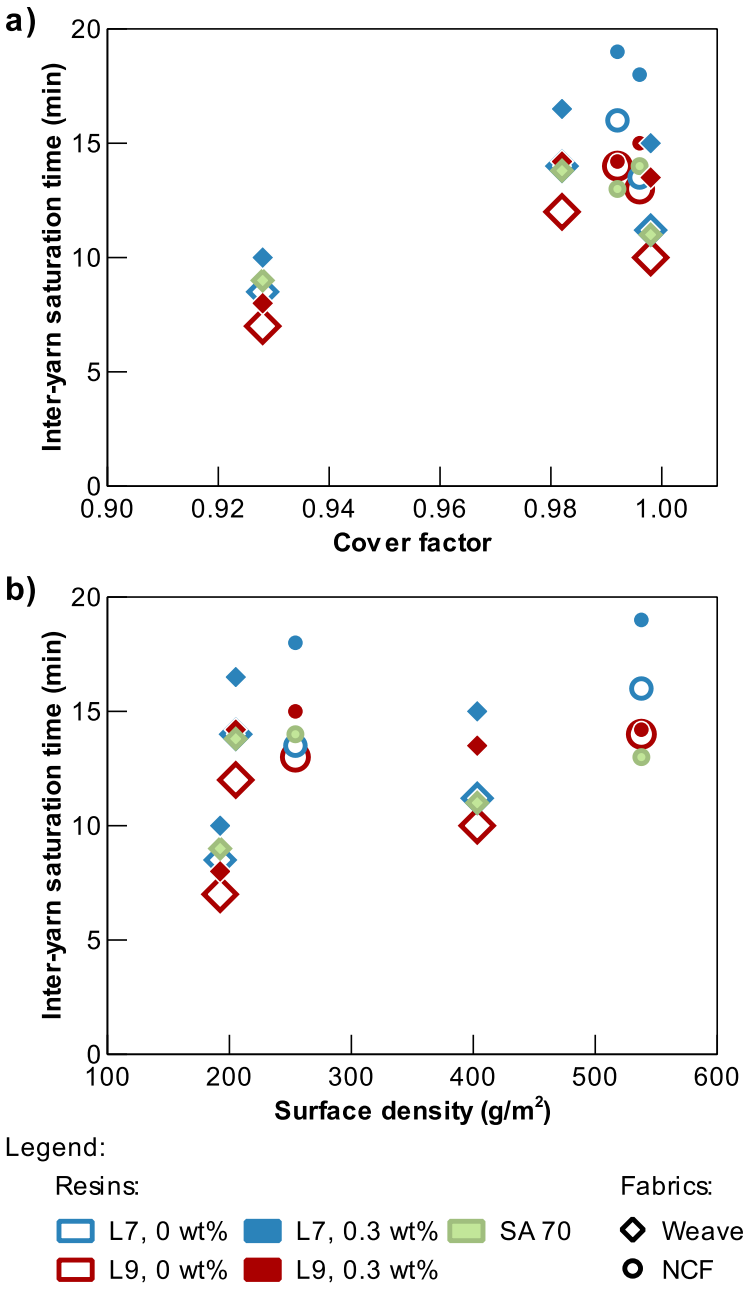


Figure 7.6: Inter-yarn saturation time for interleaved RFI based on a) cover factor and b) surface density

#### 7.2.2.3 Yarn saturation times

Yarn saturation time (Figure 7.7) varied between 4 min and 20 min. Resin formulation and CNT loading affected saturation time. Unlike saturation of inter-yarn gaps, pre-preg resin SA 70 returned the longest yarn saturation time, surpassing even those observed with resins loaded with CNTs. This was expected as viscosity of infusion resins lowers faster with increasing temperature than that of SA 70 resin, and because of the lower surface tension of SA 70 which reduces capillary pressure and flow. In the case of fabric parameters, results (Figure 7.7a) did not show any influence of the fabric cover factor and permeability, which was expected as these properties do not affect the geometry of the yarns. Conversely, strong correlation between yarn saturation time and fabric surface density was observed (Figure 7.7b). Saturation time increased linearly with the fabric surface density, at least for resins offering the longest times to saturation. It is important to note that this trend was observed with a hot-melt resin wherein resin viscosity decreased with cycle temperature/time, hence the results can only lead to the conclusion that bigger yarns required longer saturation times and that the trend is typically non-linear for a constant viscosity fluid. Interestingly, yarn saturation times were not affected significantly by different yarn float lengths and spacing between stitches (Section 5.2). This suggests that longitudinal infusion distances within a yarn have minimal impact over yarn saturation time compared to the yarn thickness, which is proportional to the fabric surface density. Thus, there is strong contribution of transverse resin flow during yarn filling.

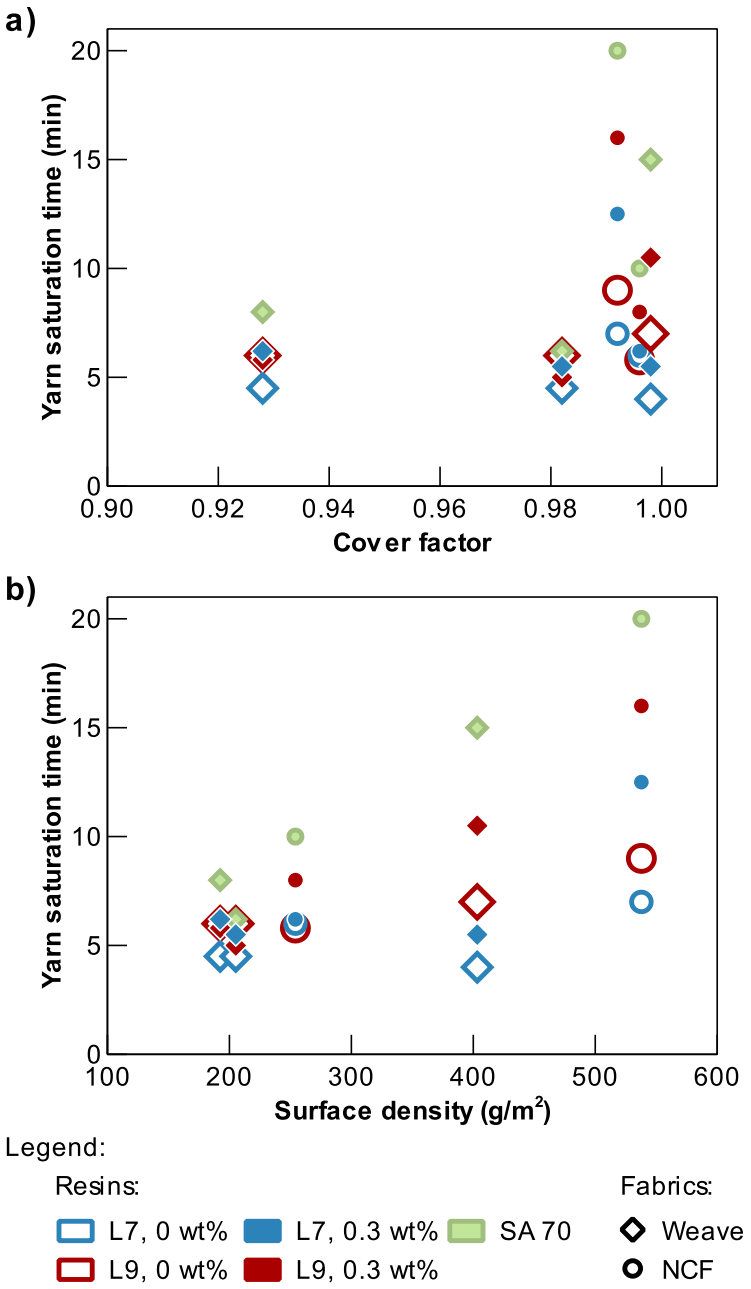


Figure 7.7: Yarn saturation time for interleaved RFI based on a) cover factor and b) surface density

## 7.3 Resin flow in bulk RFI laminates

### 7.3.1 Observations

Similar to interleaved RFI, resin in fabric stacks flowed around yarns before saturating them during bulk RFI. However, a notable distinction from the interleaved stacking configuration was that flow fronts were no longer uniform (Figure 7.8); the stacking of multiple fabric plies amplified the effect of local fabric heterogeneity on flow.

Another distinction is that in some cases bulk RFI affected the type of resin flow. In experiments featuring fabric NCF-L, the initial resin arrival at the surface of the stack occurred through capillary flow, mostly through stitches but also across yarns (Figure 7.9). This behaviour was observed with fabric NFC-L because of its low permeability compared to other fabrics (Section 5.4) that restricts inter-yarn flow significantly. In addition, resin viscosities are lower at the end of saturation in bulk RFI compared with interleaved RFI which decreases the ratio of viscous forces to capillary forces. It is interesting to note that capillary flow was more noticeable with the resin loaded with CNTs despite its higher viscosity. The increased capillary flow can be explained by CNTs piling-up in inter-yarn gaps and restricting resin flow, similarly to CNT clusters blocking inter-fibre gaps as noted by Fan et al. [16].

Even though the onset of capillary flow was observed in some experiments, it is important to note that in all cases, inter-yarn gaps were saturated before yarns.

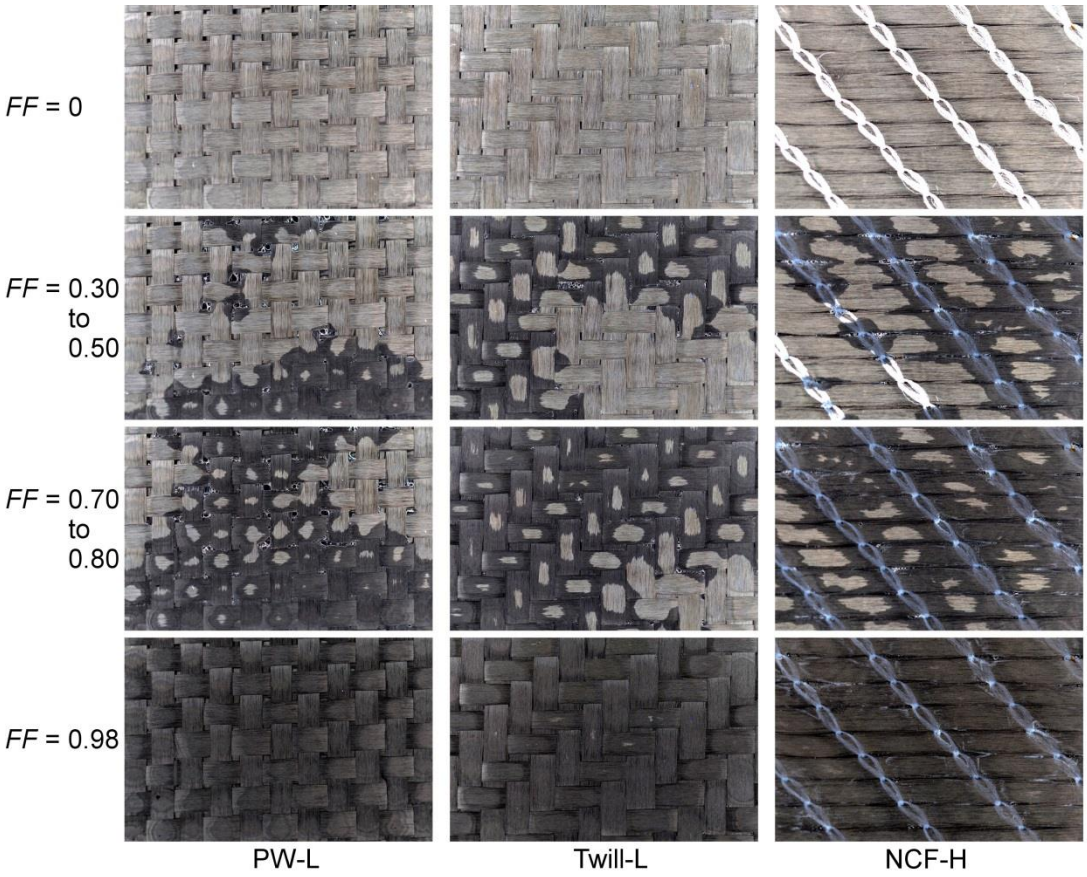


Figure 7.8: Typical resin flow in plain weave, twill and non-crimp fabrics for bulk RFI

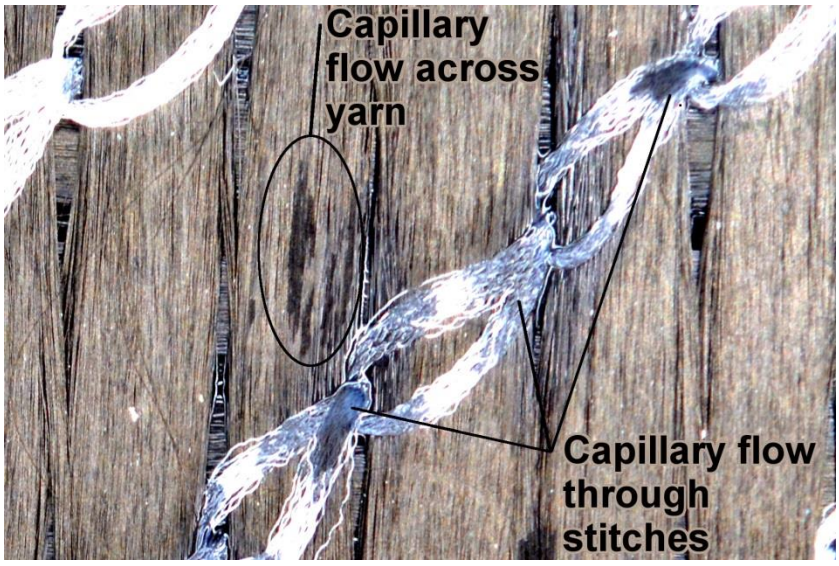


Figure 7.9: Capillary resin flow across stitches and yarns in fabric NCF-L for bulk RFI

Evolution of *FF* with the bulk stacking configuration was qualitatively similar for all combinations of fabrics and resins. A typical curve appears in Figure 7.10. There was an initial delay between the start of an experiment and the moment of resin arrival at the surface of the stack. During this time, resin infused through the first fabric plies and resin temperature increased. When resin arrived at the surface of the stack it started saturating the fabric ply at a much quicker rate than for the interleaved stacking configuration. The saturation rate of the surface of the stack was nearly constant despite differences between the permeability of inter-yarn gaps and yarns. This was caused by the non-uniform flow fronts in bulk RFI that resulted in the simultaneous saturation of inter-yarn gaps and yarns.

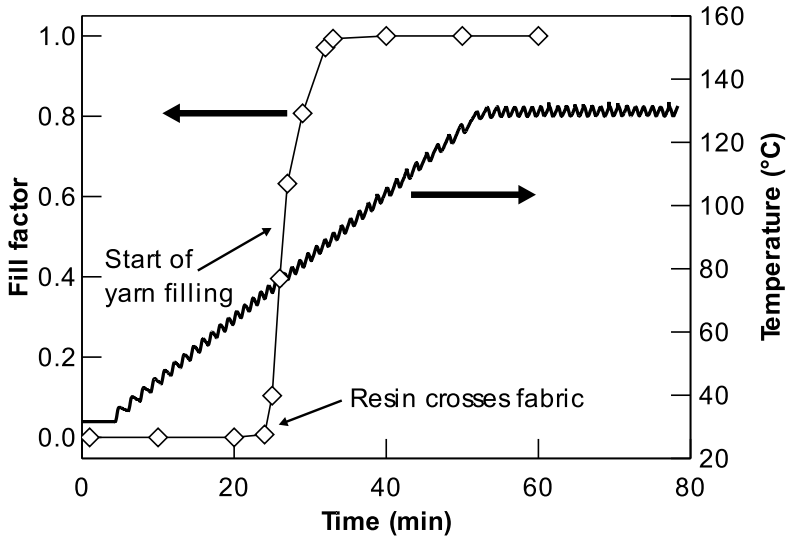


Figure 7.10: Typical fill factor and temperature progression during a standard cure cycle using bulk RFI (depiction of Twill-H fabric and resin LEO 2396)

### 7.3.2 Saturation times

Results for the total saturation times are presented, followed by those for the surface ply saturation, inter-yarn saturation and yarn saturation.

#### 7.3.2.1 Total saturation times

Total saturation times for stacks varied between 32 min and 58 min (Figure 7.11) and saturation occurred well before resin gelation. Saturation times were not significantly longer than those observed with interleaved RFI despite greater flow lengths. This is caused by the great reduction in resin viscosity that occurs during RFI processing (Section 4.5).

As expected, the higher resin viscosity imparted by CNTs increased the saturation times markedly (Figure 7.11). On average, adding 0.3 wt% of CNTs to resins increased total saturation times by 19%. For fabrics, no marked effect of the fabric cover factor was identified (Figure 7.11a). An increase in fabric surface density reduced saturation times (Figure 7.11b). This occurs because lower surface density fabrics require more fabric plies for achieving the desired laminate thickness than higher surface density fabrics, making flow more tortuous and increasing flow lengths (Figure 7.12). For similar surface densities, NCFs resulted in longer saturation times than weaves (Figure 7.11b). This is caused by larger inter-yarn gaps in weaves compared with NCFs due to the interlacing. The effects of both the surface density and fabric architecture on the saturation times are consistent with the transverse permeability values of fabrics (Section 5.4).

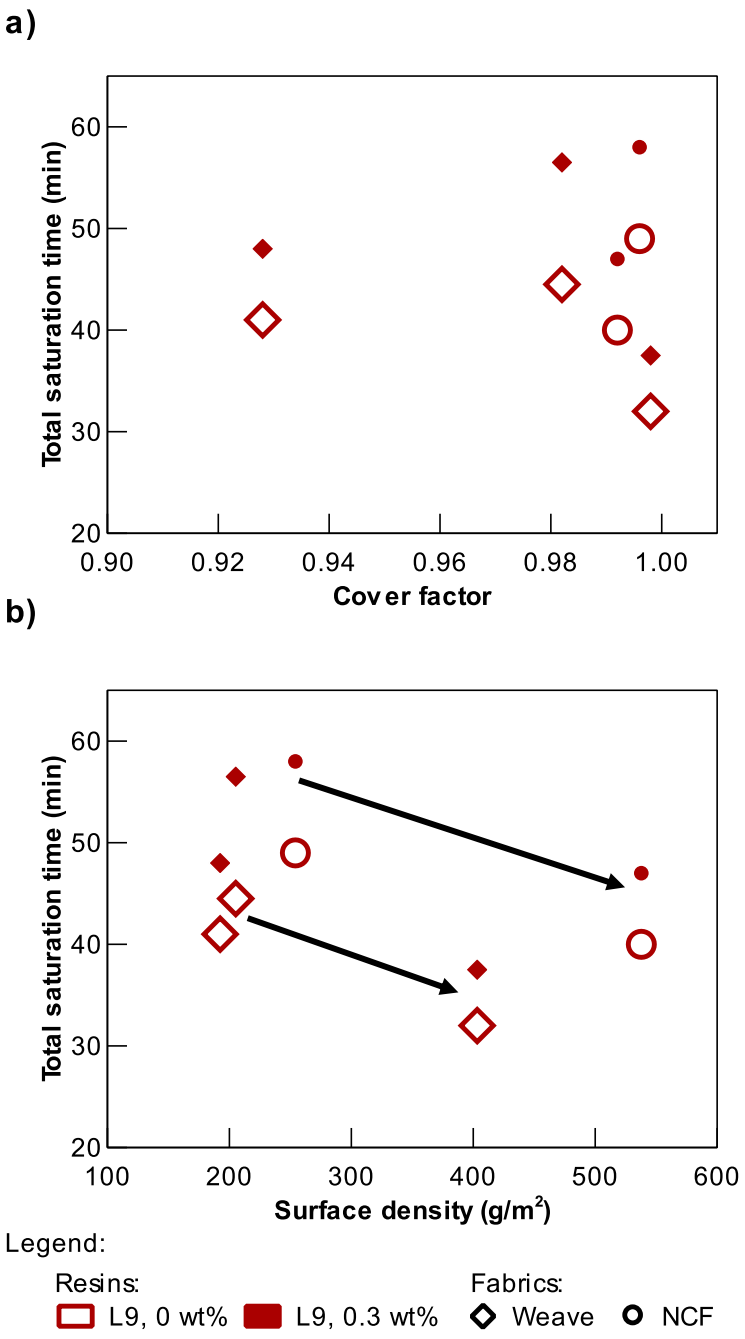


Figure 7.11: Total saturation time for bulk RFI based on a) cover factor and b) surface density

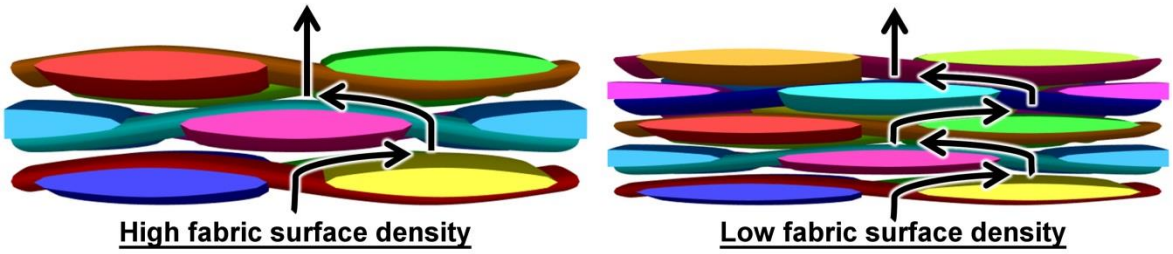


Figure 7.12: Effect of fabric surface density on resin flow tortuosity

#### 7.3.2.2 Surface ply saturation times

The time for saturating the surface ply, i.e. last ply of the stack, varied between 2 min and 9 min (Figure 7.13), which was 6 to 9 times faster than for interleaved RFI. No marked effect of the fabric cover factor was identified (Figure 7.13a). Conversely, saturation times increased significantly with fabric surface density (Figure 7.13b). This was caused mainly by differences in resin viscosity during saturation of the surface ply. Differences in viscosity occurred because resin reaches the surface ply at a higher temperature when travelling across stacks of low surface density fabrics than across stacks of high surface density fabrics.

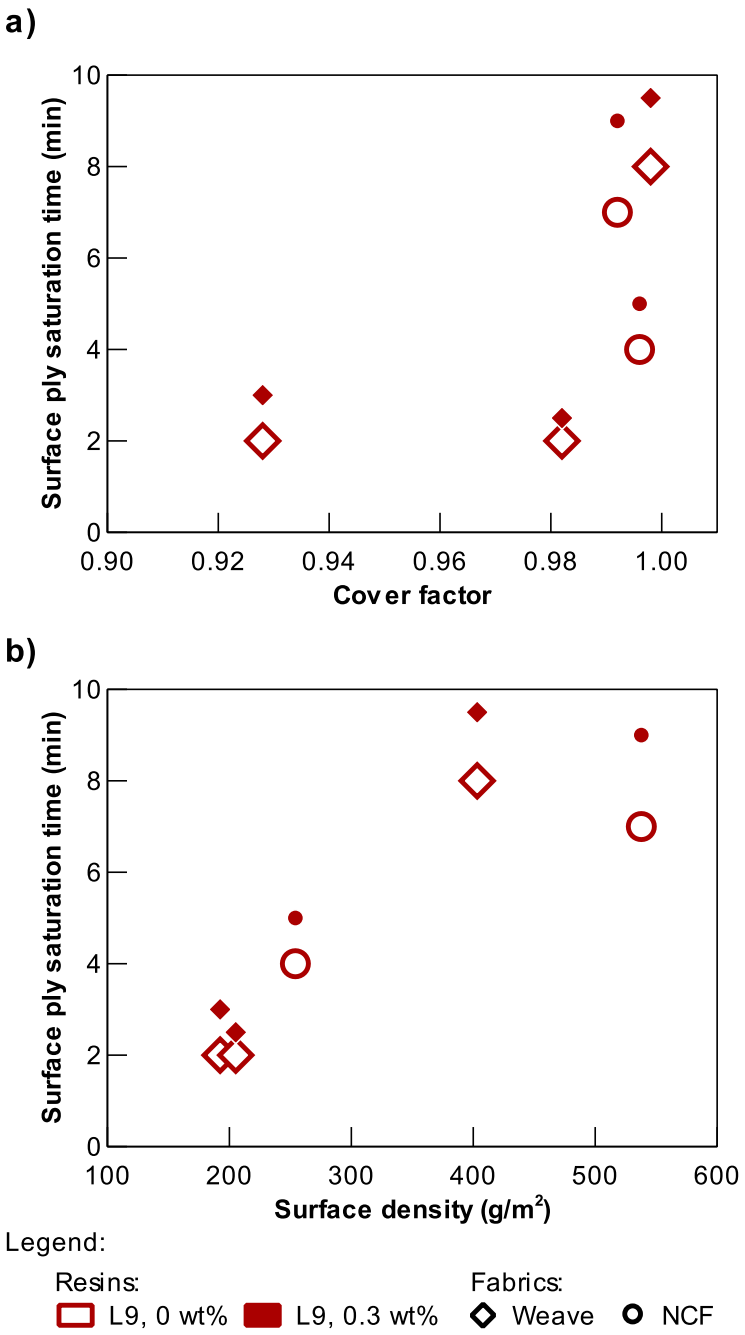


Figure 7.13: Surface ply saturation time for bulk RFI based on a) cover factor and b) surface density

#### 7.3.2.3 Inter-yarn and yarn saturation times

Values for inter-yarn saturation times and yarn saturation times appear in Figures 7.14 and 7.15, respectively. Unfortunately, no reliable characterisation could be made due to the non-uniform flow fronts in bulk RFI. In both cases, saturation times related to mixed flow, i.e. simultaneous flow in and around yarns, leading to trends of saturation times that were similar to those obtained for surface ply saturation (Figure 7.13); saturation times were not affected by the cover factor but increased with increasing fabric surface density.

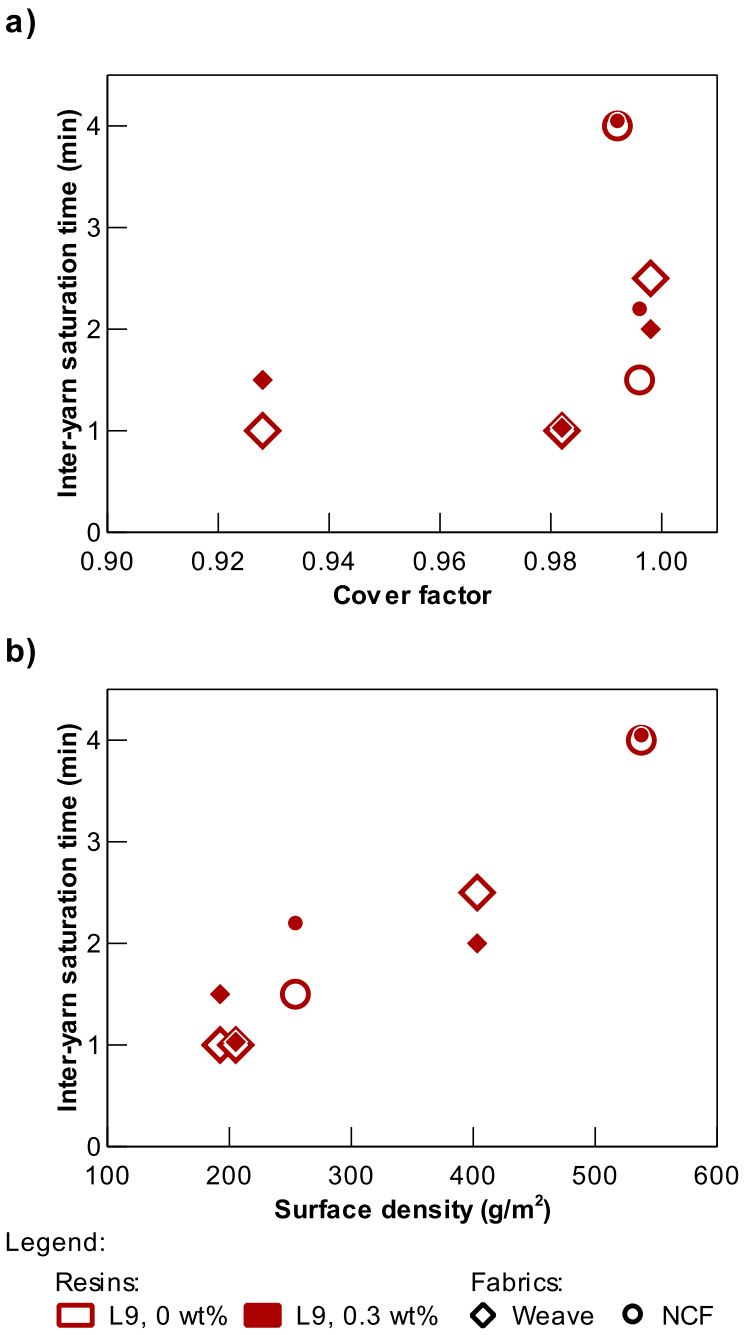


Figure 7.14: Inter-yarn saturation time for interleaved RFI based on a) cover factor and b) surface density

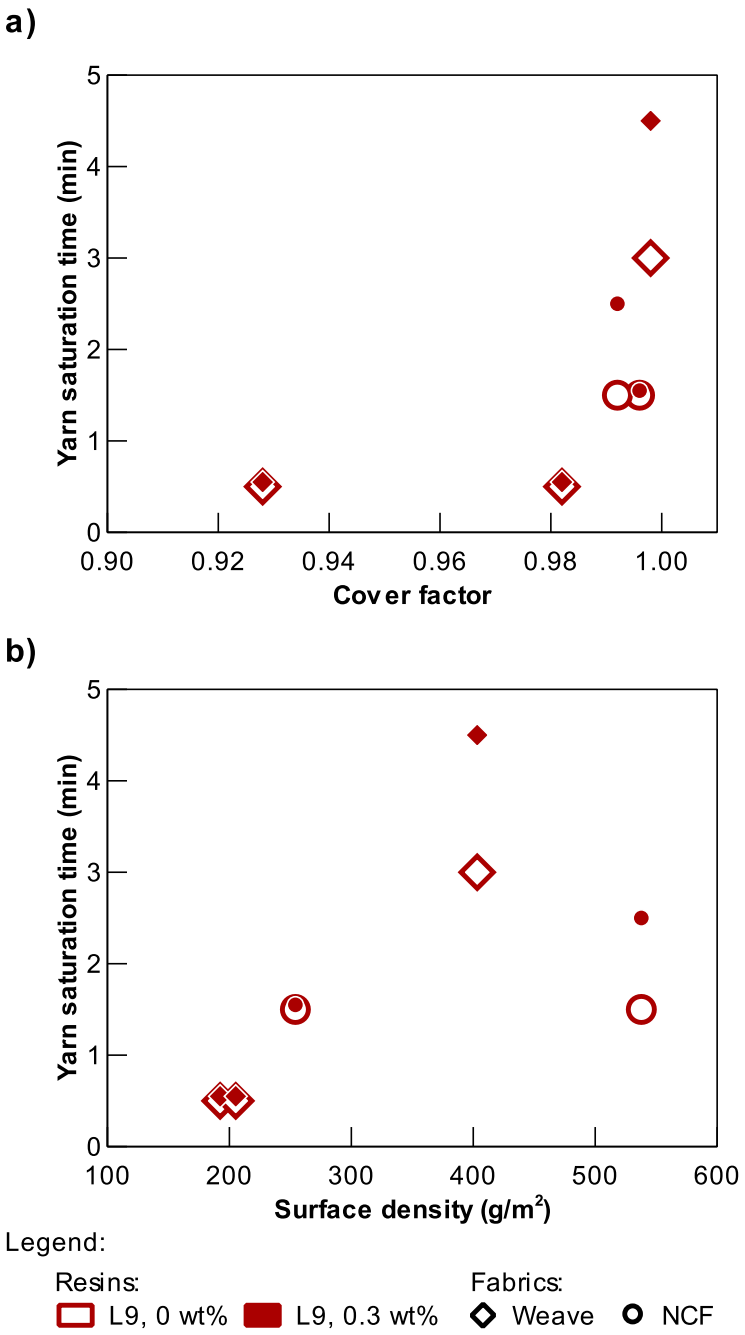


Figure 7.15: Yarn saturation time for interleaved RFI based on a) cover factor and b) surface density

## 7.4 Discussion of physical experiments on resin flow

Resin flow experiments confirmed that despite their high viscosity, semi-solid resin films undergo squeeze flow upon compaction at room temperature. Considering the high viscosity of resin films at room temperature, viscous forces will be much higher than capillary forces. This suggests that the initial resin flow in RFI will always be governed by viscous forces irrespective of the fabric type, unless little to no compaction pressure is applied. This means that resin will be forced in inter-yarn gaps first where flow resistance is lowest, before flowing inside yarns. Hence, processing of laminates featuring short infusion distances will always result in resin flow dominated by viscous forces.

As manufacturing proceeds, resin viscosity decreases drastically which increases the rate at which fabrics are saturated with resin. Results showed that this major increase in resin flow velocity led to similar saturation times between interleaved and bulk RFI. It follows that in the case of flat and relatively thin laminates, the use of bulk RFI does not lengthen processing times markedly compared to the use of interleaved RFI.

Processing parameters affected the type of resin flow in RFI. Wicking of resin during saturation of fabrics was only observed with bulk RFI and not with interleaved RFI. From the capillary number $Ca^*$ (Eqn. 2.5), the ratio of capillary to viscous forces increases with increasing resin surface tension, and decreasing contact angle, flow velocity and resin viscosity. It is expected that the contribution of the surface tension and contact angle to the occurrence of capillary flow was limited because these properties vary little with changes in temperature and degree of cure [50, 53, 160]. Resin flow velocity did not affect the occurrence of capillary flow between bulk RFI and interleaved RFI experiments. This is because resin flow velocities at the surface of stacks were faster in bulk RFI due to the great reduction in resin viscosity during processing. From the process of elimination, it is clear that the reduction in resin viscosity was the main factor leading to capillary flow. It follows that in RFI, resin flow occurring later in the processing cycle is more likely to be driven by capillary forces. Hence, for low viscosity resins, processing conditions leading to long saturation times such as stacking configurations featuring great flow lengths and the use of very low permeability fabric stacks will result in a transition from viscous to capillary flow.

Resin flow behaviour is also highly dependent on the dual-scale architecture of fabrics. Experiments showed that an increase in cover factor reduces flow across inter-yarn gaps markedly in a single layer of fabric. This behaviour can be explained by the Darcy-Weisbach equation, i.e. head loss calculations for laminar flow, which states that the pressure drop in a closed channel is equal to [161]:

$$\frac{dP}{dz} = \frac{32\mu}{D_H^{\,2}} v_z \tag{7.1}$$

where $D_H$ is the hydraulic diameter. From Eqns. 2.2 and 7.1, it follows that the permeability is proportional to the square of the channel width. Comparing the linear cover factor of fabrics PW-L and Twill-L, two weaves with similar surface densities but different cover factors, it can be seen that the average channel width at the narrowest point is 2.4 times larger for PW-L than it is for Twill-L. Eqn. 7.1 indicates that this would result in a permeability value that is 5.5 times higher, which is close to the factor of 4.5 times obtained for the transverse permeability values for those fabrics (Section 5.4). Thus, the importance of the fabric cover factor in RFI is reflected in both the saturation times and permeability results.

In bulk RFI, resin flow and saturation of inter-yarn gaps is further impeded by stacking multiple fabric plies together. Any misalignment between contiguous fabric plies results in misalignment of inter-yarn gaps, leading to a more tortuous flow. Tortuosity also increases with decreasing fabric thickness as it increases the number of plies required for achieving a targeted part thickness.

Local misalignment of contiguous plies varies substantially within a stack, leading to variations in local permeability. In relatively thick fabric stacks, the effects of these variations on resin flow superpose. Hence, bulk RFI processing will almost always lead to uneven flow, as seen in Figure 7.8.

Qualitative in-situ observation of RFI suggested that resin flow in yarns occurred mainly along fibre direction (sections 7.2.1-7.3.1), which was also noted by Cender et al. [73]. This observation is attributed to the much higher flow permeability along fibres than across fibres [153]. However, quantitative analysis revealed that the float length of yarns

and the spacing between stitches had little influence on yarn saturation times compared to the effect of yarn thickness. This indicates that yarn saturation is governed mainly by transverse flow across fibres and not longitudinal flow. This occurs because complete yarn saturation requires resin to flow across fibres, which is the least permeable flow direction, to reach the core of the yarns.

From the in-situ observation of RFI, it follows that the most important fabric parameter governing resin flow is the surface density. As discussed above, it affects both the inter-yarn and yarn saturation because it has a strong influence on tortuosity, and flow lengths in yarns. Hence, the design of a RFI process needs to account for the effect the fabric surface density.

Experiments have demonstrated that the use of a homogeneous permeability value does not provide an accurate representation of resin flow for RFI processing. Resin flow velocities around and inside yarns differ substantially, and inter-yarn permeability varies locally as observed during experiments featuring the bulk RFI stacking configuration. These local variations in resin flow velocity may result in partial saturation of composite parts as they do for LCM processes [162–167]. Thus, a holistic approach to the design of RFI processing must include the dual-scale architecture of fabrics to ensure proper material selection towards mitigating risks of processing defects.

## 7.5 Study of resin flow using computer simulations

The monitoring of resin flow in RFI at the surface of stacks showed that the fabric cover factor and surface density play a significant role in determining the kinematics of resin saturation. However, the extent of their influence on saturation could not be quantified due to changing resin viscosity during processing. These parameters were studied individually through computer simulations with 3D and 2D models. Details of the simulations are discussed in Section 3.5.

In this section, 3 relationships between stack parameters and 2 fabric parameters are presented:

1. Fabric cover factor on the through-thickness ply permeability.
2. Fabric surface density on the through-thickness stack permeability
3. Fabric surface density on the yarn saturation time.

All simulations used a plain weave model. Specific geometric parameters of the 3D models of the weave used for the simulations of the ply and stack permeability values appear in Table 7.2 while those for the 2D models of the weaves used for the yarn filling time appear in Table 7.3.

Table 7.2: Geometric description of 3D models used for calculating ply and stack permeability values

| Group | Model | # of layers | Spacing (mm) | Yarn width (mm) | Ply thickness (mm) | Surface density[a] ($g/m^2$) | $CF_x$ | $CF$ | Ply overlap |
|---|---|---|---|---|---|---|---|---|---|
| Ply permeability | FCF-01 | 1 | 2 | 1.8 | 0.4 | 400 | 0.9 | 0.99 | N/A |
| | FCF-02 | 1 | 2 | 1.6 | 0.4 | 400 | 0.8 | 0.96 | N/A |
| | FCF-03 | 1 | 2 | 1.2 | 0.4 | 400 | 0.6 | 0.84 | N/A |
| | FCF-04 | 1 | 2 | 1.0 | 0.4 | 400 | 0.5 | 0.75 | N/A |
| | FCF-05 | 1 | 2 | 0.5 | 0.4 | 400 | 0.25 | 0.44 | N/A |
| Stack permeability | FSP-01 | 1 | 2 | 1.6 | 1.6 | 1600 | 0.8 | 0.96 | Aligned |
| | FSP-02 | 2 | 2 | 1.6 | 0.8 | 800 | 0.8 | 0.96 | Aligned |
| | FSP-03 | 4 | 2 | 1.6 | 0.4 | 400 | 0.8 | 0.96 | Aligned |
| | FSP-04 | 8 | 2 | 1.6 | 0.2 | 200 | 0.8 | 0.96 | Aligned |
| | FSP-05 | 2 | 2 | 1.6 | 1.6 | 1600 | 0.8 | 0.96 | Staggered |
| | FSP-06 | 2 | 2 | 1.6 | 0.8 | 800 | 0.8 | 0.96 | Staggered |
| | FSP-07 | 4 | 2 | 1.6 | 0.4 | 400 | 0.8 | 0.96 | Staggered |

Note: [a] Approximate surface density values based on ply thickness and fabric PW-L geometry

Table 7.3: Geometric description of 2D models used for calculating yarn saturation times

| Group | Model | # of layers | Spacing (mm) | Yarn width (mm) | Ply thickness (mm) | Surface density[a] ($g/m^2$) | $CF_x$ | CF | Ply overlap |
|---|---|---|---|---|---|---|---|---|---|
| Yarn saturation: Interleaved RFI | IY-01 | 1 | 2 | 1.6 | 0.2 | 200 | 0.8 | 0.96 | N/A |
| | IY-02 | 1 | 2 | 1.6 | 0.4 | 400 | 0.8 | 0.96 | N/A |
| | IY-03 | 1 | 2 | 1.6 | 0.8 | 800 | 0.8 | 0.96 | N/A |
| | IY-04 | 1 | 2 | 1.6 | 1.6 | 1600 | 0.8 | 0.96 | N/A |
| Yarn saturation: Bulk RFI | BY-01 | 1 | 2 | 1.6 | 0.2 | 200 | 0.8 | 0.96 | Aligned |
| | BY-02 | 1 | 2 | 1.6 | 0.4 | 400 | 0.8 | 0.96 | Aligned |
| | BY-03 | 1 | 2 | 1.6 | 0.8 | 800 | 0.8 | 0.96 | Aligned |
| | BY-04 | 1 | 2 | 1.6 | 1.6 | 1600 | 0.8 | 0.96 | Aligned |

Note: [a] Approximate surface density values based on ply thickness and fabric PW-L geometry

### 7.5.1 Ply permeability based on the cover factor

The effect of the fabric cover factor on the ply through-thickness permeability was studied by varying the yarn width from 0.5 mm to 1.8 mm while keeping a constant yarn spacing of 2 mm.

Permeability values for different linear and total cover factors are presented in Figure 7.16. In the case of linear cover factors varying from 0.25 to 0.90, permeability values ranged from $2\times10^{-8}$ $m^2$ to $5\times10^{-11}$ $m^2$. Results showed that fabric permeability decreases significantly with an increase in cover factor. This behaviour relates directly to observations made during experimental work on RFI processing as the most opened fabric, fabric PW-L, provided the shortest ply saturation times.

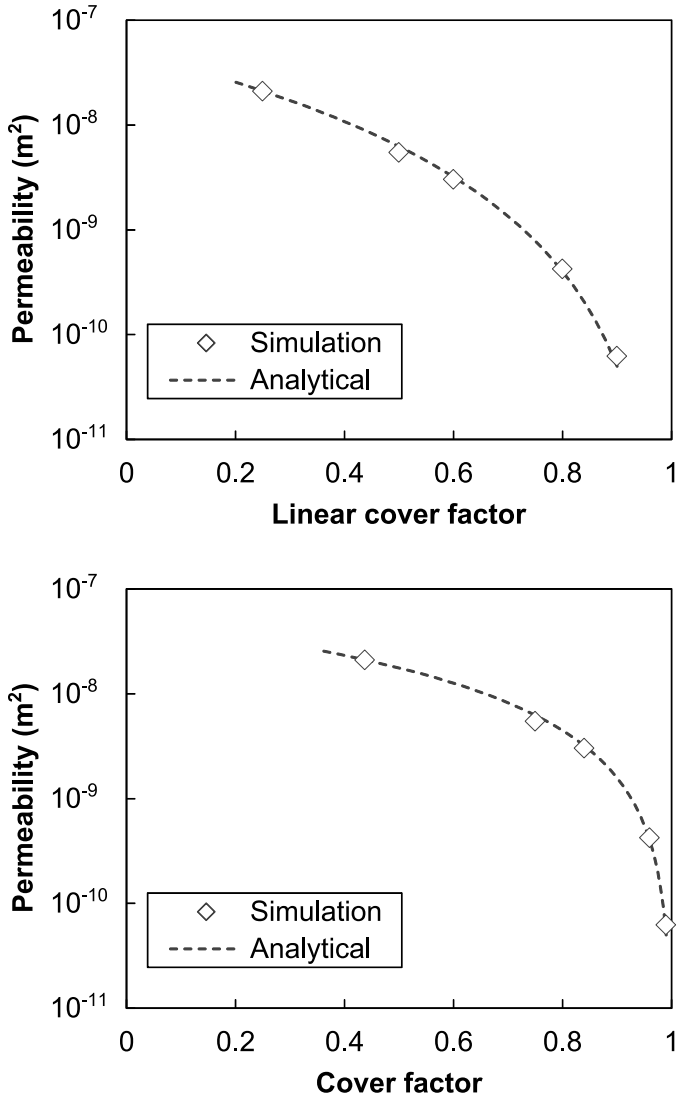


Figure 7.16: Simulation and analytical results for the through-thickness permeability of a plain weave based on fabric linear cover factor and total cover factor

An analytical model was used for estimating the change in ply permeability due to a variation in fabric cover factor. This model is based on the work of Kulichenko [168] who developed an analytical model for calculating the through-thickness permeability of woven fabrics based on the Poiseuille and Weisbach-Darcy's equations. The author proposed the following equation for the through-thickness permeability $K_z$, based on the fabric hydraulic diameter $d_h$ and gap porosity $\phi_g$ :

$$K_z = \frac{d_h^2 \phi_g}{80} \tag{7.2}$$

For a weave with identical width and spacing for the warp and weft yarns, the largest gap enabling much of the through-thickness flow in a single layer is equivalent to a square area having a side length equal to the inter-yarn spacing. Assuming that yarns are considerably wider than they are thick, and that most pressure losses occur through this gap, the equivalent hydraulic diameter would be equal to:

$$d_h = d_s \left(1 - CF_x\right) \tag{7.3}$$

where $d_s$ is the yarn spacing and $CF_x$ is the linear cover factor.

The gap porosity $\phi_g$ is equal to the opposite of the yarn fraction $V_{fy}$ ($\phi_g$ = 1- $V_{fy}$). Assuming a worst case scenario, the gap would be related to the smallest gap between yarns, and calculated from the linear cover factor as follows:

$$\phi_g = \left(1 - CF_x\right) \tag{7.4}$$

Combining equations 7.1-7.3, an equation for the through-thickness permeability can be obtained:

$$K_z = \frac{d_s^2 \left(1 - CF_x\right)^3}{80} \tag{7.5}$$

Interestingly, for this particular case permeability values derived from the analytical model follow closely those obtained from computer simulations (Figure 7.16). This is remarkable considering the somewhat crude assumption that all pressure losses occur through channels equivalent to gap sizes within the fabric. Nonetheless, it can be seen from both the analytical model and computer simulations that the permeability of a single ply of fabric varies proportionally with the cube of the linear cover factor. It follows that using a fabric with a lower cover factor is a good method for promoting resin flow in the through-thickness direction.

### 7.5.2 Stack permeability based on the fabric surface density

The effect of the fabric surface density on the through-thickness permeability of multiple stacks was further investigated with 3D simulations by varying the number of fabric plies from 1 to 8 within a ~1.6 mm, testing the effect of ply alignment: aligned or staggered contiguous plies. It should be noted that the case of 8 staggered plies could not be modelled due to meshing difficulties.

In the case of aligned plies (Figure 7.17), resin flow was channeled through the gaps between lateral yarns, enabling it to rush towards the low pressure zone. The pressure within the stack varied stepwise; a sharp pressure change was observed when resin crossed the narrowest gap between lateral yarns. As the number of plies increased the pressure drop increased as well but the change was more progressive and resin velocity became more constant in the through-thickness direction. In essence, aligned fabric plies featuring yarns that are much thinner than they are wide behave like an array of slender pipes.

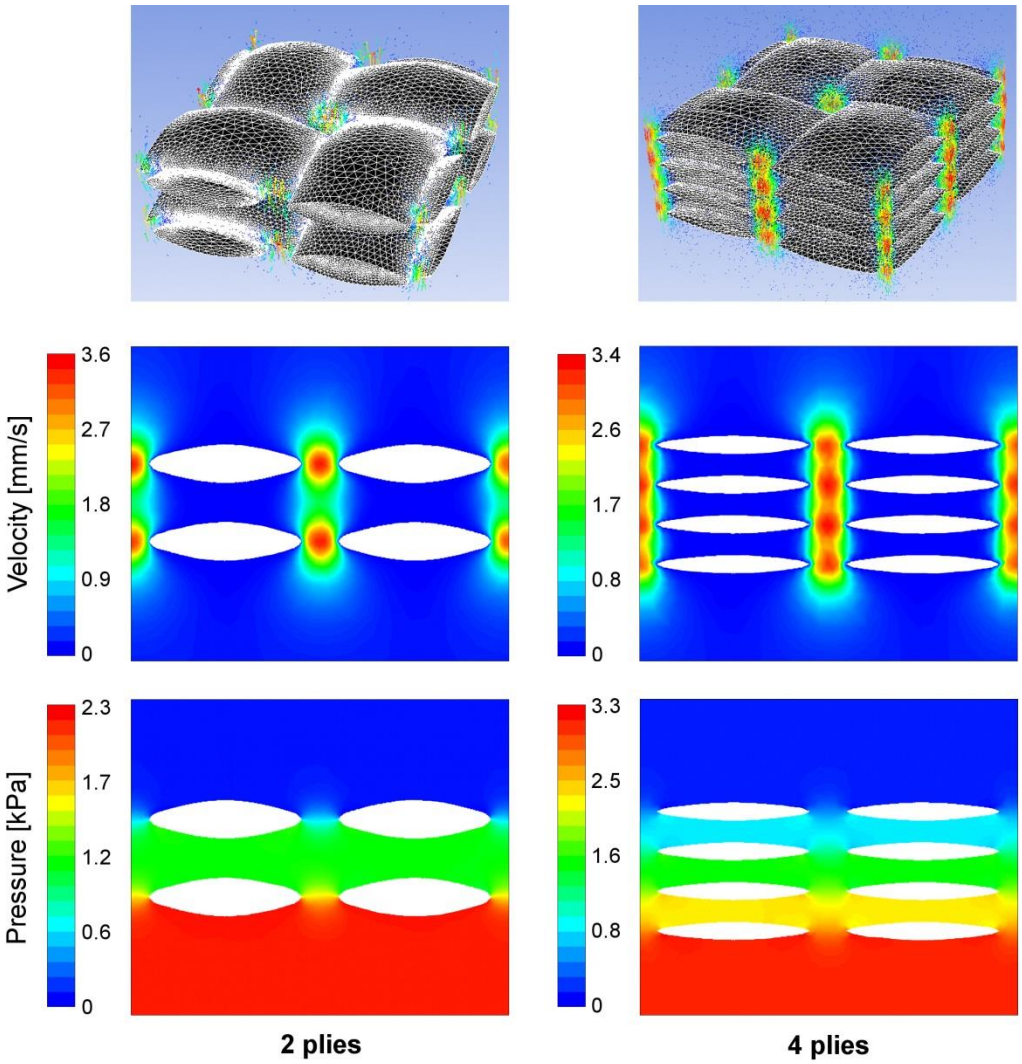


Figure 7.17: Steady state resin flow through 2- and 4-ply stacks with in aligned configuration, with corresponding resin velocities and pressures in a cross-section

In the case of staggered plies (Figure 7.18), resin flow could not rush in the through-thickness direction. It had to skirt around yarns, flowing in the in-plane direction to reach a gap that would enable ply crossing. Contrarily to the aligned case, pressure drop is minimal across the gap between lateral yarns. Instead, pressure drops the most within small gaps that developed between contacting plies. In the case of weaves, the size of these gaps appears highly dependent on the crimp angle between crossing yarns, where a higher crimp angle increases the gap size. Increasing the number of plies also increases the pressure drop across the stack. This is due in part to the change in gap geometry but also to the number of

times that resin has to deviate in the in-plane direction, which is directly proportional to the number of plies.

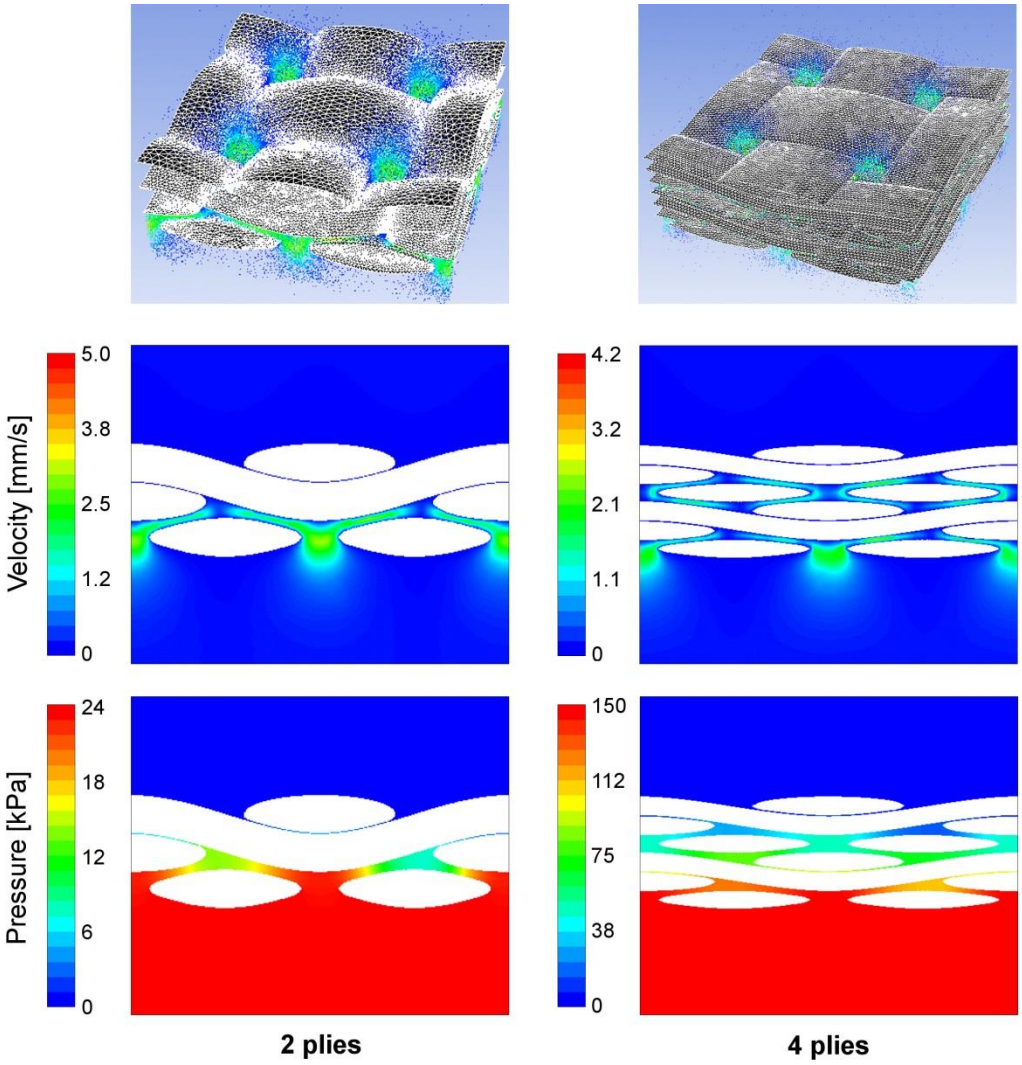


Figure 7.18: Steady state resin flow within 2- and 4-ply stacks with a staggered configuration with corresponding resin velocities and pressures in a cross-section

Permeability values calculated from the flow simulations for the aligned and staggered configurations appear in Figure 7.19. The aligned configuration featured a much higher permeability than the staggered configuration and it was affected less significantly by the number of plies in a stack. For instance, the use of fabrics that were 4 times lighter

resulted in permeability reduction of 58% and 99.3% for the aligned and staggered configurations respectively. In reality, the actual stack permeability should be between those of the simulated configuration as all plies are not fully aligned or staggered (i.e. nested).

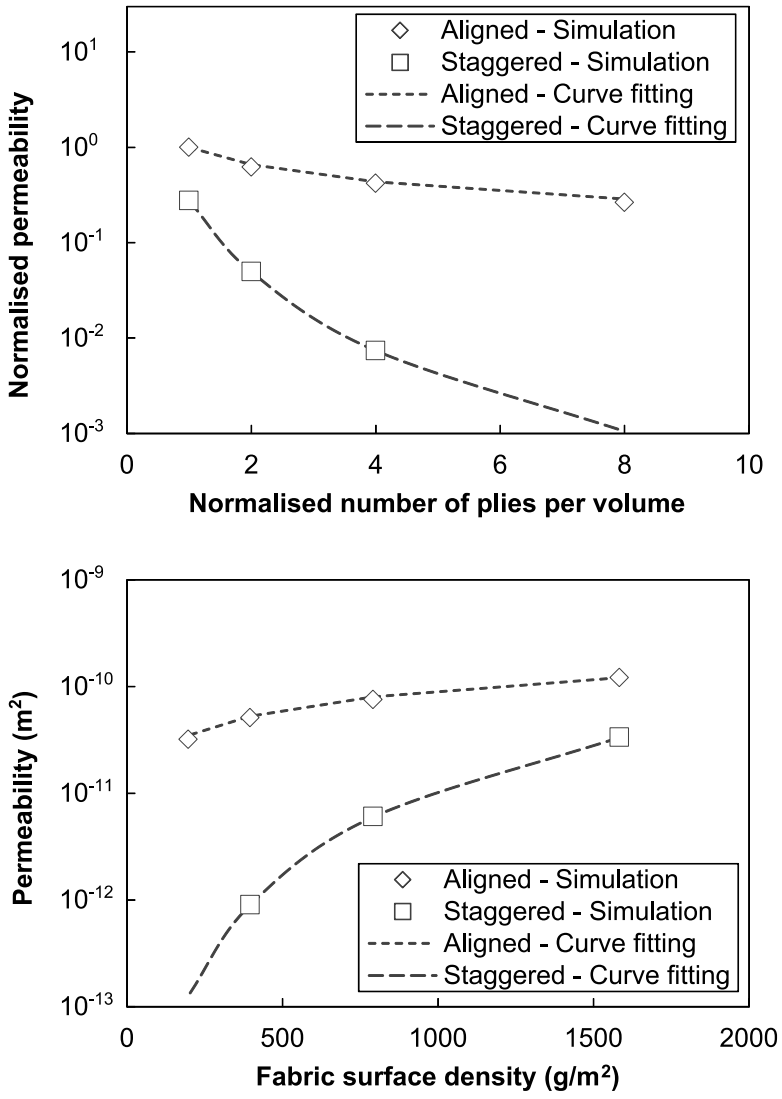


Figure 7.19: Normalised (top) stack permeability as a function of the number of plies and actual (bottom) stack permeability values as a function of the fabric surface density

Models for comparing the through-thickness permeability of fabrics featuring different surface densities used with aligned and staggered configurations were developed by curve fitting.

In the aligned configuration resin flow was restricted by gaps between yarns that acted as chokepoints. As seen in the simulations, stacks made with lighter fabrics featured more chokepoints than those made with heavier fabrics because they require more plies for achieving the desired part thickness. From this observation, an equation linking the permeability of two fabrics featuring identical cover factors to either their number of plies or surface density was proposed:

$$K^{i}_{z_{\text{Aligned}}} = K^{j}_{z_{\text{Aligned}}} \left( \frac{N_j}{N_i} \right)^m = K^{j}_{z_{\text{Aligned}}} \left( \frac{\rho^i_s}{\rho^j_s} \right)^m \tag{7.6}$$

where $K_z$ is the through-thickness permeability, $N$ is the number of fabric plies in a stack, $\rho_s$ is the fabric surface density, $m$ is a shape factor, and subscripts $i$ and $j$ represent two different fabrics featuring the same cover factor.

Shape factor $m$ is related to the yarn geometry and varies between 0 and 1. An $m$ value of 0 is equivalent to having a constant channel size where the permeability remains constant, while an $m$ value of 1 is equivalent to having a series of small perforated plates where the permeability reduces linearly with the number of plates (Figure 7.20). In the case of the modelled weave featuring an elliptic yarn profile and a cover factor of 0.8, the shape factor $m$ was evaluated at 0.63 from curve fitting the simulation results (Figure 7.19).

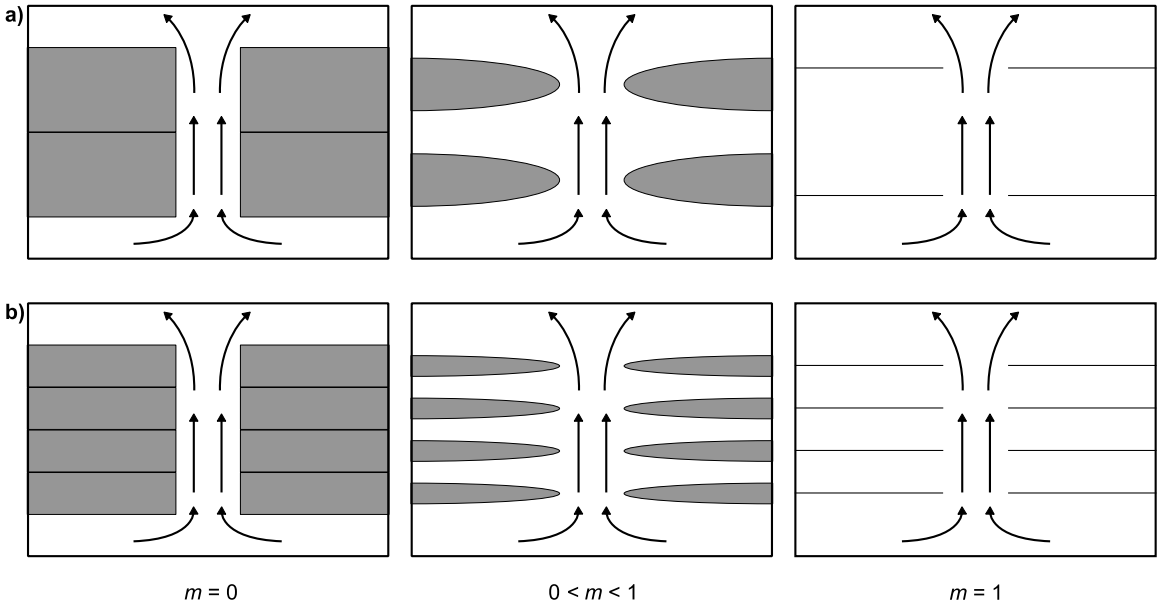


Figure 7.20: Flow within a) 2-layer and b) 4-layer stacks featuring different yarn shape factors

For the staggered case, an empirical model for estimating the through-thickness permeability was developed from the flow resistance in the through-thickness and in-plane directions. Considering that flow resistance is proportional to the flow distances and fabric permeability, and that the through-thickness and in-plane resistances are in series, the equivalent through-thickness stack permeability for the staggered ply configuration is:

$$\frac{h}{K_{z,\,\text{staggered}}} = \frac{h}{K_{z,\,\text{aligned}}} + \frac{d_x}{K_x} \tag{7.7}$$

where $h$ is the stack thickness, $K_{z,\,\text{aligned}}$ is the through-thickness permeability calculated from Eqn. 7.6, $K_x$ is the in-plane stack permeability and $d_x$ is the in-plane flow distance. Reorganising Eqn. 7.7 gives:

$$K_{z,\,\text{staggered}} = \left[ \frac{1}{K_{z,\,\text{aligned}}} + \left( \frac{d_x}{h} \right) \frac{1}{K_x} \right]^{-1} \tag{7.8}$$

The complex nature of the in-plane resin flow precludes the estimation of in-plane permeabilities and flow distances without further studies. For simplification and since both

parameters are likely affected by fabric surface densities, all parameters for the in-plane flow were grouped together into an equivalent in-plane permeability parameter $K_x^*$:

$$K_{z,\text{ staggered}} = \left[ \frac{1}{K_{z,\text{ aligned}}} + \frac{1}{K_x^*} \right]^{-1} \tag{7.9}$$

Fabric permeability values obtained from flow simulations for the staggered and aligned configurations were used in Eqn. 7.9 for calculating $K_x^*$. An empirical model based on Eqn. 7.6 was developed to relate the change in fabric surface density with $K_x^*$:

$$K_x^{*i} = K_x^{*j} \left( \frac{\rho_s^i}{\rho_s^j} \right)^n \tag{7.10}$$

where *n* is a shape factor, and subscripts *i* and *j* represent two different fabrics featuring the same cover factor. A shape factor *n* value of 2.83 for the modelled plain weave was obtained from curve fitting of simulation data (Figure 7.19). Since the shape factor is much greater than unity, this clearly shows that the change in in-plane flow resistance is attributable to more than just the number of contacting plies. It is conjectured that lighter fabrics leads to narrower in-plane channels which further increases flow resistance.

### 7.5.3 Yarn saturation based on fabric surface density

The effect of the fabric surface density on the yarn saturation was studied with multiphase flow models that featured different yarn thicknesses. Two types of models were used, one for interleaved RFI and another for bulk RFI.

In the case of interleaved RFI, models allowed resin flow into yarns from both sides of the fabric layer (Figure 7.21). Results showed that for low density fabrics, saturation occurred predominantly due to through thickness flow as suggested by the RFI experiments in Section 7.2. Conversely, in very high surface density fabrics, much heavier than those used in the experiments of Section 7.2, in-plane resin flow could contribute to the saturation of yarn crossovers. In such case, crossovers can be saturated slightly faster than the centre of yarns. However, yarn saturation remains highly dependent on the size of

yarns and surface density of fabrics as indicated by the evolution of fill factors for all models (Figure 7.22).

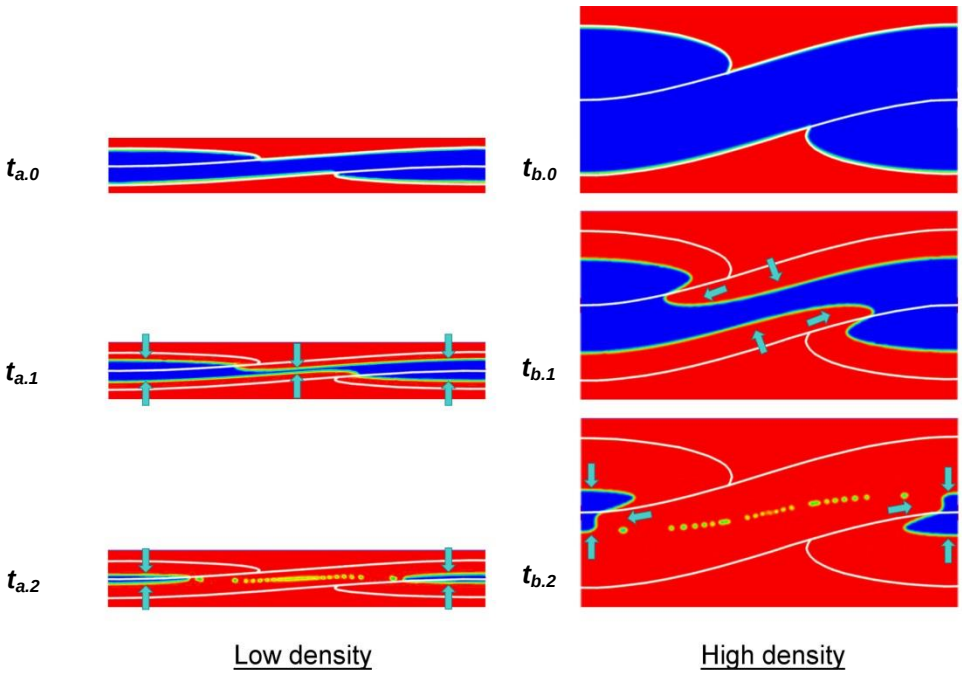


Figure 7.21 : 2D simulation of the evolution of resin (red) filling dry (blue) yarns (white outline) for low and high surface density fabrics interleaved stacking configuration

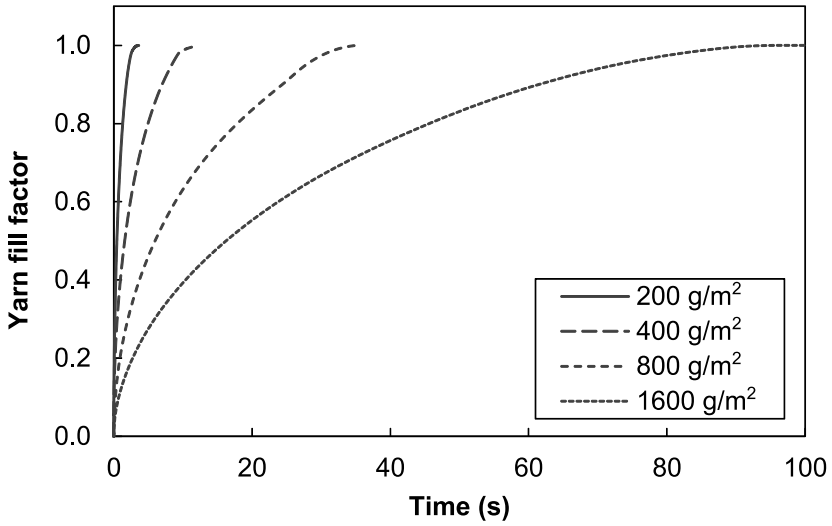


Figure 7.22: Evolution of the yarn fill factor for fabrics of different surface densities for interleaved RFI models

In the case of bulk RFI, models allowed resin flow into yarns only from the gap between yarns (Figure 7.23). Results showed that for low density fabrics, resin first saturate exposed yarns by through-thickness flow then proceeds to saturate the rest of the yarns by in-plane flow. For heavier fabrics, in-plane flow contributes to the saturation of the yarns but saturation appears to be controlled mostly by through-thickness flow. This behaviour is reflected in the evolution of the fill factors (Figure 7.24), where lighter fabrics have similar saturation times because flow is governed by in-plane flow whereas as heavier fabrics have much longer saturation times because through-thickness flow becomes more critical.

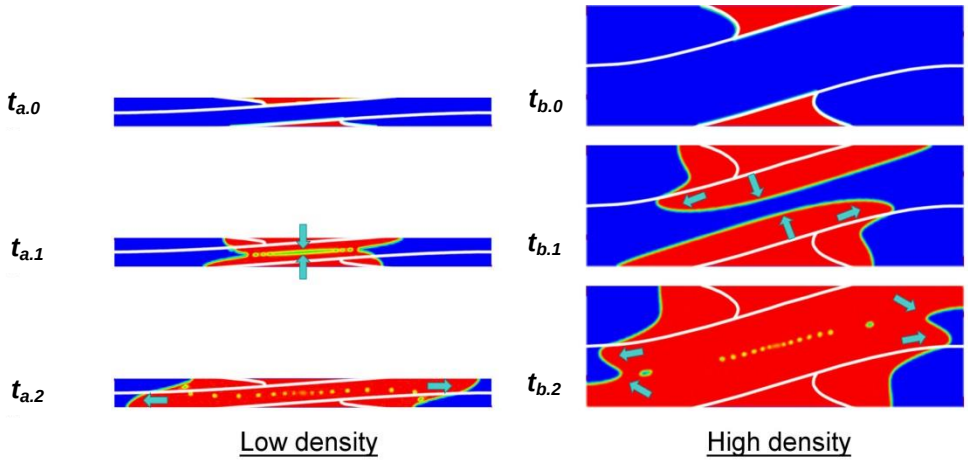


Figure 7.23 : 2D simulation of the evolution of resin (red) filling dry (blue) yarns (white outline) for low and high surface density fabrics in bulk stacking configuration

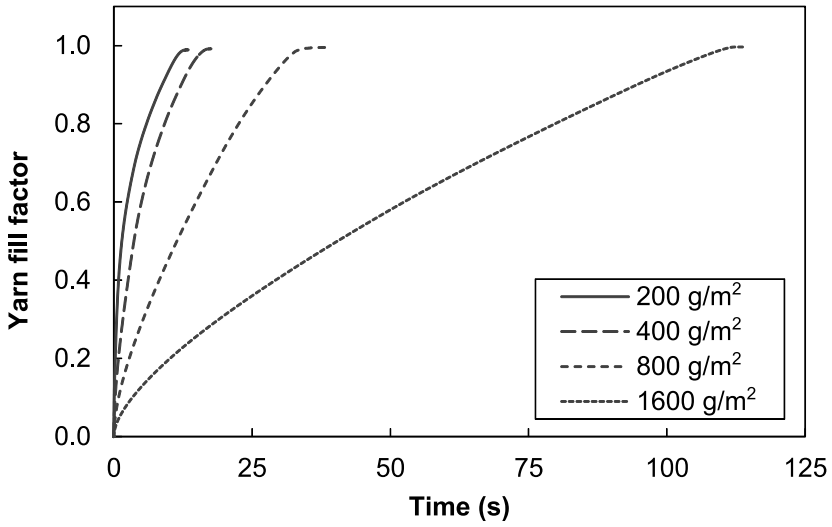


Figure 7.24: Evolution of the yarn fill factor for fabrics of different surface densities for bulk RFI models

Comparing the yarn saturation time for interleaved and bulk RFI cases (Figure 7.25), it can be seen that the lower surface area of the fabric exposed to the resin for bulk RFI than interleaved RFI increases the saturation time. However, the geometry of the fabric, most particularly the thickness of yarns, has a much more important influence over

saturation than the stacking configuration. This is because the through-thickness permeability of yarns is much lower than their in-plane permeability, making it difficult for the resin to flow across the thickness of yarns.

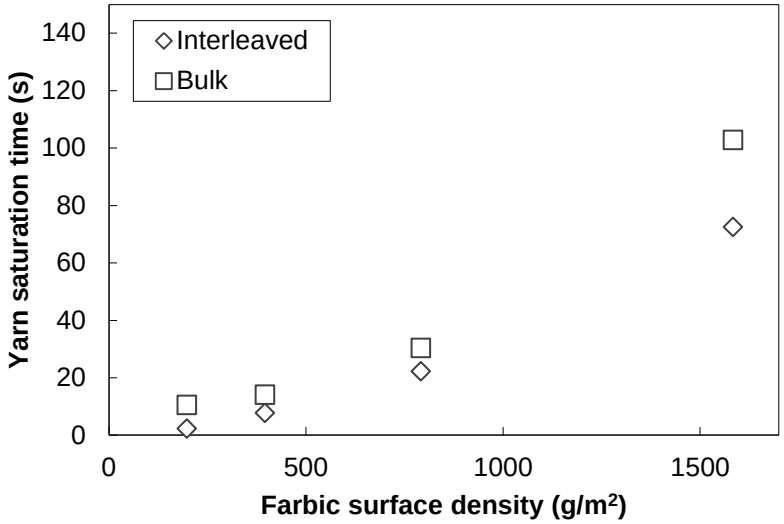


Figure 7.25: Yarn saturation times for interleaved and bulk RFI with fabrics of different surface densities

## 7.6 Remarks

Resin flow kinetics was studied for the interleaved and bulk configurations of RFI process through experiments and computer simulations. The general resin flow kinematics was found to be similar for both configurations.

During RFI, stacks of fabric and resin films are compacted together. At the start of the process, despite the low temperatures, resin viscosity is sufficiently low to enable squeeze flow into the inter-yarn gaps of the fabrics, i.e. into high permeability zones. At this point the viscosity remains high enough as to prevent any significant flow inside yarns. As the process temperature rises, resin viscosity lowers and resin flow rate increases. This

enables resin flow within yarns. In all configurations, yarn saturation is controlled mostly by through-thickness flow. However, yarn saturation can also be affected by in-plane flow due to yarn crossovers and ply overlaps. It follows that this affects bulk RFI more extensively due to contacting fabric plies.

Results showed that materials have strong influence over the saturation rates. A summary of how material properties affect saturation appears in Table 7.4.

Table 7.4: Parameters affecting saturation rates during RFI

| Change in materials | Effect on saturation rate | | | |
|---|---|---|---|---|
| | Interleaved RFI | | Bulk RFI | |
| | Inter-yarn gaps | Yarns | Inter-yarn gaps | Yarns |
| Increased resin viscosity | Lower | Lower | Lower | Lower |
| Increased cover factor | Lower | None | Lower | None |
| Increased surface density | Lower | Lower | Higher | Lower |
| Architecture: weaves vs NCFs | None | None | None | None |

The use of higher viscosity resins leads to lower flow rates. This is particularly important for toughening resins because it can result in incomplete saturation of parts.

In the case of fabrics, the use of more opened geometries increases the rate at which inter-yarn gaps are saturated. However, the most important fabric parameter affecting saturation is the fabric surface density. In both interleaved and bulk RFI, higher surface density fabrics increase yarn saturation times because they lead to greater yarn volume. In addition, for interleaved RFI, higher surface density fabrics increase slightly the saturation time of inter-yarn gaps. This is because thicker yarns lead to a greater distance between layers of resin films, increasing the amount of resin flow required for complete saturation. Conversely, in the case of the bulk RFI configuration, higher surface density fabrics reduce the saturation time of inter-yarn gaps because it results in stacks featuring fewer fabric plies, making the flow less tortuous and leads to larger inter-yarn gaps that provide less

resistance to resin flow. Interestingly, the fabric architecture tested, weave or NCF, did not affect significantly the saturation rates.

From this work, it follows that it is critical to understand the effects that materials have on resin flow for designing better manufacturing processes for PMCs. The knowledge that was developed in this work will contribute to improving the design of RFI processing by guiding material selection for achieving more uniform resin flow through the balance of yarn and inter-yarn resin flow, reducing risks of air entrapment.

# Chapter 8

## Void formation

The manufacturing of flat PMCs using RFI (Chapter 6) showed that the ILSS of composites depends greatly on their internal void content. In general, a higher void content reduces the strength of composites. Thus, improving the RFI process requires a better understanding of void formation so that parts can be made with fewer defects.

The study of void formation is tackled in three parts. Firstly, this chapter briefly discusses flow-induced voids. Secondly, most of the chapter focuses on the most important source of voids observed in this work, namely gas-induced voids due to out-of-solution volatiles. The formation of flow-induced and gas-induced voids was studied on the same PMCs as those used for characterising resin flow kinematics (Chapter 7). Thirdly, the double-bagging method is investigated for reducing voids in composites, and was studied solely with resin LEO 2396 and fabric NCF-H.

### 8.1 Flow-induced voids

Flow-induced voids result from the partial resin saturation of the fabric stack during consolidation. The two main causes of flow-induced voids are: 1) incomplete resin saturation before gelation and 2) over-bleeding.

### 8.1.1 Incomplete saturation

In-situ analysis of resin flow in Chapter 7 showed that the dual-scale permeability of fabrics leads to uneven resin impregnation in RFI. When the difference in resin velocity between resin flowing in yarns and around yarns is great, this can result in the trapping of gases that will form voids in the PMCs. This type of voids also includes voids that form when resin gelation occurs before complete saturation of the fabric. Such voids were observed with PMCs made with resin SA 70 and fabric NCF-H, where the high resin viscosity prevented complete saturation of yarns before gelation (Figure 8.1).

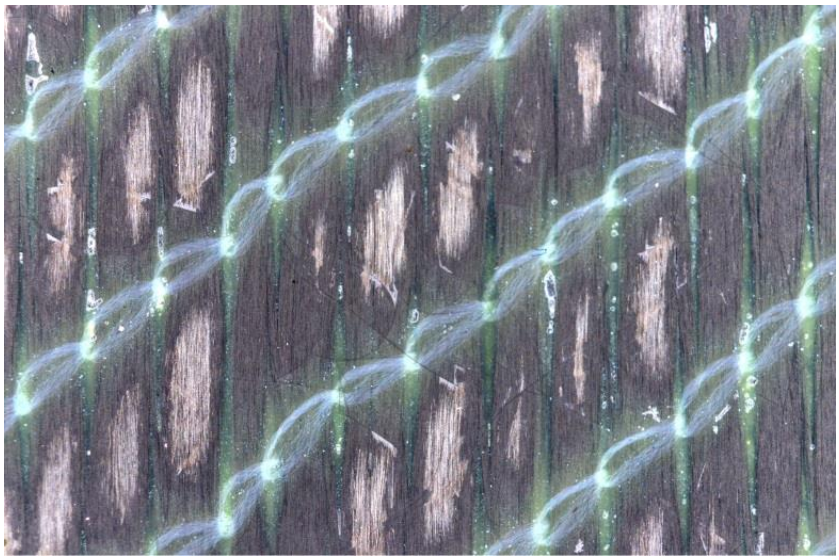

Figure 8.1: Incomplete saturation of yarns in composite made with resin SA 70 and fabric NCF-H

Incomplete saturation of yarns can be mitigated by using low surface density fabrics. As discussed in Chapter 7, this is so because yarn saturation occurs predominantly by through-thickness flow and the reduction of yarn thickness increases the saturation rate. Further analysis of this type of void formation mechanism was not pursued as it was by far the least frequent cause of voids, and because the factors affecting resin flow were discussed extensively in Chapter 7.

### 8.1.2 Over-bleeding

Another source of voids that was observed in RFI processing was the wicking of the resin from the inter-yarn gaps by the fabric reinforcement and ancillaries (Figure 8.2), a process termed over-bleeding. In this work, over-bleeding occurred because saturation of the fabric layers was achieved well before gelation of the resin. This resulted in a long period of low resin viscosity during which strong capillary forces could drive the resin to flow out of inter-yarn gaps and into the breather.

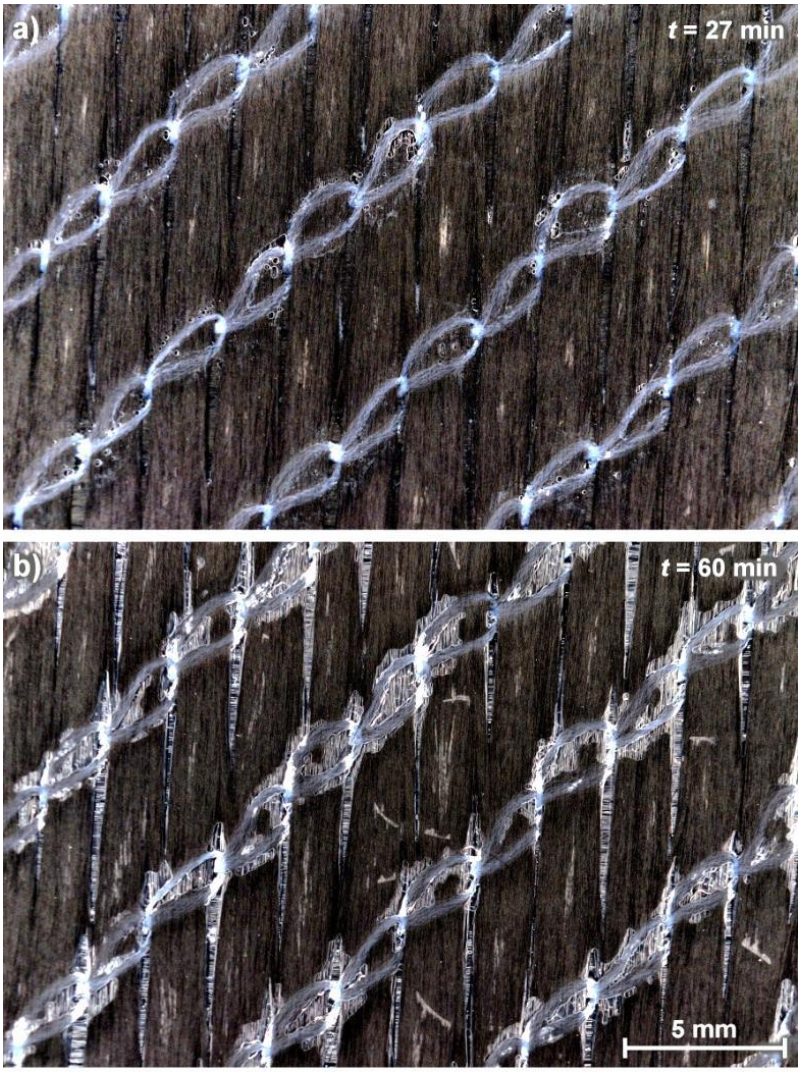


Figure 8.2: Resin distribution in interleaved RFI a) before and b) after wicking of resin LEO 2396 by fabric NCF-L

Over-bleeding was observed only in experiments featuring resin formulation L9 and not with the other resins despite similar surface tensions and contact angles. This suggests that resin viscosity is the key driver for over-bleeding. In addition, over-bleeding was only observed with fabrics NCF-L, NCF-H and Twill-H. It is conjectured that these fabrics were more affected than others due to their lower resistance to in-plane flow attributed to straight inter-yarn gaps (NCFs) or large inter-yarn gaps (Twill-H). Hence, fabrics of low permeability such as those featuring small inter-yarn gaps and those leading to greater tortuosity of resin flow can reduce risks of over-bleeding.

Despite the effect of the fabric architecture, results showed that resin viscosity was the strongest contributor to over-bleeding. However, capillary flow can only occur if there is an affinity between the resin and surrounding media. It follows that the likelihood of over-bleeding depends not only on resin viscosity but also on the surface tension and contact angle. A factor *OB* for assessing the potential for over-bleeding was defined based on the modified capillary number (Eqn. 2.5):

$$OB = \frac{\mu}{\gamma \cos\theta} \tag{8.1}$$

where $\mu$ is the lowest resin viscosity that is reached following saturation of the reinforcement, $\gamma$ is the surface tension of the resin and $\theta$ is the contact angle between the resin and fibre. *OB* values calculated for each resin at their lowest viscosity appear in Table 8.1. Results show that resin LEO 2396, which featured the greatest number of instances of over-bleeding, has an *OB* value much lower than that of other resins. Considering that over-bleeding occurred in some experiments featuring resin LEO 2397, it follows that resin systems used in RFI should feature an *OB* value above 14 s/m.

Table 8.1: Over-bleeding factor for the resin systems

| Resin | *OB* (s/m) | Observable cases of over-bleeding |
|---|---|---|
| SA 70 | 774.8 | No |
| LEO 2376 | 14.7 | No |
| LEO 2377 | 42.9 | No |
| LEO 2396 | 3.4 | Often |
| LEO 2397 | 13.8 | Sometimes |

Another method for minimising risks of over-bleeding would be to use a quantity of resin that takes into consideration not only the amount required for saturation but also for bleeding. However, if saturation occurs well before gelation this leads to significant resin wastage. This wastage may be prevented by using resin dams that seal most edges of the stack, but this limits gas extraction and can lead to more voids as seen in Section 6.3 where different bleeding configurations were tested. Instead, it is better to select a resin that will reach gelation soon after saturation.

## 8.2 Gas-induced voids

Gas-induced voids are caused by gases present in resin films or RFI stacks prior to processing. Gases that remain out of solution during RFI processing form bubbles lead to closed holes within PMCs.

In this work, gas-induced voids were studied more extensively than flow-induced voids because they were by far the most prominent source of defects in PMCs made through out-of-autoclave RFI. This is because the resin films as-received featured significant amounts of volatiles (Section 4.3), and because low resin pressures used in out-of-autoclave RFI processing limit gas dissolution in the resin.

The objective of this section is to provide a description of the kinematics of out-of-solution gases, referred hereafter as bubbles, throughout RFI processing. Results provide better insight on how voids are formed in PMCs and how material selection affected the porosity of flat laminates fabricated in Chapter 6.

### 8.2.1 Bubble kinematics

#### 8.2.1.1 Stages of bubble kinematics

Four stages of bubbles kinematics were identified throughout processing: 1) bubble migration, 2) bubble growth, 3) bubble contraction and 4) equilibrium. These general stages were observed in both interleaved and bulk RFI stacking configurations. Stages 1 and 2 occurred simultaneously. The time frame for these stages is presented in Figure 8.3 and the general evolution of bubbles that was observed with NCF and woven fabrics during RFI appears in Figure 8.4.

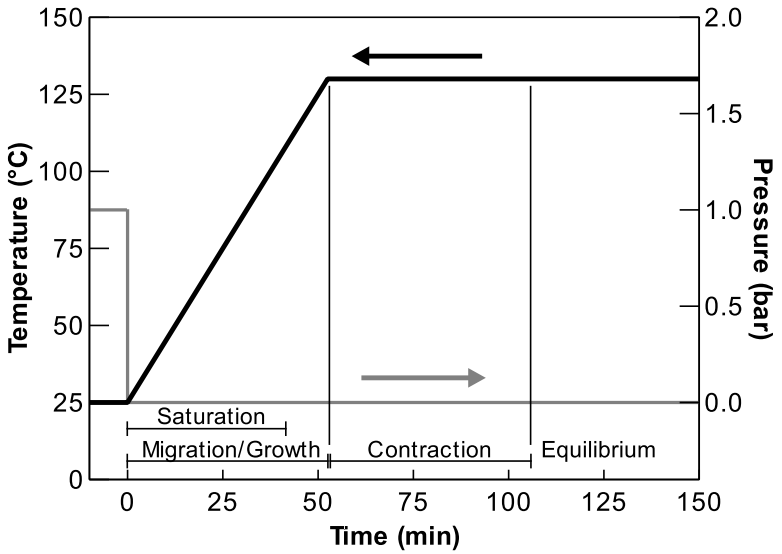


Figure 8.3: Typical stages of bubble and resin kinematics during a cure cycle

**Figure 8.4: Migration, growth and contraction of gas bubbles during interleaved RFI processing with neat resin LEO 2376 with fabric a) NCF-H and b) PW-L**

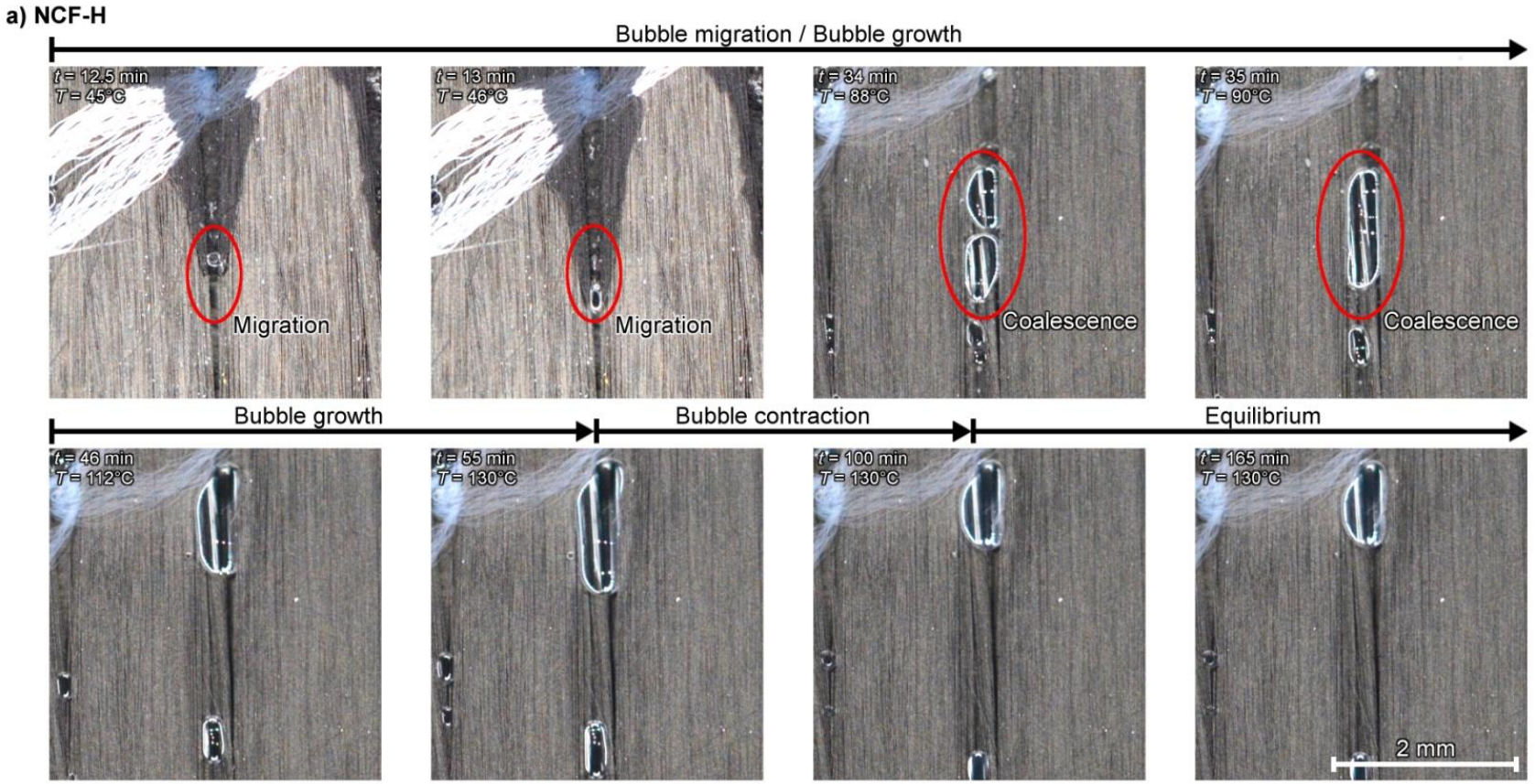

**Figure 8.4 (cont.): Migration, growth and contraction of gas bubbles during interleaved RFI processing with neat resin LEO 2376 with fabric a) NCF-H and b) PW-L**

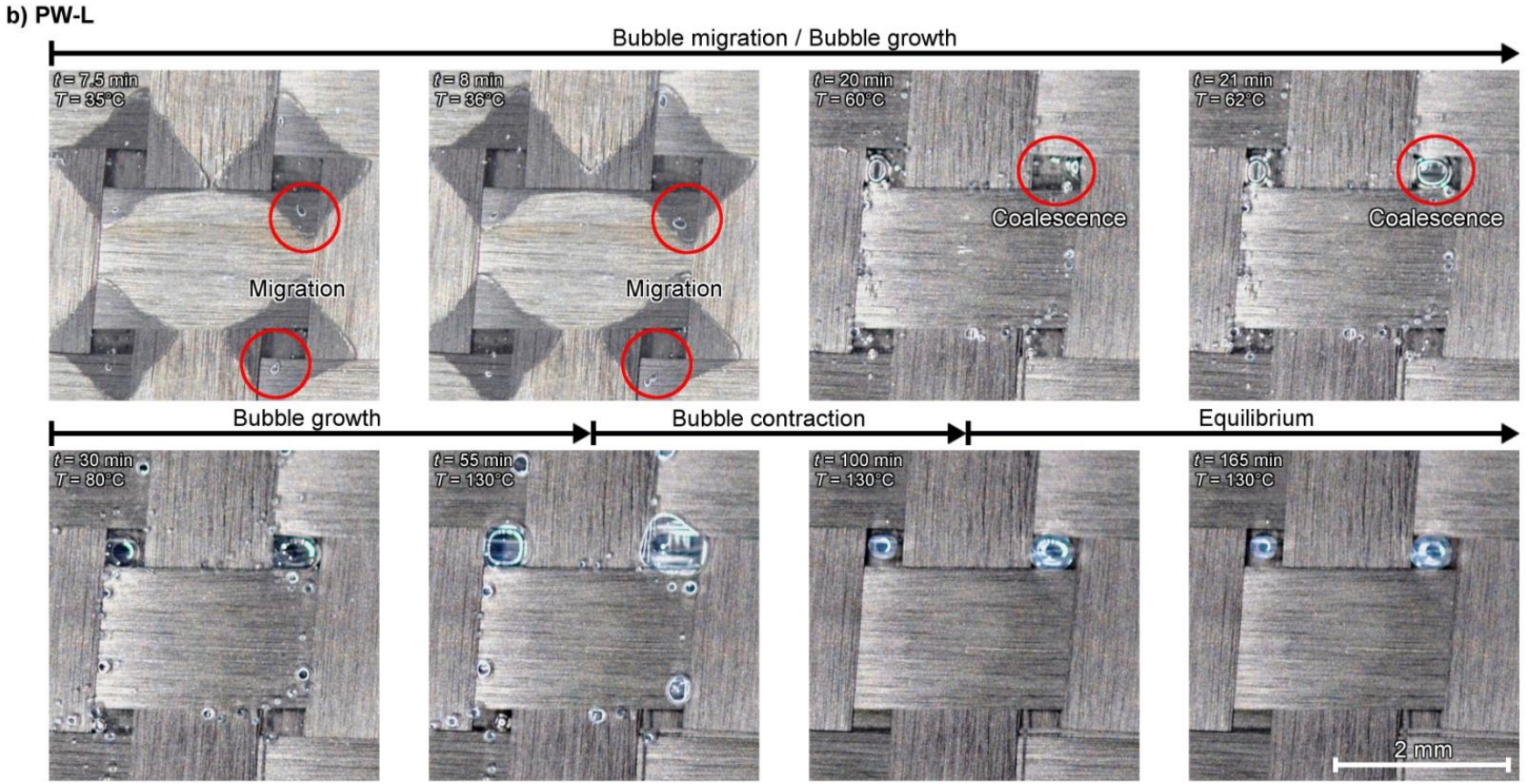

At the start of an experiment, bubbles were already present resin films (Figure 8.5). The compaction force applied by the vacuum bag triggered resin flow and bubble migration, stage 1 of bubble kinematics. Bubbles moved in gaps between yarns, never inside yarns, and always moved in the direction of resin flow. While migrating, bubbles moved slightly faster than the resin flow and could eventually overtake the flow front, leading to bubble bursting and in-situ degassing (Figure 8.6). This behaviour is consistent with observations and predictions of Gangloff et al. [169] for the mobility of gas bubbles during composite processing. Gas extraction under this mechanism was more frequent in experiments featuring the bulk stacking configuration than for experiments with the interleaved stacking configuration. In interleaved RFI, many bubbles did not escape the flow front and remained trapped in the resin. Observations also showed that large bubbles were less mobile than small bubbles and that they could be stopped by narrow inter-yarn gaps.

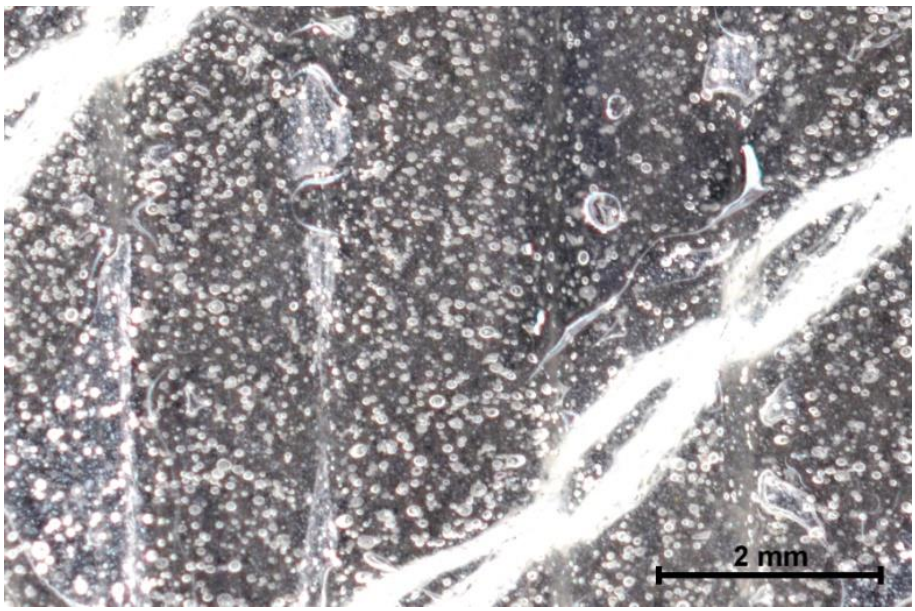


Figure 8.5: Voids in resin film LEO 2376 that was laid over fabric NCF-H prior to RFI processing

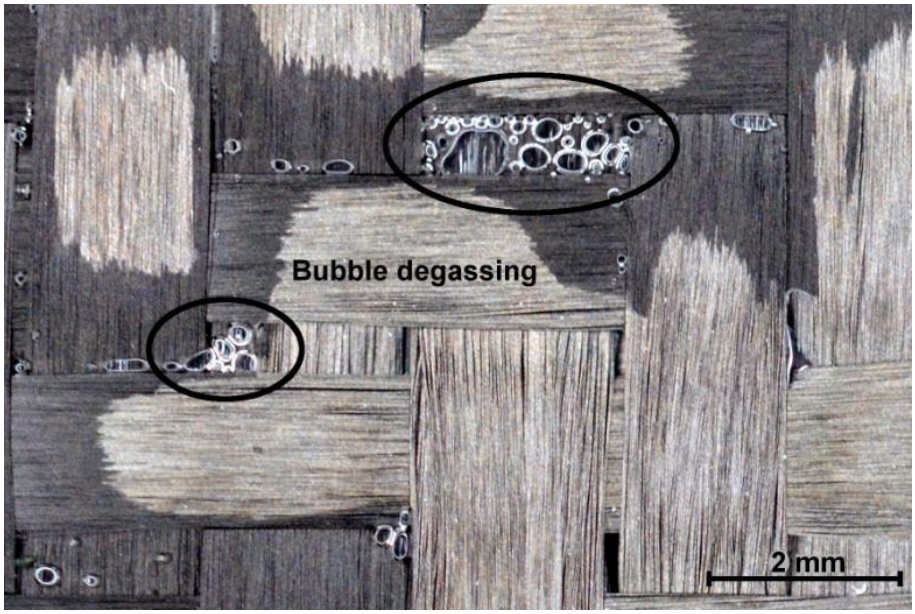


Figure 8.6: Gas bubbles at the flow front that are about to burst for bulk RFI experiment featuring fabric Twill-L and neat resin LEO 2396

Stage 2, bubble growth, started simultaneously with bubble migration. Observations suggest that coalescence of bubbles during migration (Figure 8.4) was a major source of growth. During growth, bubbles sought to maintain a low surface energy by trying to keep a high sphericity shape. This forced bubbles to relocate in large gaps between yarns. Growth continued after bubble migration and until dwell temperature was reached (Figure 8.4), showing temperature dependence as expected from an ideal gas. In some cases, bubble growth was such that the inter-yarn gaps were too narrow to allow spherical bubbles, resulting in bubbles taking the shape of these gaps.

Stage 3, bubble contraction, began at the start of the temperature dwell. Bubbles reduced in size through time (Figure 8.4). Smaller bubbles dissolved completely in the resin while larger ones did not. Before resin gelation, remaining bubbles stopped contracting and reached their final size, stage 4. All out-of-solution gases remaining after equilibrium resulted in holes in the final PMC parts.

#### 8.2.1.2 Bubble content after growth stage

Bubble content values as a function of reinforcement surface density appear in Figure 8.7, for all experiments free of over-bleeding. Results did not show any correlation between the bubble content and fabric surface density. However, bubble contents were generally higher with experiments featuring fabric Twill-H, suggesting that the fabric surface density may only affect the bubble content of weaves.

Comparing interleaved and bulk RFI it can be seen that the interleaved stacking configuration led consistently to much higher bubble contents than for the bulk stacking configuration.

For experiments featuring the interleaved stacking configuration, bubble contents were also affected greatly by the resin formulation; neat resin LEO 2396 resulted consistently in higher bubble contents. The low viscosity of this resin often led to over-bleeding and in cases free of over-bleeding, the high capillary forces coupled with the low viscosity also resulted in higher bubble contents. Conversely, other resins offered comparable bubble contents. This can be explained by similar volatile contents in the resin films (Section 4.3) and to higher resin viscosities that reduced the effect of capillary forces. Additionally, results suggested that the initial resin content in stacks had little effect over the bubble content (Figure 8.8).

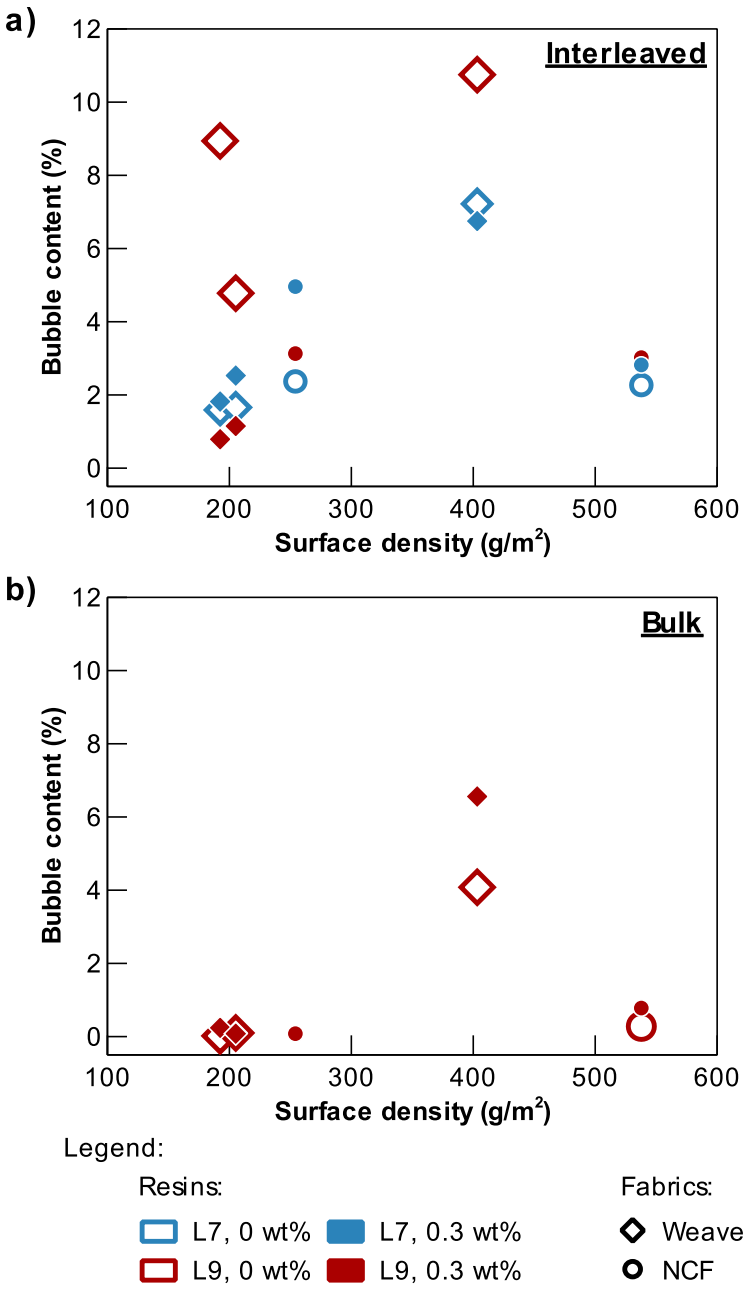


Figure 8.7: Effect of the fabric surface density on the bubble content at the surface of the stack after the growth phase for a) interleaved and b) bulk RFI stacking configurations

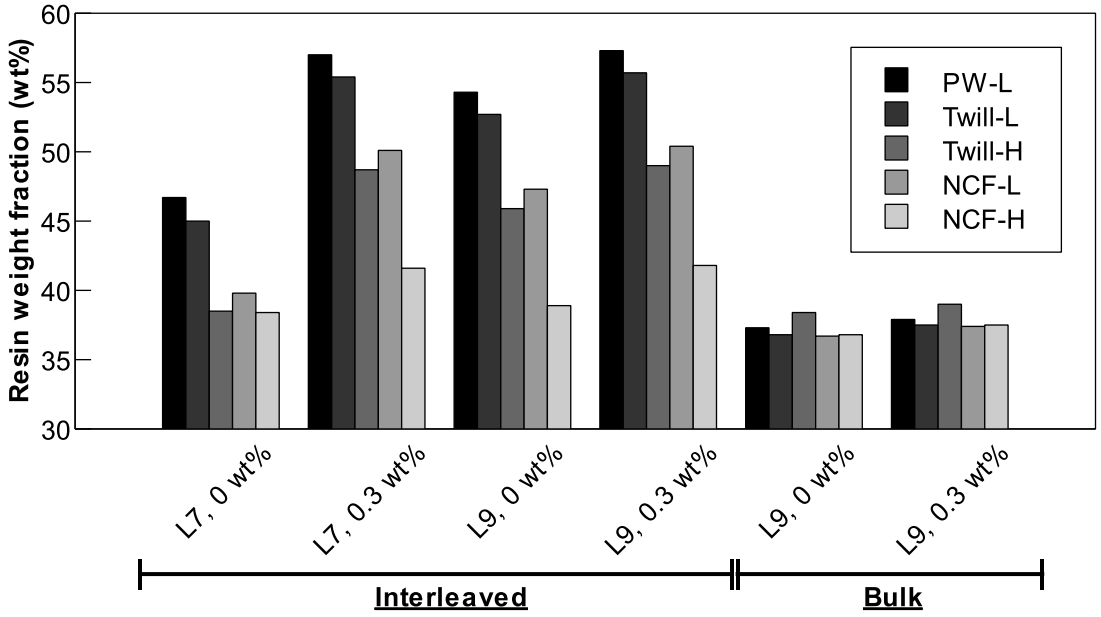


Figure 8.8: Resin content in PMCs used for characterising the kinematics of bubbles

#### 8.2.1.3 Bubble contraction

The size of bubbles was monitored during the contraction stage for experiments featuring the interleaved stacking configuration. It is worth noting that this was not done with the bulk stacking configuration due to the lack of bubbles appearing on the surface of the stacks.

During the contraction stage, bubbles reduced in size gradually until complete collapse or until they reached their final size, as shown for typical bubbles in Figure 8.9. The tracking of relatively small bubbles with a circular cross-section revealed that for lower surface density fabrics PW-L, Twill-L, and NCF-L, only the smallest bubbles collapsed completely (Figure 8.9a). The contraction rate also increased with a reduction in bubble radius; thus being able to control the maximum bubble size could help reducing the bubble content significantly. Roughly 70 min to 75 min following the beginning of the cure cycle, a strong decrease in contraction rate was observed. After that point, bubble sizes slowly stabilised. In the case of fabrics featuring higher surface densities, Twill-H and NCF-H, bubbles underwent limited contraction (Figure 8.9b) but otherwise followed the same behaviour as those monitored in experiments featuring lower surface density fabrics.

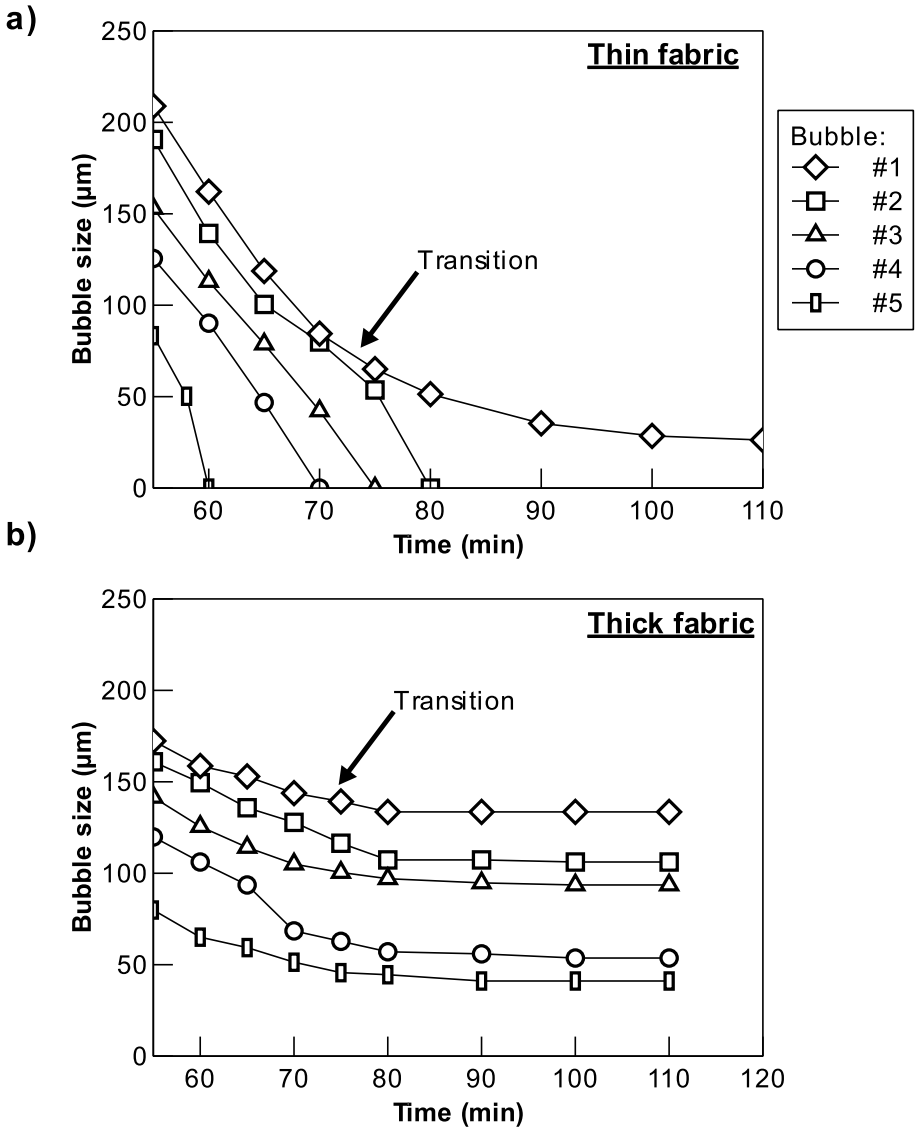


Figure 8.9: Typical bubble radii observed during the contraction stage of interleaved RFI for a) thin fabric (PW-L with LEO 2396 resin) and b) thick fabric (Twill-H with LEO 2396)

#### 8.2.1.4 Void content after gelation

Before reaching gelation, bubbles stopped contracting and reached the equilibrium stage where remaining bubbles lead to holes observed in PMCs. The resulting void content values at the surface of the stacks as a function of the fabric surface density appear in Figure 8.10 for experiments free of over-bleeding. The influence of the resin type on the surface void content values was negligible. Results did not show a direct correlation

between the fabric surface density and the surface void content. Surface void content values increased with an increase in fabric surface density for all experiments featuring weaves, but this was not observed with NCFs. Comparing interleaved and bulk RFI experiments, it can be seen that the interleaved stacking configuration led consistently to higher surface void contents than obtained with the bulk stacking configuration.

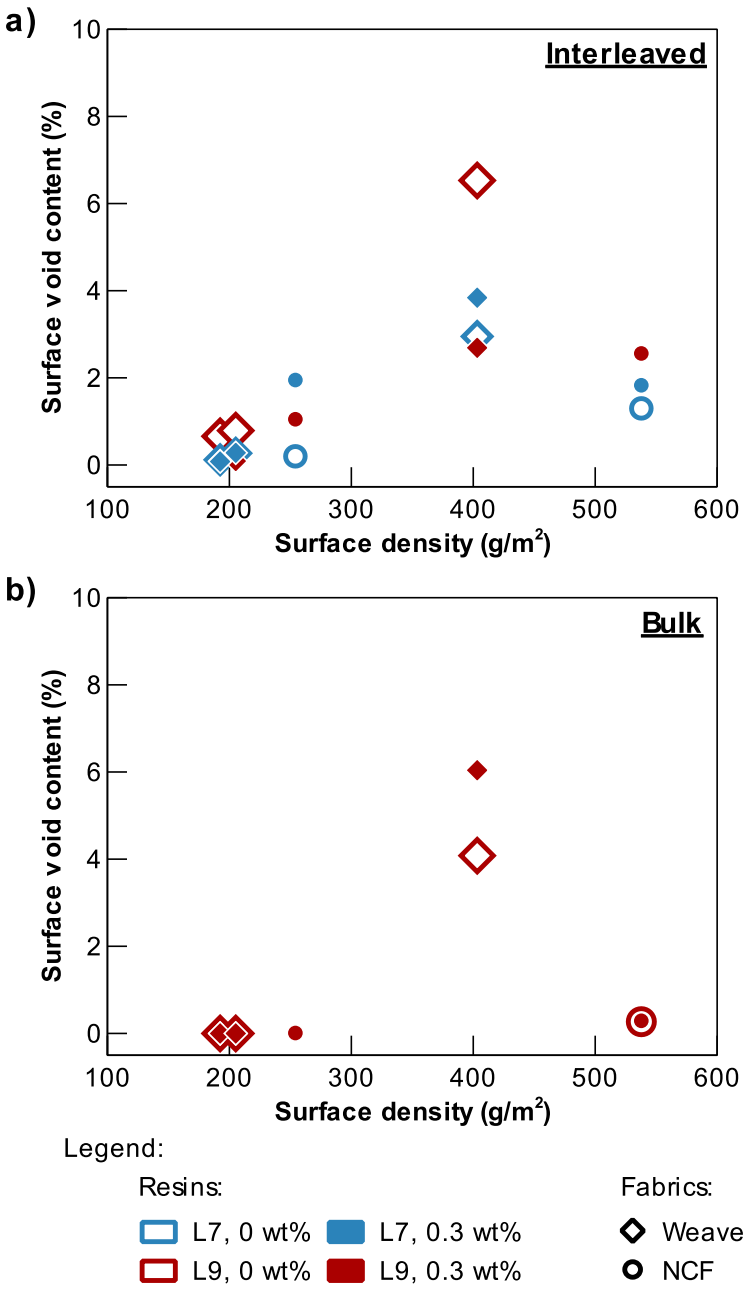


Figure 8.10: Effect of the fabric surface density on the void content at the surface of the stack after gelation for a) interleaved and b) bulk RFI stacking configurations

In general, trends for the surface void content values (Figure 8.10) differ slightly from trends for the bubble content values obtained prior to the contraction stage (Figure 8.7). Any differences were caused by different bubble contraction rates during stage 3 of bubble kinematics. Figure 8.11 shows how much bubble contents reduced during the contraction stage. Aside from a few outliers due to low bubble contents seen in experiments for the bulk stacking configuration, it can be seen that the amount of bubble contraction reduced with an increase in fabric surface density. Thus, greater bubble collapse and fewer voids in manufactured PMCs can be achieved by using thinner fabrics.

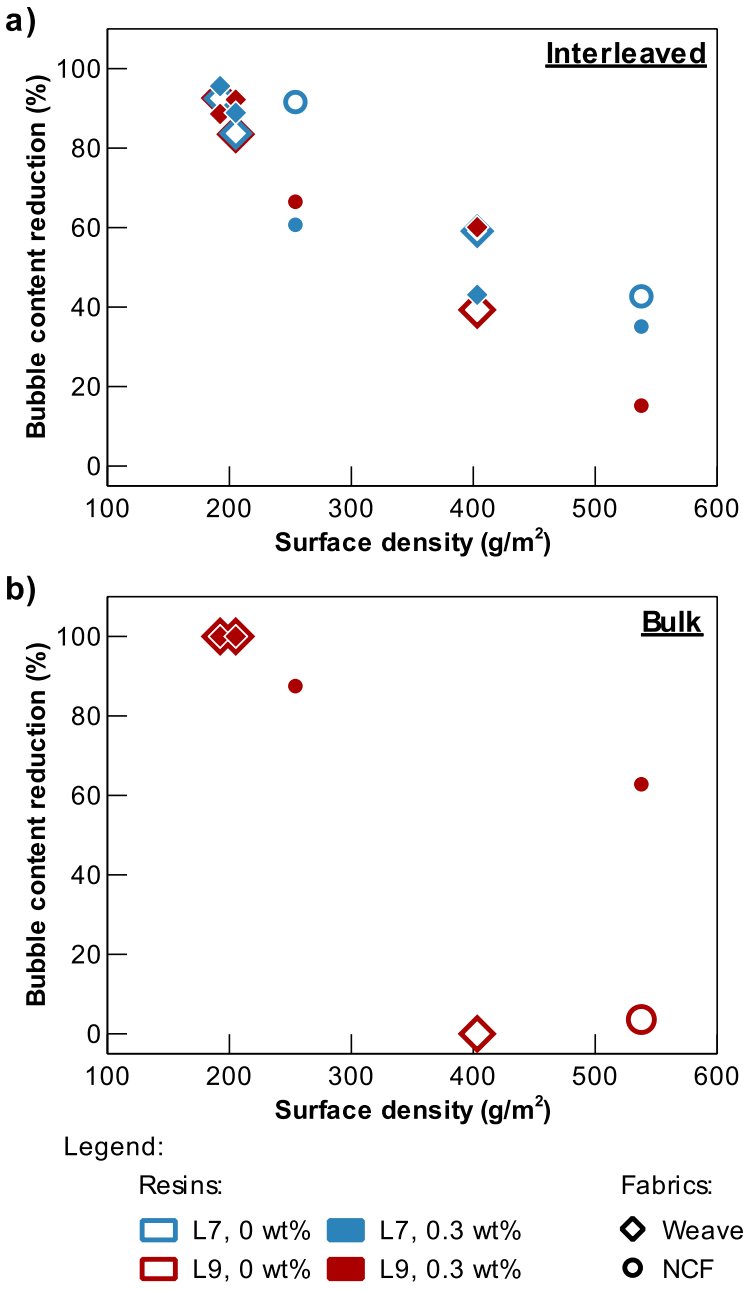


Figure 8.11: Effect of the fabric surface density on the reduction of bubble content during the contraction stage for a) interleaved and b) bulk RFI stacking configurations

### 8.2.2 Factors affecting bubble content

#### 8.2.2.1 Degassing

Experiments showed that during migration, bubbles can overtake the flow front leading to bubble bursting and degassing. This phenomenon was more common with laminates made with the bulk stacking configuration and resulted in fewer surface voids than in laminates made with the interleaved stacking configuration. This discrepancy results from a difference in resin travel distances between stacking configurations. Since bubbles can move faster than the resin flow, an increase in the resin travel distance increases the likelihood that bubbles can reach and overtake the resin flow front before saturation of the stack. In the case of the interleaved stacking configuration, resin only travels a short distance before complete stack saturation, limiting opportunities for degassing. The investigation of the cross-section of laminates also revealed that degassing is not uniform across the thickness of laminates. Void density tends to be higher on the resin infusion side and decreased gradually across the thickness of the laminate (Figure 8.12). This is due to non-uniform bubble velocity, where bubbles nearest to the flow front travelled quicker than those farther away, which is consistent with observations made by Gangloff et al. [169].

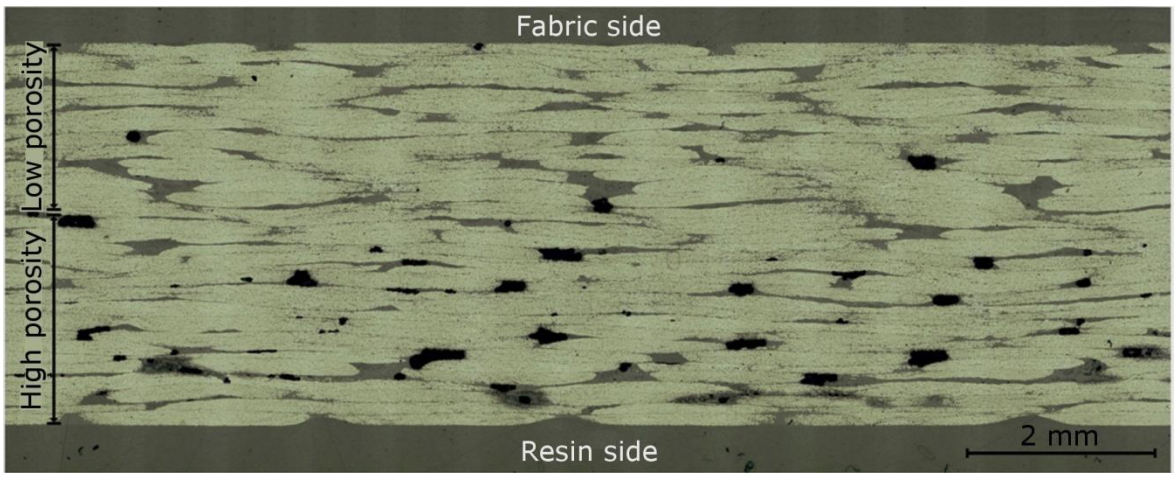


Figure 8.12: Laminate cross-section showing a change in void distribution across its thickness: bulk stacking configuration with resin LEO 2396 and fabric NCF-L

Fabric architecture also affected degassing. Results showed that only laminates featuring fabric Twill-H did not show a significant reduction in surface void content when using the bulk stacking configuration instead of the interleaved one. Incidentally, Twill-H was the fabric with the highest fabric permeability (Section 5.4) and quickest saturation for bulk RFI (Section 7.3).

Plotting the surface void content based on the saturation time obtained in Chapter 7 (Figure 8.13), it can be seen that surface voids appeared only in cases where saturation times were the shortest. It follows that fabrics leading to faster saturation times shorten the window for degassing. Further work will be required for the precise identification of parameters controlling degassing, such as the size of inter-yarn gaps and tortuosity of the path of connected inter-yarn gaps. Nevertheless, it is clear that both the fabric geometry and stacking configuration play a critical role in the degassing mechanism in RFI.

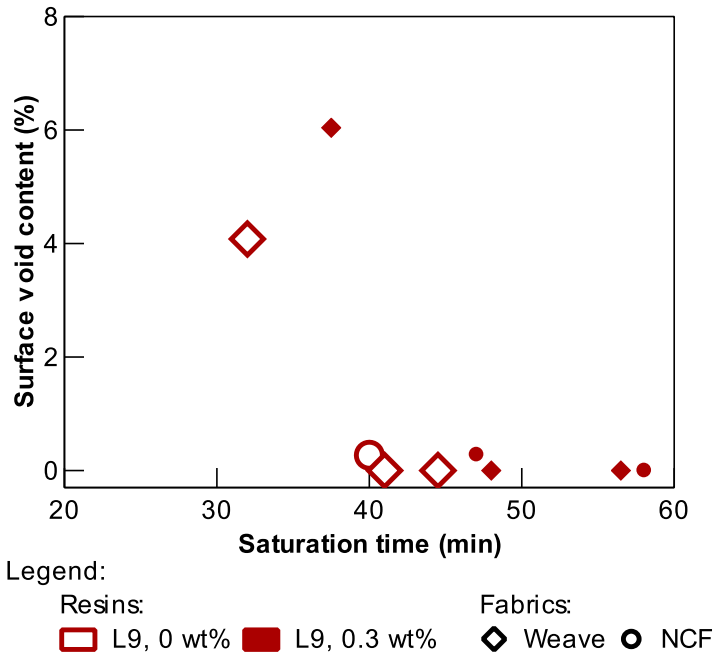


Figure 8.13: Effect of the saturation time on the surface void content after gelation for experiments conducted with the bulk stacking configuration

#### 8.2.2.2 Bubble growth and collapse

As stated previously, gases inside bubbles behave similarly to ideal gases. Based on this, bubble growth and contraction stages should be affected by pressure, temperature and mass transfer.

The growth stage was affected in part by mass transfer. On a macroscopic scale, observations have showed that bubbles coalesced, forming larger entities. On a smaller scale, there may also have been a contribution of mass diffusion across bubble boundaries, either through gas diffusing in or out of the bubbles. In this stage, it is difficult to gauge the extent of mass diffusion due to the multiple confounding factors affecting bubble growth. Pressure also likely contributed to the change in bubble size, but no measurements of the resin hydrostatic pressure were made in the experiments. Despite this, it is expected that upon saturation of the fabric stack, resin pressure would decrease with increasing bleeding as a greater fraction of the load would be transferred to the fabric reinforcement [65]. This suggests that during the latter part of the temperature rise and during the isothermal dwell, the reduction in resin pressure would contribute to bubble growth. Considering that there was a bubble contraction stage following the isothermal dwell, pressure was likely not a major factor that contributed to the change in bubble size. Finally, the last contributor to bubble growth was temperature. It was one of the most important contributors to bubble growth, as bubbles grew only during the temperature rise and stopped when the isothermal dwell was reached.

The contraction stage started at the start of the isothermal dwell. Without any changes in temperature, bubbles were free to contract. Since resin pressure appears to have had a minimal effect over the change in bubble size, it follows that mass loss was the key contributor to bubble contraction. In this case, gas inside bubbles diffused into the resin. Gas diffusion in the resin should also have occurred during the growth stage, but its effect was not significantly strong to overcome bubble growth caused by temperature rise.

Gas diffusion across a bubble-liquid interface for an isothermal system can be modelled based on the work of Plesset and Prosperetti [170] who defined an equation for mass diffusion across a spherical bubble:

$$r^2 - r_o^{\,2} \approx \frac{2D\left(c_\infty - c_s\right)\Delta t}{\rho_G} \tag{8.2}$$

where $r$ is the bubble radius, $r_o$ is the initial bubble radius, $D$ is the diffusion coefficient, $c_s$ and $c_\infty$ are the gas concentrations in the bubble $c_s$ and epoxy $c_\infty$ respectively, $\rho_G$ is the gas density within the bubble and $\Delta t$ is the growth time. The lack of information regarding the type of gas, its concentration and density inside the bubble or within the resin prevents the use of Eqn. 8.2 for calculating a diffusion coefficient. Nevertheless, for the sake of comparison within this work, all unknowns were regrouped into a single contraction coefficient $k_c$ that simplified Eqn. 8.2 to:

$$r^2 - r_o^2 = -k_c \Delta t \tag{8.3}$$

Eqn. 8.3 was used successfully for modelling the bubble radius during the contraction stage (Figure 8.14). The equation provided a better fit for small bubbles that have both a circular cross-section and that could collapse completely. Contraction coefficient values that were obtained from curve fitting appear in Figure 8.15. In the case of thin fabrics no effect of the fabric type or resin formulation was identified; all contraction coefficients were approximately 1000 μm$^2$/min. In the case of thick fabrics, contraction coefficients were generally lower than those found for thin fabrics, with the exception of those obtained with neat resin LEO 2376. These lower contraction coefficient values resulted in fewer bubbles that could collapse completely before the end of the bubble contraction stage. In this work, based on the contraction coefficients that were obtained, a bubble radius of 140 μm was defined as the upper limit for achieving complete bubble collapse.

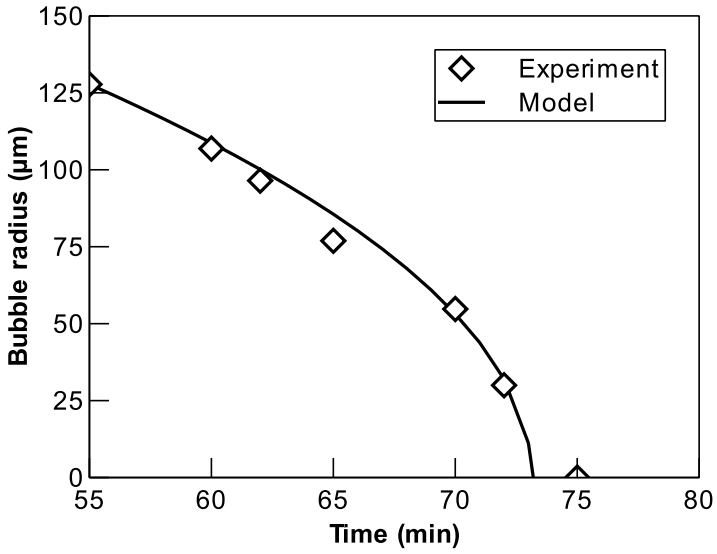


Figure 8.14: Example of the bubble contraction model fitted to experimental data: fabric PW-L, neat resin LEO 2376 and interleaved stacking configuration

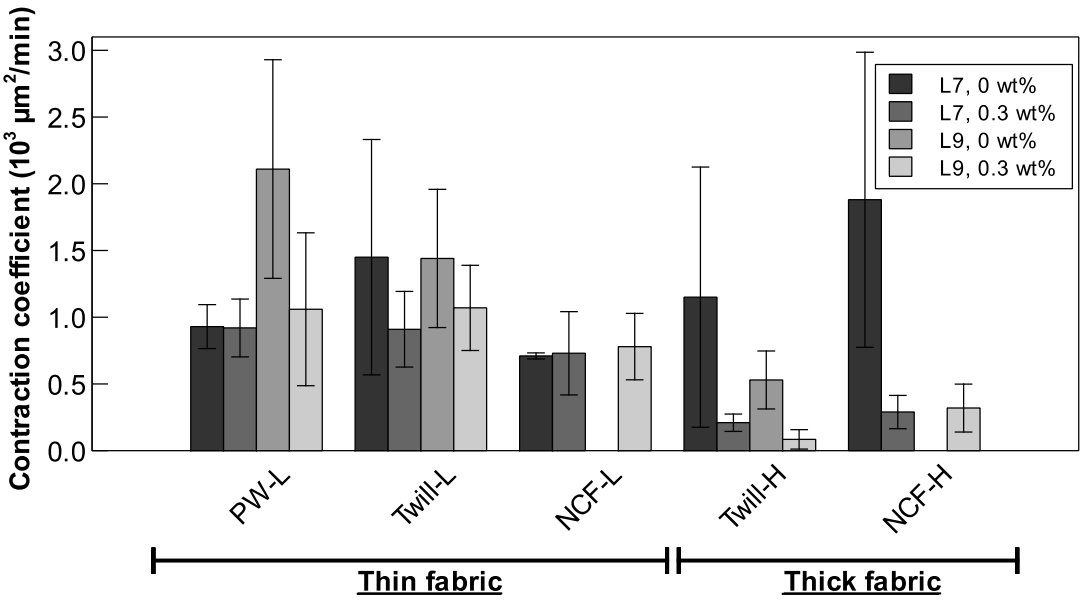


Figure 8.15: Bubble contraction coefficients for various fabric and resin combinations

The end of the contraction stage occurred before resin gelation and was followed by the equilibrium stage where remaining bubbles led to holes in PMCs. The transition from the contraction to equilibrium stages likely occurred due to the significant increase in resin viscosity caused by cross-linking. As Han and Yoo noted [171], the rate of change in bubble size decreases with increasing viscosity. Moreover, Wood and Bader showed that gas diffusion in epoxy reduces with increasing resin viscosity [172].

#### 8.2.2.3 Effect of fabrics on bubble collapse

Experiments showed that the void content in PMCs differed greatly depending on the type of fabric used. In addition, the extent of bubble contraction appears to be closely related to the fabric surface density. Results showed that thinner fabrics were better for void collapse and that bubbles featuring smaller radii have higher contraction rates. From these observations, it can be conjectured that the advantage of thinner fabrics lies in their ability to form smaller bubbles. As noted before (Section 8.2.1), bubbles settle in areas where they have sufficient space to grow unhindered, usually in inter-yarn gaps. The number and size of these gaps is linked to the geometry of the fabrics. As depicted in Figure 8.16, thinner fabrics feature more gaps in which bubbles can settle and these gaps are also smaller in size compared to those available with thicker fabrics. This helps limiting bubble coalescence, leading to smaller bubbles that feature high contraction rates.

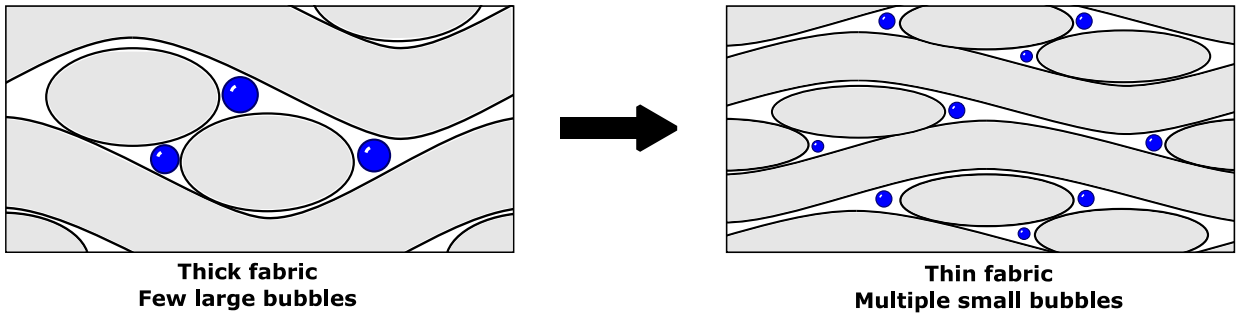


Figure 8.16: Schematics of a cross-section of a laminate with longitudinal and transverse yarns showing the effect of fabric thickness on bubble size and distribution

The surface density of fabrics also affected the contraction rate of bubbles. For example, for the same projected radius, bubbles in stacks featuring different types of fabrics did not undergo the same contraction. It is conjectured that this discrepancy comes from a variation in bubble sphericity. Considering that selected fabrics featured similar inter-yarn spacing, an increase in fabric surface density lengthens the inter-yarn gap only in the out-of-plane direction. Thus, for a same projected area, bubbles observed with thinner fabrics may actually have been flatter than those observed with thicker fabrics (Figure 8.17). A reduction in bubble sphericity would increase both the surface-to-volume ratio and diffusion. This will require further investigation since the bubble out-of-plane length was not measured in RFI experiments as observations were made only on the surface of the stacks. Nonetheless, it is clear that fabric architecture plays a key role in the final void content of PMCs.

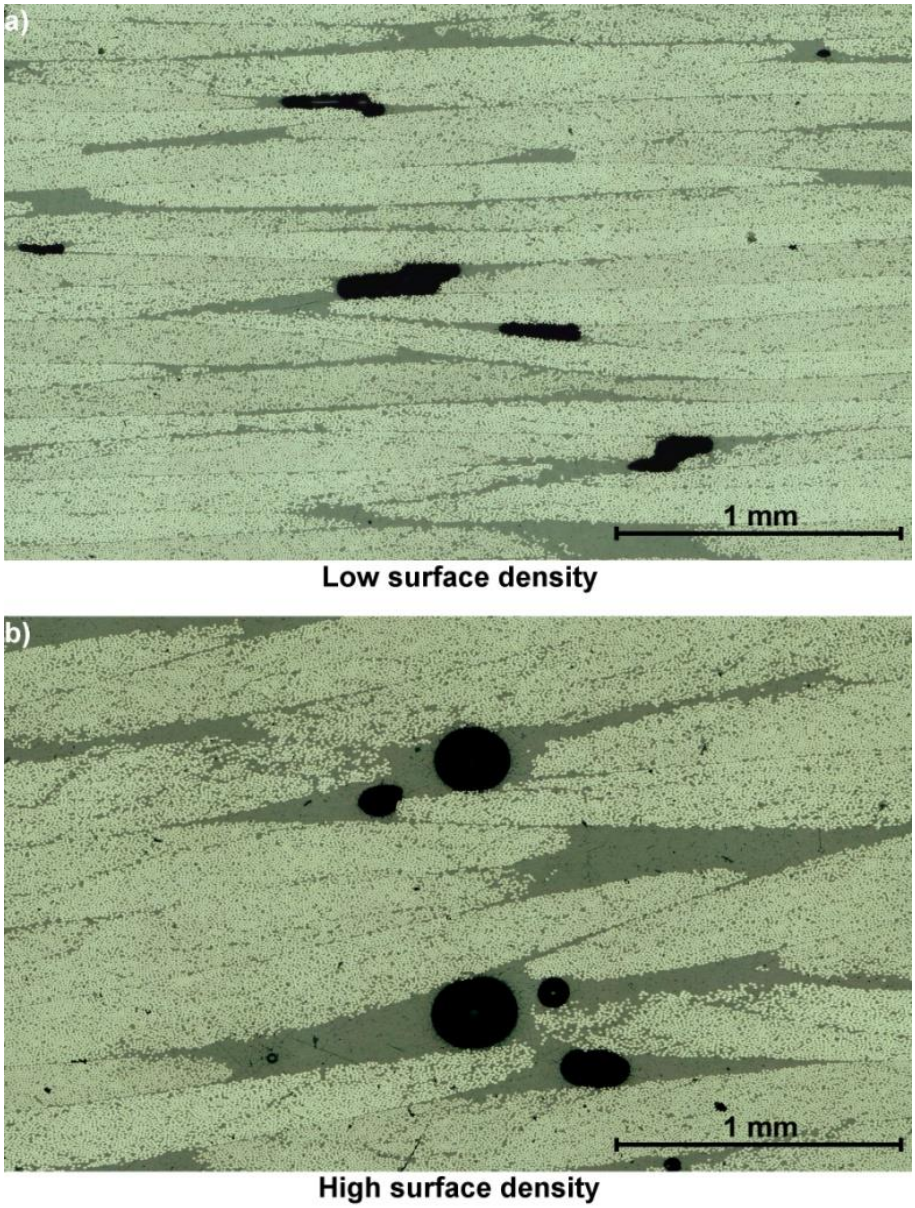


Figure 8.17: Cross-sections showing voids with varying degrees of sphericity in laminates featuring a) low surface density (Twill-L) and b) high surface density (Twill-H) fabrics

## 8.3 Double vacuum bagging

As mentioned in Section 8.2, the greatest hurdle to the fabrication of void-free PMCs is the presence of gasses trapped in resin films as-received. This could be mitigated through degassing of individual resin films prior to lamination; however, this is highly impractical because it affects the degree of cure of the resin and lengthens processing time. Material selection can help control void formation but it limits design choices. For example, voids can be minimised by using low surface density fabrics, but these fabrics increase labour and material costs. Thus, it would be desirable to find an alternative solution for reducing gas-induced voids in PMCs.

The alternative solution investigated in this work was the double vacuum bag method (section 3.2.4.5). Experiments consisted in monitoring the evolution of bubbles at the surface of resin films during RFI processing. All observations were made on the resin side of RFI stacks and testing was performed using interleaved RFI with stacks featuring resin LEO 2396 and fabric NCF-H. Three different cases were compared in this work: cases DB-1, DB-2 and DB-3.

### 8.3.1 Description of the double vacuum bagging cases

Case DB-1 (Figure 8.18) consisted of the baseline experiment and featured the standard RFI cure profile L-STD. Vacuum was pulled in the inner vacuum bag during the entire process and the outer bag was left at ambient pressure.

Case DB-2 (Figure 8.19) consisted of an experiment in which resin flow was delayed. The idea was to see whether keeping gas evacuation channels open for a longer period of time by reducing resin flow would enable greater degassing. The experiment consisted in heating the RFI stack for 100 min without pulling any vacuum. For the remainder of the cure, vacuum was pulled only in the inner bag. Thus, compaction was only applied 100 min after the start of the process.

Case DB-3 (Figure 8.20) consisted in an experiment in which resin flow was delayed but where gas diffusion could be increased by subjecting the stack to a vacuum. This was achieved by pulling a vacuum in both the inner and outer vacuum bags during the first

100 min of cure. This meant that no compaction was applied initially but that the resin was under low pressure. After that period, the vacuum was held in the inner bag but not in the outer bag resulting in compaction. It follows that out of all these cases, only case DB-3 required the double vacuum bagging method. The other methods can be achieved using a single vacuum bag.

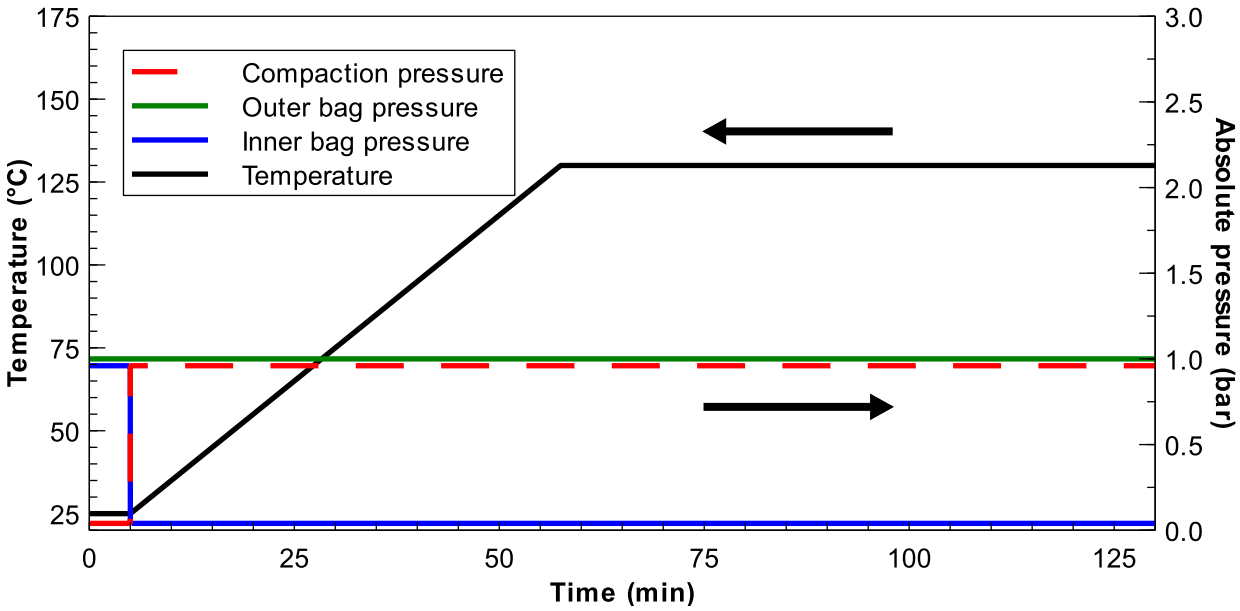


Figure 8.18: Double vacuum bagging case DB-1, standard RFI

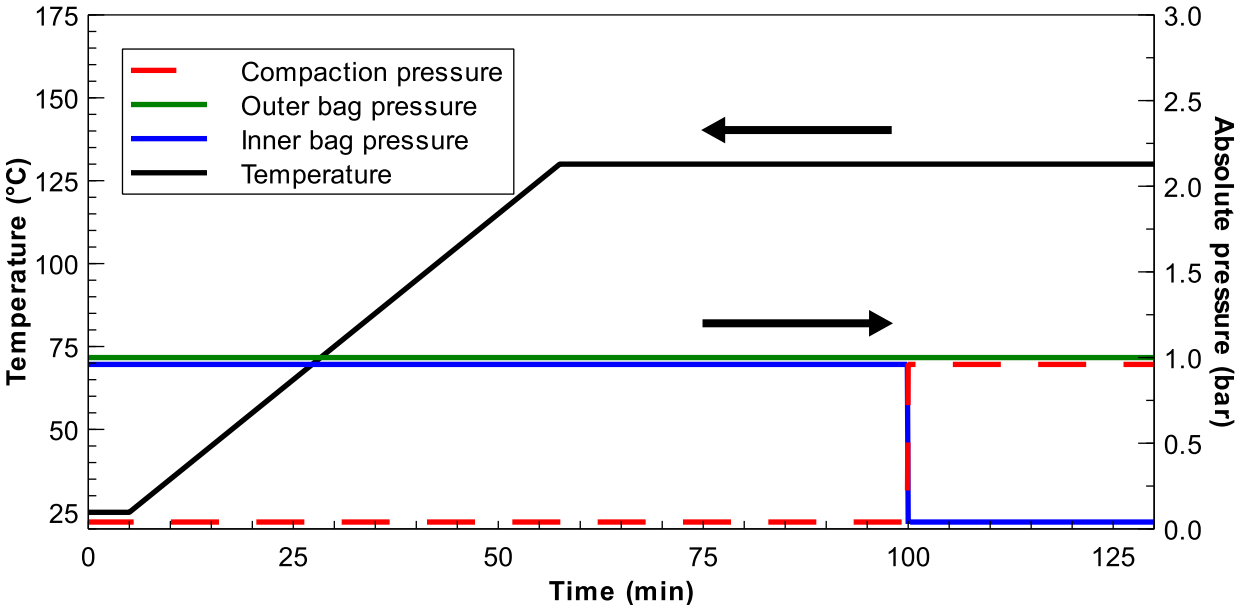


Figure 8.19: Double vacuum bagging case DB-2, delayed compaction

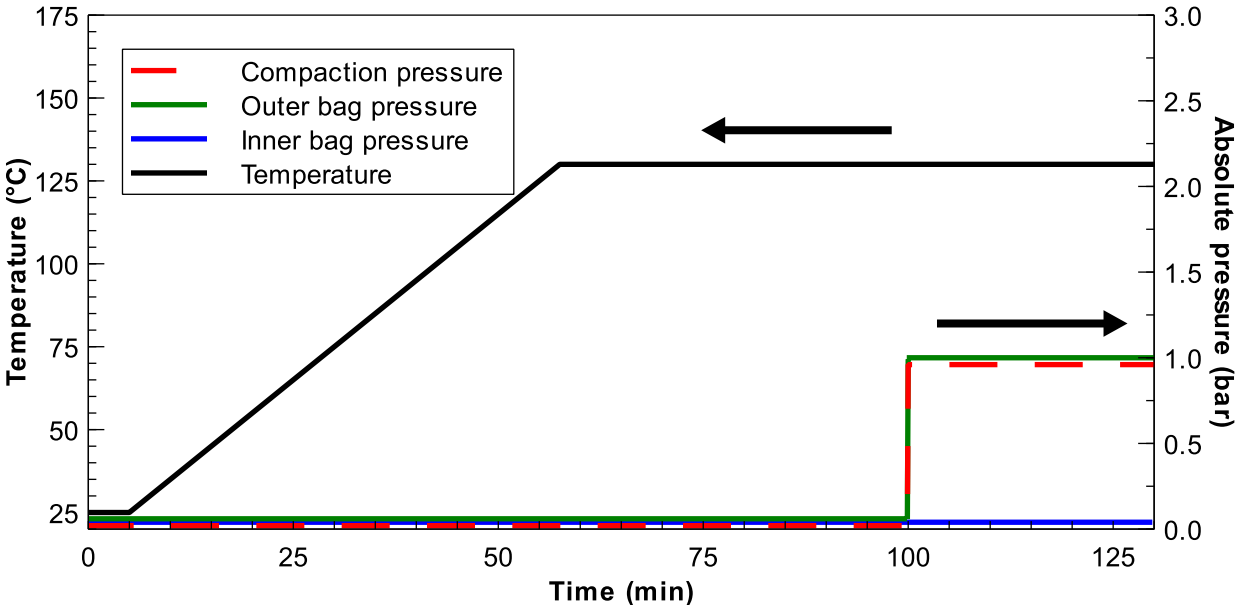


Figure 8.20: Double vacuum bagging case DB-3, degassing prior to compaction

### 8.3.2 Evolution of gas bubbles in double vacuum bagging

The evolution of gas bubbles in RFI stacks for the three cases is compared in Figure 8.21.

Case DB-1 featured the standard vacuum bagging method and the results were in agreement with those obtained in Section 8.2. Gas bubbles coalesced and grew in the initial stages of RFI. Bubbles then migrated in larger inter-yarn gaps where their growth was least restricted. The smallest bubbles dissolved before the first 40 minutes of processing while the bigger bubbles grew until 60 minutes, after which they contracted slowly until gelation. After processing, numerous bubbles remained in the composite.

**Figure 8.21: Evolution of out-of-solution gases in resin films during RFI processing for cases DB-1, DB-2 and DB-3**

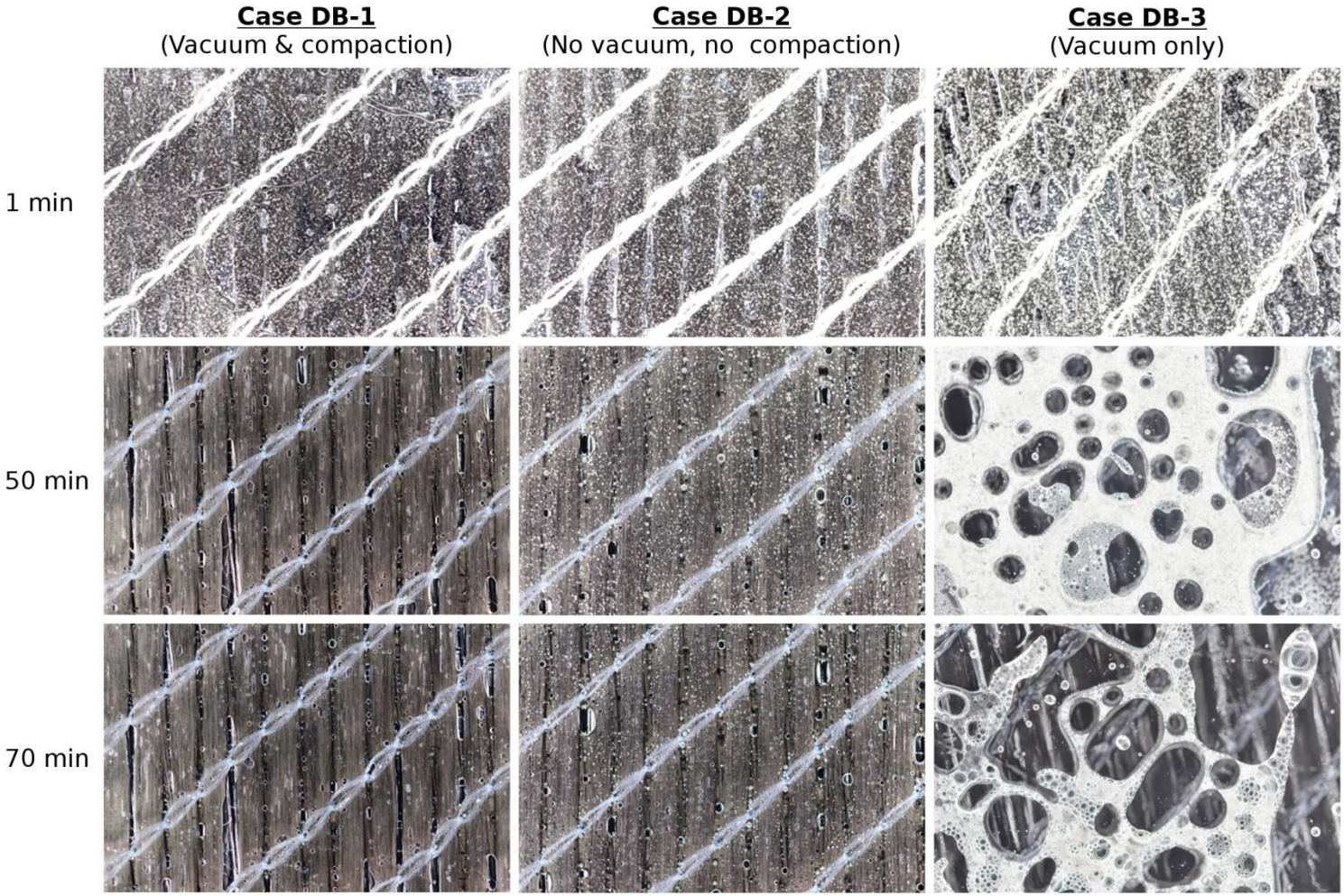

**Figure 8.21 (cont.): Evolution of out-of-solution gases in resin films during RFI processing for cases DB-1, DB-2 and DB-3**

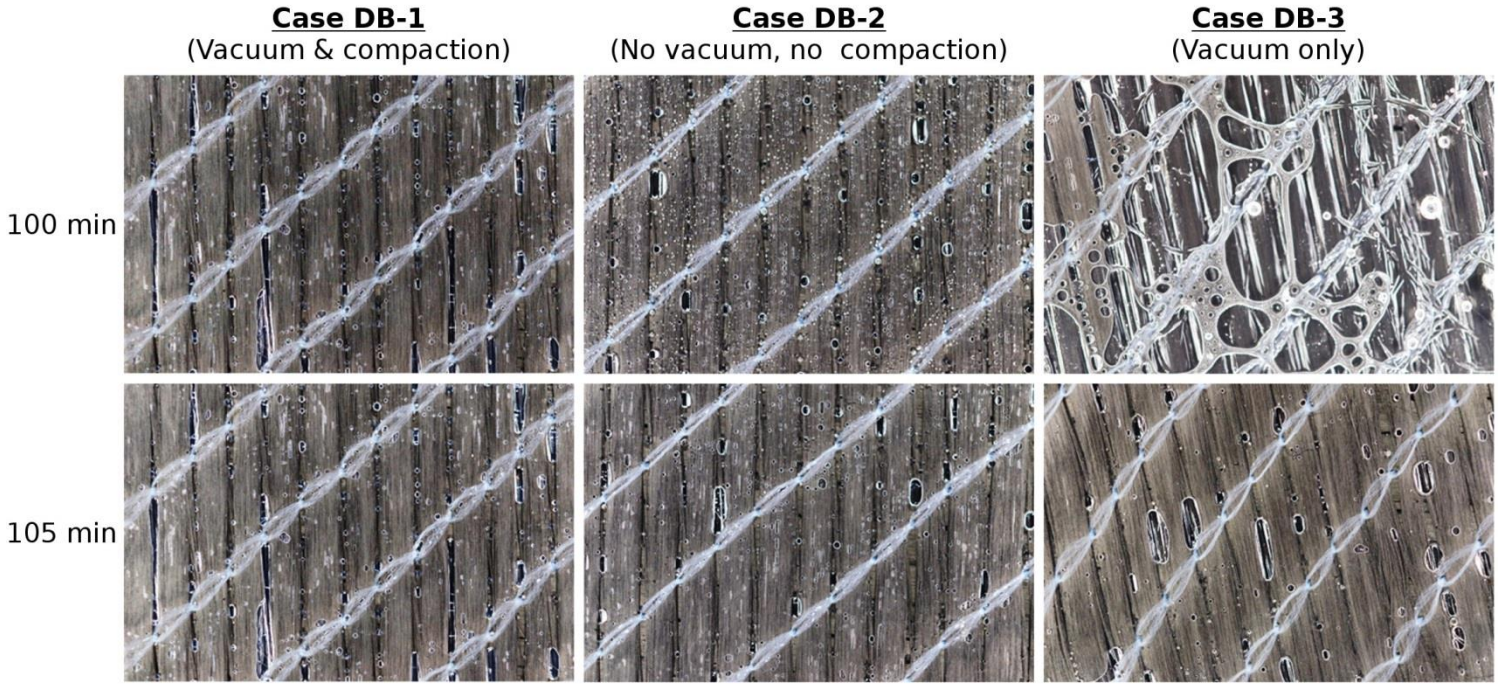

In case DB-2, gas bubbles coalesced and grew during the initial stages of RFI. However, coalescence was much less important than for case DB-1. This was caused by the lower amount of resin flow which reduced bubble migration. Consequently this limited coalescence and resulted in a greater amount of small bubbles populating the resin. At 100 min, when compaction was applied, resin flow in inter-yarn gaps occurred. This led larger bubbles to settle in inter-yarn gaps. In addition, bubble migration led to bubble coalescence, reducing the number of smaller bubbles in the stack. Qualitatively, following compaction, the size and number of bubbles appear similar to what was obtained in case DB-1. Hence, there was no noticeable increase in degassing from delaying compaction.

In case DB-3, the evolution of gas bubbles was highly different than that of the other two cases. Unlike cases DB-1 and DB-2, the resin was initially under low pressure. This caused massive growth of bubbles, leading to foaming. Smaller bubbles coalesced with larger ones, but despite close proximity, large bubbles barely merged together. Even though certain bubbles were massive and the resin film surrounding them was thin, bursting of bubbles was rare. Upon compaction, resin pressurised and bubbles shrank considerably. However, several large bubbles remained in inter-yarn gaps. Qualitatively, no extensive reduction of the amount of bubbles covering the surface of the stack was observed compared to what was obtained in cases DB-1 and DB-2. The only difference is that case DB-3 appears to features fewer microscopic bubbles than other cases.

### 8.3.3 Viability of the double vacuum bagging method

Two concepts for in-situ degassing in RFI were investigated through double vacuum bagging. They consisted of 1) delaying resin flow for keeping gas evacuation channels open for a longer period of time and 2) subjecting the resin to a vacuum for increasing gas diffusion. The prior concept was investigated with case DB-2 while case DB-3 applied the two concepts simultaneously. Unfortunately, none of the cases reduced surface voids in PMCs significantly compared with the standard bagging method of case DB-1.

It is conjectured that two main issues resulted in the underwhelming amount of degassing provided by the double vacuum bagging method. First, the method sought to delay resin flow for keeping gas evacuation channels open. The delay in compaction did

indeed prevent squeeze flow of resin in inter-yarn gaps, but it could not stop capillary flow in yarns due to a decrease in resin viscosity from the increasing process temperatures. Hence, the saturation of interconnected yarns blocked gas evacuation channels, limiting degassing. Second, even though some gas evacuation channels might have been opened for a longer period of time and the pressure difference between the resin and vacuum might have fostered greater diffusion, diffusion is still a relatively slow process as seen in Section 8.2. It is highly likely that the time provided for diffusion was too short for achieving any major amount of degassing. Hence, double vacuum bagging cannot be recommended as a potential method for reducing voids in PMCs while minimising processing time by not having a dedicated degassing step in the manufacturing process.

## 8.4 Remarks

The main contribution of this chapter is that it is the first to provide a thorough and complete analysis of void formation during RFI. This was achieved by studying the formation of flow-induced voids and volatile gas-induced voids in PMCs. In-situ observations of resin flow and out-of-solution gases, as well as the study of different resins and fabric reinforcements led to a high degree of confidence in the analysis. The analysis of void formation also provided the knowledge required for explaining the differences in porosity observed in PMCs presented in Chapter 6.

Flow-induced voids were caused by incomplete saturation of RFI stacks and by over-bleeding. The major findings of the work regarding such voids are:

- High surface density fabrics feature thick yarns that are difficult to saturate with high viscosity resins, leaving micro-voids in PMCs.
- Resins featuring very low viscosity are more inclined to wicking which results in over-bleeding and macro-voids in inter-yarn gaps.
- Over-bleeding parameter *OB* was proposed to assess risks of over-bleeding.

Gas-induced voids were the most common source of voids in PMCs. They are caused by out-of-solution gases that remain in the resin after gelation and are attributed to the

initial volatile content in resin films. The major findings of the work regarding the formation of such voids are:

- Four kinematic stages for out-of-solution gases occur during RFI: 1) bubble migration, 2) bubble growth, 3) bubble contraction and 4) equilibrium.
- Bubbles migrate in the direction of resin flow.
- Bubbles move slightly faster than resin flow which can lead to degassing. Longer flow distances enable greater degassing during processing, explaining the lower porosity of PMCs made with bulk RFI than PMCs made with interleaved RFI.
- Bubble growth is mostly attributable to bubble coalescence and thermal expansion.
- Bubble contraction is caused by gas diffusion into the resin across bubble boundary. Smaller bubbles can dissolve more easily in the resin due to their higher surface-to-volume ratio that increases diffusion.
- Bubble shape is affected significantly the by fabric architecture.
- Low surface density fabrics lead to smaller and more numerous inter-yarn gaps that reduce coalescence and size of bubbles. This improves gas dissolution significantly.

This chapter also investigated the use of the double vacuum bagging method for improving degassing of the resin during the RFI process. The objectives were to provide air evacuation channels for degassing and subjecting the resin to low pressures for increasing diffusion. Unfortunately, no significant reduction in surface voids were observed with the double vacuum bagging method compared to the use of a single vacuum bag. Hence, it appears that without adding a dedicated degassing step to RFI, the only method for reducing gas-induced voids in PMCs is through material selection, such as using low surface density fabrics for controlling dissolution of gases in the resin or using resins with a very low volatile content.

# Chapter 9

## Distribution and filtration of CNTs in PMCs

Preliminary work on flat laminates in Chapter 6 showed that CNTs can improve the interlaminar shear strength (ILSS) of PMCs. On average, improvements of 8.5% to the ILSS were observed which is underwhelming considering the intrinsic properties of individual CNTs. Results also showed that the added benefits of CNTs depended greatly on the fibre reinforcements and resins used. This chapter discusses how RFI processing can affect the distribution of CNTs in multi-scale PMCs and why improvements to the ILSS were limited.

The investigation of RFI for the fabrication of multi-scale composites was divided into three parts based on the stacking configuration and type of resin flow that can occur during RFI. Two main types of flow were studied for bulk RFI, in-plane flow and through-thickness flow. Lastly, through-thickness flow for interleaved RFI was investigated. For visualisation, Figure 9.1 depicts stacking configurations leading to these types of flow for a stiffened PMC. A list of processing experiments performed for this work appears in Table 9.1.

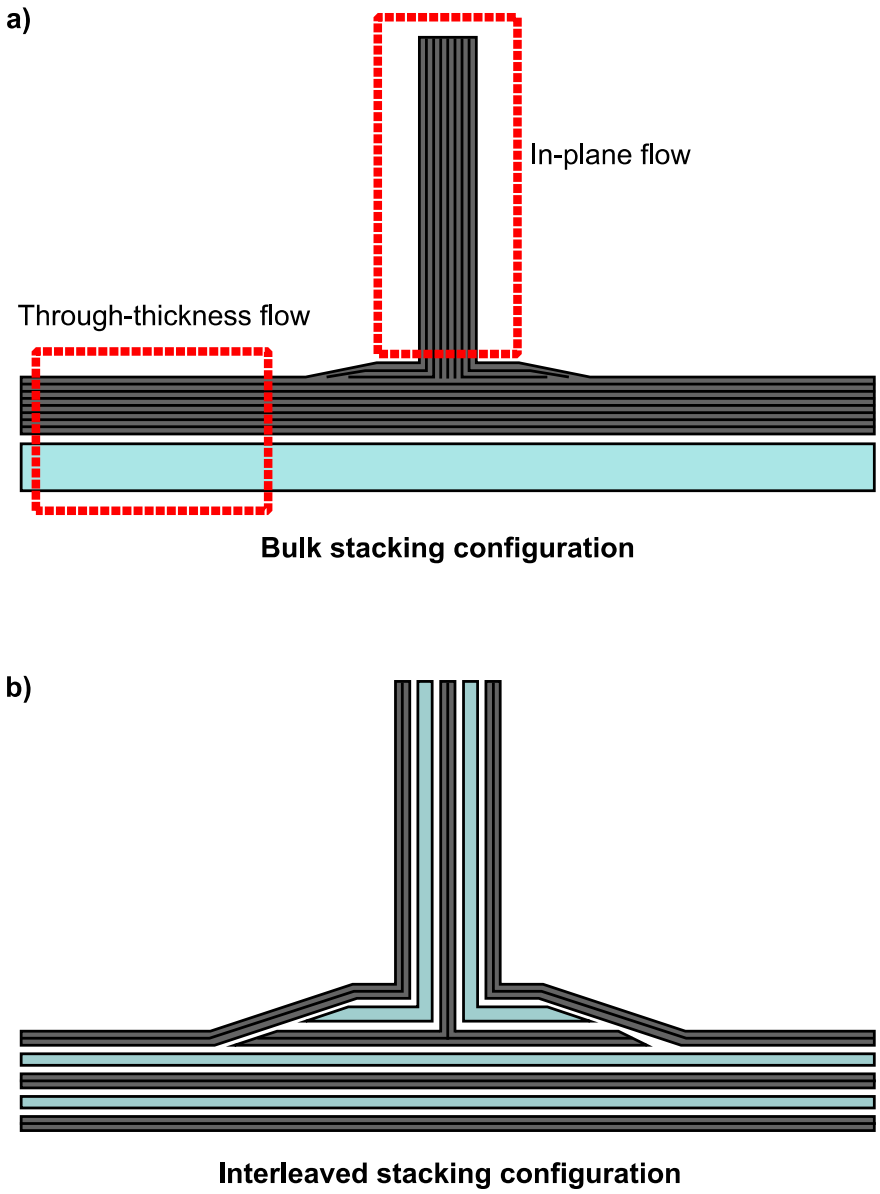


Figure 9.1: Stacking configurations for a blade-stiffened panel showing the distribution of fabric (grey) and resin (blue) layers, a) bulk stacking configuration with highlighted regions of through-thickness flow in the skin and in-plane resin flow in the stiffener, and b) interleaved stacking configuration

Table 9.1: List of experiments performed for the distribution of CNTs in multi-scale PMCs

| Stacking configuration | Flow direction | Resin | Fabric | Dimension |
|---|---|---|---|---|
| Bulk | In-plane | LEO 2397 | Twill-G | 120 mm length |
| | Through-thickness | LEO 2397 | Twill-G, Twill-L, NFC-H | 10 mm thick |
| | Through-thickness | LEO 2377/2397 | PW-L, Twill-L, Twill-H, NCF-L, NCF-H | 4 mm thick |
| Interleaved | Through-thickness | All LEO resins | PW-L, Twill-L, Twill-H, NCF-L, NCF-H | 4 mm thick |

## 9.1 Bulk RFI: in-plane infusion

### 9.1.1 Description

LEO 2397 resin was infused in-plane across fabric Twill-G. Infusion was performed in a closed cavity with a fibre volume fraction of 65%. Glass fibres were used for better contrast with CNTs, improving the visual observation of filtration.

### 9.1.2 Results

The resin travelled a maximum distance of 12 cm before gelation. Strong filtration of CNTs was observed in the resulting laminate as indicated by a change in matrix colour from pitch black near the resin inlet to yellow at the outlet (Figure 9.2). Analysis of surface images of the PMC obtained from transmitted light microscopy was used for characterising filtration. Three images were taken every 12 mm from the inlet: one image at each edges and one in the middle of the PMC. Results for the fraction of the surface that was pitch black (Figure 9.3) showed that filtration started before resin travelled a distance of 7.5 cm from the inlet. In addition to the change of colour, the surface of the composite also changed texture. At the inlet the surface was smooth but 4 cm away pin holes populated the surface. The transition in surface texture resulted from a change in the type of resin flow,

from viscous to capillary. The filtration happened mostly in the zone of capillary resin flow. It is thus believed that the change from viscous to capillary flow accentuated CNT filtration because gaps between fibres are much narrower than those between yarns, which increases filtration as discussed later in Section 9.2.

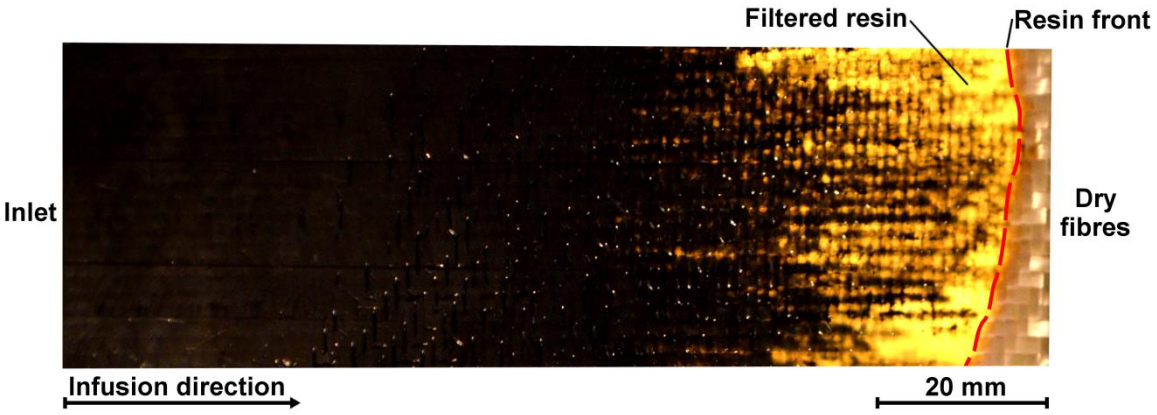


Figure 9.2: CNT filtration after in-plane resin infusion

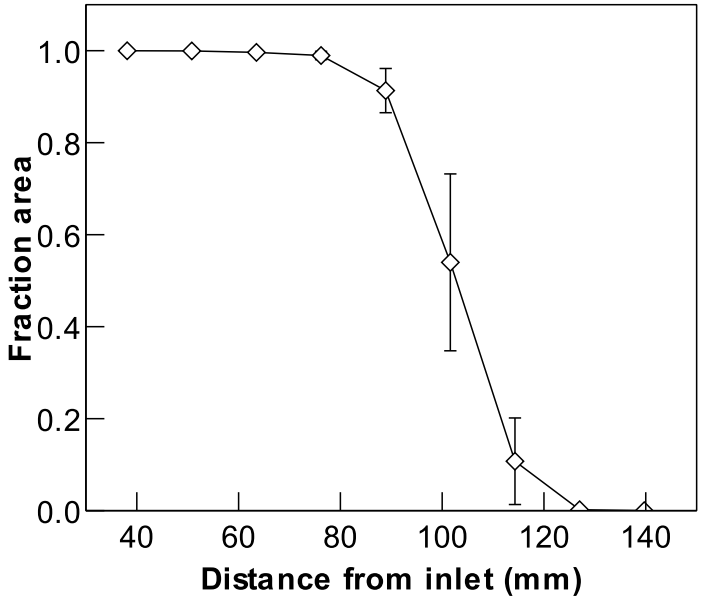


Figure 9.3: Fraction of the surface of the in-plane infusion laminate covered in dark areas based on the distance from the resin inlet

## 9.2 Bulk RFI: through-thickness infusion

### 9.2.1 Description

Two groups of experiments were performed for assessing the viability of bulk RFI for fabricating multi-scale composite skins. The aim of the first group of experiments was to investigate CNT filtration for an extreme case where a PMC skin was 10 mm thick. The aim of the second group of experiments was to characterise the effect that the type of fabric has on CNT filtration, and was performed on 4 mm thick PMCs (Table 9.1).

### 9.2.2 CNT filtration in 10 mm thick laminates

Three 10 mm thick multi-scale laminates were fabricated successfully despite the higher viscosity of the LEO 2397 CNT modified resin. The laminates featured different reinforcements with distinct types of fibre, architecture and surface density.

Visual inspection of the laminates showed that inter-yarn regions were black on both the resin and fabric sides of the composites, suggesting that some CNTs flowed across the entire laminate during RFI. This was particularly apparent for the laminate featuring glass fabric Twill-G (Figure 9.4) where the out-of-plane surfaces, which are normally clear without CNTs, were now completely black.

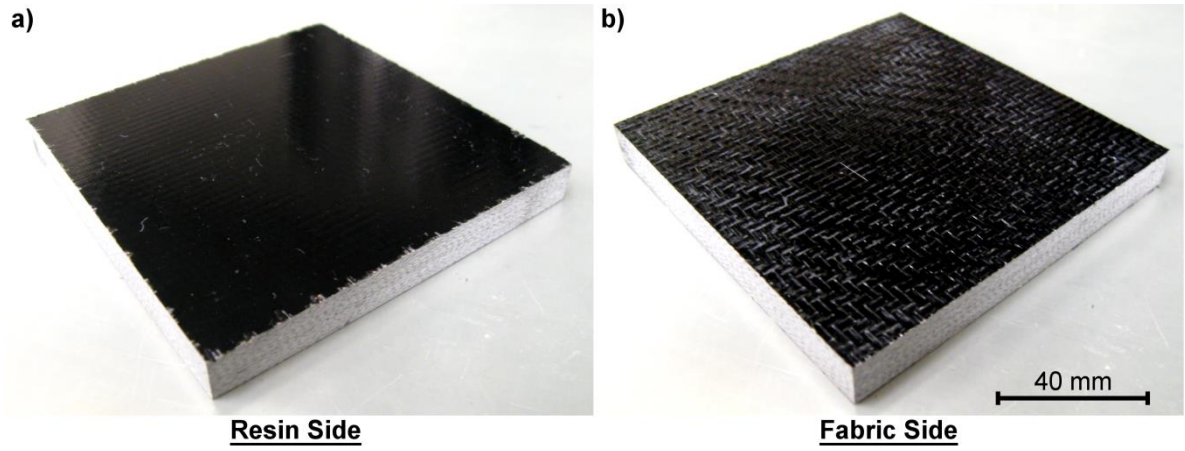


Figure 9.4: Thick glass composite after through-thickness infusion using the bulk stacking configuration, a) resin side and b) fabric side

Thin cross-sections of laminates were inspected using transmitted light microscopy. The glass fibres of fabric Twill-G offered better contrast for observing CNTs (Figure 9.5), but carbon fibre laminates also showed similar distribution of CNTs (Figure 9.6). Results showed that the resin films lost their relatively uniform distribution of CNTs (Section 4.4) during processing. This agrees well with observations made on the nano-modified resin alone, without fabric reinforcements, by CRIAQ COMP-501 team members based at McGill University [173].

Segregation of the resin and CNTs led to two types of resin regions; clear resin regions with low CNT content and dark resin regions rich in CNTs. The CNT rich regions were surrounded by low CNT regions and took the form of clusters that were distributed within inter-yarn regions, across the entire thickness of the laminates. Very few dark regions were seen inside yarns and those that were are located mostly in the outer borders of yarns. Hence, the tight fibre network of yarns was an effective filter for CNTs.

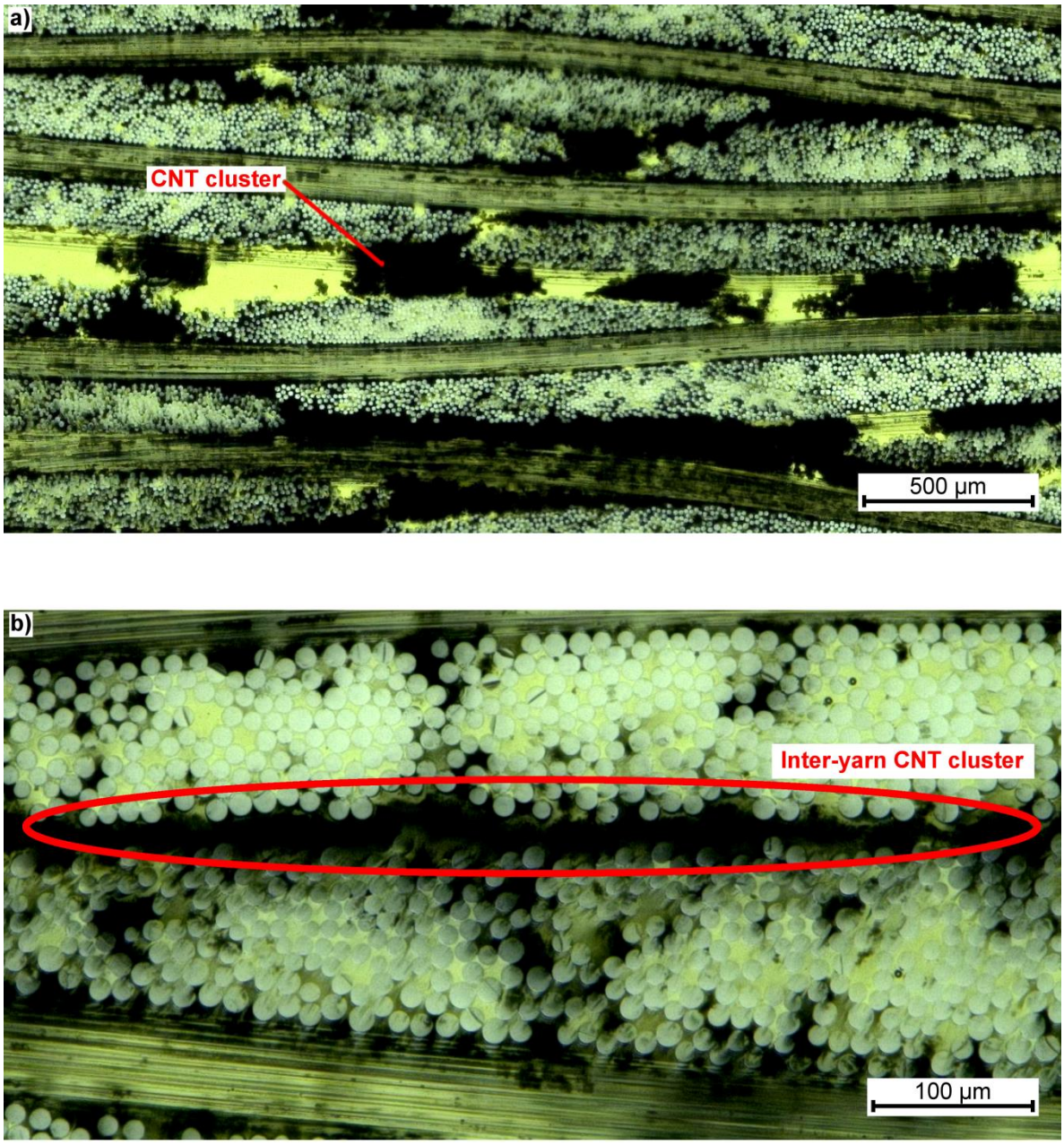


Figure 9.5: Cross-section of Twill-G 10 mm thick laminate observed through transmitted light microscopy showing CNTs distributed in a) multiple fabric layers and b) in yarns

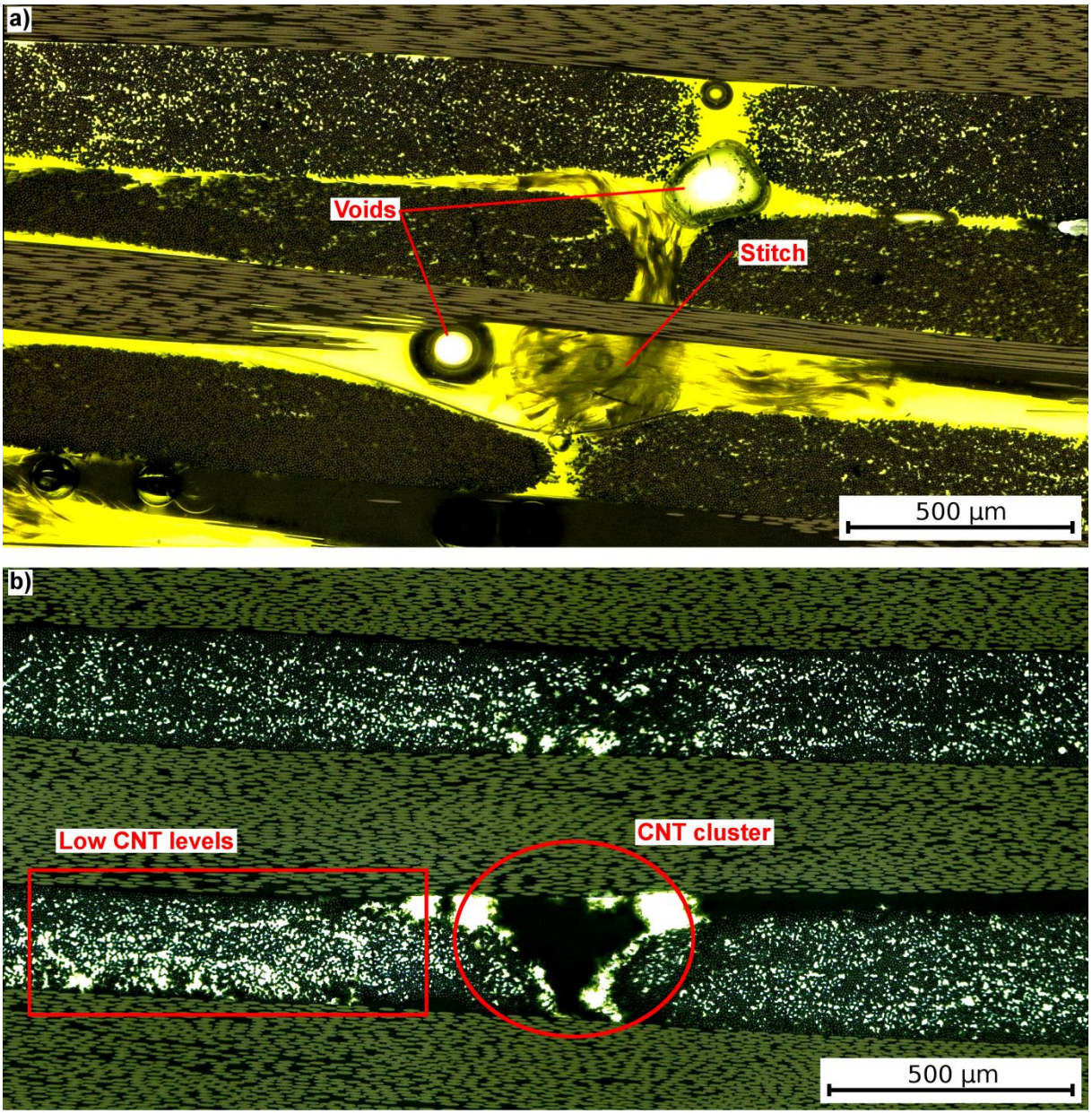


Figure 9.6: Cross-section of NCF-H laminates observed through transmitted light microscopy showing a a) laminate without CNTs (resin LEO 2396) and b) laminate with CNTs (resin LEO 2397)

Image contrast analysis was used for quantifying filtration across the glass fibre laminate. Results from 4 cross-sections (Figure 9.7) showed that the fraction area of CNT rich regions was high near on the resin film side of the stack. The fraction area then reduced steadily until equilibrium was reached. Thus, the first few fabric layers were responsible for most filtering. Any CNT clusters that were not filtered by these initial

fabric layers were likely sufficiently small to avoid filtration altogether. A similar behaviour was observed for in-plane resin flow by Zeiler et al. [129] . Unfortunately, this behaviour could not be verified for the carbon fibre laminates because of a lack of contrast between the carbon fibres and the CNTs.

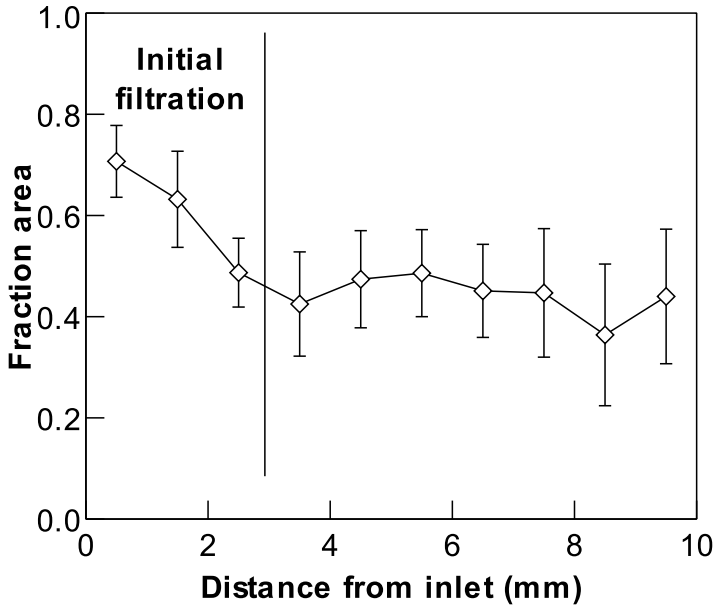


Figure 9.7: Fraction area of CNT rich regions for cross-sections of 10 mm thick Twill-G laminate based on the distance from the resin inlet

### 9.2.3 Effect of fabrics on CNT filtration

The effect that the geometry of fabrics has on CNT filtration during through-thickness flow in bulk RFI was studied on 4 mm thick laminates. A single laminate was studied per carbon fibre fabric (Table 9.1).

Visual inspection of the surface of laminates, both resin and fabric sides, showed that inter-yarn regions were populated with dark CNT clusters (Figures 9.8 and 9.9). The amount of CNT clusters that were observed differed between the fabric and resin sides of the laminates, suggesting filtration.

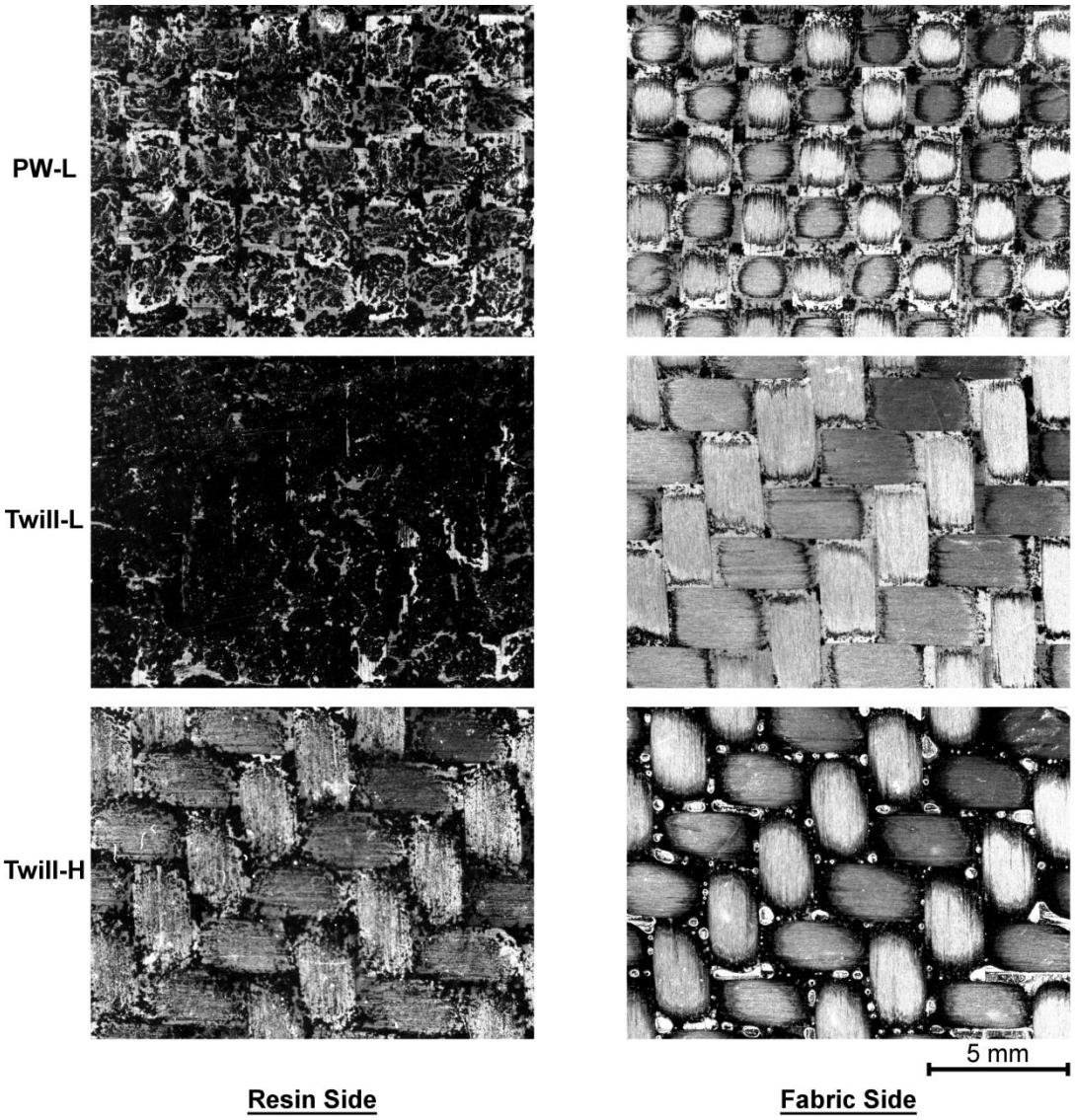


Figure 9.8: CNT distribution on the resin and fabric sides of bulk RFI laminates featuring woven fabrics

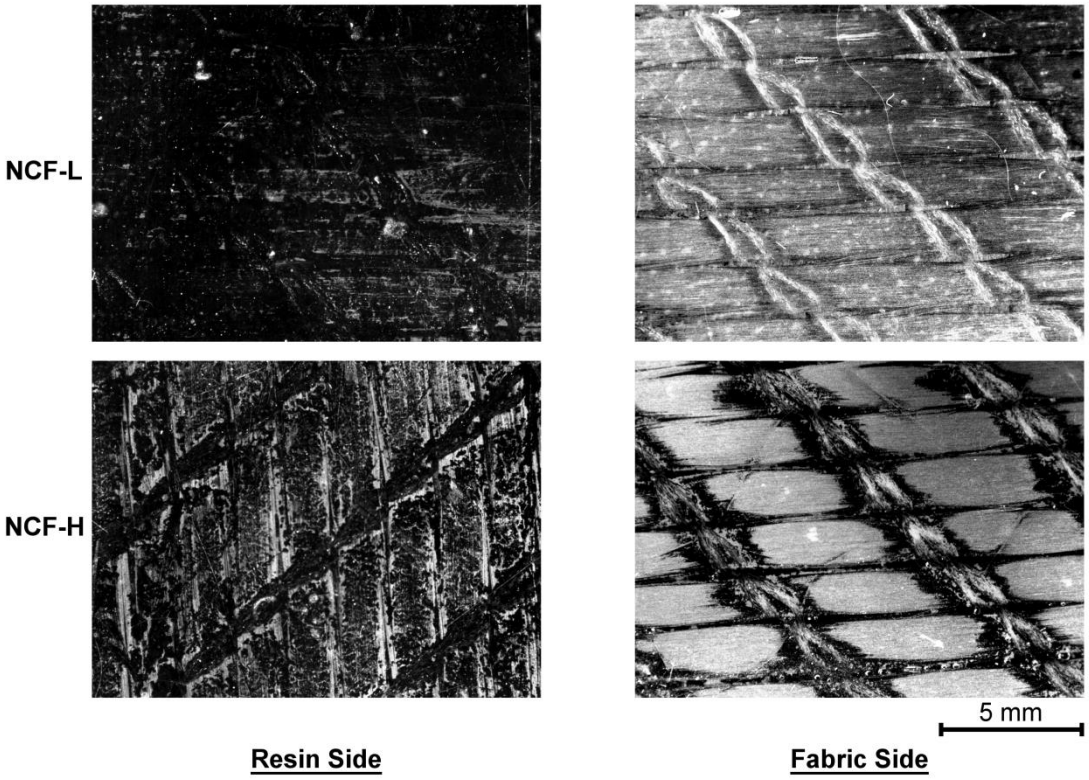


Figure 9.9: CNT distribution on the resin and fabric sides of bulk RFI laminates featuring NCFs

Quantitative analysis of CNT filtration was achieved by using image analysis, comparing the fraction area of dark regions between the top (fabric side) and bottom (resin side) of the laminates. More than 10 measurements were taken per laminate. Results appearing in Figure 9.10 show significant influence of the fabrics on CNT filtration. For example, no filtration was observed for the laminate featuring fabric Twill-H, while complete filtration occurred with fabric NCF-L. Results show that for both twills and NCFs, filtration decreased with increasing fabric surface density. Twill fabrics also led to less filtration than NCF fabrics. Finally, comparing fabrics PW-L and Twill-L, it can be seen that the reduction in fabric cover factor reduced filtration markedly. These differences between fabrics are all explained by the number and size of inter-yarn gaps, similarly to the kinematics of resin flow (Section 7.4). The interlacing, cover factor and surface density have a direct effect over the size of inter-yarn gaps and particle size that are filtered. Surface density also affected tortuosity of the resin flow and longer resin flow increases

filtration. It is also interesting to note that trends for CNT filtration correlate with those of transverse fabric permeability values (Section 5.4).

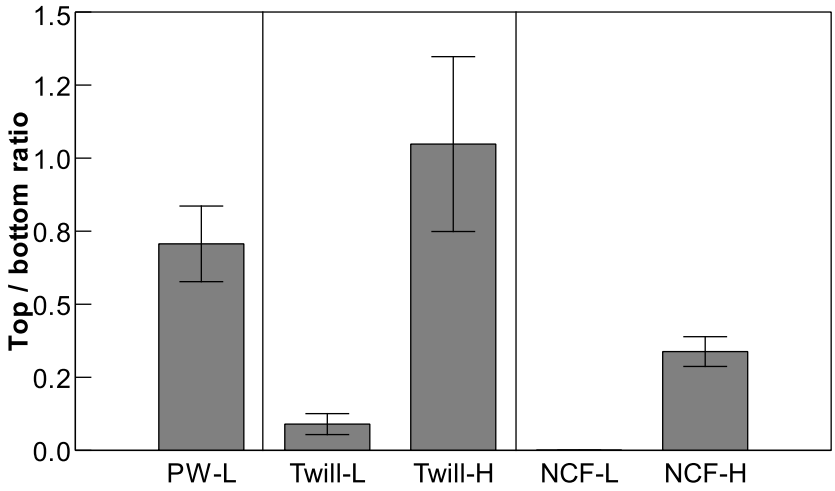


Figure 9.10: Ratio of surfaces of the fabric side to resin side that are covered in dark CNT rich areas for 4 mm thick bulk RFI laminates

## 9.3 Interleaved RFI

### 9.3.1 Description

CNT distribution in laminates made with interleaved RFI was studied for several carbon fibre fabrics and resin formulations (Table 9.1). CNT distribution was studied by inspecting the surfaces and cross-sections of laminates.

### 9.3.2 Results

Inspection of laminate cross-sections showed that similarly to bulk RFI (Section 9.2) many CNTs agglomerated and populated inter-yarn gaps (Figure 9.11a). Very few CNT clusters were observed inside yarns (Figure 9.11b). However, unlike bulk RFI, a uniform

distribution of CNT clusters was observed across the thickness of laminates due to the interleaving of resin films.

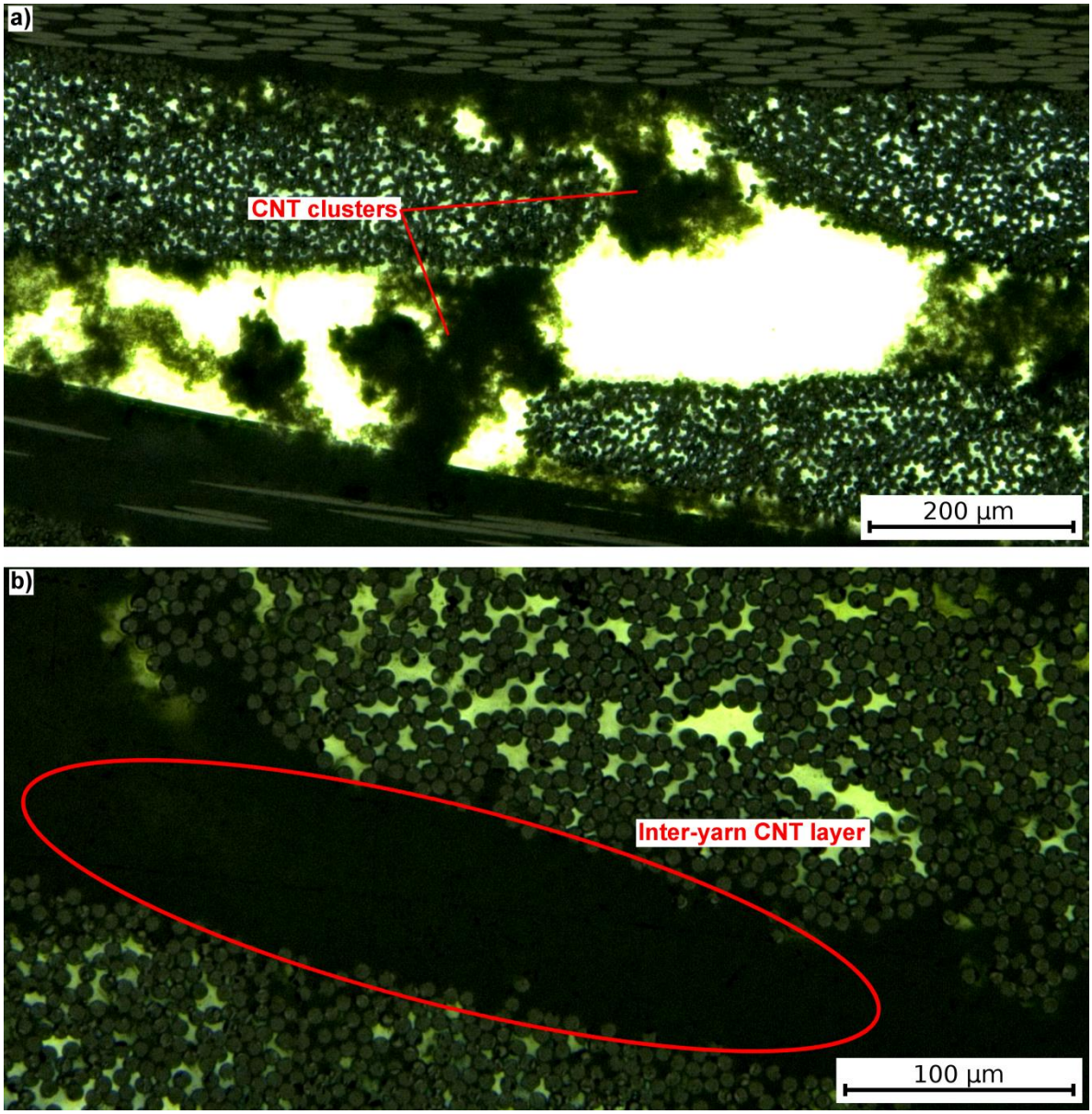


Figure 9.11: Cross-section of NCF-H laminate made with interleaved RFI observed through transmitted light microscopy showing CNTs distributed in a) inter-yarn gaps and b) in yarns

A qualitative comparison of the surface coverage of CNTs in laminates made with interleaved and bulk RFI appears in Figure 9.12. Results show that the coverage of dark areas in laminates made with interleaved RFI falls between that of the resin and fabric sides

of laminates made with bulk RFI, with the exception of laminates made with fabric Twill-H due to the absence of filtration. This was expected as interleaving reduces resin flow distances, limiting filtration and ensuring a more uniform distribution of CNTs. In addition, results do not show much difference in the fraction area of resin CNT rich regions between the LEO 2377 and LEO 2397 resins, suggesting they both had a similar effect on CNT clustering.

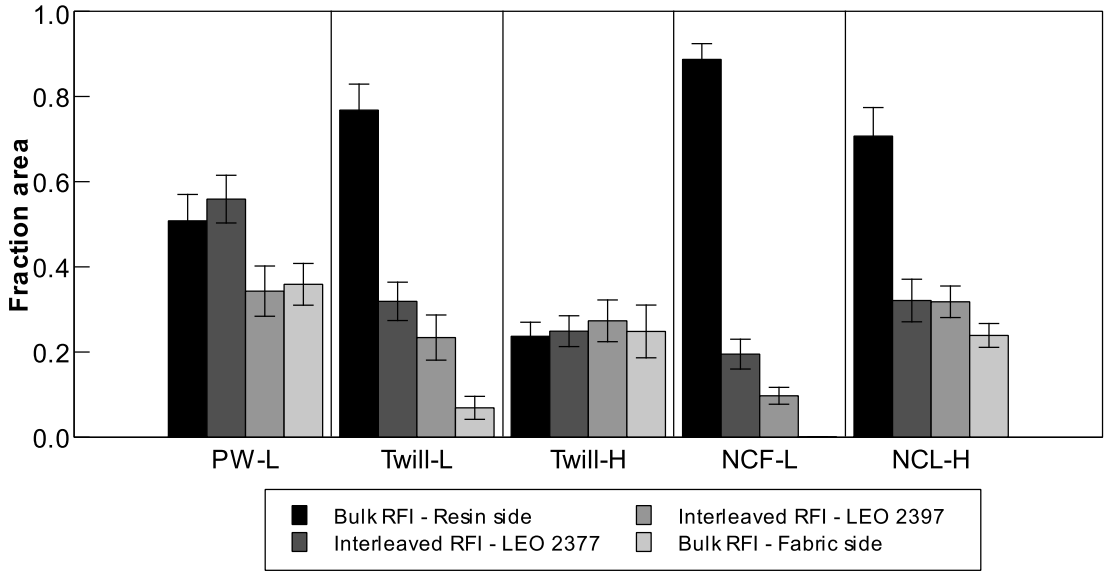


Figure 9.12: Fraction area of dark regions at the resin and fabric surfaces of bulk RFI laminates, and surfaces of interleaved RFI laminates made with LEO 2377 and LEO 2397 resins

## 9.4 Discussion

### 9.4.1 Clustering and filtration

Bulk and interleaved RFI were investigated for fabricating multi-scale composites. Results showed that in the case of bulk RFI, significant filtration of CNTs occurred during in-plane and through-thickness resin flow across fabric reinforcements. Despite a more uniform distribution of CNTs when using interleaved RFI due to the shorter distances

travelled by the resin during infusion, CNT distribution in PMCs remains heterogeneous. It was found that CNTs in PMCs made by either bulk or interleaved RFI grouped in clusters within inter-yarn gaps, and that few CNT clusters were located inside yarns. The lack of a high concentration of CNTs inside yarns results from filtration by the dense fibre network in yarns. In-situ observations of resin flow showed that yarns are particularly effective to filter CNT clusters. As seen from Figure 9.13, during infusion CNT clusters are stopped at the yarn boundaries creating a black outline around yarns. It is believed that such accumulation of CNTs can restrict resin flow, explaining why greater capillary resin flow was observed with CNT-modified resins as opposed to neat resins during bulk RFI (Section 7.3).

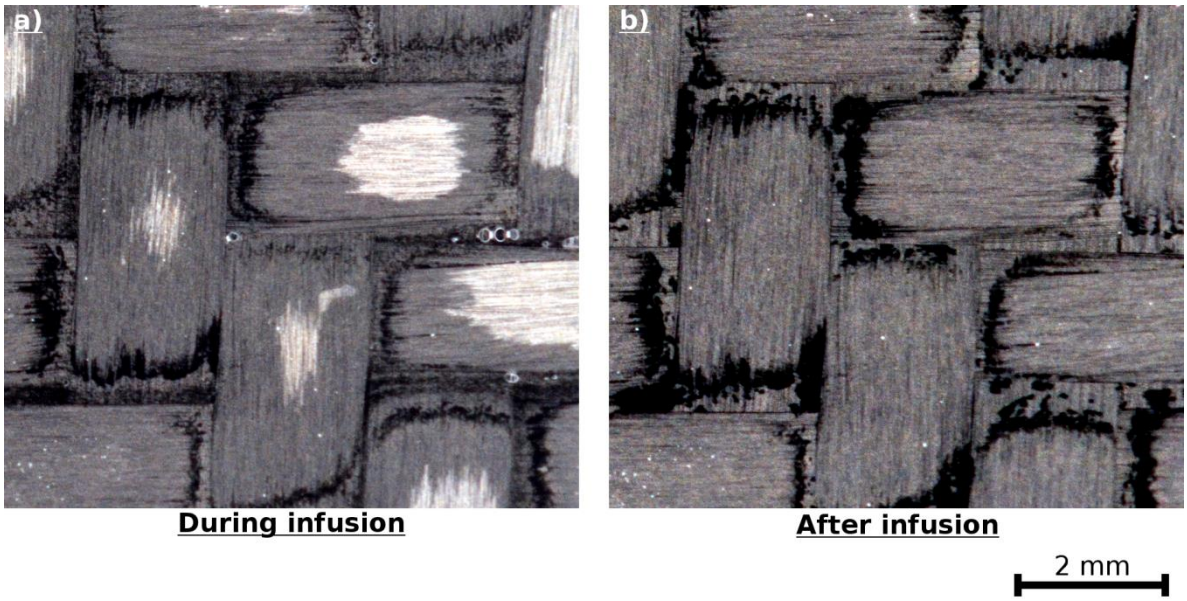


Figure 9.13: CNTs massing at the yarn boundaries due to filtering, showed a) during infusion and b) after infusion for bulk RFI with LEO 2397 resin and Twill-L fabric

Achieving a more uniform distribution of CNTs in composites requires the elimination of clusters. The inspection of the resin films as-received (Section 4.4) showed that initially, CNTs were well dispersed in the resin, suggesting that CNT clustering occurred during processing. This was confirmed by in-situ observations of resin flow showing that at a specific temperature, CNTs agglomerate. Visually, the transition consisted of the black coloured resin becoming a clear resin populated with black globules (Figure 9.14). The agglomeration coincided with the reduction in resin viscosity due to the

increase in temperature (Section 4.5). At lower resin viscosities, CNTs have more mobility and there are no forces sufficiently strong to prevent CNT flow. CNTs then agglomerate together due to attraction forces that seek to reduce the surface energy of the system. Based on caul plate temperatures, CNT agglomeration occurred around 80°C.

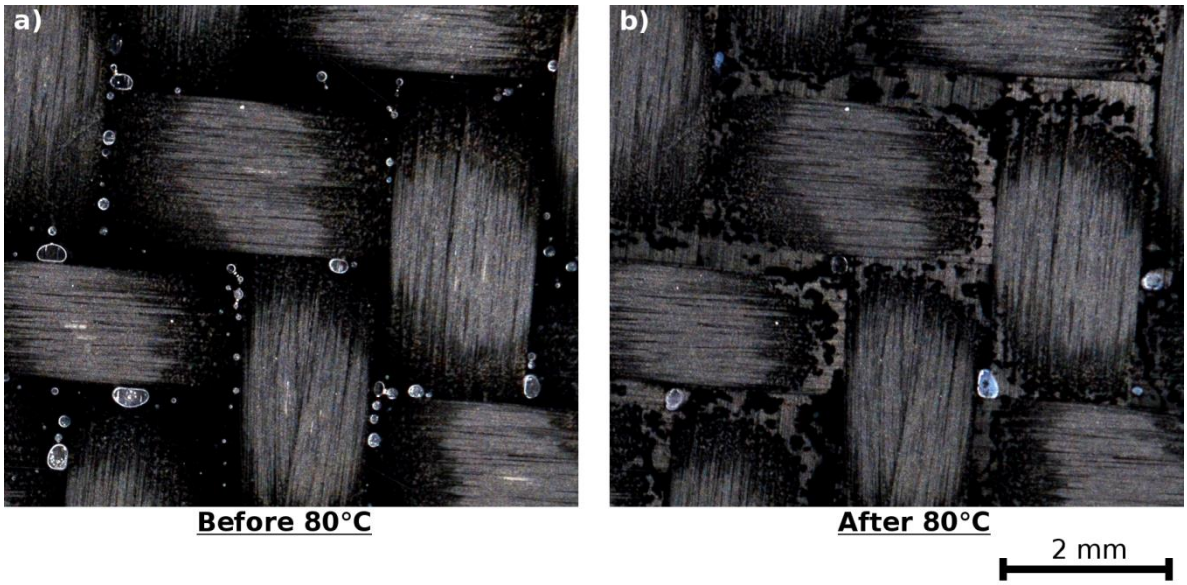


Figure 9.14: Comparison of the CNT distribution at the surface of a laminate featuring Twill-L fabric and LEO 2377 resin during processing, a) before reaching 80°C, b) after reaching 80°C

The investigation of multi-scale composites revealed that three different types of CNT flow can occur during fabrication (Figure 9.15). These types of flow occur sequentially but depending on processing conditions they may not all be present.

Stage 1 describes CNT flow at the beginning of RFI. CNTs flow with the resin in inter-yarn gaps. Uniformity of the CNT distribution remains equivalent to that observed in the resin films as-received due to the low initial processing temperatures. At that point, high resin viscosity and low yarn permeability prevent significant resin flow inside yarns. Resin that managed to flow inside yarns is able to carry CNTs without significant filtering if CNTs are well dispersed. This stage was observed at the beginning of all in-situ interleaved RFI flow experiments, but no significant signs of it remained after cure due to the occurrence of Stage 2.

Stage 2 describes CNT flow after clustering. As processing temperatures increase, resin viscosity decreases and CNTs agglomerate due to increased mobility. The lower viscosity enables faster and better resin flow inside yarns but significant CNT filtering occurs in yarns because CNT clusters are much wider than inter-fibre gaps. Hence, at that point, no significant amount of CNTs can penetrate inside yarns and those CNTs flowing in inter-yarn gaps are grouped in clusters, leading to heterogeneous properties in the resin matrix. Results showed that CNT filtering also occurred in inter-yarn gaps and that it influenced by the type of fabric used. Actually, there was a direct correlation between the amount of inter-yarn CNT filtering and the transverse permeability of fabrics for through-thickness flow. Similarly to resin flow, filtration is affected by the size and number of inter-yarn gaps, as well as tortuosity. For example, gaps act like a sieve that filters specific size of CNT clusters, where narrower gaps are able to filter smaller CNT clusters. Similarly, increasing the tortuosity of resin flow increases the probability of filtration. In this work, Stage 2 was observed in all multi-scale PMCs.

Stage 3 describes CNT flow when resin viscosity reduces to such extent that capillary forces become dominant over viscous forces. In this case, resin flow occurs predominantly inside yarns where CNT clusters cannot progress, leading to important filtering. This stage only occurs if resin flow is not complete upon reaching these low resin viscosities. In this work, this was only observed in bulk RFI with through-thickness resin flow in low permeability fabrics, and during in-plane flow. In addition, it is believed that Stage 3 can occur earlier if CNT clusters become so large that they restrict flow in inter-yarn gap. Based on these three stages, it follows that it is best to complete fabrication of multi-scale PMCs in Stage 1 only in order to maximise the uniformity of CNT distribution in PMCs.

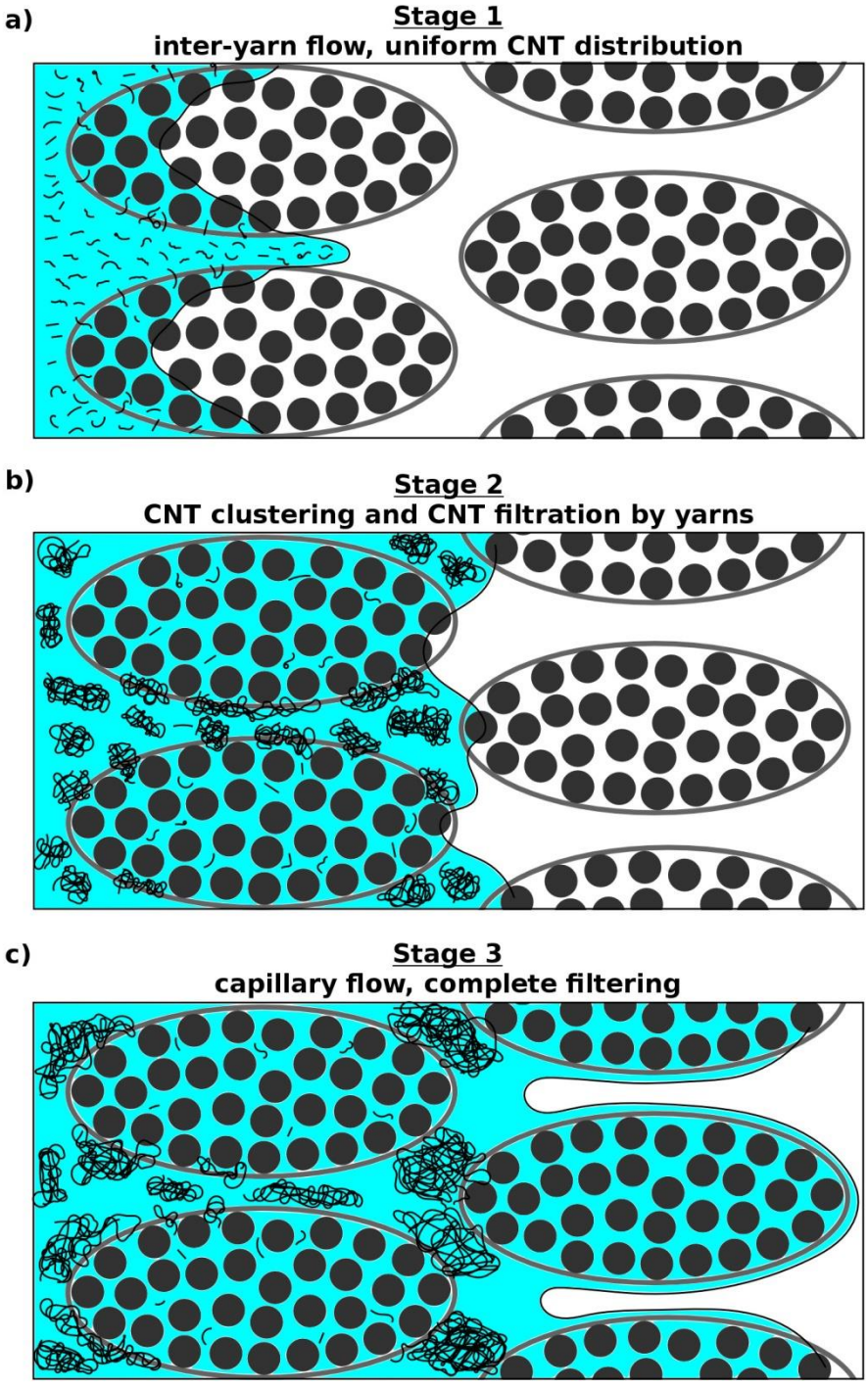


Figure 9.15: Stages of CNT distribution during RFI: a) uniform CNT distribution during inter-yarn flow, b) CNT clustering and c) complete filtering due to capillary flow

### 9.4.2 Limiting CNT clustering

It is conjectured that the lower than expected mechanical properties of multi-scale composites observed in Section 6.6 resulted from the heterogeneous distribution of CNTs in PMCs. The study of CNT distribution in this chapter showed that clustering was caused by the low processing viscosities of the resin which provided too much mobility to CNTs. Based on this observation, experiments were conducted to assess the potential of using higher processing viscosities to mitigate CNT clustering. This was studied by processing composites at lower temperatures.

Multi-scale composites featuring Twill-L and NCF-H fabrics were fabricated using interleaved RFI and cure cycle L-LCT, i.e. cure at 60°C, which is lower than the 80°C limit identified for clustering. The low temperature cure extended for 72 hours in order to achieve resin gelation. This processing time was based on cure kinetics models and viscosity models presented by Khoun et al. [174] using parameters provided by CRIAQ COMP-501 team members based at McGill university [175]. Composites were then post-cured at 200°C for 2 hours.

The lower processing temperatures of cure cycle L-LCT improved the uniformity of CNT dispersion compared with the standard processing temperatures of cure cycle L-STD. Looking at the surface of composites, it was seen that following consolidation, resin in inter-yarn gaps was populated by black globules when cure cycle L-STD was used (Figure 9.16a) but the resin had a uniform black colour when cure cycle L-LCT was used (Figure 9.16b). The improvement in CNT distribution can also be seen in cross-sections of composites (Figure 9.17). Regions of high CNT concentration were much bigger than at 130°C and were connected together, filling most of the inter-yarn gaps. In addition, most of the resin surrounding the fibres inside yarns was black, confirming the presence of CNTs. Hence without clustering, less filtering of CNTs was observed. Despite the major improvement in the uniformity of the CNT distribution provided by cure cycle L-LCT, higher resin viscosities led to processing issues. Resin viscosity was such that it limited significantly resin flow into yarns, resulting in high porosity levels (Figure 9.17).

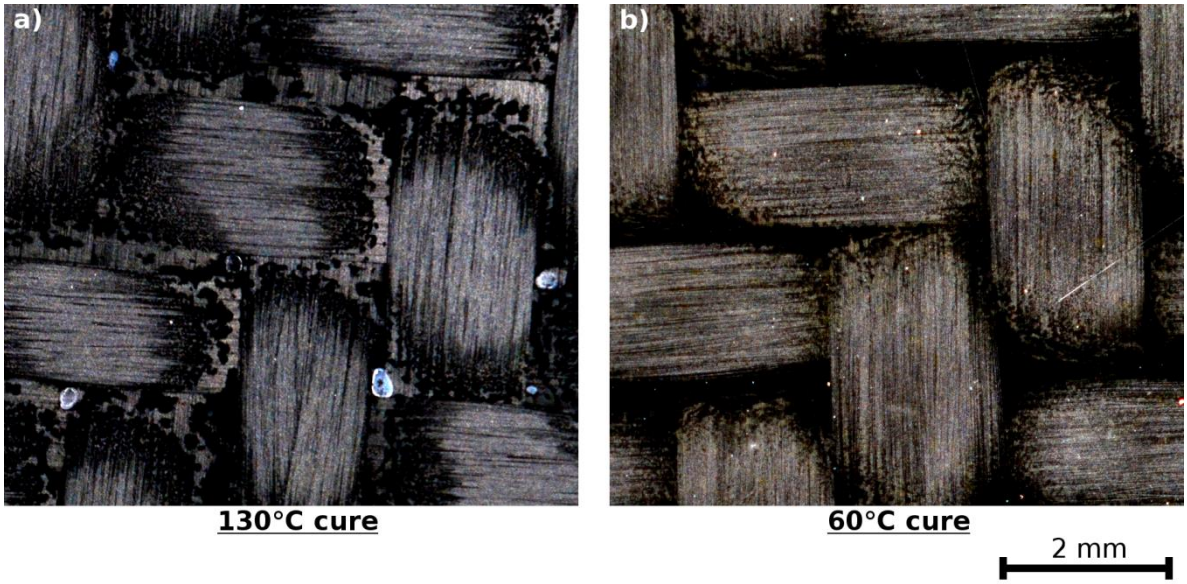


Figure 9.16: Distribution of CNTs at the surface of a laminate featuring Twill-L textile and L7 resin after a a) standard cure at 130°C and b) low temperature cure at 60°C

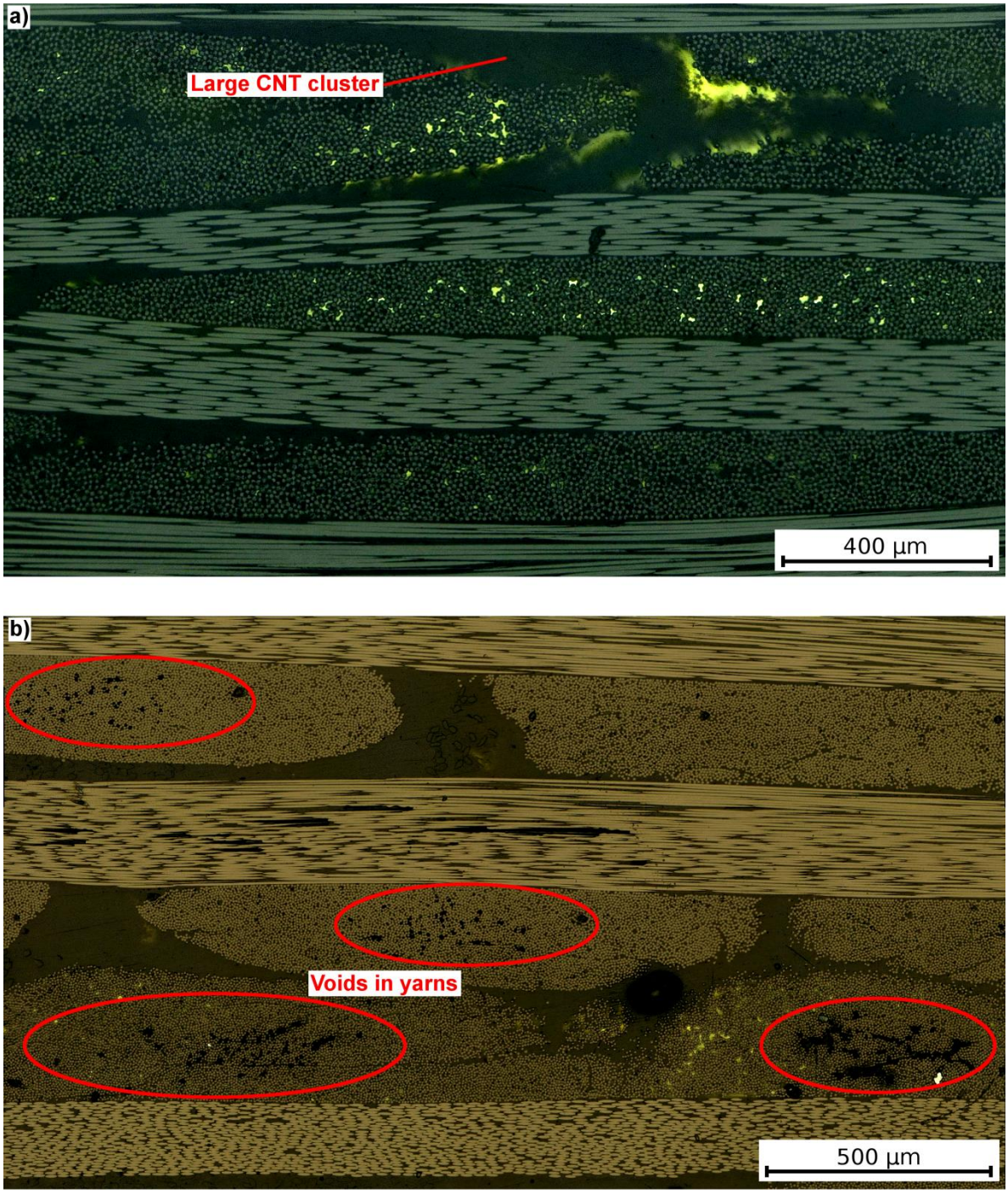


Figure 9.17: Cross-sections of laminates cured at 60°C observed through transmitted-light microscopy for resin LEO 2377 and fabric a) Twill-L and b) NCF-H

Short-beam strength experiments were performed to see whether improvements in mechanical performance resulting from a more uniform CNT distribution were more significant than reductions in performance caused by increased porosity. Results from preliminary experiments on flat laminates (Chapter 6) showed that in general, ILSS increases with decreasing porosity levels. Values of ILSS obtained for multi-scale composites cured following cure cycle L-STD, i.e. cure temperature of 130°C, were compared with those obtained with cure cycle L-LCT, i.e. cure temperature of 60°C (Figure 9.18). Results showed no statistically significant improvement in ILSS obtained from a more uniform distribution of CNTs. This result is in part due to greater porosity caused by higher resin viscosity. Another reason is that, as showed by the inspection of cross-sections (Figure 9.17), the distribution of CNTs was not completely uniform. CNT clusters were much larger than for the standard cure, but regions featuring low CNT content were present, in which cracks may propagate more easily. Another reason for the lack of strong improvement may be due to poor adhesion between CNTs and the epoxy chains; this was not studied in this work but should be part of future investigations. Nonetheless, there were signs suggesting that a more uniform distribution of CNTs can improve the interlaminar properties. In the case of multi-scale composites featuring fabric Twill-L (Figure 9.17a), the 60°C cure temperature led to ILSS values that were on par with those obtained with the 130°C cure temperature despite much higher porosity. Additionally, for the same porosity level, a 60°C cure temperature led to an increase in average ILSS values compared with a 130°C cure. In spite of promising signs, improvements were not observed in multi-scale composites featuring fabric NCF-H (Figure 9.1b). However, it is worth noting that CNTs did not offer any statistical improvements to composites cured at 130°C compared to neat resin composites.

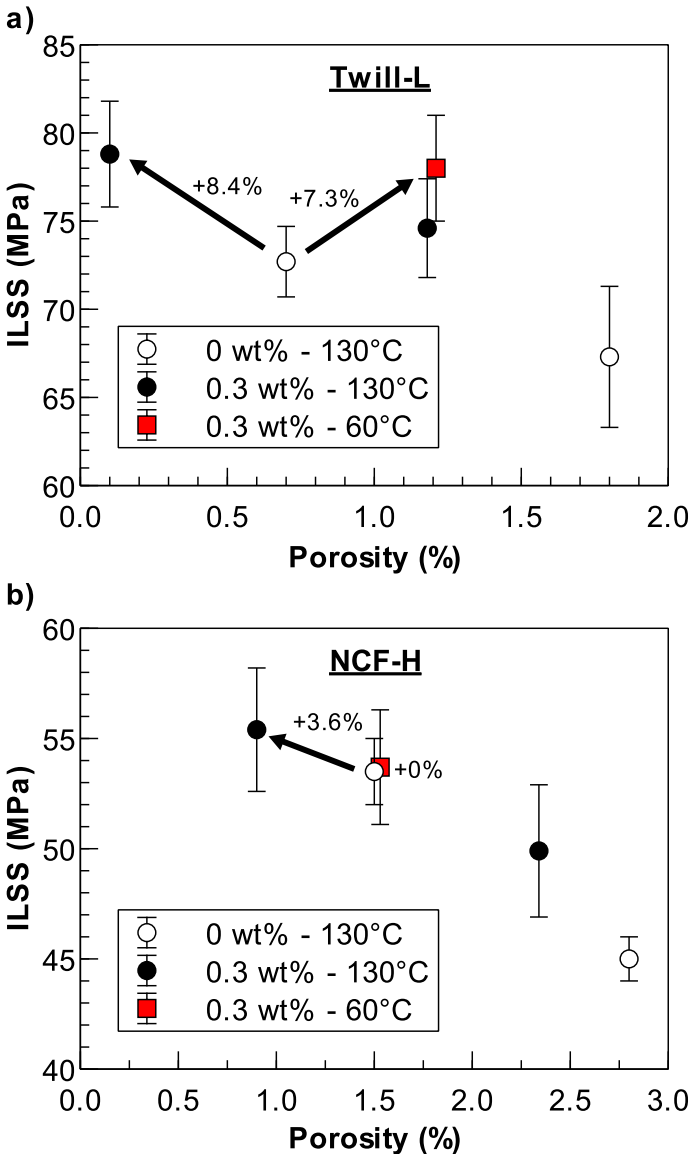


Figure 9.18: ILSS of laminates processed with interleaved RFI featuring neat resin cured at 130°C and resin loaded with 0.3 wt% of CNTs cured at 60°C and 130°C for fabric a) Twill-L and b) NCF-H

## 9.5 Remarks

The main contribution of this chapter is that it is the first to investigate and describe the change in CNT distribution during the processing of multi-scale composites through RFI. The work also studied thoroughly the potential for the fabrication of multi-scale composites through various RFI methods. For example, the work presented a direct comparison of CNT distribution between in-plane resin flow and long-and short-distance through-thickness resin flow. Moreover, this was achieved for the same material system which enables effective and meaningful comparisons. The work was performed on different types of resins and fabrics which led to a high degree of confidence in the observations. In addition, a method was proposed for reducing clustering of CNTs during fabrication.

The major findings of the work are:

- CNT distribution changes during processing from a relatively uniform dispersion to segregated clusters. In addition, capillary flow can result in near-complete filtering.
- CNT clustering occurs due to the low viscosity of the resin at processing temperatures greater than 80°C for the materials tested.
- CNT clustering causes heterogeneous matrix properties that minimise benefits provided by CNTs to the ILSS of PMCs.
- The dense fibre network in yarns leads to significant filtering of CNTs that further decreased the uniformity of the CNT distribution.
- Filtration in inter-yarn gaps is also observed in bulk RFI. The extent of filtering depends on the type of fabric and it is closely related to the permeability of fabrics.

- Interleaved RFI is the favoured RFI method for producing multi-scale composites as the very short infusion distances eliminate CNT filtration in inter-yarn gaps. However, it does not prevent filtration by the tight fibre network inside yarns.
- A solution was devised for improving the uniformity of the CNT distribution by reducing the amount of CNT clustering. This was achieved through processing at low temperatures that reduced CNT mobility. However, the benefits of a more uniform distribution of CNTs were negated by increased amounts of voids in PMCs.

The work showed that interleaved RFI is a good method for limiting filtration of CNTs. Despite this, improvements in mechanical performance from the use of CNTs in composites are marginal due to heterogeneous properties of the matrix resulting from CNT clustering and intra-yarn CNT filtration. In addition, results showed that altering the processing conditions is not a good avenue for improving CNT dispersion. It follows that any major improvement to the interlaminar strength of multi-scale composites will have to originate from further work on the chemistry of materials. Stronger chemical bonds between the resin and CNTs will improve load transfer to the latter, further enhancing mechanical properties. Even though this work did not lead to the development of a revolutionary method for producing multi-scale composites, it led nonetheless to a much better understanding of factors affecting the change in the uniformity of the CNT dispersion during processing. This will help guide work for the developments of future generations of multi-scale PMCs.

# Chapter 10

## Fabrication of delta-stringer panels

Work presented in previous chapters examined key differences in the processing of flat PMC panels made with neat and nano-modified resins. The fabrication of flat panels is relatively straightforward but those panels are not always representative of real PMC parts that often feature complex geometries. No work published in the open literature discusses the challenges of making such parts from multi-scale PMCs using out-of-autoclave RFI. Hence, the next step undertaken towards this thesis was to investigate scaling-up the RFI process by fabricating demonstrator panels that are representative of real structures.

The type of part that was selected for this work is a delta-stringer which consisted of a triangular shape stiffener co-cured to a flat skin (Figure 10.1). It was chosen based on recommendations received from Bombardier Aerospace. In addition to being a common type of structure used in airframes, the part was chosen for the presence of several geometrical intricacies including:

1) curved sections
2) non-uniform part thickness
3) small radii
4) hollow interior

The names given to each areas of the delta-stringer appear in Figure 10.2.

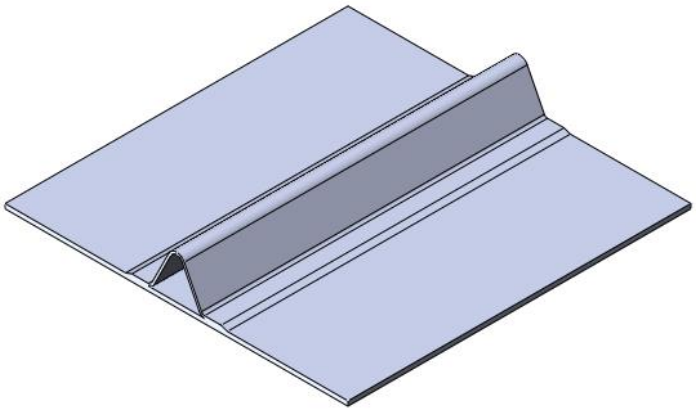

Figure 10.1: CAD model of the delta-stringer demonstrator panel

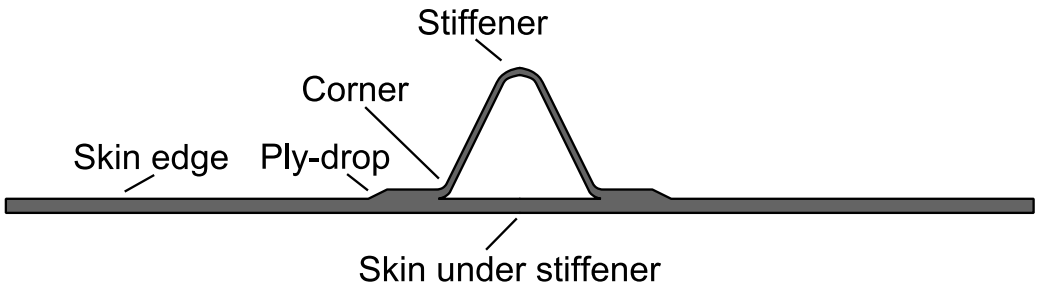


Figure 10.2: Areas of interest across the profile of delta-stringers

Preliminary work for selecting a processing method for delta-stringers was performed on small-scale parts due to limited availability of the materials. The most promising method that was tested was then used for producing large-scale demonstrator parts. It should be noted that the small- and large-scale parts featured the same stiffener geometry but differed by the size of the skin and length of the stiffener.

This chapter is divided into three parts. Firstly, two potential methods for fabricating delta-stringers using RFI are described. They are the rigid mandrel and inflatable mandrel methods. Secondly, the methods are evaluated by comparing preliminary small-scale PMC parts made with neat resins SA 70 and LEO 2376. Thirdly, two large-scale demonstrator panels made using the solid mandrel method are characterised to investigate the viability of the out-of-autoclave RFI process for fabricating multi-scale PMC parts.

A list of all delta-stringers discussed in this section appears in Table 10.1. All delta-stringers were made using fabric reinforcement NCF-HB and featured a quasi-isotropic stacking configuration that was symmetric in the skin and stiffener, based on stacking sequence $[(90/0), (45/-45)]_{NS}$. Dimensions for the large-scale delta-stringers are presented in Figure 10.3. As noted above, the stiffener geometry was the same for the small- and large-scale delta-stringers.

Table 10.1: Description of delta-stringer panels

| Group | Method | Panel | Fabric | Resin | Size (mm) | Caul plate | Ply-drop |
|---|---|---|---|---|---|---|---|
| Preliminary (small-scale) | Inflatable mandrel | IM-PT | NCF-HB | SA 70 | 100 × 150 | Rigid PMC | No |
| | | IM-P | NCF-HB | SA 70 | 100 × 150 | Rigid PMC | No |
| | | IM-L | NCF-HB | LEO 2376 | 100 × 150 | Rigid PMC | No |
| | Solid mandrel | SM-P | NCF-HB | SA 70 | 100 × 190 | None | Yes |
| | | SM-L-01 | NCF-HB | LEO 2376 | 100 × 190 | None | Yes |
| | | SM-L-02 | NCF-HB | LEO 2376 | 100 × 190 | Rubber | Yes |
| Large-scale | Solid mandrel | LS-neat | NCF-HB | LEO 2376 | 300 × 300 | Rubber | Yes |
| | | LS-CNT | NCF-HB | LEO 2377 | 300 × 300 | Rubber | Yes |

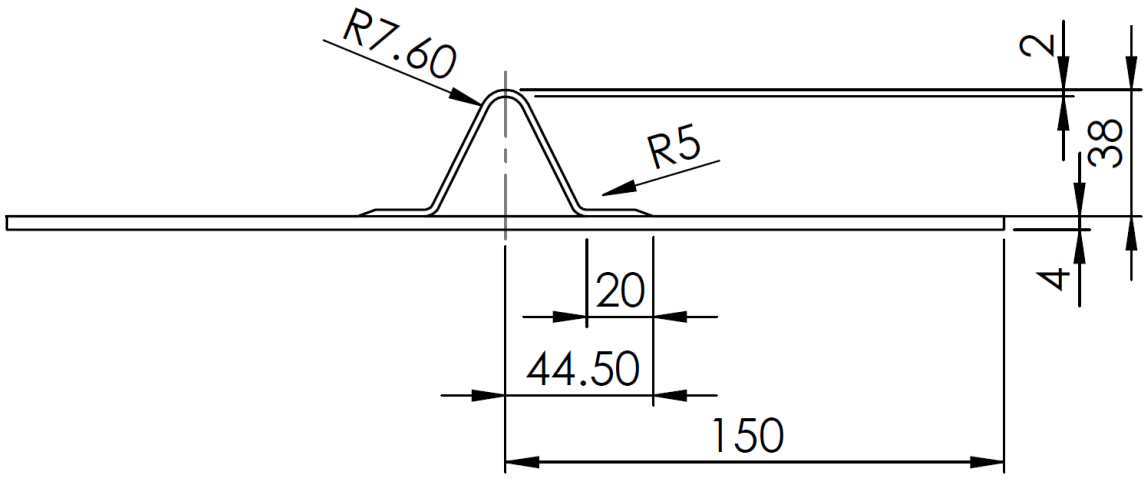


Figure 10.3: Profile of the large-scale delta-stringer demonstrator panels (dimensions in mm)

## 10.1 Proposed methods for producing delta-stringers

Delta-stringers were produced by co-curing the skin and stiffener, using interleaved RFI. This was preferred over bulk RFI to minimise CNT filtration in the multi-scale composites as discussed in Chapter 9. Two vacuum bagging methods were compared for consolidating the delta-stringers: the rigid mandrel and inflatable mandrel methods. These methods differed only by the type of tooling used for forming the hollow section of the delta-stringer, the type of caul plate, and the presence of a ply-drop. Both methods used the same edge bleeding configuration as vacuum bagging method I-6.

The rigid mandrel method consisted in 1) laying the outer skin over a flat aluminium tool, 2) adding an aluminium mandrel to form the hollow section of the delta-stringer, 3) laying the fibre layers for the stiffener over the mandrel (Figure 10.4) and 4) putting the assembly under a vacuum bag. Unlike bagging method I-6, no rigid caul plate was used because it could not apply constant pressure on curved sections of the delta-stringer during processing, due to significant changes in stack geometry with resin flow. Instead, the rigid caul plate tooling was either replaced with a peel-ply or with a flexible tool consisting of a 1 mm thick silicone rubber sheet. The mandrel was machined to final dimensions and it was wrapped in release film for removal after cure. It should also be noted that parts featured a ply-drop, unlike those made with the inflatable mandrel method.

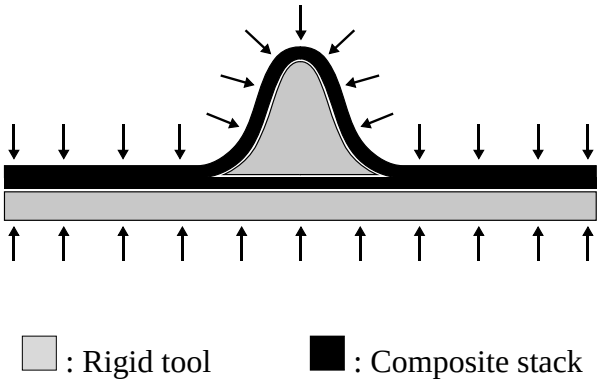


Figure 10.4: Schematic of the rigid mandrel method where arrows represent external pressure

The inflatable mandrel method consisted in 1) laying the outer skin on a flat aluminium tool, 2) laying the stiffener inside a rigid caul plate, 3) joining the skin and stiffener together (Figure 10.5), 4) adding an inflatable mandrel in the hollow section of the delta-stringer, and 5) putting the assembly under a vacuum bag. The rigid caul plate was fabricated using carbon/epoxy SE 70 prepreg from Gurit; the shape was formed using the solid aluminium mandrel presented above. The inflatable mandrel consisted of a vacuum bag tube exposed to ambient air and pressure (Figure 10.6). It was sealed onto the vacuum bag covering the delta-stringer. Pulling a vacuum inside the vacuum bag resulted in the expansion of the mandrel towards the fabric/resin stack, compressing the stack against the tool and rigid caul plate. The inflatable mandrel featured a circumference much bigger than the perimeter of the hollow section, ensuring that it could expand effortlessly during RFI. A peel ply or release film was added on the surface of the lay-up, inside the hollow section, for easy removal of the inflatable mandrel. It should be noted that delta-stringers made with the inflatable mandrel did not feature any ply drop as this would have required significantly more investment for fabricating and optimising the rigid PMC caul plate.

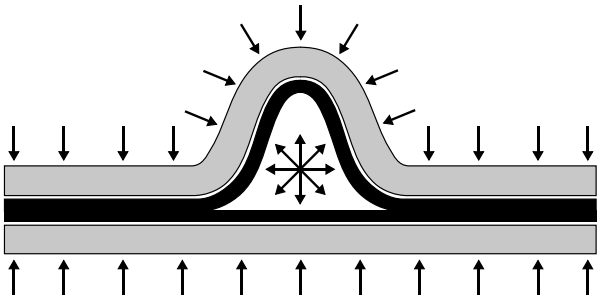

: Rigid tool and caul plate : Composite stack

Figure 10.5: Schematic of the inflatable mandrel method where arrows represent applied pressure

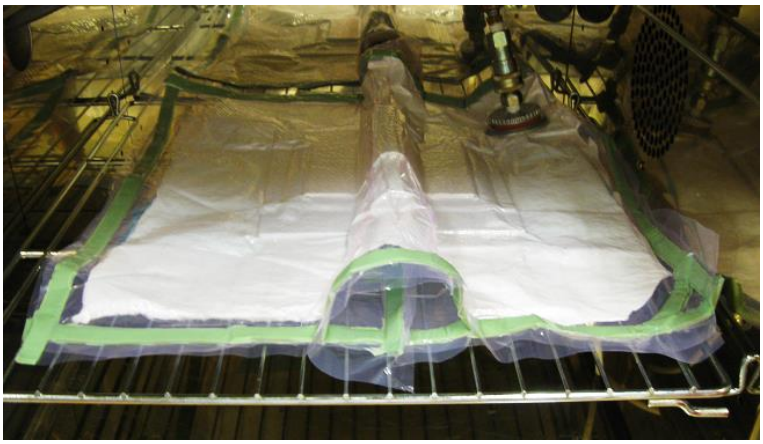

Figure 10.6: Vacuum bagged delta-stringer with the inflatable mandrel method

Following bagging, the delta-stringers were consolidated using cure cycles L-STD and S-STD for parts made with resins LEO 2376 and SA 70, respectively.

## 10.2 Preliminary delta-stringers

Preliminary delta-stringers were fabricated for selecting the best method for fabricating large-scale demonstrator panels. First, a qualitative analysis of the ease of

fabrication and processing defects is presented. Then, pull-out strengths of the preliminary delta-stringers are compared.

### 10.2.1 Solid mandrel method

Typical stacks and demoulded delta-stringer parts for the solid mandrel method appear in Figure 10.7.

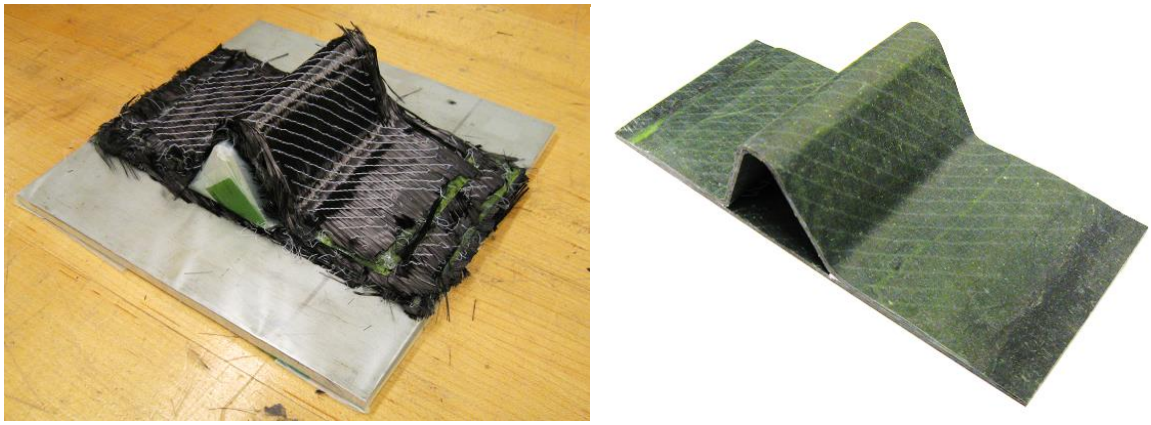

Figure 10.7: Delta-stringer SM-P before (left) and after (right) fabrication

#### 10.2.1.1 Effect of the mandrel

The solid mandrel enabled precise dimensions of the hollow section, resulting in very low radii for corners where the skin and stiffener meet. The use of the solid mandrel also facilitated lay-up of the skin and stiffener, and enabled the use of a simple vacuum bag, reducing manual labour markedly. However, demoulding was extremely difficult because the mandrel was trapped in the part due to important epoxy shrinkage during cure. The extraction of the mandrel required the application of an important force, often with the aid of a universal testing machine. For very long parts or curved hollow sections, it is critical that the solid mandrel be collapsible.

#### 10.2.1.2 Surface roughness

The skin of the delta-stringer in contact with the aluminium tool featured a smooth finish, similarly to flat laminates (Chapter 6). However, the absence of a rigid caul plate on the inner surface of the delta-stringers resulted in rougher surfaces.

In cases without any rigid or flexible caul plates, the surface of the delta-stringer was highly textured. Even after the removal of the peel-ply, bagging artefacts remained. All the wrinkles of the vacuum bag were transferred directly to the surface of the parts (Figure 10.8). The effects of the bagging could be mitigated by using a flexible rubber caul plate (SM-L-02), yielding a much smoother surface (Figure 10.8). However, the flexible caul plate could not achieve the same level of smoothness as observed for flat PMCs made with a rigid caul plate (Chapter 6); the flexible caul plate still resulted in local variation in PMC thickness.

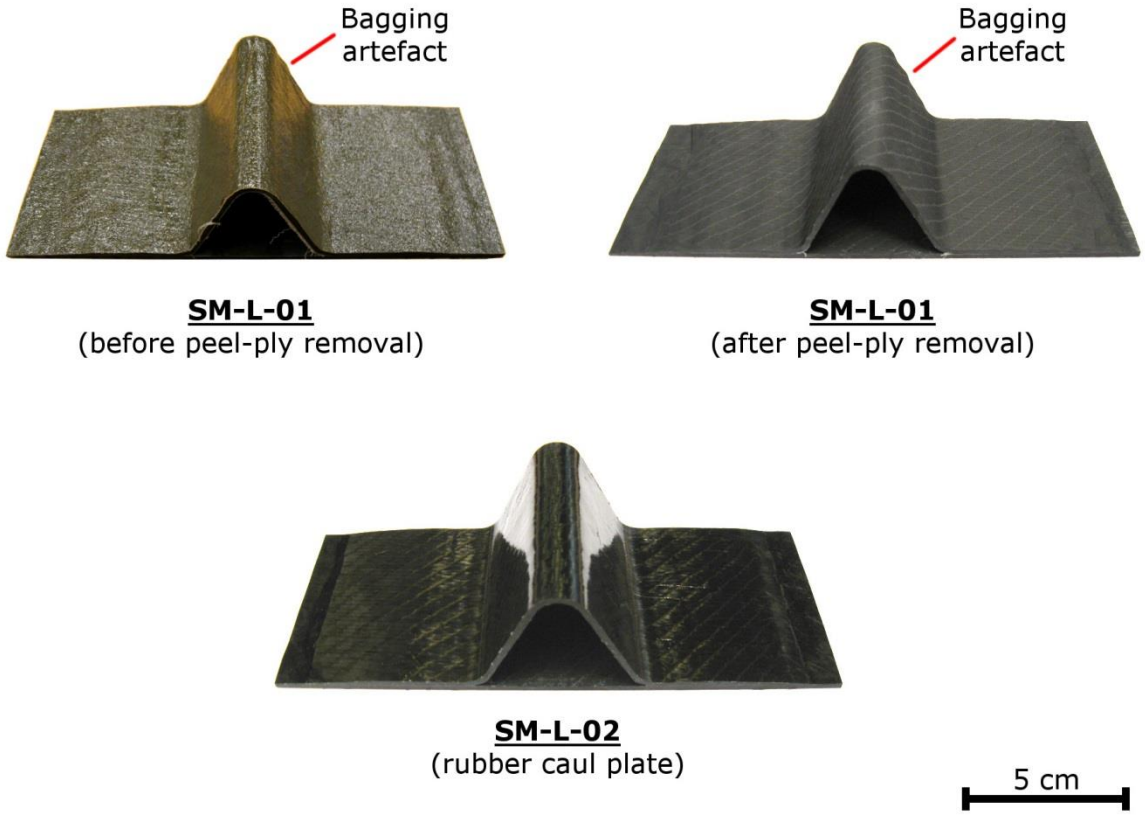


Figure 10.8: Delta-stringers SM-L-01 and SM-L-02 showing the effects of the peel-ply and flexible rubber caul plate on the surface roughness of PMCs

#### 10.2.1.3 Part thickness

The high flexibility of the vacuum bagging ancillaries and lack of caul plate ensured a good distribution of pressure over the delta-stringer during fabrication. Ignoring the surface texture, the part thickness appeared relatively constant across all flat sections of the delta-stringers (Figure 10.9).

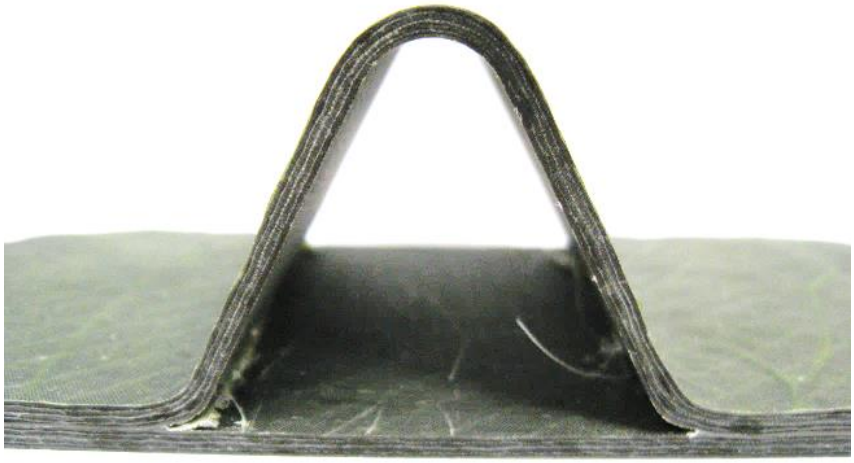

Figure 10.9: Cross-section of SM-P delta-stringer

Along curved sections of the part, thickness was not always uniform. Thickness in the corners where the skin and stiffener meet appeared marginally higher than in flat sections. This may have been caused by the rigidity of the composite stack, preventing its forming to tight radii. However, personnel experience from the fabrication of the rigid caul sheet for the inflatable method suggests that the greater compliance of dry fabrics in RFI enables the forming of smaller radii corners compared with what may be achieved with pre-preg materials.

### 10.2.2 Inflatable mandrel method

A representative stack and demoulded delta-stringer for the inflatable mandrel method appear Figure 10.7.

Figure 10.10: Delta-stringer IM-L before (left) and after (right) fabrication

#### 10.2.2.1 Effect of the inflatable mandrel

The bagging configuration required for the inflatable mandrel method was significantly more complex than that of the solid mandrel method. The addition of the inner bag for the hollow section increased labour for making and sealing the vacuum bag. However, the greatest challenge was to ensure that proper expansion of the bag could be achieved throughout RFI, providing consistent compaction of the fabric/resin stacks despite changes in stack geometry due to resin flow.

The first attempt at the inflatable mandrel method (delta-stringer IM-PT) resulted in non-uniform and incomplete expansion of inner bag (Figure 10.11). The delta-stringer featured rounded corners and resin rich areas even though the bag was slightly larger than the targeted post-consolidation dimensions. This occurred because the bag was constrained locally by the friction with the stack, limiting expansion. The issue was mitigated in later experiments by using a peel-ply between the inner bag and stack for reducing friction, and by using an inner bag three times larger than the hollow section.

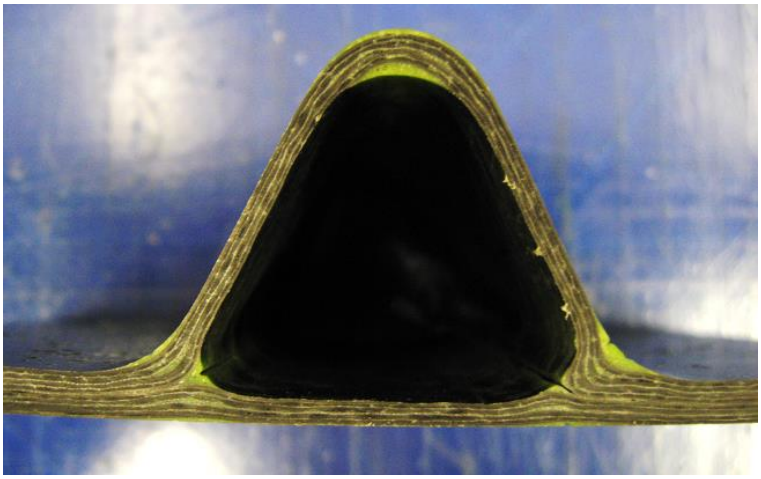

Figure 10.11: Thick corners due to a lack of expansion for delta-stringer IM-PT

The use of an oversized mandrel did not solve all issues regarding bag expansion. Despite all the excess bagging material, the mandrel could not always force itself into the corners at the junction of the skin and stiffener (Figure 10.12), leading to uneven and random compaction in the corners. This resulted in surface defects such as wrinkling (Figure 10.13).

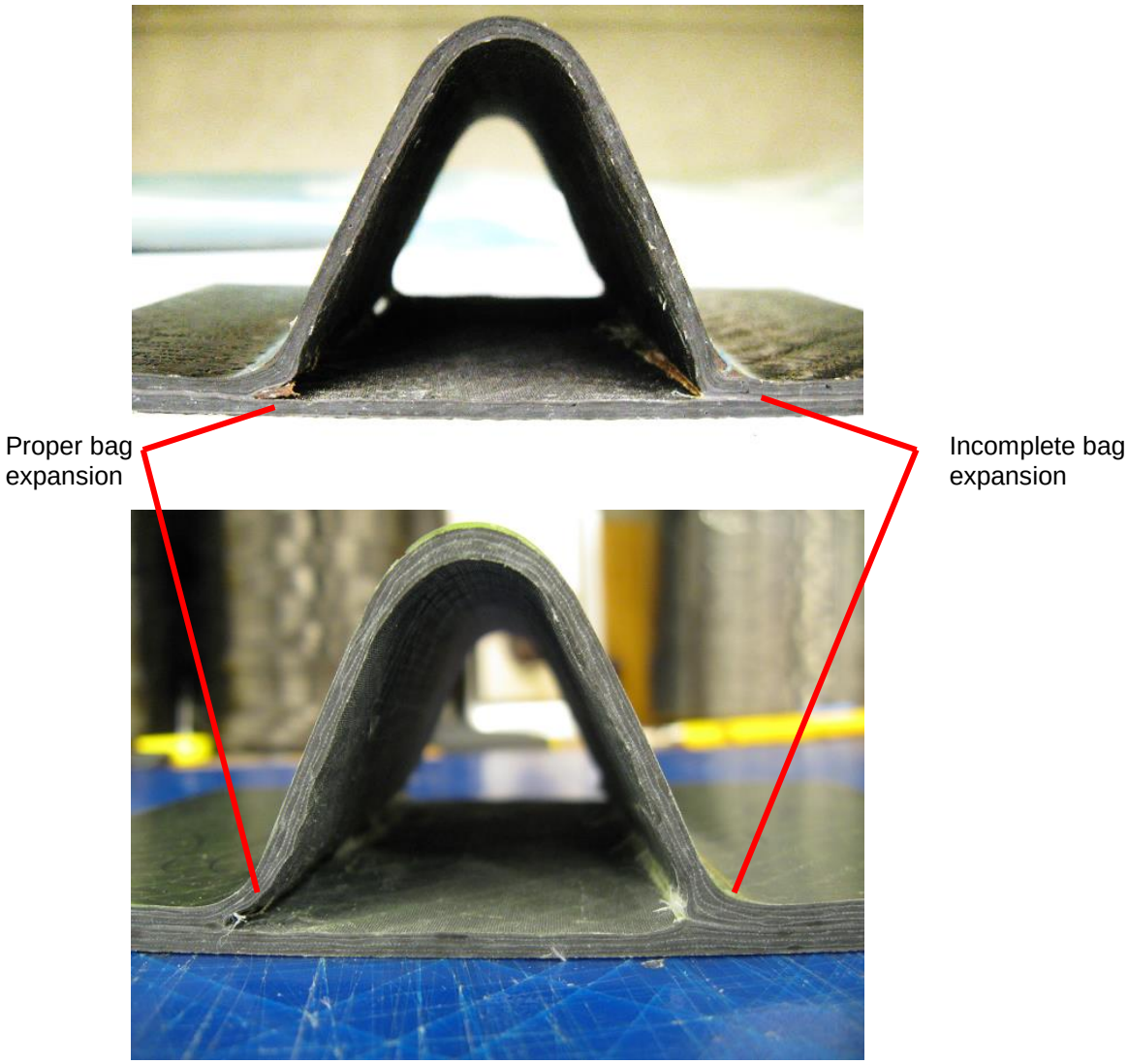


Figure 10.12: Cross-section of delta-stringers IM-L (top) and IM-P (bottom)

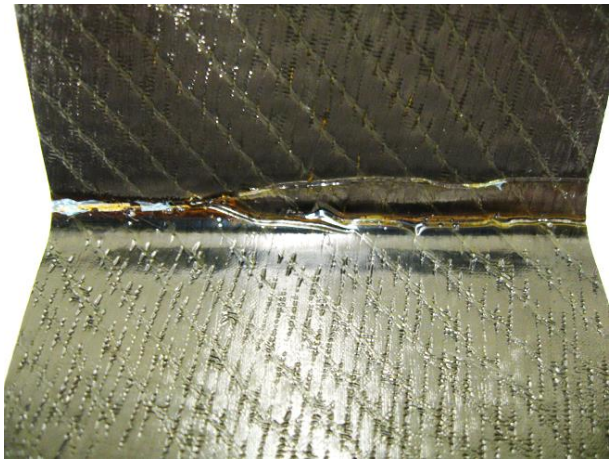

Figure 10.13: Imprint of a wrinkled release film at corner of delta-stringer IM-L

Considering that bag expansion in the corner of the delta-stringer is extremely complex, the best solution for mitigating risks of improper bag expansion would be to modify the delta-stringer geometry. For example, the sharp corners could be replaced with rounded corners in which the bag could expand much more reliably. Such geometry may be achieved by filling the corners with fill fibres.

#### 10.2.2.2 Surface roughness

The rigid caul plate used for producing delta-stringers resulted in flat and smooth exterior surfaces, similar to those obtained with flat laminates (Chapter 6). Conversely, the hollow section featured a rougher surface because it was not in contact with a rigid surface.

#### 10.2.2.3 Part thickness

The thickness of flat sections appeared relatively constant. Conversely, at the corners of the skin and stiffener, thickness was highly dependent on the expansion of the inflatable mandrel. In general, thickness at the corners was much higher than in other regions of the delta-stringer.

### 10.2.3 Pull-out strength

Pull-out experiments were performed on 4 preliminary delta-stringers, investigating the effect of the resin formulation, forming method and repeatability. The delta-stringers selected for testing were IM-P, SM-P, SM-L-01 and SM-L-02.

Load versus displacement curves for pull-out experiments performed on preliminary delta-stringers appear in Figure 10.14 and fracture toughness $G_I$ values appear in Table 10.2. Results from delta-stringers SM-L-01 and SM-L-02 showed that the pull-out behaviour and fracture toughness were consistent between parts made with the same forming method, in this case the solid mandrel, given that parts feature the same fibres and resin matrix.

Experiments showed that the crack initiation load, i.e. maximum load, for delta-stringers IM-P and SM-P that featured toughened pre-preg resin SA 70 was approximately twice that of SM-L-01 and SM-L-02 featuring infusion resin LEO 2376. Similarly, fracture toughness $G_I$ was 2 to 3.5 times larger for delta-stringers made from resin SA 70 than those made with LEO 2376. It follows that crack initiation and propagation can be delayed significantly by toughening the resin matrix.

The method for forming the hollowed section of the stringer also affected the mechanical behaviour during pull-out experiments. For the same resin matrix, the inflatable mandrel method of delta-stringer IM-P resulted in a higher crack initiation load than the solid mandrel method of delta-stringer SM-P. This difference was attributed to the shape of the hollowed section. At the joint of the stiffener and skin, delta-stringer SM-P featured a much sharper corner than delta-stringer IM-P, increasing stress concentration and reducing the load required for crack initiation. Conversely, the crack propagation load was much lower with the inflatable mandrel of delta-stringer IM-P than the solid mandrel of delta-stringer SM-P. It is conjectured that use of the flexible rubber caul sheet in the solid mandrel method resulted in a much more uniform compaction of fabric/resin stacks than the rigid composite caul plate in the inflatable mandrel method. The higher compliancy of the flexible caul sheet enabled it to adapt to any local thickness variations in the fabric/resin stacks. This would inevitably limit zones of low fibre fraction which were

found to be detrimental to $G_I$ [176]. Further work will be required to confirm this; nonetheless, results showed that despite the lower crack initiation load of delta-stringer made with a solid mandrel, these delta-stringers perform better against crack propagation.

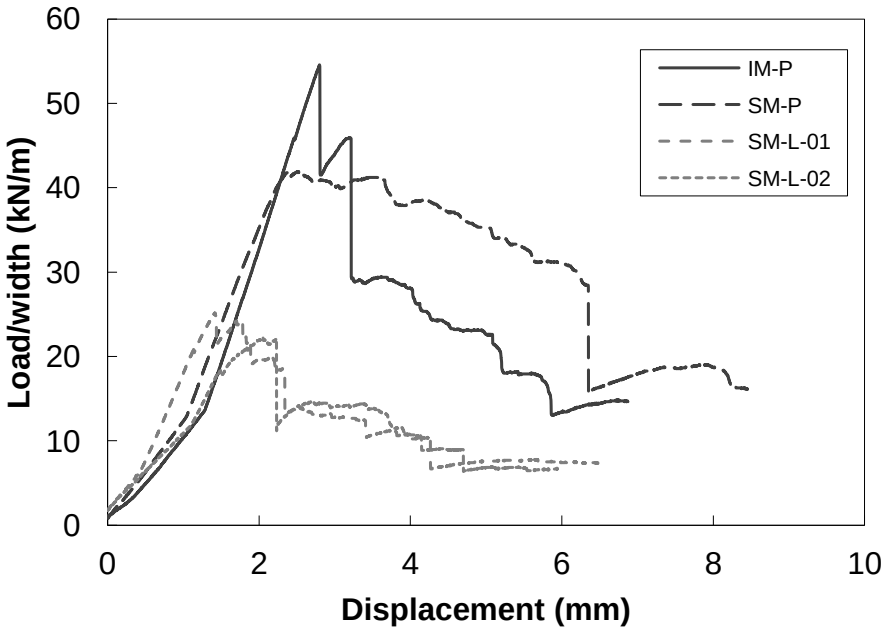


Figure 10.14: Load versus displacement curves for pull-out experiments with the preliminary delta-stringers

Table 10.2: Results of pull-out experiments for preliminary delta-stringers

| Specimen | Crack initiation load (kN/m) | Displacement at failure (mm) | $G_I$ ($J/m^2$) |
|---|---|---|---|
| IM-P | 54.5 | 6.9 | 1210 |
| SM-P | 41.9 | 9.3 | 2100 |
| SM-L-01 | 25.2 | 6.5 | 590 |
| SM-L-02 | 24.8 | 6.0 | 555 |

## 10.3 Large-scale delta-stringer demonstrators

Two large-scale delta-stringer demonstrator panels were fabricated successfully: LS-neat that featured neat resin LEO 2376 and LS-CNT featuring nano-modified resin LEO 2377. Both were fabricated using the solid mandrel method because work presented in Section 10.2 showed that it provided parts that were more consistent and more faithful to the desired part profile, and because it led to the best resistance against crack propagation. Five panel slices were studied for thickness measurements, and three of those were used for mechanical testing. A single slice was prepared for microscopy and porosity measurements.

### 10.3.1 Inspection

Visual inspection of the demonstrator panels revealed that the 2 parts featured comparable surface finish and exterior profiles (Figure 10.15). The surfaces were smooth due to the rubber caul sheet, and free of pin holes.

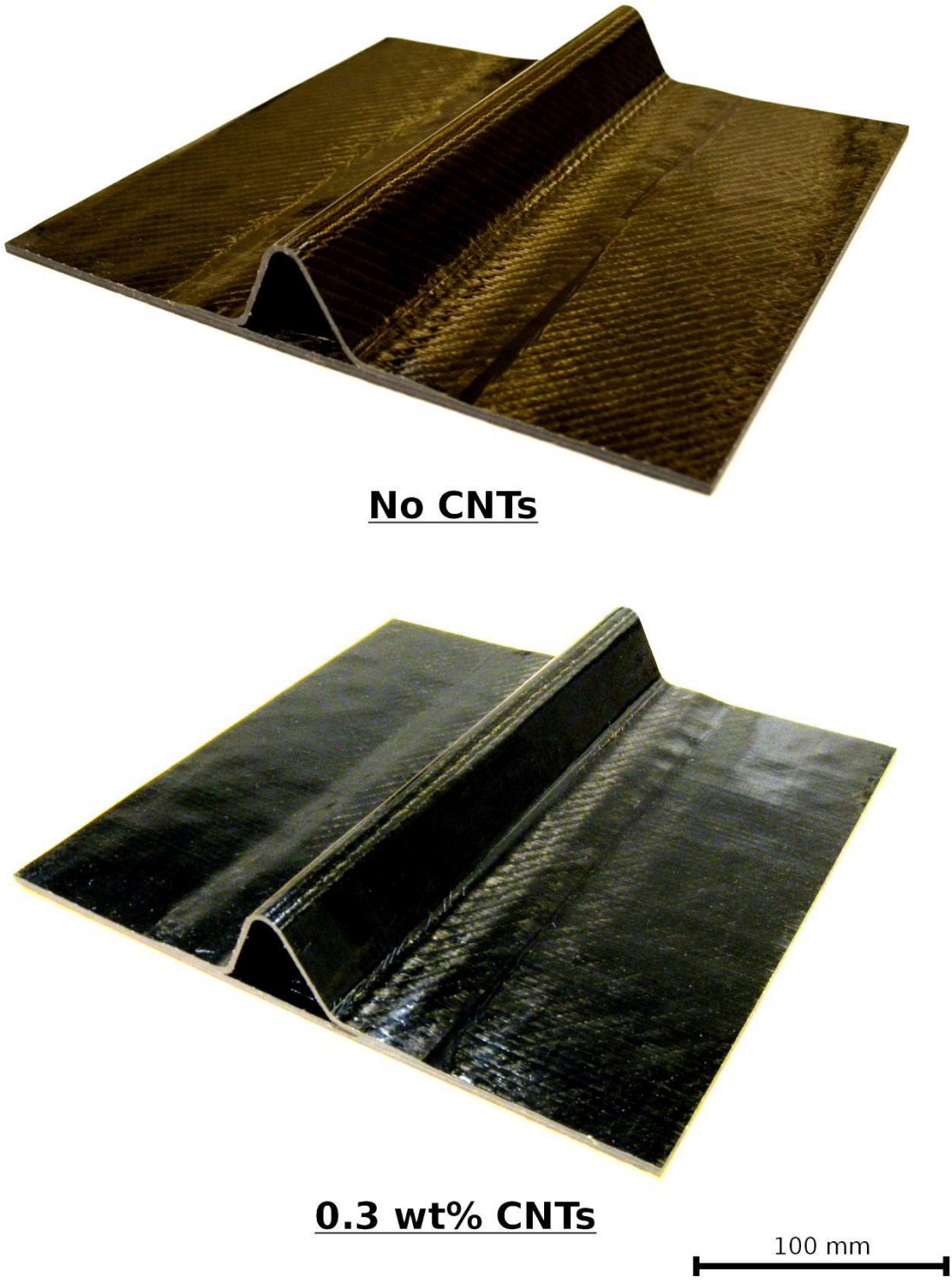


Figure 10.15: Large-scale delta-stringer demonstrator panels LS-neat (top) and LS-CNT (bottom)

The variation in PMC thickness across slices of demonstrator panels is quantified in Figure 10.16. Thickness was highly consistent between slices of a given demonstrator panel. Moreover, thickness was relatively consistent between demonstrator panels despite the use of different resins. The only significant differences occurred in the stiffener and in the skin below the stiffener, where the PMC was thinner by approximately 3% in LS-CNT than in LS-neat.

General observations could be made regarding both demonstrator panels. Flat skin sections of the demonstrator panels featured a relatively uniform thickness. It was only in curved regions that resin rich regions developed. The bend at the tip of the stiffener was slightly thicker than the rest of the stiffener. However, most discrepancies originated from the corners where the stiffener meets the skin (Figure 10.16a). The concave geometry coupled with the small radius of curvature prevented the vacuum bag from applying effective compaction. This minute issue is not of concern because in a real application, the corner would be filled with fibres for reducing stress concentration (Figure 10.17). The sharp geometry was only used in this work to test the limit of the RFI process. Hence, work showed that RFI could produce complex geometry PMCs and multi-scale PMCs reliably.

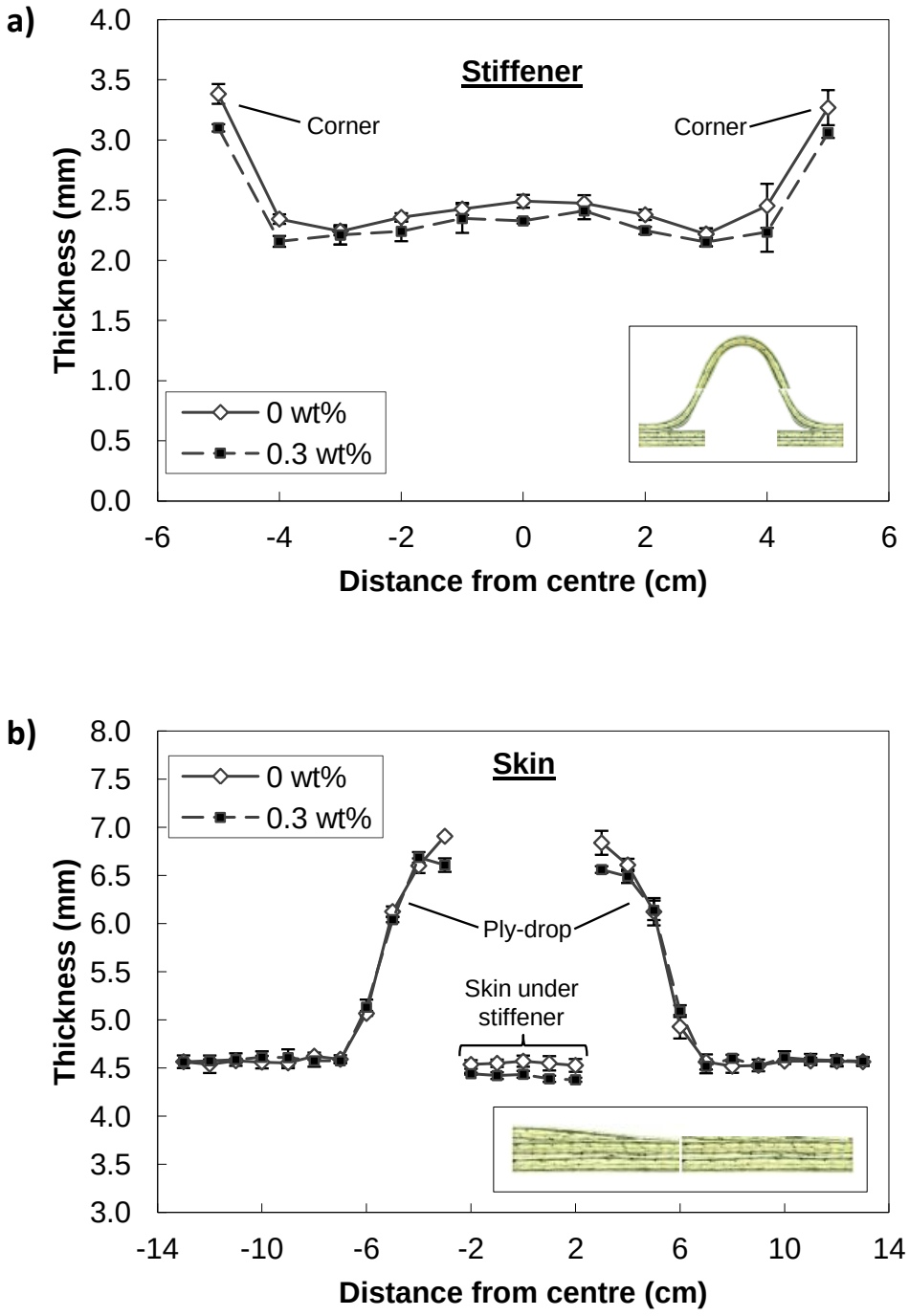


Figure 10.16: Thickness variation across the LS-neat (0 wt%) and LS-CNT (0.3 wt%) delta-stringer demonstrators, in the a) stiffener and b) skin

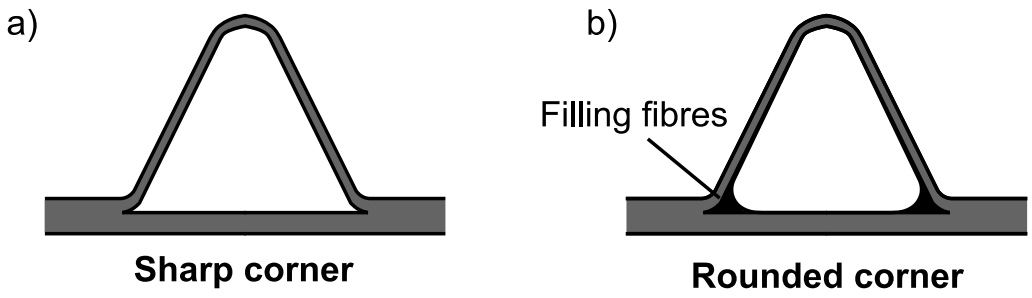


Figure 10.17: Shape of the delta-stringer, a) tested geometry and b) ideal geometry

Micrographs of the cross-sections appear in Figure 10.18. Microscopy revealed that the thickness of individual fabric layers was relatively constant throughout the entire demonstrator panels, regardless of the change in geometry such as bends, joints and ply-drops. This resulted from friction forces that restricted relative motion between fabric layers and stretched fabrics, ensuring uniform thickness. This friction was caused by the debukling of the stack, i.e. reduction in stack thickness, during resin flow.

Microscopy showed that most variations in local thickness (Figure 10.16) were attributed to resin rich zones that developed around the fabric layers due to the inability of the fabric stack and bagging to deform around small radii during debulking. This is seen clearly in the corners where the stiffener meets the skin (Figure 10.18), wherein resin fills the gap between the fabric and the solid mandrel.

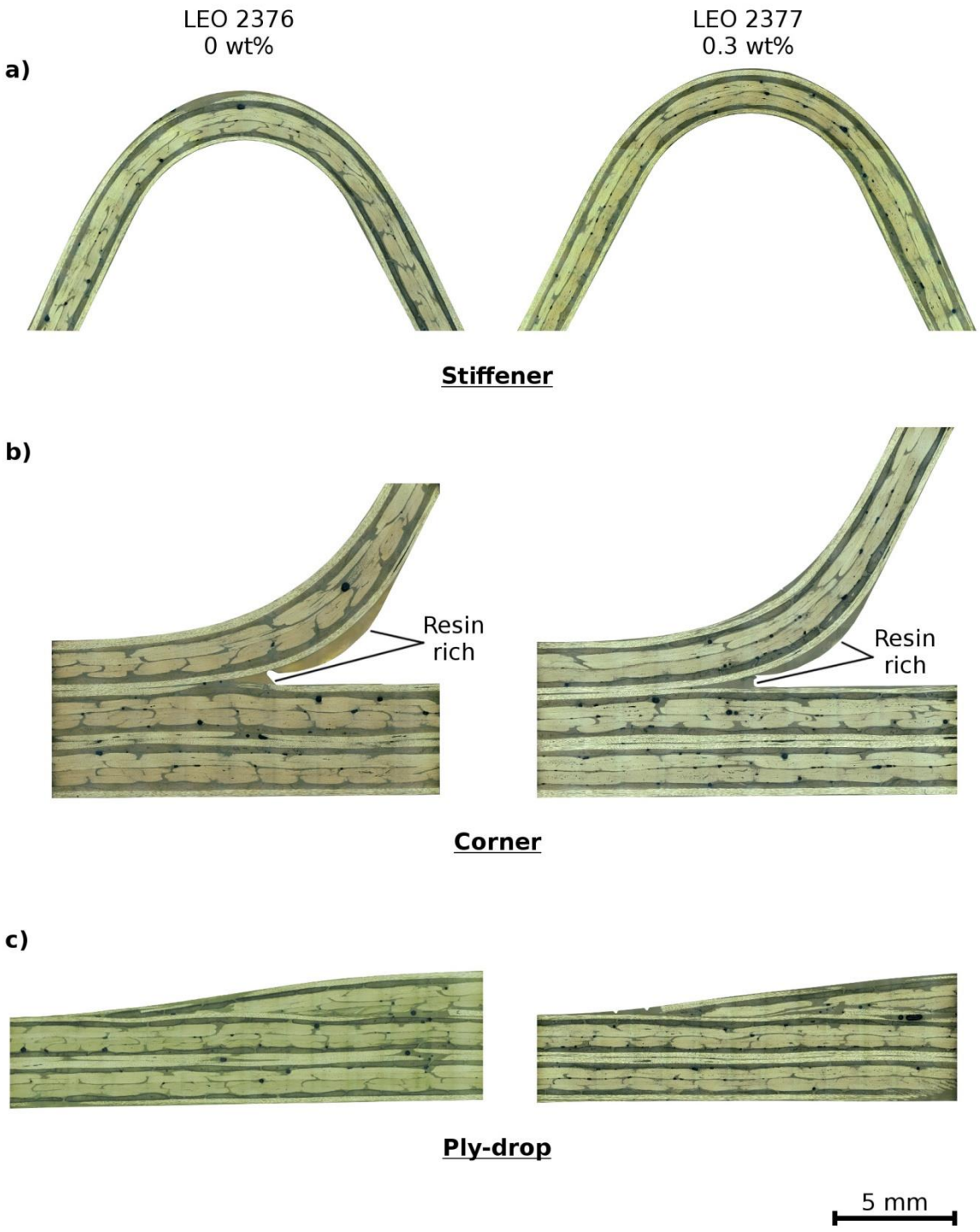


Figure 10.18: Cross-sections of large-scale delta-stringer demonstrator panels LS-neat (left) and LS-CNT (right) for the a) stiffener, b) corner of the stiffener/skin and c) ply-drop

### 10.3.2 Porosity

Microscopy showed that similarly to flat panels made with LEO family resins (Chapter 6), most voids were located in inter-yarn gaps. In addition, it was observed that the porosity content varied throughout the cross-section of demonstrator panels.

Global and local porosity values were obtained for demonstrator panels (Figure 10.19). A single cross-section was analysed per panel as results are expected to be relatively representative of the whole panel given the pull-out strength values obtained in section 10.3.3. The average global porosity of demonstrator LS-neat was low at 0.6%. Conversely, demonstrator LS-CNT featured high levels of porosity at 1.4%, despite the use of CNTs that generally lower porosity (Chapter 6). This glaring contrast with results obtained for flat PMCs suggested that an issue occurred during fabrication. The lower PMC thickness of stiffener and skin under the stiffener of demonstrator panel LS-CNT compared with that of LS-neat indicates that porosity was likely caused by an insufficient amount of resin, i.e. resin starvation. Based on results from flat PMCs and demonstrator panel LS-neat, it is believed that proper fabrication of LS-CNT would have resulted in a multi-scale PMC part featuring low porosity content.

Results also showed that porosity was affected locally within parts, and trends were consistent between demonstrator panels (Figure 10.19). Porosity was lowest in regions under the flexible caul sheet where few changes in the lay-up occurred, such as the regions of the stiffener and skin near the edges of the panel. The marginal increase in porosity for the ply-drop and corners where the stiffener meets the skin suggested that out-of-autoclave RFI was as effective for fabricating complex geometry PMC parts as it was for making flat PMCs. The only concern is that porosity was much higher in the skin under the stiffener than in the remainder of the panels. Without further testing, it is difficult to know the exact cause of this issue. However, it is interesting to note that highest porosity was observed in regions under the solid mandrel, where the stack is not exposed to the flexible caul sheet. From this, it is conjectured that higher porosity might have resulted from a change in compaction pressure around the solid mandrel or from lower breathing that hindered degassing. In the latter case, it is possible that the flexible caul sheet was more permeable than the aluminium, which would increase gas diffusion out of the resin.

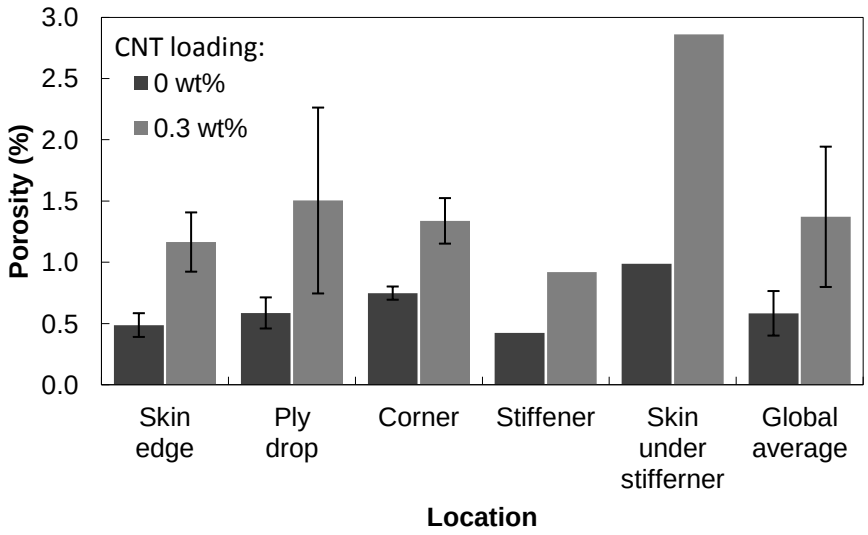


Figure 10.19: Local and global porosity of large-scale delta-stringer demonstrator panels LS-neat (0 wt%) and LS-CNT (0.3 wt%)

### 10.3.3 Pull-out strength

Pull-out experiments were performed on the large-scale delta-stringer demonstrator panels. As with the preliminary delta-stringers, testing showed that crack propagation was unstable and this was reflected in the experimental data by the jagged load versus displacement curves (Figure 10.20). The mechanical behaviour was highly consistent between specimens, except for minor differences in the displacement at failure. Results showed that on average the crack initiation load and displacement at failure were 20% lower for LS-CNT specimens than LS-neat specimens. The $G_I$ value for LS-neat was 645 J/m$^2$ ± 125 J/m$^2$, which falls in the range of values obtained in Section 10.2.3, suggesting that the effect of scale was negligible. The $G_I$ value of LS-CNT was 525 J/m$^2$ ± 73 J/m$^2$, 20 % lower than that of LS-neat. Considering that CNTs improve the ILSS (Chapter 6), this lower performance of LS-CNT than LS-neat is attributed entirely to its higher porosity content. Unfortunately, the difference in porosity between both demonstrator panels prevented any viable assessment of the effect of CNTs on $G_I$.

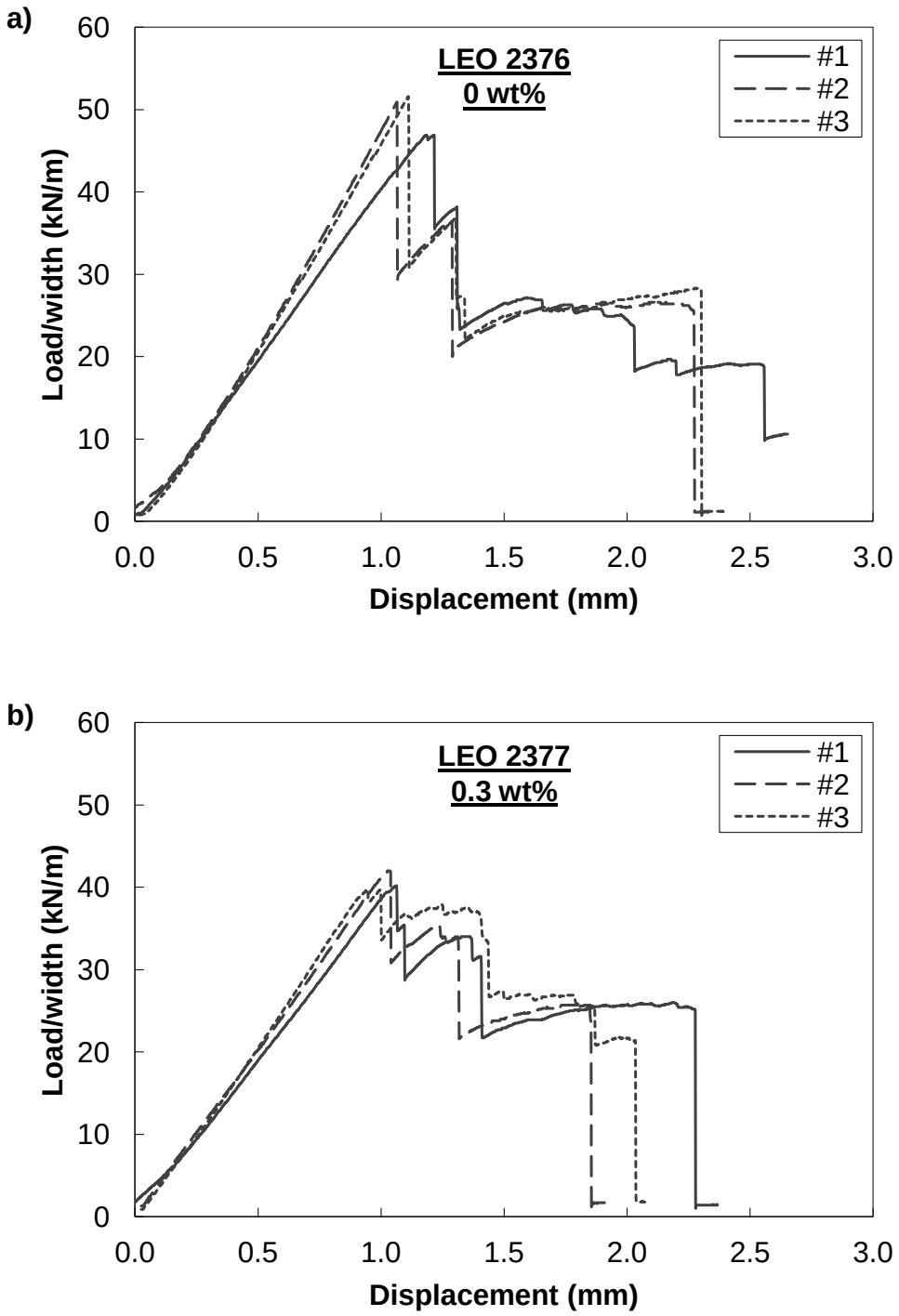


Figure 10.20: Load versus displacement curves for pull-out experiments with the large-scale demonstrator panels a) LS-neat and b) LS-CNT

## 10.4 Remarks

This chapter investigated the scale-up of out-of-autoclave RFI for fabricating PMCs and multi-scale PMCs. This was achieved by fabricating delta-stringers featuring a complex geometry that included small radius bends and hollow sections.

Two fabrication methods were investigated: the solid mandrel and inflatable mandrel methods. Both methods featured advantages and limitations; nonetheless, both were used successfully for fabricating PMC parts. The solid mandrel method provided the best fidelity to the targeted part geometry and led to greater $G_I$ values. However, the extraction of the mandrel was highly difficult due to the shrinkage of the PMC during cure. Conversely, the inflatable mandrel method provided much easier removal of the mandrel and greater crack initiation load. However, the bagging was much more complex, increasing labour, and sharp corners could not be formed reliably. In this work, the solid mandrel method was selected for fabricating large-scale delta-stringer demonstrator panels despite its faults because it was the most consistent method. It is worth noting that the fabrication of the delta-stringer could be improved and future work should investigate other methods, such as the use of a collapsible mandrel for easier demoulding. This was not pursued in this work because the objective was to fabricate a part featuring a complex geometry, which was achieved.

The main contribution of the work presented in this chapter is the successful fabrication by out-of-autoclave RFI of a large-scale delta-stringer demonstrator made of a multi-scale PMC. The fabrication of such a complex structure made from multi-scale PMC is not reported in literature. The multi-scale PMC demonstrator panel LS-CNT featured the same physical appearance and similar part thicknesses than neat PMC demonstrator panel LS-neat. Hence, the addition of CNTs did not have an adverse effect on fabrication. However, no improvements to $G_I$ were observed from the addition of CNTs despite the higher ILSS measured from flat panels in Chapter 6. This is attributable to high porosity content of demonstrator panel LS-CNT, due to resin starvation. Nonetheless, ILSS results from Chapter 6 suggest that $G_I$ of LS-CNT would not have been significantly higher than that of LS-neat for the same porosity content. Conversely, results showed that $G_I$ can be improved significantly by using an elastomer toughened epoxy such as SA 70.

It follows that multi-scale PMCs featuring a complex geometry can be fabricated effectively through out-of-autoclave RFI. However, CNTs should not be used for improving interlaminar strength of PMCs because there are more effective ways for achieving that goal. Nonetheless, multi-scale PMC structures featuring CNTs may be worthwhile for other applications, namely those requiring greater electrical conductivity.

# Chapter 11

## Conclusion

The work presented herein sought to validate the viability of out-of-autoclave RFI processing for fabricating multi-scale carbon fibre PMCs featuring epoxy modified with CNTs, following a methodology that can be used at industrial scale. A wide array of materials and processing parameters were investigated to ensure that the assessment of RFI was thorough. This led to the successful fabrication of flat plates and of a technical demonstrator made from multi-scale PMC loaded with 0.3 wt% of CNTs (chapters 6 and 10). The work showed that the processing methodology when using an interleaved stacking configuration did not need to be altered when using epoxy reinforced with CNTs, which confirms the viability of the process for producing multi-scale PMCs. However, the addition of CNTs offered marginal improvements to the ILSS of PMCs, only 8.5% on average. Other factors such as the void content and fabric selection were found to have a more significant effect on the ILSS than CNTs. This observation ushered the need for a more thorough quantitative description of the RFI process for acquiring a greater knowledge of RFI which will help engineers and manufacturers design better PMC parts.

The development of a thorough description of the RFI process for manufacturing PMCs and multi-scale PMCs was achieved through in-situ observations of RFI and was conducted based on three focus areas that are discussed below: 1) kinematics of resin saturation, 2) void formation and 3) distribution and filtration of CNTs. The discussion of all 3 focus points is followed by a description of the contributions made through the thesis, and by recommendations for future work.

## 11.1 Kinematics of resin saturation

The kinematics of resin saturation in RFI is well understood at the macroscopic scale [41, 58–62, 64, 65, 67, 177] where the fibre reinforcement is assumed to behave as a homogeneous porous medium. The macroscopic description of resin flow is useful for defining a processing window that prevents large unsaturated regions in RFI parts. However, fibre reinforcements are heterogeneous media, leading to locally uneven flow fronts as the resin does not flow at the same rate around and inside yarns. The merging of these flow fronts results in air entrapment and flow-induced voids in PMC parts.

Prior to this work, limited information was available in the literature regarding the kinematics of resin saturation at the microscopic scale in RFI. Most work focused on presenting methods for characterising resin flow in semi-preg materials [72–75, 178]; no comprehensive study of the effect that material properties have on resin saturation during RFI was available.

This work enabled a complete and generalised description of the kinematics of resin saturation during RFI based on direct observation of resin flow, for a wide spectrum of material properties, various RFI stacking configurations and resin flow simulations (Chapter 7). This descriptive work confirmed that in any type of RFI, resin flow always begins to saturate inter-yarn regions before saturating the yarns due to the use of a hot-melt resin. Then, as both the resin viscosity and flow front velocity reduce during RFI processing, the capillary forces can come to dominate over viscous forces leading resin flow to become driven by the wicking of yarns. It is thus clear that the heterogeneous structure of fibre reinforcements always leads to uneven flow fronts at the microscopic scale.

Resin flow around and inside yarns can be influenced significantly by the fibre reinforcement geometry. It was readily understood that the kinematics of resin flow at the macroscopic scale can be linked to the global permeability value of the fibre reinforcement. However, this work showed that the out-of-plane permeability is governed by the size of inter-yarn gaps and tortuosity of resin flow. More generally, the work showed that the flow rate of resin around yarns can be increased by selecting a fibre reinforcement that features a

low cover factor and thick yarns, resulting in larger inter-yarn gaps and fewer plies in PMCs, which reduce tortuosity and resin flow length. Conversely, resin flow inside yarns was found to be dominant on transverse flow across fibre bundles. The saturation rate of yarns thus increased significantly with the reduction of yarn thickness.

The knowledge developed regarding local resin flow within heterogeneous fibre reinforcements provides valuable information to help engineers and manufacturers better select materials for optimising resin flow inside and around yarns during RFI processing and reduce risk of air entrapment.

## 11.2 Void formation

The work presented in Chapter 6 showed that the ILSS of PMCs is strongly influenced by the presence of voids. Some studies [23, 34, 36, 38, 39, 69, 70] tried to optimise the RFI process for reducing the void content in PMC parts by investigating the effect of different processing parameters. However, no prior work provided a thorough explanation of the source of voids in PMCs.

This work enabled a complete and generalised description of the kinematics of void formation during RFI based on direct observation, a wide spectrum of material properties and various RFI stacking configurations (Chapter 8). The work identified 2 types of voids: flow-induced voids and gas-induced voids.

Flow-induced voids are caused by uneven resin flow resulting from the heterogeneity of the fibre reinforcement. In this work, such voids were formed due to incomplete saturation of yarns and to the wicking of resin. The incomplete saturation of yarns was attributed to the use of a high viscosity resin and fabric featuring thick yarns. These voids can be mitigated by applying the knowledge developed during the study of the kinematics of resin saturation. Some voids also resulted from over-bleeding caused by yarns wicking resin out of inter-yarn gaps. These voids occur when capillary forces dominate over viscous forces. An over-bleeding parameter was developed for guiding the selection of materials and processing parameters that reduce the risk of over-bleeding.

The work showed that gas-induced voids, resulting from out-of-solution gases, were by far the most prominent source of voids in PMCs manufactured by RFI. Different stages of the kinematics of out-of-solution gases were identified, including bubble migration, bubble growth, bubble contraction and equilibrium. The migration of bubbles could result in bubbles being extracted out of the resin if the resin flow length was sufficiently long. This resulted PMCs featuring fewer voids when they were fabricated using the bulk stacking configuration compared to the interleaved stacking configuration. This opens opportunities for future work related to the optimisation of the resin distribution within RFI stacks. The work also showed the importance of reinforcement selection on the contraction of bubbles and dissolution of gasses. The selection of fibre reinforcements that limit the size of bubbles, such as low surface density fabrics, is highly beneficial for the reduction of the void content in PMCs as the gas dissolution rate is increased dramatically with a reduction in bubble size.

The knowledge developed regarding the kinematics of void formation provides solutions for reducing voids in PMCs. More importantly, the work allowed for a better understanding of the sources of voids and their formation, providing the missing link between the input process parameters of RFI and the final void content in PMC parts. This knowledge can help engineers and manufacturers to better target their effort for mitigating voids in PMC parts instead of blindly investigating the effect of processing parameters.

## 11.3 Distribution and filtration of CNTs

Resin film infusion was investigated as a potential candidate for manufacturing multi-scale PMCs that have increased ILSS through the addition of CNTs. Prior to this work, RFI was used for producing multi-scale PMCs [5, 6], but even though only marginal improvements to the interlaminar properties had been achieved, no thorough study of the effect that the RFI processing conditions have on the distribution and filtration of CNTs within PMCs was conducted.

This work enabled a thorough assessment of the distribution of CNTs within PMCs manufactured through RFI based on direct observation of the RFI process, for various RFI

stacking configurations and a wide array of fibre reinforcement architectures (Chapter 9). The limited improvement in ILSS provided by the CNTs in multi-scale PMCs was attributed in part to the heterogeneous CNT distribution within PMCs.

The work showed that the distribution of CNTs within PMCs is affected significantly by the RFI stacking configuration. CNT distribution and filtration were characterised for in-plane and through-thickness resin flow using the bulk stacking configuration, and also for cases using the interleaved stacking configuration. In all configurations of RFI, the dense fibre network of yarns act as an effective filter for bundles of CNTs. Conversely, inter-yarn gap are much more permeable to CNTs but still lead to filtering when using long resin flow lengths. For through-thickness resin flow using the bulk stacking configuration, the amount of CNT filtering was related to the through-thickness permeability value of the fibre reinforcement.

Even though CNT filtering can be minimised through the selection of highly permeable fibre reinforcements and use of an interleaved stacking configuration, achieving a homogeneous distribution of CNTs remains difficult due to the CNT clustering that occurs during RFI. CNT clusters lead to resin regions featuring high and low concentrations of CNTs, lowering the mechanical strength of the matrix compared to cases featuring a uniform CNT distribution. In addition, CNT clusters are filtered more easily than discrete CNTs, preventing CNT from flowing inside yarns and even between yarns themselves.

The work showed that CNT clusters appear in RFI parts even when there is a uniform distribution of CNTs in resin films, as-received. Direct observation of the RFI process showed that clustering occurs at higher process temperatures, when a critical resin viscosity value is reached; at lower viscosities, the viscous forces are not sufficiently strong to prevent the agglomeration of CNTs. In light of this observation, a solution was proposed for reducing clustering. PMCs were fabricated at a lower temperature but with a longer processing time to maintain the same degree of cure, resulting in higher resin viscosities during processing. This method reduced significantly CNT clustering and even allowed for minimal CNT filtration by yarns. However, the higher resin viscosity led to a significant

increase in void content which counterbalanced any increase in ILSS that would have been provided by a more uniform distribution of CNTs.

Even though the work did not enable the development of a new RFI approach that can harness the full potential of CNTs for improving the ILSS of PMCs, it nonetheless identified key issues that need to be addressed for manufacturing strong multi-scale PMCs.

## 11.4 Contributions

The work performed towards the completion of the thesis led to four original contributions in the field of engineering.

1. This work is the first to characterise in full the effect that the dual-scale architecture of fabrics has on local resin flow inside and around yarns during RFI. The characterisation is valid for both the interleaved and bulk stacking configurations. This information is valuable for helping engineers and manufacturers select fibre reinforcements towards reducing risks of flow-induced voids in PMCs. The knowledge is not only applicable to RFI, but also to all types of PMC manufacturing that features through-thickness resin flow, including but not limited to PMCs manufactured with semi-pregs, certain types of resin transfer mouldings methods, and wet compression moulding.

2. This work is the first to characterise in full the sources of voids in PMCs made through RFI. The main source of voids in PMCs was out-of-solution gases. Void formation was detailed and categorised in 4 kinematic stages of out-of-solution gases: migration, growth, contraction and equilibrium. The work also provided valuable information for selecting fibre reinforcements that reduce voids in PMCs by promoting gas dissolution through the control of the size of gas bubbles. Ultimately, this work provides tools for identifying sources of voids, helping engineers and manufacturers better target their efforts towards reducing voids in PMCs made through RFI. The knowledge that was developed is also applicable to most types of PMC manufacturing processes, especially for low pressure processes such as out-of-autoclave manufacturing featuring pre-pregs and vacuum-assisted resin transfer moulding that do not provide sufficient resin pressure to maintain gases in solution.

3. This work is the first characterise in full the effect that RFI has on the distribution and filtration of CNTs in multi-scale PMCs. The work showed that the homogeneity of the CNT distribution is affected by the filtration of the fibre reinforcement but mostly by the clustering of CNTs during processing. Ultimately, the work identified processing conditions and materials for guiding the fabrication of multi-scale PMCs using RFI. The findings are also applicable to any other type of PMC manufacturing processes as difficulties in achieving a uniform CNT distribution are not bound solely to a specific manufacturing process. Instead processing difficulties result mostly from material selection, either from a low compatibility between the resin and CNTs or from a fibre reinforcement geometry that leads to filtration.

4. This work resulted in the fabrication of demonstrator parts, leading to the first assessment of the scalability of RFI for manufacturing multi-scale PMCs.

In addition, the work was presented in two conferences [179, 180] and a paper [181] written in collaboration with CRIAQ partners and submitted to Composites Science and Technology.

## 11.5 Future work

The thesis investigated in great detail how material selection and processing conditions affect the kinematics of resin flow and void formation in PMCs, and CNT distribution in multi-scale PMCs. The work enabled the identification of two key areas for improving the RFI process.

Firstly, a reliable method needs to be developed for reducing voids in PMCs. In this work, it was showed that the use of low surface density weaves is an effective method for minimising voids; however, this limits material selection greatly; low surface density fibre reinforcements are also more expensive than others. Considering that voids in RFI parts are mostly caused by out-of-solution gases, future work should seek to develop an effective method for degassing resin films prior to RFI, or for achieving resin degassing during RFI by optimising resin distribution in RFI stacks.

Secondly, a solution must be developed for achieving a uniform distribution of CNTs within multi-scale PMCs without increasing the void content. This work showed that for out-of-autoclave RFI, the use of higher processing viscosities is not a viable solution due to increased manufacturing defects and processing time. It is believed that the ideal solution must come from the optimisation of the chemical compatibility between the resin matrix and the CNTs. This will reduce clustering and enable greater load transfer to CNTs. When this is addressed, RFI is expected to be an ideal candidate for manufacturing multi-scale PMCs.

# References

[1] Bibo G. A., and Hogg P. J., 1998, "Influence of reinforcement architechture on glass-fibre/epoxy composite systems," Compos. Sci., **58**, pp. 803–813.

[2] Mattheij P., Gliesche K., and Feltin D., 2000, "3D reinforced stitched carbon/epoxy laminates made by tailored fibre placement," Compos. Part A Appl. Sci. Manuf., **31**(6), pp. 571–581.

[3] Hillermeier R. W., Hayes B. S., and Seferis J. C., 1999, "Processing of highly elastomeric toughened cyanate esters through a modified resin transfer molding technique," Polym. Compos., **20**(1), pp. 155–165.

[4] Bin L., Lixin C., Jianna D., Huixin Z., and Fengfei L., 2011, "A thermosetting phenolic film and its application in the resin film infusion," J. Compos. Mater., **46**(3), pp. 285–290.

[5] Anand A., Harshe R., and Joshi M., 2013, "Resin film infusion: Toward structural composites with nanofillers," J. Appl. Polym. Sci., p. n/a-n/a.

[6] Mirjalili V., 2010, "Aspects of the fracture toughness of carbon nanotube modified epoxy polymer composites," McGill University.

[7] Ma P.-C., Siddiqui N. A., Marom G., and Kim J.-K., 2010, "Dispersion and functionalization of carbon nanotubes for polymer-based nanocomposites: A review," Compos. Part A Appl. Sci. Manuf., **41**(10), pp. 1345–1367.

[8] Sahoo N. G., Rana S., Cho J. W., Li L., and Chan S. H., 2010, "Polymer nanocomposites based on functionalized carbon nanotubes," Prog. Polym. Sci., **35**(7), pp. 837–867.

[9] Geng Y., Liu M. Y., Li J., Shi X. M., and Kim J. K., 2008, "Effects of surfactant treatment on mechanical and electrical properties of CNT/epoxy nanocomposites," Compos. Part A Appl. Sci. Manuf., **39**(12), pp. 1876–1883.

[10] Dean J. M., Lipic P. M., Grubbs R. B., Cook R. F., and Bates F. S., 2001, "Micellar structure and mechanical properties of block copolymer-modified epoxies," J. Polym. Sci. Part B Polym. Phys., **39**(23), pp. 2996–3010.

[11] Zheng S., Wang J., Guo Q., Wei J., and Li J., 1996, "Miscibility, morphology and fracture toughness of epoxy resin/poly(styrene-co-acrylonitrile) blends," Polymer (Guildf)., **37**(21), pp. 4667–4673.

[12] Kinloch A. J., Yuen M. L., and Jenkins S. D., 1994, "Thermoplastic-toughened epoxy polymers," J. Mater. Sci., **29**, pp. 3781–3790.

[13] Fan Z., Santare M. H., and Advani S. G., 2008, "Interlaminar shear strength of glass

fiber reinforced epoxy composites enhanced with multi-walled carbon nanotubes," Compos. Part A Appl. Sci. Manuf., **39**(3), pp. 540–554.

[14] Yourdkhani M., and Hubert P., 2013, "Quantitative dispersion analysis of inclusions in polymer composites," ACS Appl. Mater. Interfaces, **5**(1), pp. 35–41.

[15] Mirjalili V., Yourdkhani M., and Hubert P., 2012, "Dispersion stability in carbon nanotube modified polymers and its effect on the fracture toughness," Nanotechnology, **23**(31), pp. 1–8.

[16] Fan Z., Hsiao K., and Advani S. G., 2004, "Experimental investigation of dispersion during flow of multi-walled carbon nanotube / polymer suspension in fibrous porous media," Carbon N. Y., **42**, pp. 871–876.

[17] Aktas L., Dharmavaram S., Hamidi Y. K., and Cengiz Altan M., 2008, "Filtration and breakdown of clay clusters during resin transfer molding of nanoclay/glass/epoxy composites," J. Compos. Mater., **42**(21), pp. 2209–2229.

[18] Fan Z., and Advani S. G., 2005, "Characterization of orientation state of carbon nanotubes in shear flow," Mech. Eng., **46**, pp. 5232–5240.

[19] Thostenson E. T., and Chou T., 2002, "Aligned multi-walled carbon nanotube-reinforced composites : processing and mechanical characterization," J. Phys. D. Appl. Phys., **35**, pp. L77–L80.

[20] Wang Q., Dai J., Li W., Wei Z., and Jiang J., 2008, "The effects of CNT alignment on electrical conductivity and mechanical properties of SWNT/epoxy nanocomposites," Compos. Sci. Technol., **68**(7–8), pp. 1644–1648.

[21] Qiu J., Zhang C., Wang B., and Liang R., 2007, "Carbon nanotube integrated multifunctional multiscale composites," Nanotechnology, **18**(27), p. 275708.

[22] Frost M., Solanki D., and Mills A., 2003, "Resin film infusion process of carbon fibre composite automotive body panels," SAMPE J., **39**(4), pp. 44–48.

[23] Gause L. W., and Alper J. M., 1988, "Braided to net section graphite / epoxy composite shapes," J. Compos. Technol. Res., **10**(2), pp. 33–46.

[24] Storage K., and Childers P., 2009, "Innovative solution for improving non-autoclave resin film infusion (RFI) composite repair," SAMPE 2009 Spring symposium conference proceedings, vol. 54, May 18-21, Baltimore, MD, USA, pp. 1–18.

[25] Marsh G., 2002, "Resin film infusion- composites cost reducer," Reinf. Plast., (February), pp. 44–49.

[26] Corporation H., 2013, "HexFIT®" [Online]. Available: http://www.hexcel.com/products/wind-energy/whexfit.

[27] WILDER R., 2005, "Prepreg materials advance marine design into the future" [Online]. Available: http://www.jeccomposites.com/news/composites-news/prepreg-

materials-advance-marine-design-future.

[28] Letterman L. E., 1986, "Resin film infusion process and apparatus," pp. 1–6.

[29] Uchida H., Yamamoto T., and Takashima H., 2001, "Development of low-cost, damage resistant composites using RFI processing," SAMPE J., **37**(6), pp. 16–20.

[30] Mitchell J., Floyd A., Starratt D., Vaziri R., and Poursartip A., 2001, "Strain-softening of stitched RFI composites," Proceedings of the 33rd ISTC, November 5-8, Seattle, WA, USA, pp. 1–13.

[31] Takatoya T., and Susuki I., 2003, "Mechanical evaluation of 3-dimensional textile composites," Proceedings of the 35th ISTC, Sept. 28 - OCt. 2, Dayton, OH, USA, pp. 1–9.

[32] Susuki I., Shinya M., and Yasui Y., 1997, "Mechanical properties of 3-D carbon/bismaleimide heat resistant composites," Proceedings of the 11th ICCM, July 14-18, Gold Coast, Australia, pp. 614–624.

[33] Stenard S., Story T., Mitchell S., Price R., Blanton L., and Xie M., 2003, "From SBIR to production: Braided preforms and RFI combine for low-cost integrally stiffened structures," Proceedings of the 35th ISTC, Sept. 28 - OCt. 2, Dayton, OH, USA, pp. 1–14.

[34] Garschke C., Weimer C., Parlevliet P. P., and Fox B. L., 2012, "Out-of-autoclave cure cycle study of a resin film infusion process using in situ process monitoring," Compos. Part A Appl. Sci. Manuf., **43**(6), pp. 935–944.

[35] Fiedler L., Barré S., Molina J. I., and Voto C., 2003, "TANGO composite fuselage platform," SAMPE J., **39**(1), pp. 57–63.

[36] Thompson J. E., 2004, "Compaction and cure of resin film infusion prepregs," Virginia Polytechnic Institute and State University.

[37] Bader M. G., 1997, "Materials and process selection for cost-performance effective laminates," Proceedings of the 11th ICCM, July 14-18, Gold Coast, Australia, pp. 621–629.

[38] Karal M., 2001, NASA/CR-2001-210650, AST composite wing program, executive summary.

[39] Qi B., Raju J., Kruckenberg T., and Stanning R., 2000, "A resin film infusion process for manufacture of advanced composite structures," Compos. Struct., **47**(1999), pp. 471–476.

[40] Booker G. A., and Leon L. R., 2005, "Lowering the cost for composites used as secondary aircraft structure," Proceedings of the 15th ICCM, June 27-July 2, Durban, South Africa, pp. 1–10.

[41] Han N., Suh S., Yang J., and Hahn H., 2003, "Resin film infusion of stitched stiffened composite panels," Compos. Part A Appl. Sci. Manuf., **34**(3), pp. 227–236.

[42] Kruckenberg T., Qi B., Falzon P., Liu X. L., and Paton R., 2001, "Experimental and predicted in-plane flow height measurements for stiffened structures made using resin film infusion process," SAMPE J., **37**(3), pp. 28–34.

[43] Caba A. C., 1998, "Verification of a three-dimensional resin film infusion process simulation model," Virginia Polytechnic Institute and State University.

[44] Loos A. C., 2001, "Low-cost fabrication of advanced polymeric composites by resin infusion processes," Adv. Compos. Mater., **10**(2), pp. 99–106.

[45] HexPly M65: Product data, Hexcel Corp., October 2005.

[46] ST 70FR Fire retardant glass structural SPRINT, Gurit Ltd., PDS-ST 70FR Glass -9-0610.

[47] Ahn K. J., Seferis J. C., and Berg J. C., 1991, "Simultaneous measurements of permeability and capillary pressure of thermosetting matrices in woven fabric reinforcements," Polym. Compos., **12**(3), pp. 146–152.

[48] Gutowski T. G., Morigaki T., and Cai Z., 1987, "The consolidation of laminate composites," J. Compos. Mater., **21**(February), pp. 172–188.

[49] Dai Z., Zhang B., Shi F., Li M., Zhang Z., and Gu Y., 2011, "Effect of heat treatment on carbon fiber surface properties and fibers/epoxy interfacial adhesion," Appl. Surf. Sci., **257**(20), pp. 8457–8461.

[50] Page S. A., Berg J. C., and Månson J.-A. E., 2001, "Characterization of epoxy resin surface energetics," J. Adhes. Sci., **15**(2), pp. 153–170.

[51] Lee W. J., Seferis J. C., and Berg J. C., 1988, "Characterizing high performance composite processability with dynamic fiber wettability measurements," Polym. Compos., **9**(1), pp. 36–41.

[52] Hoecker F., and Karger-Kocsis J., 1996, "Surface energetics of carbon fibers and its effects on the mechanical performance of CF/EP composites," J. Appl. Polym. Sci., **59**, pp. 139–153.

[53] Cheng C., and Lin H., 2008, "Measurement of surface tension of epoxy resins used in dispensing process for manufacturing thin film transistor-liquid crystal displays," IEEE Trans. Adv. Packag., **31**(1), pp. 100–106.

[54] Cheng R., Jang S., and An L., 2009, "Wettability of epoxy resin on carbon fiber," Acta Polym. Sin., **4**(April), p. 2009.

[55] Massoudi R., and King A. D. J., 1974, "Effect of pressure on the surface tension of water. Adsorption of low molecular weight gases on water at 25°," J. Phys. Chem., **78**(22), pp. 2262–2266.

[56] Lee S. M., 1992, Handbook of composite reinforcements, John Wiley & Sons.

[57] Oroojalian F., Omidi M., Ranjbartaznji M., and Alagheband M., 2012, "A study of wetting characteristics of carbon nanotubes / epoxy on carbon fibre surface,"

Proceedings of the 20th Annual International Conference on Composites/Nano Engeneering, Jul. 22-28, Beijing, China, pp. 1–2.

[58] Caba A. C., Rattazzi D., Batra R., and Loos A. C., 1999, "Verification of a simulation model for RFI of complex shaped composite structures," J. Reinf. Plast. Compos., **18**(16), pp. 1465–1478.

[59] Park C. H., and Saouab A., 2009, "Analytical modeling of composite molding by resin infusion with flexible tooling: VARI and RFI processes," J. Compos. Mater., **43**(18), pp. 1877–1900.

[60] Joshi S. C., Liu X.-L., Lam Y. C., and Sheridan J., 1999, "Simulation of resin film infusion process using finite element/nodal control volume approach," Adv. Compos. Lett., **8**(3), pp. 101–104.

[61] Loos A. C., and MacRae J. D., 1996, "A process simulation model for the manufacture of a blade-stiffened panel by the resin film infusion process," Compos. Sci. Technol., **56**(3), pp. 273–289.

[62] Loos A. C., Rattazzi D., and Batra R. C., 2002, "A three-dimensional model of the resin film infusion process," J. Compos. Mater., **36**(10), pp. 1255–1273.

[63] Mei Y., Shilin Y., and Hua T., 2006, "Simulation of the resin film infusion process based on the finite element method," J. Wuhan Univ. Technol. Sci. Ed., **21**(4), pp. 180–182.

[64] Park J., and Kang M. K., 2003, "A numerical simulation of the resin film infusion process," Compos. Struct., **60**(4), pp. 431–437.

[65] Li D., Nie Y., Zhou X., and Cai L., 2011, "Numerical modeling of resin film infusion process with compaction and its application," CMES, **72**(2), pp. 149–166.

[66] Myslinski P. J., 1997, "Analysis of cyanate ester resins and graphite fabric for use in resin film infusion processing," Virginia Polytechnic Institute and State University.

[67] Blest D. C., McKee S., Zulkifle A. K., and Marshall P., 1999, "Curing simulation by autoclave resin infusion," Compos. Sci. Technol., **59**, pp. 2297–2313.

[68] Sevostianov I. B., Verijenko V. E., Klemperer C. J. von, and Chevallereau B., 1999, "Mathematical model of stress formation during vacuum resin infusion process," Compos. Part B Eng., **30**(5), pp. 513–521.

[69] Margueres P., Lopez Torres J., Perie J.-N., and Collombet F., 2008, "Combined approach for the characterization of composites manufactured by RFI and industrial application," J. Compos. Mater., **42**(2), pp. 189–209.

[70] Shim S.-B., Ahn K., Seferis J. C., Berg A. J., and Hudson W., 1995, "Cracks and microcracks in stitched structural composites manufactured with resin film infusion process," J. Adv. Mater., **26**(4), pp. 48–62.

[71] Grunenfelder L. K., Centea T., Hubert P., and Nutt S. R., 2013, "Effect of room-temperature out-time on tow impregnation in an out-of-autoclave prepreg," Compos. Part A Appl. Sci. Manuf., **45**, pp. 119–126.

[72] Thomas S., Bongiovanni C., and Nutt S. R., 2008, "In situ estimation of through-thickness resin flow using ultrasound," Compos. Sci. Technol., **68**(15–16), pp. 3093–3098.

[73] Cender T. A., Simacek P., and Advani S. G., 2013, "Resin film impregnation in fabric prepregs with dual length scale permeability," Compos. Part A Appl. Sci. Manuf., **53**, pp. 118–128.

[74] Tavares S. S., Michaud V., and Månson J.-A. E., 2010, "Assessment of semi-impregnated fabrics in honeycomb sandwich structures," Compos. Part A Appl. Sci. Manuf., **41**(1), pp. 8–15.

[75] Centea T., and Hubert P., 2012, "Modelling the effect of material properties and process parameters on tow impregnation in out-of-autoclave prepregs," Compos. Part A Appl. Sci. Manuf., **43**(9), pp. 1505–1513.

[76] Centea T., and Hubert P., 2014, "Out-of-autoclave prepreg consolidation under deficient pressure conditions," J. Compos. Mater., **48**(16), pp. 2033–2045.

[77] Grunenfelder L. K., and Nutt S. R., 2010, "Void formation in composite prepregs – Effect of dissolved moisture," Compos. Sci. Technol., **70**(16), pp. 2304–2309.

[78] Sevostianov I., Verijenko V. E., and Klemperer C. J. von, 2000, "Mathematical model of cavitation during resin film infusion process," Compos. Struct., **48**(1–3), pp. 197–203.

[79] Agius S. L., and Fox B. L., 2015, "Rapidly cured out-of-autoclave laminates: Understanding and controlling the effect of voids on laminate fracture toughness," Compos. Part A Appl. Sci. Manuf., **73**, pp. 186–194.

[80] Wood J. R., and Bader M. G., 1994, "Void control for polymer-matrix composites (1): Theoretical and experimental methods for determining the growth and collapse of gas bubbles," Compos. Manuf., **5**(3), pp. 139–147.

[81] Hamill L., Centea T., and Nutt S., 2015, "Surface porosity during vacuum bag-only prepreg processing: Causes and mitigation strategies," Compos. Part A Appl. Sci. Manuf., **75**, pp. 1–10.

[82] Arafath A. R. A., Fernlund G., and Poursartip A., 2009, "Gas transport in prepregs: model and permeability experiments," Proceedings of the 17th International Conference on Composite Materials, July 27-31, pp. 1–9.

[83] Wood J. R., and Bader M. G., 1994, "Void control for polymer-matrix composites (2): experimental evaluation of a diffusion model for the growth and collapse of gas bubbles," Compos. Manuf., **5**(3), pp. 149–158.

[84] Advani S. G., and Arefmanesh A., 1993, "Bubble growth and collapse in

viscoelastic liquids," Advances in Transport Processes, A.S. Mujumdar, and R.A. Mashelkar, eds., Elsevier, pp. 445–499.

[85] Kardos J. L., Duduković M. P., McKague E. L., and Lehman M. W., 1983, "Void formation and transport during composite lamiante processing: An initial model framework," Composite materials: Quality assurance and processing, C.E. Browning, ed., ASTM International, Baltimore, USA, pp. 96–109.

[86] Trochu F., Ruiz E., Achim V., and Soukane S., 2006, "Advanced numerical simulation of liquid composite molding for process analysis and optimization," Compos. Part A Appl. Sci. Manuf., **37**(6), pp. 890–902.

[87] Lv P., Feng Y. Y., Zhang P., Chen H. M., Zhao N., and Feng W., 2011, "Increasing the interfacial strength in carbon fiber/epoxy composites by controlling the orientation and length of carbon nanotubes grown on the fibers," Carbon N. Y., **49**(14), pp. 4665–4673.

[88] Storck S., Malecki H., Shah T., and Zupan M., 2011, "Improvements in interlaminar strength: A carbon nanotube approach," Compos. Part B Eng., **42**(6), pp. 1508–1516.

[89] Fan Z., and Advani S. G., 2007, "Rheology of multiwall carbon nanotube suspensions," J. Rheol. (N. Y. N. Y)., **51**(4), pp. 585–604.

[90] Yu M.-F., Lourie O., Dyer M. J., Moloni K., Kelly T. F., and Ruoff R. S., 2000, "Strength and Breaking Mechanism of Multiwalled Carbon Nanotubes Under Tensile Load," Science (80-. )., **287**(5453), pp. 637–640.

[91] Wei X., Chen Q., Peng L., Cui R., and Li Y., 2009, "Tensile Loading of Double-Walled and Triple-Walled Carbon Nanotubes and their Mechanical Properties," (Cvd), pp. 17002–17005.

[92] Peng B., Locascio M., Zapol P., Li S., Mielke S. L., Schatz G. C., and Espinosa H. D., 2008, "Measurements of near-ultimate strength for multiwalled carbon nanotubes and irradiation-induced crosslinking improvements," Nat Nano, **3**(10), pp. 626–631.

[93] Khandoker N., Hawkins S. C., Ibrahim R., Huynh C. P., and Deng F., 2011, "Tensile strength of spinnable multiwall Carbon Nanotubes," Procedia Eng., **10**, pp. 2572–2578.

[94] Demczyk B. G., Wang M., Cumingd J., Hetamn M., Han W., Zettl A., and Ritchie R., 2002, "Direct mechanical measurements of the tensile strength and elastic modulus of multi-walled carbon nanotubes.," Mater. Sci. Eng. A., **334**(1–2), pp. 173–178.

[95] Wang M. S., Golberg D., and Bando Y., 2010, "Tensile tests on individual single-walled carbon nanotubes: Linking nanotube strength with its defects," Adv. Mater., **22**(36), pp. 4071–4075.

[96] Wang Z. ., Gao R. ., Poncharal P., de Heer W. ., Dai Z. ., and Pan Z. ., 2001,

"Mechanical and electrostatic properties of carbon nanotubes and nanowires," Mater. Sci. Eng. C, **16**(1–2), pp. 3–10.

[97] Aliev A. E., Lima M. H., Silverman E. M., and Baughman R. H., 2010, "Thermal conductivity of multi-walled carbon nanotube sheets: radiation losses and quenching of phonon modes," Nanotechnology, **21**(3), p. 35709.

[98] Bauer M. L., Pham Q. N., Saltonstall C. B., and Norris P. M., 2014, "Thermal conductivity of vertically aligned carbon nanotube arrays: Growth conditions and tube inhomogeneity," Appl. Phys. Lett., **105**(15).

[99] Gao B., Chen Y. F., Fuhrer M. S., Glattli D. C., and Bachtold A., 2005, "Four-point resistance of individual single-wall carbon nanotubes," Phys. Rev. Lett., **95**(19), pp. 4–7.

[100] Li C., Thostenson E. T., and Chou T. W., 2008, "Effect of nanotube waviness on the electrical conductivity of carbon nanotube-based composites," Compos. Sci. Technol., **68**(6), pp. 1445–1452.

[101] Bachtold A., Henny M., Terrier C., Strunk C., Schönenberger C., Salvetat J. P., Bonard J. M., and Forró L., 1998, "Contacting carbon nanotubes selectively with low-ohmic contacts for four-probe electric measurements," Appl. Phys. Lett., **73**(2), pp. 274–276.

[102] Berger C., Yi Y., Wang Z. L., and Heer W. a De, 2002, "Multiwalled carbon nanotubes are ballistic conductors," Nature, **365**, pp. 363–365.

[103] Li Q., Li Y., Zhang X., Chikkannanavar S. B., Zhao Y., Dangelewicz A. M., Zheng L., Doorn S. K., Jia Q., Peterson D. E., Arendt P. N., and Zhu Y., 2007, "Structure-dependent electrical properties of carbon nanotube fibers," Adv. Mater., **19**(20), pp. 3358–3363.

[104] Li Y.-L., Kinloch I. A., and Windle A. H., 2004, "Direct Spinning of Carbon Nanotube Fibers from Chemical Vapor Deposition Synthesis," Sci. (Washington, DC, United States), **304**(5668), pp. 276–278.

[105] McEuen P. L., Fuhrer M. S., and Park H., 2002, "Single-walled carbon nanotube electronics," IEEE Trans. Nanotechnol., **1**(1), pp. 78–84.

[106] Zhou W., Vavro J., Guthy C., Winey K. I., Fischer J. E., Ericson L. M., Ramesh S., Saini R., Davis V. A., Kittrell C., Pasquali M., Hauge R. H., and Smalley R. E., 2004, "Single wall carbon nanotube fibers extruded from super-acid suspensions: Preferred orientation, electrical, and thermal transport," J. Appl. Phys., **95**(2), pp. 649–655.

[107] Zhu H. W., Xu C. L., Wu D. H., Wei B. Q., Vajtai R., and Ajayan P. M., 2002, "Direct Synthesis of Long Single-Walled Carbon Nanotube Strands," Science (80-. )., **296**(5569), pp. 884–886.

[108] Montazeri A., Javadpour J., Khavandi A., Tcharkhtchi A., and Mohajeri A., 2010, "Mechanical properties of multi-walled carbon nanotube/epoxy composites," Mater.

Des., **31**(9), pp. 4202–4208.

[109] Ma P. C., Mo S. Y., Tang B. Z., and Kim J. K., 2010, "Dispersion, interfacial interaction and re-agglomeration of functionalized carbon nanotubes in epoxy composites," Carbon N. Y., **48**(6), pp. 1824–1834.

[110] Shaffer M. S. P., and Windle A. H., 1999, "Fabrication and characterization of carbon nanotube/poly(vinyl alcohol) composites," Adv. Mater., **11**(11), pp. 937–941.

[111] Sandler J., Shaffer M. S. ., Prasse T., Bauhofer W., Schulte K., and Windle A. ., 1999, "Development of a dispersion process for carbon nanotubes in an epoxy matrix and the resulting electrical properties," Polymer (Guildf)., **40**(21), pp. 5967–5971.

[112] Geng H., Rosen R., Zheng B., Shimoda H., Fleming L., Liu J., and Zhou O., 2002, "Fabrication and Properties of Composites of Poly(ethylene oxide) and Functionalized Carbon Nanotubes," Adv. Mater., **14**(19), pp. 1387–1390.

[113] Liao Y. H., Marietta-Tondin O., Liang Z., Zhang C., and Wang B., 2004, "Investigation of the dispersion process of SWNTs/SC-15 epoxy resin nanocomposites," Mater. Sci. Eng. A, **385**(1–2), pp. 175–181.

[114] Gong X., Liu J., Baskaran S., Voise R. D., and Young J. S., 2000, "Surfactant-assisted processing of carbon nanotube/polymer composites," Chem. Mater., **12**(4), pp. 1049–1052.

[115] Kim M., Park Y. Bin, Okoli O. I., and Zhang C., 2009, "Processing, characterization, and modeling of carbon nanotube-reinforced multiscale composites," Compos. Sci. Technol., **69**(3–4), pp. 335–342.

[116] Lau K., Lu M., Chun-ki Lam, Cheung H., Sheng F.-L., and Li H.-L., 2005, "Thermal and mechanical properties of single-walled carbon nanotube bundle-reinforced epoxy nanocomposites: the role of solvent for nanotube dispersion," Compos. Sci. Technol., **65**(5), pp. 719–725.

[117] Shaffer M. S. P., Fan X., and Windle a. H., 1998, "Dispersion and packing of carbon nanotubes," Carbon N. Y., **36**(11), pp. 1603–1612.

[118] Sandler J. K. W., Kirk J. E., Kinloch I. A., Shaffer M. S. P., and Windle A. H., 2003, "Ultra-low electrical percolation threshold in carbon-nanotube-epoxy composites," Polymer (Guildf)., **44**(19), pp. 5893–5899.

[119] Pötschke P., Fornes T. D., and Paul D. R., 2002, "Rheological behavior of multiwalled carbon nanotube/polycarbonate composites," Polymer (Guildf)., **43**(11), pp. 3247–3255.

[120] Rahman M. M., Zainuddin S., Hosur M. V., Malone J. E., Salam M. B. A., Kumar A., and Jeelani S., 2012, "Improvements in mechanical and thermo-mechanical properties of e-glass/epoxy composites using amino functionalized MWCNTs," Compos. Struct., **94**(8), pp. 2397–2406.

[121] Rahman M., Hosur M., Zainuddin S., Vaidya U., Tauhid A., Kumar A., Trovillion J., and Jeelani S., 2013, "Effects of amino-functionalized MWCNTs on ballistic impact performance of E-glass/epoxy composites using a spherical projectile," Int. J. Impact Eng., **57**, pp. 108–118.

[122] Ayatollahi M. R., Shadlou S., Shokrieh M. M., and Chitsazzadeh M., 2011, "Effect of multi-walled carbon nanotube aspect ratio on mechanical and electrical properties of epoxy-based nanocomposites," Polym. Test., **30**(5), pp. 548–556.

[123] Guo J., Liu Y., Prada-Silvy R., Tan Y., Azad S., Krause B., Pötschke P., and Grady B. P., 2014, "Aspect ratio effects of multi-walled carbon nanotubes on electrical, mechanical, and thermal properties of polycarbonate/MWCNT composites," J. Polym. Sci. Part B Polym. Phys., **52**(1), pp. 73–83.

[124] Gojny F. H., Wichmann M. H. G., Fiedler B., Bauhofer W., and Schulte K., 2005, "Influence of nano-modification on the mechanical and electrical properties of conventional fibre-reinforced composites," Compos. Part A Appl. Sci. Manuf., **36**(11), pp. 1525–1535.

[125] Sánchez M., Campo M., Jiménez-Suárez A., and Ureña A., 2013, "Effect of the carbon nanotube functionalization on flexural properties of multiscale carbon fiber/epoxy composites manufactured by VARIM," Compos. Part B Eng., **45**(1), pp. 1613–1619.

[126] Wichmann M. H. G., Sumfleth J., Gojny F. H., Quaresimin M., Fiedler B., and Schulte K., 2006, "Glass-fibre-reinforced composites with enhanced mechanical and electrical properties - Benefits and limitations of a nanoparticle modified matrix," Eng. Fract. Mech., **73**(16), pp. 2346–2359.

[127] Bekyarova E., Thostenson E. T., Yu A., Itkis M. E., Fakhrutdinov D., Chou T. W., and Haddon R. C., 2007, "Functionalized single-walled carbon nanotubes for carbon fiber-epoxy composites," J. Phys. Chem. C, **111**(48), pp. 17865–17871.

[128] Zhou H. W., Mishnaevsky L., Yi H. Y., Liu Y. Q., Hu X., Warrier A., and Dai G. M., 2016, "Carbon fiber/carbon nanotube reinforced hierarchical composites: Effect of CNT distribution on shearing strength," Compos. Part B Eng., **88**, pp. 201–211.

[129] Zeiler R., Khalid U., Kuttner C., Kothmann M., Dijkstra D. J., Fery A., and Altstädt V., 2014, "Liquid composite molding-processing and characterization of fiber-reinforced composites modified with carbon nanotubes," AIP Conf. Proc., **1593**, pp. 503–507.

[130] Godara A., Mezzo L., Luizi F., Warrier A., Lomov S. V., van Vuure A. W., Gorbatikh L., Moldenaers P., and Verpoest I., 2009, "Influence of carbon nanotube reinforcement on the processing and the mechanical behaviour of carbon fiber/epoxy composites," Carbon N. Y., **47**(12), pp. 2914–2923.

[131] Grimmer C. S., and Dharan C. K. H., 2010, "Enhancement of delamination fatigue resistance in carbon nanotube reinforced glass fiber/polymer composites," Compos. Sci. Technol., **70**(6), pp. 901–908.

[132] Song Y. S., 2007, "Multiscale fiber-reinforced composites prepared by vacuum-assisted resin transfer molding," Polym. Polym. Compos., pp. 458–461.

[133] Warrier A., Godara A., Rochez O., Mezzo L., Luizi F., Gorbatikh L., Lomov S. V., VanVuure A. W., and Verpoest I., 2010, "The effect of adding carbon nanotubes to glass/epoxy composites in the fibre sizing and/or the matrix," Compos. Part A Appl. Sci. Manuf., **41**(4), pp. 532–538.

[134] De Greef N., Gorbatikh L., Godara A., Mezzo L., Lomov S. V., and Verpoest I., 2011, "The effect of carbon nanotubes on the damage development in carbon fiber/epoxy composites," Carbon N. Y., **49**(14), pp. 4650–4664.

[135] Zhou Y., Pervin F., Rangari V. K., and Jeelani S., 2006, "Fabrication and evaluation of carbon nano fiber filled carbon/epoxy composite," Mater. Sci. Eng. A, **426**(1–2), pp. 221–228.

[136] Godara A., Gorbatikh L., Kalinka G., Warrier A., Rochez O., Mezzo L., Luizi F., van Vuure A. W., Lomov S. V., and Verpoest I., 2010, "Interfacial shear strength of a glass fiber/epoxy bonding in composites modified with carbon nanotubes," Compos. Sci. Technol., **70**(9), pp. 1346–1352.

[137] Aldajah S., and Haik Y., 2012, "Transverse strength enhancement of carbon fiber reinforced polymer composites by means of magnetically aligned carbon nanotubes," Mater. Des., **34**, pp. 379–383.

[138] Chu H., Zhang Z., Liu Y., and Leng J., 2015, "Self-response multi-functional composite material base on carbon nanotube paper using deicing, flame retardancy, thermal insulation, and lightning-strike protection," Proceedings of SPIE 9432, Behavior and Mechanics of Multifunctional Materials and Composites, San Diego, California, United States , March 8.

[139] Thostenson E. T., and Chou T. W., 2006, "Carbon nanotube networks: Sensing of distributed strain and damage for life prediction and self healing," Adv. Mater., **18**(21), pp. 2837–2841.

[140] Jiménez-Suárez A., Campo M., Sánchez M., Romón C., and Ureña A., 2012, "Influence of the functionalization of carbon nanotubes on calendering dispersion effectiveness in a low viscosity resin for VARIM processes," Compos. Part B Eng., **43**(8), pp. 3482–3490.

[141] Jiménez-Suárez A., Campo M., Sánchez M., Romón C., and Ureña A., 2012, "Dispersion of carbon nanofibres in a low viscosity resin by calendering process to manufacture multiscale composites by VARIM," Compos. Part B Eng., **43**(8), pp. 3104–3113.

[142] Leo 2376 - Datasheet, Nanoledge.

[143] AKD 2396 – Datasheet, Nanoledge.

[144] Innovium FLY: Aerospace applications, Nanoledge.

[145] Lucas P., and Roth T., 2010, "LEO semi-solid resin film," JEC Compos. Mag., **54**(January), pp. 53–55.

[146] Baytubes C 150 P, Bayer MaterialScience, Ed. 2008-03-10.

[147] Delivery programme and characteristics for Tenax® HTS filament yarn, GmbH, TohoTenax Europe, (04/2011).

[148] HTS40 technical data sheet, Toho Tenax America, inc., PLS 020 Rev F 10 Apr 2012.

[149] Rebouillat S., Letellier B., and Steffenino B., 1999, "Wettability of single fibres - beyond the contact angle approach," Adhes. Adhes., **19**, pp. 303–314.

[150] 2012, ASTM Standard D1259-06: Standard test methods for nonvolatile content of resin solution, ASTM International.

[151] 2006, ASTM Standard D2344/D2344M - 00: Standard test method for short-beam strength of polymer matrix composite materials, ASTM International, Barr Harbour, PA, USA.

[152] Sherburn M., 2007, "Geometric and Mechanical Modelling of Textiles," University of Nottingham.

[153] Gebart B. R., 1992, "Permeability of unidirectional reinforcements for RTM," J. Compos. Mater., **26**(8), pp. 1100–1133.

[154] Dave R., Kardos J. L., and Duduković M. P., 1987, "A model for resin flow during composite processing part 2: Numerical analysis for unidirectional graphite/epoxy laminates," Polym. Compos., **8**(2), pp. 123–132.

[155] Yang Y., 2013, "Thermal conductivity of carbon fibre fabrics and multi-scale composites with heat transfer simulations for RFI manufacturing," University of Ottawa.

[156] Wheeler D. J., 1987, Understanding industrial experimentation, SPC Press, Knoxville, TN, USA.

[157] Sihn S., Kim R. Y., Kawabe K., and Tsai S. W., 2007, "Experimental studies of thin-ply laminated composites," Compos. Sci. Technol., **67**, pp. 996–1008.

[158] Amacher R., Cugnoni J., Botsis J., Sorensen L., Smith W., and Dransfeld C., 2014, "Thin ply composites : Experimental characterization and modeling of size-effects," Compos. Sci. Technol., **101**, pp. 121–132.

[159] Baril-Gosselin S., and Li C., 2016, "Characterizing and Predicting the Effects of Weave Geometry on Mode I Fracture Toughness of Composites," Proceedings of the 31st Annual Technical Conference of the American Society for Composites, Williamsburg, VA, September 19-21.

[160] Page S. A., Mezzenga R., Boogh L., Berg J. C., and Månson J.-A. E., 2000, "Surface energetics evolution during processing of epoxy resins," J. Colloid

Interface Sci., **222**(1), pp. 55–62.

[161] Fox R. W., McDonald A. T., and Philip J. Pritchard, 2004, Introduction to fluid mechanics, John Wiley & Sons.

[162] Leclerc J. S., and Ruiz E., 2008, "Porosity reduction using optimized flow velocity in Resin Transfer Molding," Compos. Part A Appl. Sci. Manuf., **39**(12), pp. 1859–1868.

[163] Molnar J. A., Trevino L., and Lee L. J., 1989, "Liquid flow in molds with prelocated fiber mats," Polym. Compos., **10**(6), pp. 414–423.

[164] Rohatgi V., Patel N., and Lee L. J., 1996, "Experimental investigation of flow-induced microvoids during impregnation of unidirectional stitched fiberglass mat," Polym. Compos., **17**(2), pp. 161–170.

[165] Patel N., Rohatgi V., and Lee L. J., 1995, "Micro scale flow behavior and void formation mechanism during impregnation through a unidirectional stitched fiberglass mat," Polym. Eng. Sci., **35**(10), pp. 837–851.

[166] Chung Hae Park, and Woo L., 2011, "Modeling void formation and unsaturated flow in liquid composite molding processes: a survey and review," J. Reinf. Plast. Compos., **30**(11), pp. 957–977.

[167] Kang M. K., Lee W. Il, and Hahn H. T., 2000, "Formation of microvoids during resin-transfer molding process," Compos. Sci. Technol., **60**(12–13), pp. 2427–2434.

[168] Kulichenko A. V., 2005, "Theoretical analysis, calculation, and prediction of the air permeability of textiles," Fibre Chem., **37**(5), pp. 371–380.

[169] Gangloff J. J., Daniel C., and Advani S. G., 2014, "A model of two-phase resin and void flow during composites processing," Int. J. Multiph. Flow, **65**, pp. 51–60.

[170] Plesset M. S., and Prosperetti A., 1977, "Bubble dynamics and cavitation," Annu. Rev. Fluid Mech., **9**, pp. 145–185.

[171] Han C. D., and Yoo H. J., 1981, "Studies on structural foam processing. IV. Bubble growth during mold filling," Polym. Eng. Sci., **21**(9), pp. 518–533.

[172] Wood J. R., and Bader M. G., 1995, "Modelling the behaviour of gas bubbles in an epoxy resin: Evaluating the input parameters for a diffusion model using a free-volume approach," J. Mater. Sci., **30**(4), pp. 916–922.

[173] Yourdkhani M., 2013, "Aspects of Nanoparticles Dispersion and Interaction in Polymer Nanocomposites," McGill University.

[174] Khoun L., Centea T., and Hubert P., 2010, "Characterization Methodology of Thermoset Resins for the Processing of Composite Materials - Case Study: CYCOM 890RTM Epoxy Resin," J. Compos. Mater., **44**(11), pp. 1397–1415.

[175] McGill University, 2013, Report: Cure kinetics model LEO resin.

[176] Gill A. F., Robinson P., and Pinho S., 2009, "Effect of variation in fibre volume fraction on modes I and II delamination behaviour of 5HS woven composites manufactured by RTM," Compos. Sci. Technol., **69**(14), pp. 2368–2375.

[177] Wysocki M., Larsson R., and Toll S., 2009, "Modelling the consolidation of partially impregnated prepregs," Proceedings of the 17th International Conference on Composite Materials, pp. 1–10.

[178] Centea T., and Hubert P., 2011, "Measuring the impregnation of an out-of-autoclave prepreg by micro-CT," Compos. Sci. Technol., **71**(5), pp. 593–599.

[179] Baril-Gosselin S., and Robitaille F., 2015, "Characterisation of resin flow and void formation in RFI," Proceedings of the 20th International Conference on Composite Materials, Jul. 19-24, pp. 1–10.

[180] Baril-Gosselin S., and Robitaille F., 2017, "Filtration and dispersion of carbon nanotubes during resin film infusion," CANCOM2017 – Canadian International Conference on Composites, Montreal, Qc, July 17-20, pp. 1–10.

[181] Yourdkhani M., Liu W., Baril-Gosselin S., Robitaille F., and Hubert P., "Manuscript submitted for publication: Carbon nanotube-reinforced carbon fibre-epoxy composites manufactured by resin film infusion," Compos. Sci. Technol.

# Appendices

## Appendix A: Literature values of surface energy and contact angles

Table A.1: Literature values of surface energy for epoxy and carbon fibres

| Material | Condition | Technique | Formulation /type | Temperature (°C) | Total surface tension ($mJ/m^2$) |
|---|---|---|---|---|---|
| Epoxy resins | Uncured | Wilhelmy method | DGEBA | Room | 36.3 [50] |
| | | | TGMDA | " | 41.4 [50] |
| | | | WC-68 (DPDGE) | " | 36.08 [51] |
| | | | LY 556 | Room | 42 [52] |
| | | Sessile drop, inverse method | E51 (DGEBA) | " | 34.75 [53] |
| | | | Epoxy 618 | 30 | 47.5 [54] |
| | Cured | Wilhelmy method | DGEBA | Room | 35.1 [50] |
| | | | TGMDA | " | 35.5 [50] |
| | | IGA | E51 (DGEBA) | 30°C | 45.78 [49] |
| | | | DGEBA | Room | 46.1 [50] |
| | | | TGMDA | " | 46.9 [50] |
| Carbon fibre | No sizing | Wilhelmy method | Idemitsu | Room | 40.1 [52] |
| | | | Tenax HTA 5001 | " | 41.1 [52] |
| | Epoxy-based sizing | Wilhelmy method | Tenax HTA 5131 | Room | 47.2 [52] |
| | | IGA | T300B-3000-40B | 30°C | 39-40.5 [49] |

IGA: Invert gas chromatography

Table A.2: Wettability of epoxy resins on carbon fibres

| Technique | Resin formulation | Fibre | Sizing | Temperature (°C) | Contact angle (°) |
|---|---|---|---|---|---|
| Sessile drop | Epoxy 618 | T700SC | Epoxy-based | 30 | 15 [54] |
| | LY 5052 | Toray T300 | Not mentioned | Not mentioned | 44 [57] |
| | LY 564 | Toray T300 | Not mentioned | Not mentioned | 41 [57] |
| Wilhelmy method | WC-68 (NPDGE) | Thornel T300 | UC 309 (Epoxy-based) | Room | 33 [51] |
| | WC-68 (NPDGE) | Thornel T300 | None | " | 30 [51] |
| | E51 | Toray T300B | 40B | " | 42.5 [49] |
| Direct tangent method | Cured LY 556 | Idemitsu | Not mentioned | Room | 50 [52] |
| | Cured LY 556 | Tenax HTA 5001 | None | " | 45.5 [52] |
| | Cured LY 556 | Tenax HTA 5131 | Epoxy-based | " | 41.5 [52] |

# Appendix B: Effect of the number of fabric plies on fibre volume fraction

During thesis work the compaction curves of the fabrics were obtained from stacks composed of twelve plies. No other stacking configurations were tested due to limited availability of some fabrics. Nonetheless, the effects of the number of plies and number of repeats were investigated using fabric NCF-HP, the fabric with highest availability. Testing was performed through repetitive compaction. A total of 3 repeats consisting of 51 compaction cycles at 1 MPa were done for stacks of 3 and 6 fabric plies.

Currently, results for the evolution of the fibre volume fraction at 1 MPa for stacks of 3 and 6 plies appear in Figures B.1-B.2 respectively. Results show that repeatability of the measurements is relatively good and that the standard deviation is less than ±0.7% of fibre volume fraction. The average values of repeats for stacks of 3 and 6 plies appear in Figure B.3. The increase in number of plies from 3 to 6 increased the fibre volume fraction values by approximately 1% of fibre volume fraction, which is not statistically significant. Further analysis is required for assessing the effect of the 12 plies stacks that are used other fabrics.

Finally, it should be noted that the test was stopped in the middle of repeat #1 for the compaction with 6 fabric plies. The stack was put away for several hours before the repetitive compactions resumed. The handling of the fabrics led to fibre reorganisation that lowered the fibre volume fraction slightly. It took approximately 5 compaction cycles to recover the lost compaction. Hence, the effects of pre-compaction are somewhat diminished by fabric handling.

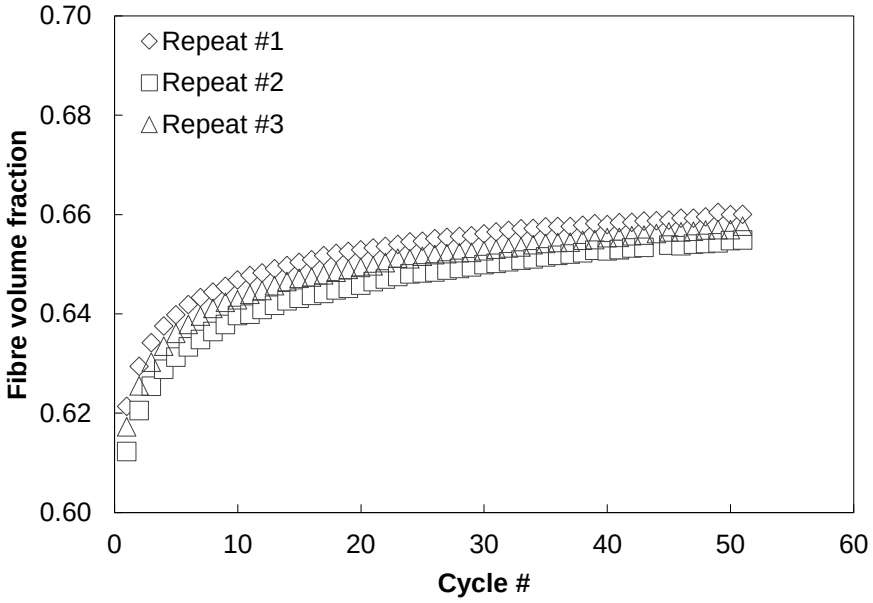


Figure B.1: Fibre volume fraction values as a function of the compaction cycle for stacks of 3 plies of fabric NCF-HP compacted at 1 MPa

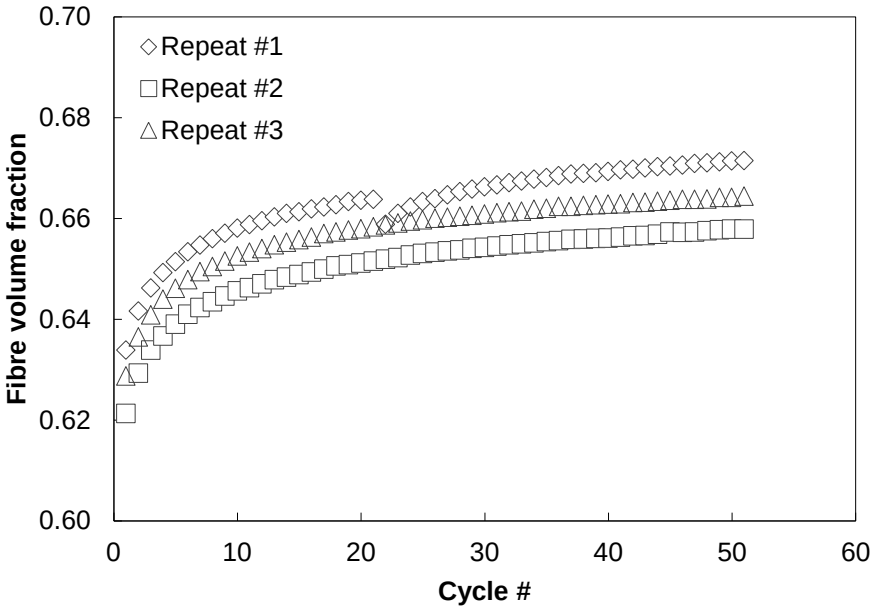


Figure B.2: Fibre volume fraction values as a function of the compaction cycle for stacks of 6 plies of fabric NCF-HP compacted at 1 MPa

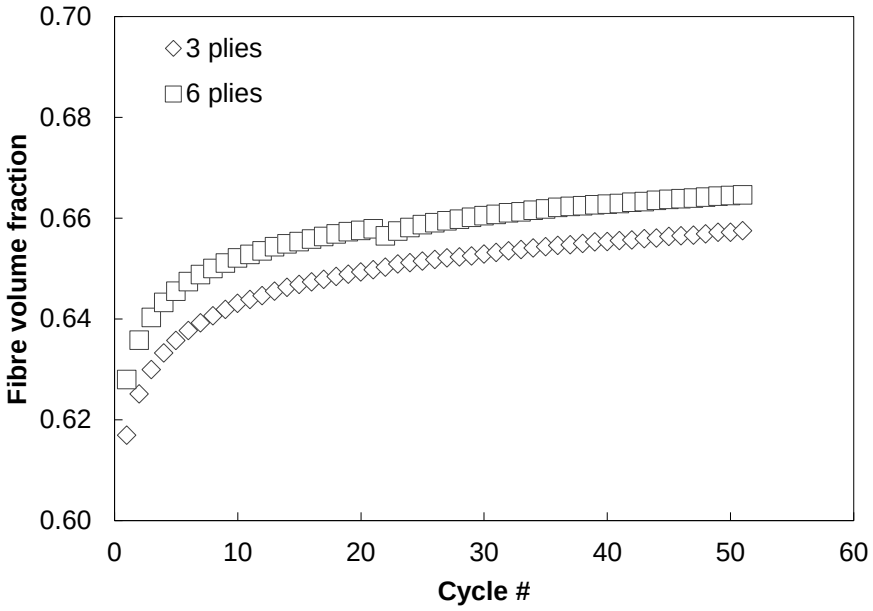


Figure B.3: Comparison of the average fibre volume fraction values as a function of the compaction cycle between stacks of 3 plies and 6 plies of fabric NCF-HP compacted at 1 MPa

# Appendix C: Fill factor evolution for interleaved RFI experiments

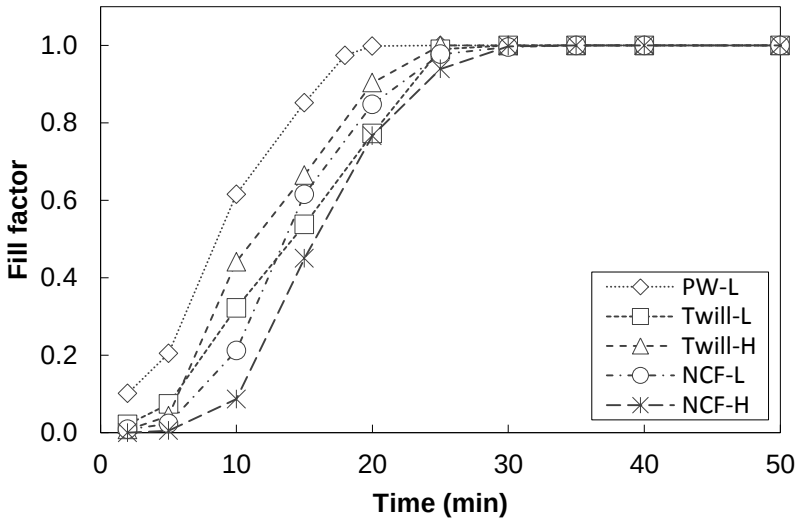


Figure C.1: LEO 2376 resin fill factor evolution during interleaved RFI processing

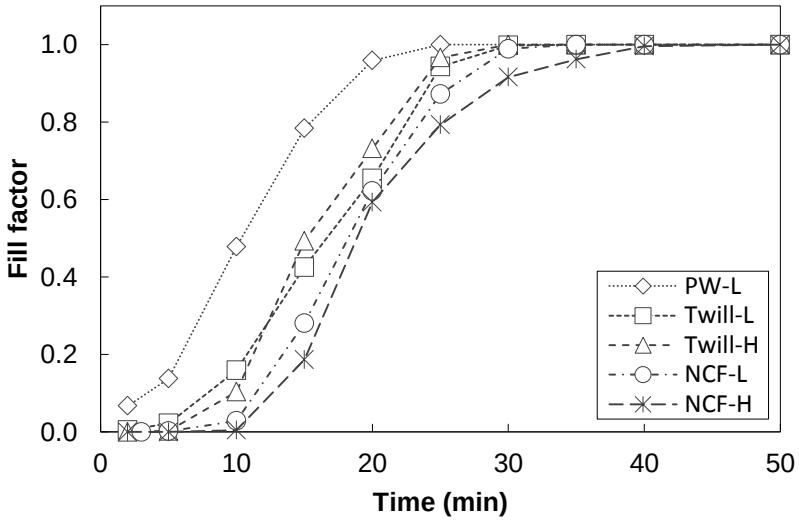


Figure C.2: LEO 2377 resin fill factor evolution during interleaved RFI processing

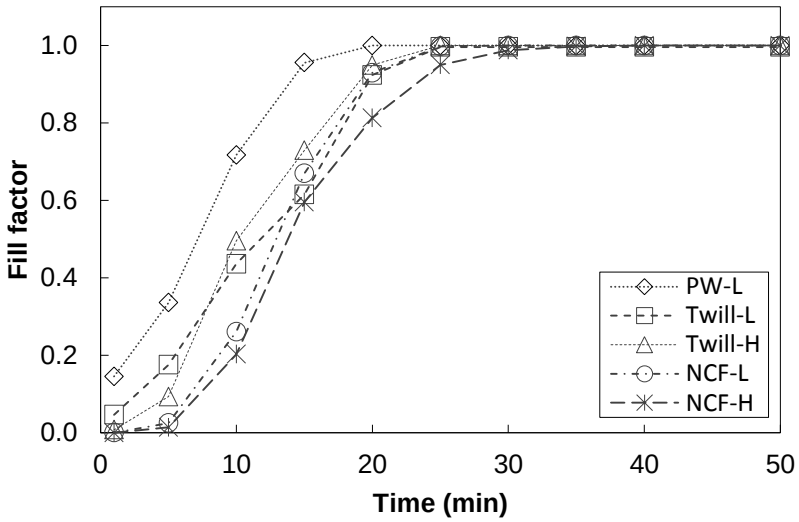


Figure C.3: LEO 2396 resin fill factor evolution during interleaved RFI processing

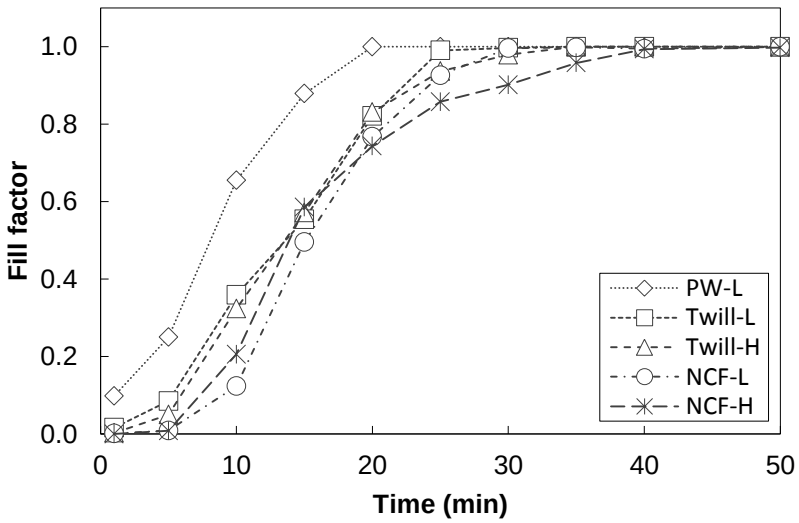


Figure C.4: LEO 2397 resin fill factor evolution during interleaved RFI processing

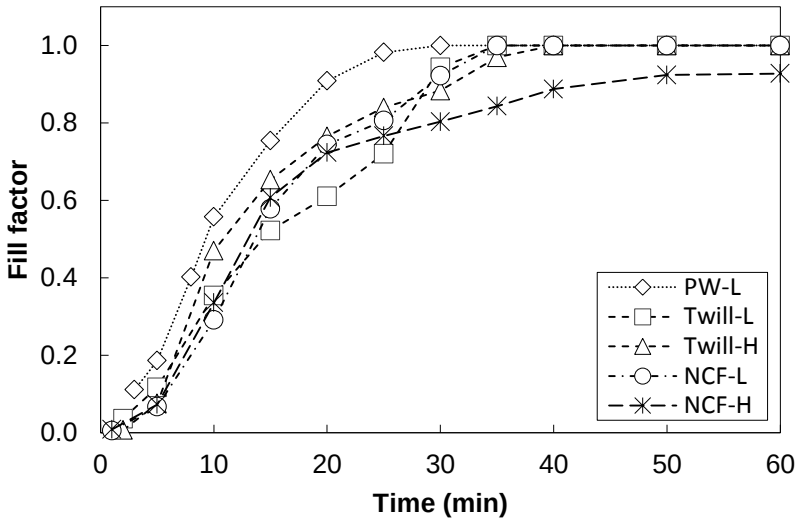


Figure C.5: SA 70 resin fill factor evolution during interleaved RFI processing

# Appendix D: Fill factor evolution for bulk RFI experiments

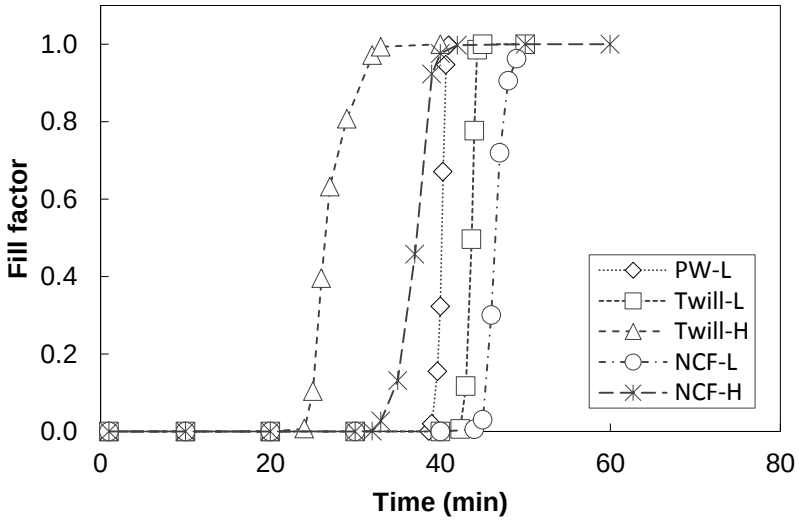


Figure D.1: LEO 2396 resin fill factor evolution during bulk RFI processing

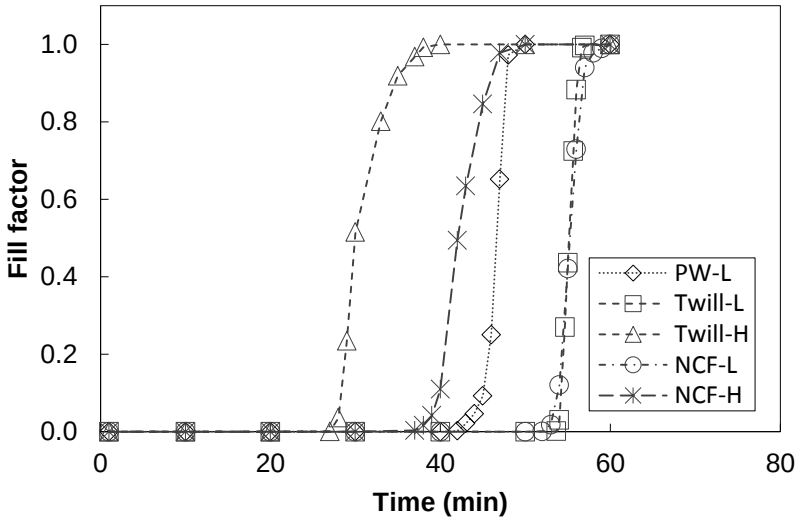


Figure D.2: LEO 2397 resin fill factor evolution during bulk RFI processing